The Study of the Diffuse X-ray Background between 150 eV and 280 eV with the Diffuse X-ray Spectrometer (DXS)

By

Jeffrey Paul Morgenthaler

A DISSERTATION SUBMITTED IN PARTIAL FULFILLMENT OF THE

REQUIREMENTS FOR THE DEGREE OF

DOCTOR OF PHILOSOPHY

(PHYSICS)

at the

UNIVERSITY OF WISCONSIN – MADISON

1998

Abstract

The Space Physics Group and the Space Science and Engineering Center of the University of Wisconsin have designed and built a novel instrument, the Diffuse X-ray Spectrometer (DXS), for the spectroscopic study of the diffuse X-ray background. Each of the two identical units consists of a one foot by two foot curved lead stearate crystal panel and a position-sensing proportional counter. The crystal panels reflect X-ray photons into the proportional counters according Bragg's law. The instrument, sensitive to X-ray photons between 42 Å and 83 Å with $\Delta\lambda$ (FWHM) $\sim$2.5 Å, observed the X-ray background for about 40,000 seconds on Space Shuttle flight STS 54 in January 1993. This thesis presents the formulation of the detector response functions from pre- and post-flight calibration data and the data reduction methods used for the in-flight spectral data. The resulting estimates of the wavelength scale accuracy (0.3 Å), the flat-field response (corrected to better than 3%), the absolute flux calibrations ($\sim$10%), and the detailed agreement of the spectral shape of the instrument response to three mono-energetic input sources are also discussed. Several plasma emission models are compared to the observed spectra, none of which fit satisfactorily. These results constrain current theories concerning the origin and nature of the diffuse X-ray background.

Acknowledgments

I would like to acknowledge the contributions of the following people to the DXS project:

University of Wisconsin Space Science and Engineering (SSEC) Personnel

Project Manager:
Robert Paulos

Engineers and Technicians:
Fred Best
Nicolas Ciganovich
Michael Dean
Timothy Dirkx
Mark Mulligan
Dave Petre
Evan Richards
Jerry Sitzman
John Short
Mark Werner

Computer Programmers:
Dean Dionosotes
William Hibbard
W. Warren Miller
Scott Mindock
Brian Paul
W. Walter Wolf

Contents

List of Tables

List of Figures

Chapter 1

Introduction

The goal of this chapter is to provide the reader with a brief overview of observations and theories of the diffuse X-ray background for photon energies in the range 78 eV to 284 eV. This chapter reviews the evidence that these photons are likely produced by a hot (10^6 K) plasma that fills a void (or bubble) in the more dense, cooler material in the Galactic interstellar medium. Direct evidence of the thermal origin of the diffuse X-ray background in this energy range will be shown.

1.1 Early Observations

In 1962, a sounding rocket carrying Geiger counters was flown to observe X-rays predicted to be coming from the moon. Instead, the experiment detected an X-ray point source, now known as Cygnus X-1, and a diffuse source of X-rays, the diffuse X-ray background. The experiment carried three Geiger counters, two of which worked properly. The two working counters had mica windows of differing thickness. The different X-ray absorption cross sections of the windows allowed for a crude spectral measurement which suggested that the flux of X-rays coming from the point source and the diffuse source were "soft," that is with the majority of their flux arriving below the instrument lower energy sensitivity of 2 keV (Giacconi *et al.* 1962). The diffuse flux detected by the Giacconi group was isotropic and therefore assumed to be cosmic (e.g. Gould & Sciama 1964).

In the late 1960s several groups observed the cosmic soft X-ray flux predicted by Giacconi *et al.* with mechanically collimated thin windowed "flow" proportional counters (e.g. Bunner *et al.* 1969 and references 1-3 therein). These detectors had sensitivity to X-rays with energies as low as ∼150 eV. The goal of these experiments was to probe Galactic structure by observing the absorption of the cosmic X-rays by neutral material in Galactic interstellar space.

Detection of soft X-ray flux in the plane of the Galaxy, where very large absorption was

expected, suggested that part of the soft X-ray flux was not cosmic but local to the Galaxy, or to the solar neighborhood (Bunner *et al.* 1969). Diffuse X-ray observations in the direction of the Small Magellanic Cloud have set a limit on the contribution of the extragalactic component of the diffuse X-ray background at energies below 284 eV at 25% (McCammon *et al.* 1971). ROSAT detected a clear shadow of the Moon in the soft X-ray background (Schmitt *et al.* 1991). The question is then, what is responsible for this flux of soft X-rays that originates somewhere between the Moon and the Magellanic Clouds?

1.2 Elementary Astrophysics

According to Williamson *et al.* (1974), the X-ray background from $\sim$100 eV to 284 eV likely originates from "widely distributed regions of interstellar gas with temperatures in the region of 10^6 K." Since this hypothesis has remained essentially unchallenged for 23 years, it is important to review its basis and continued evidence for its support.

With the following argument, Williamson *et al.* rejected the possibility that the soft X-ray background might originate from non-thermal mechanisms, including synchrotron emission in the Galactic magnetic field and inverse Compton scattering from the cosmic microwave background and starlight:

> ...the lifetime of the 3.5×10^{13} eV electron required to produce 0.25 keV electrons in a 3×10^{-6} gauss field is less than 10^4 years due to inverse Compton and synchrotron losses.... Electrons of $\sim$240 MeV can scatter the 3° [cosmic microwave background] radiation into the very soft X-ray region, but the required number of energetic electrons is unreasonably large. Their energy density would be 10^2 eV cm^{-3}, and the flux of high energy γ-rays (E > 100 MeV) produced by bremsstrahlung of these electrons on the interstellar gas would be $\sim$10^3 times that measured. Electrons of $\sim$6 MeV can scatter starlight into the very soft X-ray region. But the energy density of these electrons would be 1500 eV cm^{-3}, and there would result an interstellar ionization rate $\sim$250 times the upper limit set by Field, Goldsmith, & Habing (1969).

The observed smoothness of the soft X-ray background rules out the possibility that stars or other point sources are responsible (Vanderhill *et al.* 1975; Levine *et al.* 1977). Juda (1988)

rules out the possibility that the X-ray background detected in the plane of the Galaxy might be the result of the scattering of extra-galactic X-rays from interstellar dust grains. The shadow of the moon (Schmitt *et al.* 1991) indicates that a very local solar component is unlikely. The simplest remaining explanation is that an X-ray emitting plasma is filling a large fraction of at least the local Galactic neighborhood.

Plasma with temperatures in the neighborhood of 10^6 K radiates X-rays, primarily in the form of atomic emission lines (Raymond & Smith 1977). Thus, an important test of the consistency of the thermal plasma hypothesis is the detection of emission lines in the spectrum of the soft X-ray background. Using gas scintillation proportional counters, Inoue *et al.* (1979) detect the 570 eV OVII emission line toward Hercules. A sounding rocket using silicon detectors saw diffuse OVII, OVIII, CV, and CVI soft X-ray emission lines between 300 eV and 1000 eV near the North Polar Spur (Schnopper *et al.* 1982). The Space Physics group and the University of Wisconsin designed a detector with even better spectral resolution sensitive down to energies as low as 150 eV (Borken & Kraushaar 1976). With some modifications, this experiment became the Diffuse X-ray Spectrometer (DXS), the subject of this thesis. As shown briefly in §1.5 and in more detail in Chapter 6, the DXS spectra clearly show the presence of many atomic lines, thus confirming the thermal origin of the diffuse soft X-ray background.

1.3   More Observations: Sky Surveys

McCammon & Sanders (1990) wrote a review article concerning the observation and theoretical study of the diffuse X-ray background from the mid 1970's to 1990. During this time, three soft X-ray all-sky surveys were conducted with moderate (6 and 3 degree) spatial resolution: Wisconsin (McCammon *et al.* 1983), SAS 3 (Marshall & Clark 1984), and HEAO-1 (Garmire *et al.* 1992). The Wisconsin survey obtained some spectral energy resolution by using proportional counters with different window coatings. The Wisconsin survey was complimented by partial sky coverage at very low energies, ranging from 78 eV to 188 eV (Bloch *et al.* 1986; Bloch 1988; Juda 1988). As discussed in McCammon & Sanders (1990), the broad-band spectra of these surveys are consistent with emission from a plasma at 10^6 K, but themselves do not preclude another emission mechanism.

Since 1990, the ROSAT all-sky survey (Snowden *et al.* 1995, 1997) has been completed.

Snowden *et al.* (1995) compare the total counting rates in the individual energy bands of all four surveys at coarse spatial resolution and find agreement for most of the bands within a few percent. The largest discrepancy between the ROSAT and other surveys is in the 160 eV–284 eV band where the X-ray flux inferred from the ROSAT counting rate is systematically 10% higher than the other surveys at this energy. Snowden *et al.* (1995) attribute this discrepancy to a 10% over-estimate of the ROSAT effective area in the 160 eV–284 eV band.

Snowden *et al.* (1990) summarize the implications of the spatial variation found in the soft X-ray background. The counting rates in the two spectral bands below $\sim$188 eV are correlated, with the brightest emission in each occuring at high Galactic latitudes. The emission in the next higher band (160 eV–284 eV) is also strongest at high latitudes, but not as well correlated with the lower energy bands as they are with each other. Snowden *et al.* argue that because the absorption cross section of the neutral interstellar medium is substantially different in these three bands, it is unlikely that much absorbing material is found along the line of sight to the source of the X-ray emission, since that would distort the observed correlation (see also Juda 1988).

The physical picture proposed by Snowden *et al.* puts the Sun inside of a cavity that is relatively free from neutral interstellar material. Additional evidence supporting this model is the anti-correlation of the X-ray with neutral HI emission. An anti-correlation would be expected if the source of X-rays was behind the absorbing material, but the magnitude and behavior as a function of energy would be much different. Rather, Snowden *et al.* attribute the anti-correlation to a *displacement* of the neutral material formerly inside the cavity, so that in directions where the emission is strongest, the cavity extends the furthest and has displaced the most neutral material, resulting in the lowest HI column density.

1.4   More Astrophysics: The Local Bubble

Several possible theoretical interpretations of observational evidence outlined in the previous section (§1.3) are discussed in a review article by Cox & Reynolds (1987). The model favored by Cox & Reynolds is one in which the Sun occupies a cavity, or bubble, in the neutral interstellar medium that has been formed by one or more supernova explosions within a few tens of parsecs from the Sun. Cox & Reynolds argue that the bubble is about 10^7 years old and near thermal equilibrium. The bubble is not spherical, but peanut shaped as viewed from the

Galactic center, about 200 parsecs high and 50–100 parsecs wide (Snowden *et al.* 1990). This is the shape expected for an explosion in an ambient medium with a vertical pressure gradient. Other models considered by Cox & Reynolds do not postulate a pressure-confined bubble but rather predict that the conditions in the immediate several hundred parsecs are typical of the interstellar medium.

In addition to verifying the general thermal nature of the diffuse X-ray background, one of the goals of the DXS project is to provide constraints on models that predict X-ray spectral emission in the DXS pass band. Chapter 6 discusses several such models.

1.5   The DXS observation

It is important to consider what parts of the sky DXS observed in order to understand what constraints DXS can put on theories of the origin of the diffuse X-ray background. DXS observed a swath of the sky 15° high and ∼140° wide roughly aligned with the Galactic plane, centered at a Galactic longitude of 230°. The absorption length of photons with energies below 284 eV in typical Galactic mid-plane material is less than 100 pc. This is small compared with the distance of Sun from the center of the Galaxy (∼10 kpc). Thus, in diffuse X-rays, DXS observed only local emission. DXS also observed parts of the Vela and MonoGem supernova remnants. The Vela remnant is about 500 pc away (e.g. Kahn *et al.* 1985), the MonoGem remnant, ∼300 pc away (Nousek *et al.* 1981).

What should the DXS spectra look like? Even before the prediction that the soft X-ray background was caused by hot gas, work had begun on calculating the emission properties of plasmas (Cox & Tucker 1969). This work found that the primary cooling mechanisms for gas between 10^4 and 10^7 K are not continuum processes, but rather the emission of lines of the ionized elements in the carbon to iron range. Subsequent work calculated as a function of temperature and atomic abundance the distribution of ionic states of the more common atomic species and the major emission lines expected for a plasma in equilibrium, given the state-of-the-art atomic physics at that time (Raymond & Smith 1977). For a solar abundance plasma at 10^6 K, the hybrid Raymond & Smith/Liedahl (1997) equilibrium plasma model discussed in §6.2.4 contains thousands of atomic lines in the 150 eV to 284 eV range, as shown in Figure 1.

What do the DXS spectra actually look like? Figure 2 shows one of the measured DXS spectra fit by a single temperature equilibrium plasma emission model described in §6.2.4.
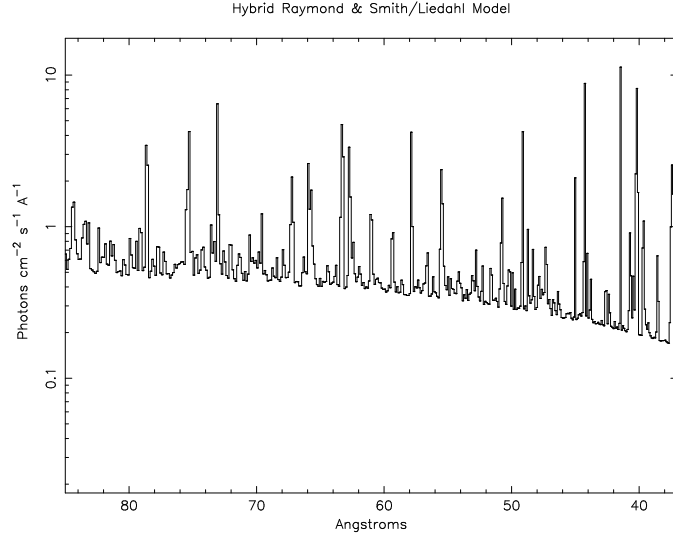
Figure 1: Hybrid Raymond & Smith/Liedahl (1997) equilibrium plasma emission spectrum model for $T = 1.23 \times 10^6$ K.

Though the model is not formally a good fit, it clearly shows that the major features of the DXS spectrum can be reproduced with an equilibrium plasma model. The major spectral features observed by DXS are complexes of individual atomic lines which are blended due to the limits in the instrument's resolving power. This is the evidence for the thermal origin of the diffuse X-ray background for emission in the DXS pass-band. A more detailed discussion of these results and comparison to other equilibrium and non-equilibrium plasma emission models can be found in Chapter 6.

How well is the DXS instrument understood? Chapter 2 discusses the construction of the DXS instrument and the models of its performance. The post-flight calibration of the instrument is discussed in Chapter 3. A summary of the calibration results can be found in Figure 3, which shows the combined DXS calibration spectrum overlayed with a composite model of the three calibration sources. As argued in Chapter 3, the most noticeable discrepancy between model and calibration, found in the boron K-α line at 67 Å, is likely due to do an inaccurate model of the calibration source, rather than an inaccurate instrument response model.

The possibility that the poor quality of the model fits to in-flight spectra are due to problems in the collection or reduction of the in-flight data is addressed in Chapters 4 and 5. To summarize, simple tests show that the reduction methods are self consistent and repeatable and
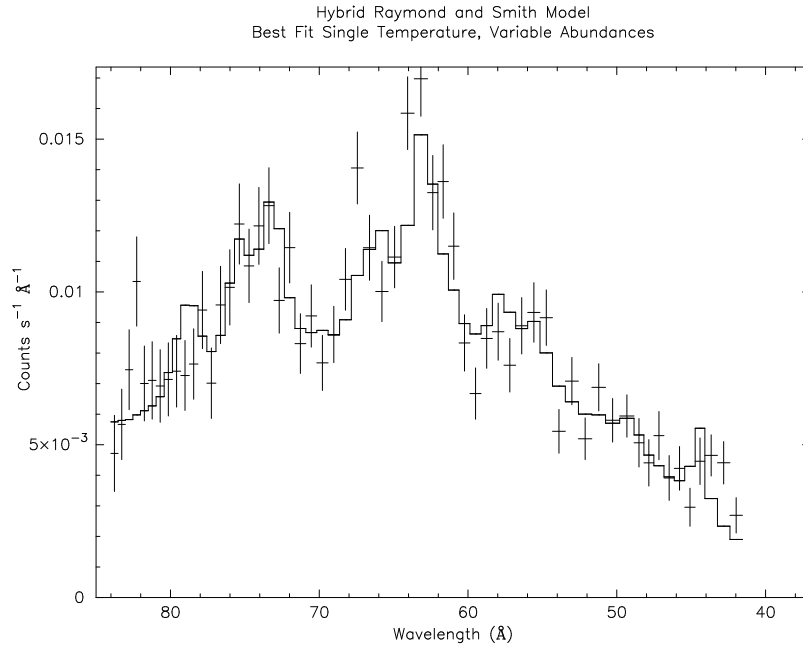
Figure 2: Composite DXS spectrum best fit to a single temperature hybrid Raymond & Smith/Liedahl (1997) equilibrium plasma model shown in Figure 1 and discussed in §6.2.4.

that the X-rays detected by DXS came from outside the instrument. However, there was an unexpected ∼20% change in total DXS counting rate over the flight. In spite of this variation, the DXS counting rate is always within 20% of the counting rate inferred from earlier all-sky surveys and the *shape* of the spectrum used for model spectral fitting does not substantially change. Therefore, the poor quality of the model fits to the flight spectra are likely due to inadequate models.

Finally, Chapter 7 discusses how the body of evidence presented in this thesis supports the conclusion that the diffuse X-ray background between 150 eV and 284 eV is the result of thermal processes, most likely a plasma near equilibrium at $\sim 10^6$ K.

8
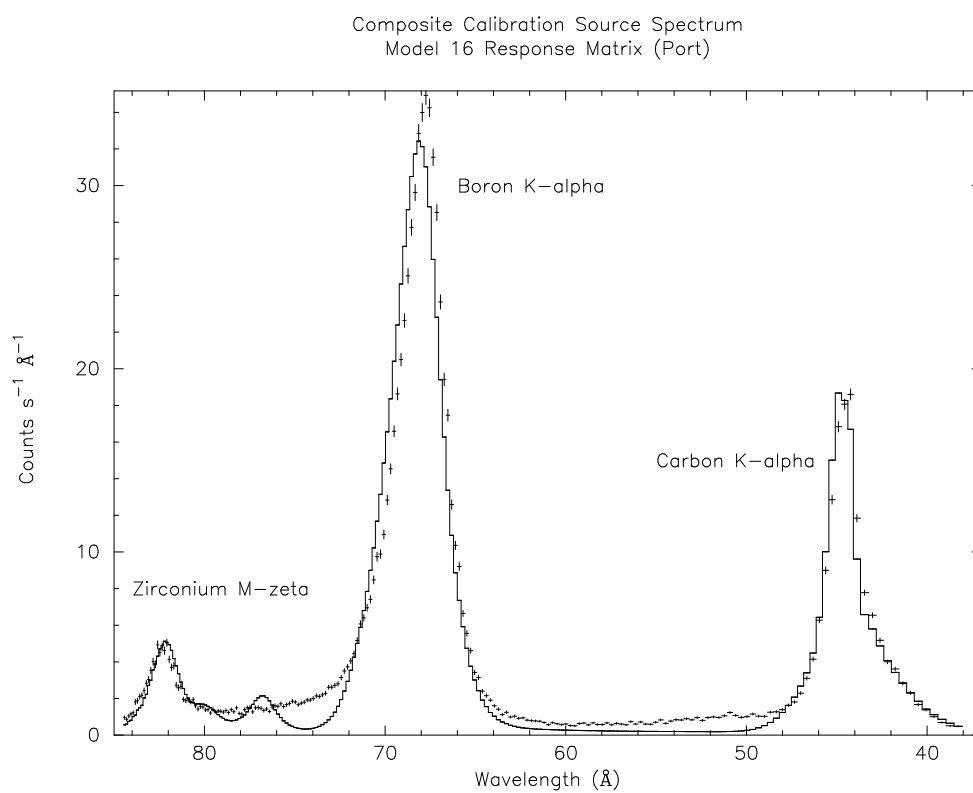
Figure 3: Model fits to three DXS post-flight calibration sources. Same as Figure 63 but with a linear Y-axis.

Chapter 2

The DXS Experiment

This chapter describes the design and construction of the Diffuse X-ray spectrometer (DXS) and its function as a Space Shuttle Payload of Opportunity. The first section in this chapter is a general description of how the instrument works. Sections 2.2 and 2.3 describe in detail the two most important components of the instrument, the X-ray reflecting crystal panels and the position-sensing proportional counters. The important details of flight operations are presented in §2.4, and §2.5 describes in detail the model of the spectrometer that is used in the spectral fitting of the data.

2.1 Introduction

Bragg reflection is the fundamental physical principle that allows the Diffuse X-ray Spectrometer (DXS) to measure the spectrum of the soft X-ray background with sufficient accuracy to determine the presence of atomic lines. Photons Bragg reflect from crystal materials that have regularly spaced planes of X-ray scattering atoms. The spacing between the scattering planes, D, and the wavelength of the incident light, λ, determine the reflection angle, α, according to the equation:

$$\frac{n\lambda}{2D} = \sin \alpha \qquad (2.1)$$

The integer n, also known as the *order* of the Bragg reflection, is the difference in path length (in units of wavelength) between parallel rays scattering from adjacent surfaces. Figure 4 illustrates the well-known derivation of the Bragg law.

The design of DXS takes advantage of the fact that Bragg reflection relates reflection angle to energy. Figure 5 shows a cross-sectional view of one of the DXS detectors. The detector has three major working parts: the X-ray reflecting crystal panel, the collimator, and the position-sensing proportional counter. Photons Bragg reflect from the crystal panel
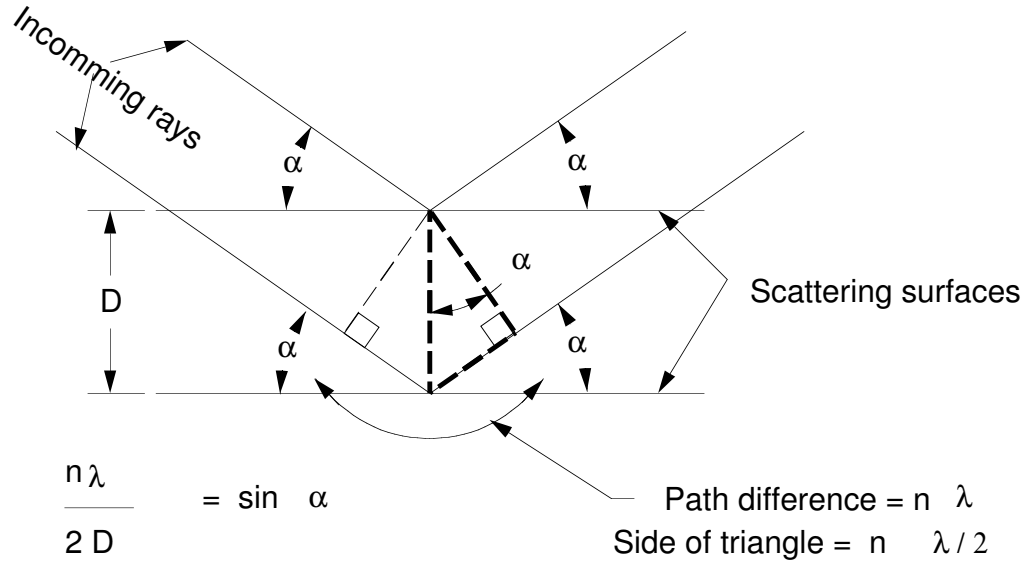
Figure 4: Derivation of the Bragg law of reflection. Constructive interference occurs when the angle of the reflection equals the angle of the incidence and the path difference between incoming rays differs by an integer number of wavelengths (nλ).

and are directed toward the proportional counter. The collimator stops any photons from entering the proportional counter unless they are within $\sim 15°$ of the line perpendicular to the entrance window of the proportional counter (i.e., vertical in Figure 5). This constraint, together with the curve of the crystal panel, causes low energy (long wavelength) photons to enter the position-sensing proportional counter on one side and high energy (short wavelength) photons on the other, thus providing spectral energy dispersion.

Note that photons of different energies pictured schematically in Figure 5 enter the instrument aperture from different directions. In order to collect photons of all energies in the instrument pass-band from an extended region on the sky, the whole crystal panel and proportional counter system is rotated back and forth about its center of mass. The entire apparatus is shown in Figure 6.

Figure 7 shows the position of the two DXS instruments in the shuttle bay. When scanning the sky, each instrument collects X-ray photons from a 15° by $\sim 170°$ swath of the sky with the long dimension of the swath aligned with the wings of the shuttle orbiter (see cover illustration).

The spectral resolving power of DXS is limited by the intrinsic resolving power of the lead stearate crystal, the collimator opening angle, and the spatial resolution of the position sensing
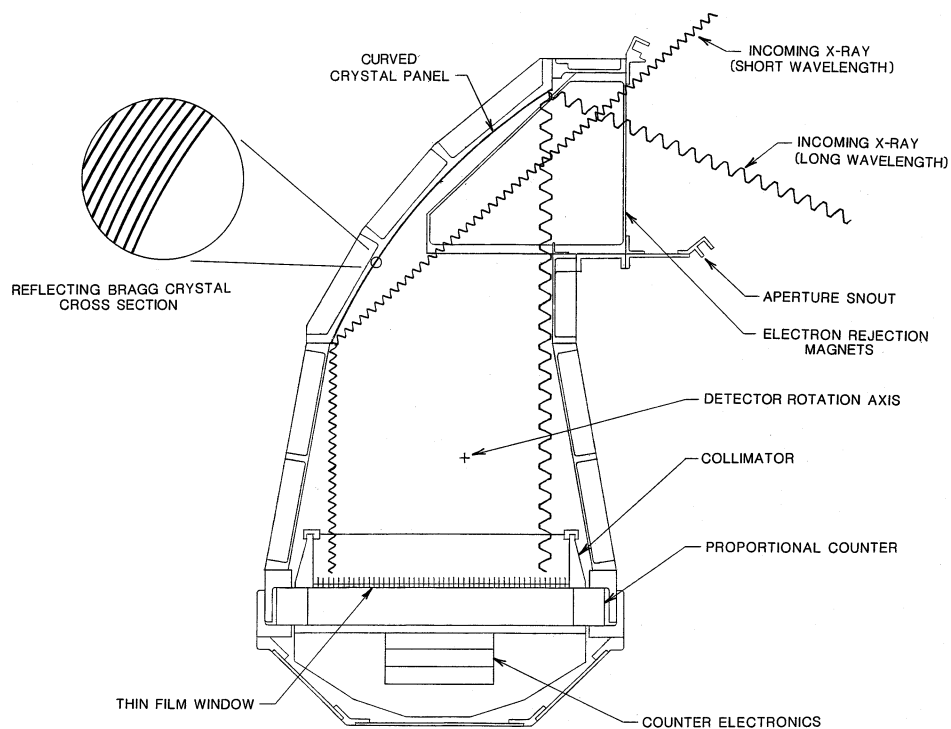
Figure 5: Cross-sectional view of one of the DXS detectors showing photon paths and some of the detector's major parts. The X-ray reflecting crystal panel is made of 200 layers of lead stearate.

SUN SENSOR
- Detects high
  ambient light levels

GAS FILL PORTS

APERTURE SEAL PLATE
- Keeps sunlight and dust
  from crystal panel

RADIATION MONITOR
(Hidden from view)
- Monitors the charged particle
  environment on-orbit

LATCH ASSEMBLY
- Secures the detector
  during launch and landing

DETECTOR
PROPORTIONAL COUNTER
DETECTOR INTERFACE UNIT
CALIBRATION TUBE & ELECTRONICS
COUNTER FILTER
LEAD STEARATE CRYSTAL PANEL

SCAN MOTOR
- Rotates the detector
  back and forth by ~180°

DETECTOR FILTER
- Reduces radiated emissions

ELECTRICAL
INTERFACE
BOX
- The power and signal
  connection to the
  SPOC avionics

POWER CONVERTER SUBSYSTEM
- DC power conversion box

GAS MANIFOLD BOX
- Regulates and monitors
  gas pressure

CONTROL ELECTRONICS ASSEMBLY
- Consists of the Detector Controller
  and Motor/Solenoid Driver

SPOC PLATE

GAS BOTTLE HOUSING
- Contains P10 gas
  for the proportional counter

DIFFUSE X-RAY SPECTROMETER

Figure 6: Assembly drawing of one of the DXS instruments showing major components. SPOC stands for "Shuttle Payload of Opportunity Carrier" and P10 gas is 90% argon and 10% methane.

SHEAL-I Configuration

SPOC Mounting Plate

Side of Shuttle Bay

Diffuse X-Ray Spectrometers

Back of SPOC Mounting Plate

SPOC Avionics

Rigid Harness Boom

GAS Adapter Beams

Side of Shuttle Bay
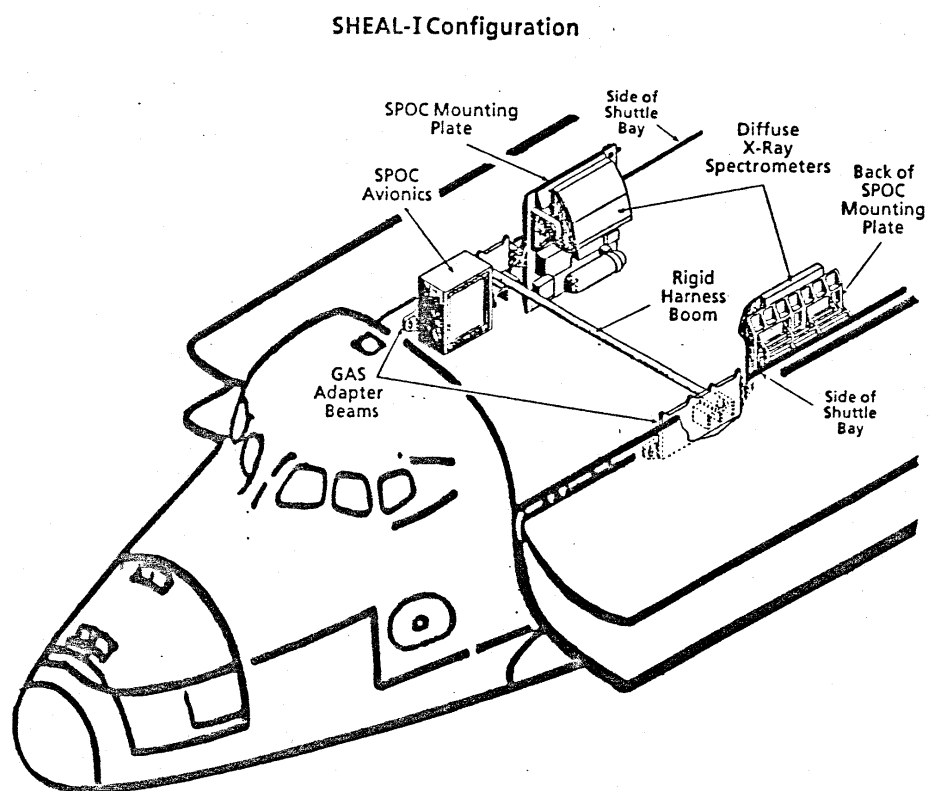
Figure 7: DXS instruments mounted to shuttle.

proportional counter. Because of the importance of each of these subsystems in determining the final performance of the detectors, their construction and function are considered in detail in the following sections.

Most of the parts of the DXS instrument were designed, built, and assembled at either the Space Physics Laboratory or the Space Science and Engineering Center (SSEC) of the University of Wisconsin at Madison. Any details not covered in this document may be gleaned from the DXS project documentation, which is kept at the SSEC.

2.2   Crystal Panels

As described above, the curved crystal panels provide a relationship between photon energy and reflection angle by the Bragg law (Equation 2.1). In order to Bragg reflect X-rays with energies below 284 eV, or wavelengths longer than 44 Å, the DXS crystal needed to have a $2D$ spacing of greater than 88 Å. Such a large spacing is not available in naturally grown crystals. Instead, a Langmuir–Blodgett multi-layer pseudo-crystal of lead stearate was used. The lead stearate multilayers used for DXS have a $2D$ spacing of 101.5 Å (see "$2D$ spacing of lead-stearate" subsection of §3.2.3). Note that in this text, I often use the word "crystal" to mean multi-layer pseudo-crystal.

In the original DXS proposal, another spectrometer pair, using thallium acid phthalate (TAP) with $2D$ spacing of 25.6 Å was designed to cover wavelengths from 11 Å to 22 Å. This spectrometer was never built due to funding constraints.

2.2.1   Crystal Panel X-ray Reflectivity

In real crystal reflection experiments, the angles of reflection for a significant fraction of incident photons deviate from the nominal Bragg angle by as much as one degree. The distribution of reflectance as a function of the angle of incidence is know as the "rocking curve" of a crystal. Another important quantity not described by the Bragg law is the total efficiency of the reflection, or the integrated reflectivity of a crystal.

Henke *et al.* (1982) use approximations to electro-magnetic scattering theory to calculate rocking curves and integrated reflectivities for ideal Langmuir–Blodgett multilayers. They

compare their work to other theoretical calculations, but not to measurements of real mul-tilayers. Measurements show that the rocking curve width is significantly wider than that calculated by Henke *et al.* (1982). Henke, Gullikson, & Davis (1993) calculate the effect of non-ideal multilayer structure on integrated reflectivity but not on rocking curve width.

Because there was no accurate theoretical treatment of actual lead stearate multi-layers at the time DXS was built, the Wisconsin space physics group conducted a series of experiments to determine the X-ray multi-layer reflective properties empirically. One apparatus, located at the Space Physics Laboratory on the University of Wisconsin–Madison campus consisted of a long (∼3 meter) evacuated collimating pipe attached to a Henke X-ray tube. The various target materials (most often boron) were used in the Henke X-ray tube to produce characteristic atomic line emission. At the other end of the collimating pipe, crystal samples were mounted to a turntable. Small proportional counters mounted near the turntable were used to measure the initial beam intensity and reflected beam intensity. Repeated measurements on the same crystals over time show that the accuracy of this system in determining peak and integrated reflectivity is 10∼15% (see §2.2.3).

Rocking curves at low energies could not be accurately measured with the Henke X-ray tube device since the intrinsic resolving power of the lead stearate Bragg multi-layers was high enough to resolve the line shape of the X-ray source used in the apparatus. Instead, rocking curves were measured with an X-ray monochromator connected to the Tantalus II synchrotron light source at the Physical Sciences Laboratory (PSL) in Stoughton, Wisconsin. Due to the difficulty of access to this facility, rocking curves were only measured on an early sample of multilayers.

The most exhaustive set of rocking curve data was taken on a multi-layer produced by Henke's group at the University of Hawaii, named "Henke #2." Figures 8, 9, and 10 show the original Henke #2 data together with the results of an empirical model fit to the data. The empirical model has four components: the specular reflectivity of the crystal, given in Henke *et al.* (1982), which is dominant at low reflection angles; two Gaussian components that define the Bragg reflection peak, and a one sided Lorentzian component that provides the observed excess between the specular reflection domain and the low angle side of the Bragg peak. The two Gaussian components of the model peak at the same angle, but have different heights and widths. The ratio of Gaussian widths and heights were fit to the data as functions of wavelength and reflection angle, respectively. The full-width at half-max (FWHM) of the
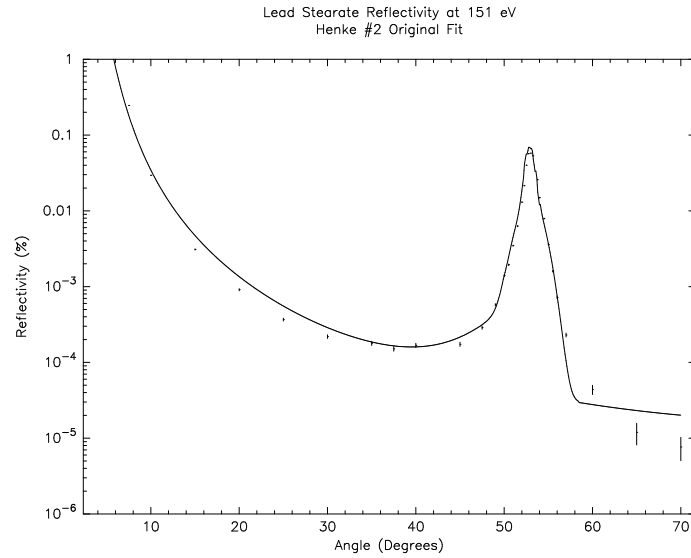
Figure 8: Lead stearate reflectivity as a function of angle at 151 eV. Model based on the "Henke #2" crystal.

sum of the Gaussian components was also fit as a function of wavelength. The normalizations of the Gaussian components was set by the integrated reflectivity within four degrees of the peak, which was fit as a function of wavelength. The Lorentzian component, which was fit as a function of reflection angle, was also included in the model calculation of the integrated reflectivity, so that the normalization of the whole model curve could be accurately fit to the data.

Estimates for the rocking curve of the second and third order Bragg reflections were constructed from the first order reflection shapes in the model 14 response matrix (see Appendix A). Insufficient data were collected to fit the integrated reflectivity of the second and third order reflections as a function of energy. Instead, the second and third order integrated reflectivity functions were assumed to be a constant factor below the first order integrated reflectivity function. The factors were constructed from aluminum K-α and carbon K-α multi-reflection data. The integrated reflectivity of the second order carbon K-α peak is a factor of 2.2 below that of the first order carbon K-α peak. The ratio of the integrated reflectivities of the second and third order Aluminum K-α peaks is 1.13. Thus, the ratio between first and third order at all energies has been taken to be 2.0. It is important to note that the ratio between the integrated reflectivities of the first and second order Aluminum K-α peaks is 6.8. Thus, for the

Lead Stearate Reflectivity at 183 eV
Henke #2 Original Fit
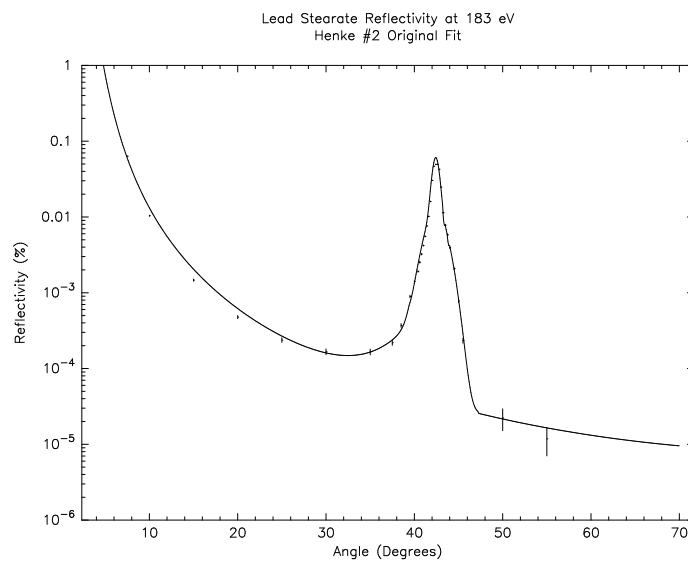
Figure 9: Lead stearate reflectivity as a function of angle at 183 eV. Model based on the "Henke #2" crystal.

Lead Stearate Reflectivity at 277 eV
Fit to Henke #2 Sample Crystal
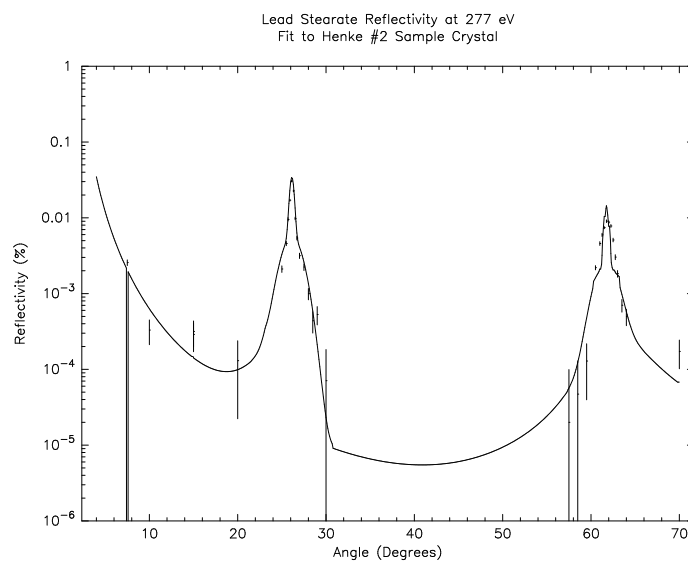
Figure 10: Lead stearate reflectivity as a function of angle at 277 eV. Model based on the "Henke #2" crystal.

Figure 11: Lead stearate intrinsic resolving power, $\lambda/\Delta\lambda$ as a function of energy.

higher energies in the DXS pass-band, the modeled integrated reflectivity of the second and third orders may be high by up to a factor of three.

The model FWHM of the Henke #2 crystal can be used to estimate the intrinsic resolving power, $\lambda/\Delta\lambda$, of the lead stearate crystals used in DXS. Figure 11 plots this as a function of energy. Keep in mind that with a $2D$ spacing of 101.5 Å, lead stearate cannot reflect X-rays with energies less than 122 eV.

2.2.2 Fabrication of the DXS Crystal Panels

Like other Langmuir–Blodgett multilayer pseudo-crystals, the DXS lead stearate crystals are synthetically grown (Charles 1971; Henke 1964). A drop of stearic acid was placed on the surface of a large tank of water with lead atoms dissolved in it. The lead bonds to one end of the stearic acid chain to form lead stearate. Since the lead end of the 25 Å long molecule is hydrophilic and the other end hydrophobic, the molecules stand on end at the surface of the water. A long float was then used to compress the molecules together on the surface of the tank of water. A large sheet of Plexiglas ($0.030 \times 6 \times 14$ inches) was then dipped in and out of the tank of water. On each pass of the plastic through the water, a monolayer of the lead stearate molecules is deposited on the sheet of plastic. If in one layer, the hydrophilic, lead end of the molecule faces toward the plastic, the next layer deposits with the lead end facing

Table 1: Integrated reflectivity of flight crystal panels at 183,3 eV.

Instrument	Crystal Number	Integrated Reflectivity ($\times 10^{-4}$ radians)
Port	402	6.2
	409	6.3
	405	6.3
	403	8.1
Average:		6.73
Starboard	410	8.0
	404	6.6
	419	6.4
	414	6.4
Average:		6.85
Henke #2		6.05

away from the plastic. Figure 1 of Charles (1971) shows this process schematically. The result is planes of lead atoms separated by ∼50Å from each other by a relatively low-Z material. In this way, 100 planes of lead atoms with a $2D$ spacing of ∼100 Å were deposited on the sheets of plastic to form the DXS flight "crystals."

After creation, the integrated reflectivity of each new crystal panel was measured in the space physics Henke tube apparatus at boron K-α (183.3 eV). The integrated reflectivities of the four crystal panels used in each instrument are listed in Table 1. The average of the Port crystal panel reflectivities is 11% above that of Henke #2, the Starboard average is 13% above that of Henke #2. Thus, the early models of the DXS crystal panel reflectivity simply scaled the Henke #2 integrated reflectivity by 12%. Section 3.2 discusses more sophisticated modifications to the crystal panel reflectivity based on the post-flight calibration data.

After selection based on their integrated and peak X-ray reflectivities, four of the sheets of plastic were then mounted to the inside of the aluminum cylindrical section shown in Figure 5. The first step in the mounting procedure was to coat the inside of the aluminum cylindrical section with double sided tape. Next, starting at the upper end of the cylindrical section, with the end of the plastic braced with a special jig, each sheet was slowly rolled into place. An ice pick was used to push the crystal panel against the adhesive at many points (∼100) without causing large-scale damage to the lead stearate crystals.

Figure 12: Time history of the Port long term witness crystal (crystal #6). The vertical line shows the time of the flight. The last point was taken after the flight.

2.2.3   Witness Crystal System

In order to monitor any environmental conditions that might affect the X-ray reflection properties of the flight crystals, two small "witness crystals" were mounted near each set of flight crystals at all times. One of the crystals, the "long term" crystal was removed once every ~1.5 years and its reflectivity measured. These crystal would then immediately be replaced. The other crystal mounted near the flight crystal was one of a pair of crystals called the "short term" or "swap out" crystals. These crystals were swapped every few months. After each swap, the reflectivity of the recently removed crystal was measured. Other witness crystals not mounted with the flight crystals were kept in a variety of environments and also measured periodically. Figures 12 through 17 show the time history of the integrated reflectivity of the "long term" and "swap out" crystals. The measurements are not of high quality; however, if outlying points are discarded, the plots show that the integrated reflectivity before and after the flight are consistent with the same value. This suggests that the main crystal panel reflectivities were also unaffected by the flight, and they did not degrade during storage before flight.

Figure 14: Time history of one of the the Port swap out witness crystals (crystal #3). The vertical line shows the time of the flight.

Figure 16: Time history of one of the the Starboard swap out witness crystals (crystal #4). The vertical line shows the time of the flight.

Figure 17: Time history of one of the the Starboard swap out witness crystals (crystal "A"). The vertical line shows the time of the flight.

2.3   Position-Sensing Proportional Counters

The position-sensing proportional counters used in DXS are shown schematically in Figures 18 and 19. A thin ($< 1\mu$m) plastic window supported by a fine mesh and the collimator structure (not shown in these figures) contains the counter filling gas at a pressure of 800 torr at 20 C but also allows soft X-ray photons to pass through with reasonable efficiencies (see §3.1.1).

Once inside the proportional counter, an X-ray photon is absorbed photo-electrically by the filling gas, which in the case of DXS is P-10 (90% methane and 10% argon). The resulting photo-electron produces several more electron-hole pairs, which are caused to drift apart by an electric field induced by a 1600 V–1700 V potential difference between anode wires and the proportional counter walls. When the electrons near a main anode wire, they are accelerated enough to ionize other gas atoms. The resulting avalanche of charge is collected on the main anode wire and converted to a voltage pulse by a charge sensing amplifier connected to the wire. One voltage pulse is generated per input photon and the height of the voltage pulse is proportional to the energy of the input photon; hence the name proportional counter.

The charge avalanche onto a main anode induces a mirror charge on the ground-plane

Crystal Panel

Prop Counter Window

Main Anodes

Ground Plane wires (96)
grouped by fours into
24 segments

Lower Veto Anodes

~11"
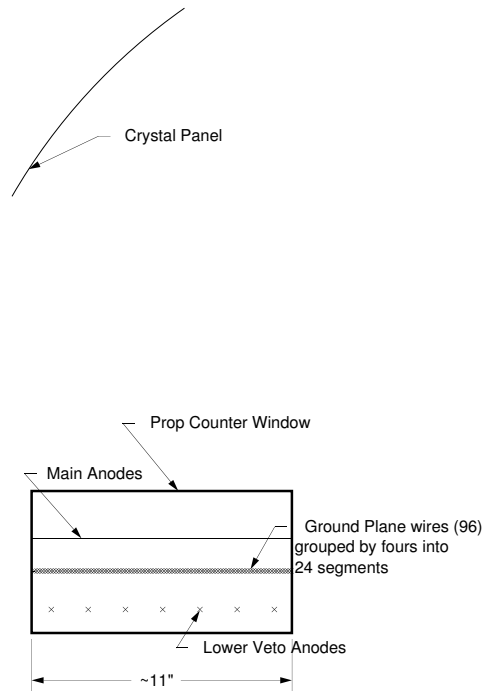
Figure 18: Schematic view of a DXS proportional counter and crystal panels, dispersion cut. The main anode and side veto wires run parallel to the page, the ground-plane and lower veto wires run out of the page. Reflective side of crystal panels are facing to the right.
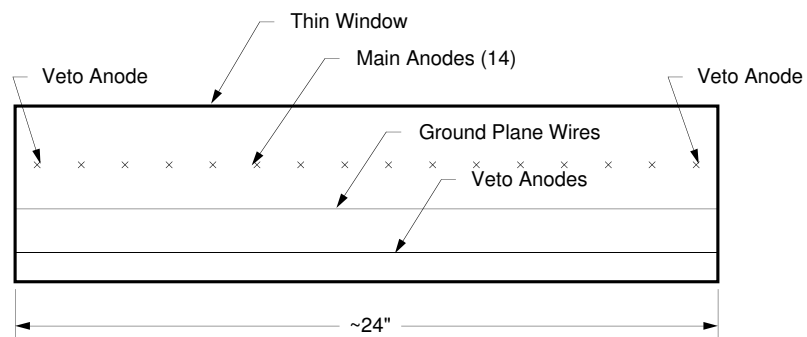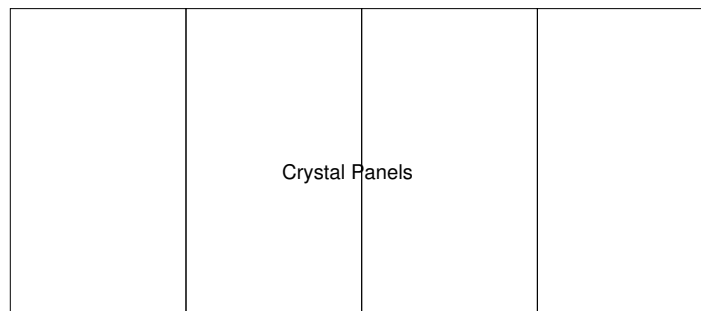
Figure 19: Schematic view of a DXS proportional counter and crystal panels, cross-dispersion cut. The main anode and side veto wires run out of the page, the ground-plane and lower veto wires run parallel to the page. Reflective side of crystal panels are facing the viewer (i.e. as viewed from the right of Figure 18).

wires, with the most charge induced on the wires closest to the avalanche event. The ground-plane wires are themselves connected to charge-sensitive amplifiers which provide signals that are used determine the original position of the X-ray event. Thus, the DXS proportional counters simultaneously produce pulse height and one-dimensional position information.

2.3.1 Position Determination

A two-step algorithm is used to convert the 24 ground plane segment signals into a position on the proportional counter. The first step in the algorithm is to estimate the position of the X-ray event by comparing the ratio of the two highest signals to a table of boundary ratios that were determined empirically during the instrument construction phase. This gives the position accurate to one tenth of a ground plane segment, 0.0457 inches, or one "POS." The results of the spectrometer modeling program presented in §2.5.4 show that this position resolution is high compared to the intrinsic resolving power of the instrument. In the worst case, there are four POS per spectrometer resolving element.

The next part of the algorithm calculates the square of the difference between the measured distribution of the five highest ground plane signals and a grid of sample distributions recorded for sources at evenly spaced positions. The grid spacing is again one tenth of a ground plane segment. Only the three grid points about the first-guess position are evaluated. Finally, a parabolic interpolation of the position of the χ^2 minimum is used to determine the best position of the X-ray event. The value of the square difference distribution at this minimum is used as the "goodness of fit parameter" (GOF). This two-step algorithm is capable of determining the position of a single event to a fraction of the grid spacing, or, in the case of DXS, less than $\frac{1}{100}$ inch. Even with this level of integral linearity, differential non-linearity can cause problems when attempting to measure the count rate as a function of position in the proportional counters. Section 3.1.2, on flat-fielding, discusses the problem of differential non-linearity in more detail.

2.3.2 Details of Construction

In order to increase reliability, half of the main anode wires are connected to one amplifier and half to another. In the original design, the wires alternated and the amplifiers were referred to as the "even" and "odd" amps. The Starboard counter is still configured this way. In the Port

counter, however, the first seven main anode wires (on the left in Figure 18) are connected to the "odd" amplifier and the second seven to the "even." The "even" side of the Port instrument is also the side where the witness crystals are kept, the gain-monitoring cal-tube is mounted (see §2.3.3), and is the more aft when the instrument is mounted in the shuttle.

The arrangement of the wires in the Port proportional counter makes the ratio of the counting rates in the two anode groups sensitive to source gradients in the cross-dispersion direction on the sky. The sensitive length of the proportional counter in the cross-dispersion direction is ∼20 inches (see Figure 19). The path length of a photon from the instrument entrance aperture to the proportional counter window ranges from 25 to 27 inches (best shown in Figure 5). Because the 15° collimation occurs just above the proportional counter window (in fact the collimator supports the window) and the entrance aperture of the instrument is 24 inches wide in the cross dispersion direction, about 1/3 of the counter at either end (7 inches) is shadowed from sources viewed at extreme cross-dispersion collimation angles. The "odd" side of the Port counter is shadowed from sources brighter toward the shuttle nose, or north in Galactic coordinates, and the "even" side from sources toward the south in Galactic coordinates (see §2.4).

The veto wires are present in the proportional counter to reject energetic charged particle events. As shown in Figures 18 and 19, the veto anodes surround the main anodes on three sides. An energetic charged particle traveling any direction except perpendicular to the page in Figure 19 or diagonally through the edges of Figure 18 will create a track of charge that will trigger a nearly simultaneous pulse on the main and veto anodes. These pulses are fed into a coincidence rejection circuit that prevents the event from being processed by the rest of the proportional counter electronics. Charged particles that pass perpendicular to the page in Figure 19 are rejected because they have very low "goodness of fit" parameters, and particles that pass diagonally through the edges of Figure 18 are recognized by their detected positions (position channels 1-20 and 220-240).

Because the main anode wires are flanked by two veto wires, the sensitive length of the proportional counter in the cross-dispersion direction is set by the balance of potential between these veto wires and the main anode wires. The main anodes are nominally held at 1715 V, the side veto anodes at 1658 V. The main anodes are on 1.5 inch centers and the veto anodes 1.25 inches away from the outside main anodes. Using $ln(r)$ potentials for wires, the balance of potentials occurs 0.63 inches away from the last main anode. Thus, the effective length of

the proportional counter is 20.76 inches.

The DXS telemetry was handled by the Shuttle Payload of Opportunity interface which operates in two modes: a high bandwidth "KU" mode, and a lower bandwidth "PCM" mode. The instrument was designed so that all of the engineering functions of the instrument could be telemetered in PCM mode. Unfortunately, there was not enough room in PCM mode to transmit the 24 ground plane amplifier values for each X-ray event. Instead, the first step of the position determination algorithm described in §2.3.1 was coded into each instrument's on-board processor. The goodness-of-fit parameter for the first step in the algorithm is the difference between the model sum of the two highest ground plane segments and the actual sum of the two highest ground plane segments (normalized to the main anode pulse height). Positions determined with the on-board algorithm are called "POS" and positions determined with the full algorithm are called "SR-POS." The corresponding goodness of fit parameters are "GOF" and "SR-GOF." At times I will be lazy with my nomenclature and refer to a position channel as a POS, whether or not it is a POS or SR-POS unit, since nominally they are both 0.0457 inches wide and only differ in the differential non-linearity (flat-field) correction.

The entrance aperture of the DXS instruments contain sets of magnets that are designed to deflect energetic energy electrons that have been noted to contaminate other datasets (McCammon *et al.* 1983; Burrows 1982). One of the magnets is shown face-on in Figure 5. There are three such magnets in each instrument, positioned at the seams between the crystal panels (see Figure 19). The magnets produce a field of 100-200 Gauss, which is sufficient to trap electrons with energies below 3 keV. Electrons are deflected counter clockwise in Figure 5 so that they will will not hit the crystal panels, which would produce fluorescent Carbon K-α X-rays. Electrons with energies of about 20 keV deflect so that it is possible for them to hit the proportional counter window without deflecting off of the collimator. Electrons with these energies lose about 3 keV as they travel through the window, so would deposit enough charge to be rejected by the hardware upper level discriminator.

2.3.3   Gain Monitoring

Both the gas gain and amplifier gains in the proportional counter were monitored before, during and after the flight. The amplifier gains were measured by connecting a calibrated charge pulser to the input of the charge amplifiers. The gains of both main anode and all 24 ground plane amplifiers were measured in this way. The amplifier offsets were measured by

sampling the signal when the pulser was not running. At all times, the amplifier gains have been stable to within one analog to digital converter channel. The offsets were not as stable: during the flight they systematically were 1 channel higher than pre- and post-flight values. The offset change is about 10% of typical ground plane signals and has been ignored in the data reduction process thus far.

The gas gains of each proportional counter ware measured with a small Crookes X-ray generating tube or "cal tube." The cal tube of each proportional counter is situated between two of the slats that form the cross-dispersion direction collimator and shines a small beam of aluminum K-α X-rays directly into the counter. The exit aperture of the Crookes tube is very close to the proportional counter window so that the aluminum K-α X-rays are not significantly attenuated, regardless of the ambient atmosphere surrounding the instrument.

2.4   Flight Operations

The DXS instrument was inserted into a 28.5° inclination low-Earth orbit aboard the Space Shuttle Endeavour on January 13, 1993. The shuttle orbit was very nearly circular, at an altitude of ∼300 km. Figure 6 shows that the spectrometers can pivot about the roll axis of the shuttle, but no other. Also, the spectrometer must scan through a large angle around this axis (∼60°) in order to detect all the X-rays in its passband coming from one point on the sky. For these reasons, the orientation of shuttle orbiter itself is plays a key role in the experimental observations.

The DXS field of view is a a 15° by ∼170° swath, with the long dimension of the swath aligned with the wings of the shuttle orbiter (see cover illustration). In order to maximize counting statistics, the DXS field of view was centered on the same section of the sky for the entire flight. However, in low Earth orbit, such a large section of the sky is not visible 100% of the time because of occultation by the Earth and exposure to the Sun. Furthermore, the due to the high relative speed between the orbiter and the residual atmosphere, the direct impact of oxygen atoms from the residual atmosphere is capable of depositing enough energy to damage the lead stearate crystal panels. Thus, for about 3/4 of each orbit, the instrument remained in the aperture closed or "stow" position. For a January flight, the best patch of the sky to observe was in the general direction of the Galactic anti-center.

The ∼90 minutes orbital period of the shuttle provides a natural period to experimental

operations. About 20 minutes before each sky-looking session, the instrument was turned on and background data taken with the instrument aperture closed. At the end of this period, the cal tube was turned on in order to measure the gas gain in the proportional counter. A few minutes before each DXS observing period, the shuttle orbiter was oriented so that the vector perpendicular to its belly, pointed out of the cargo bay pointed at the Galactic anti-center. In this orientation, the boundary for sky-looking observations is determined by the impact angle of the residual atmosphere with the shuttle orbiter. When this angle dropped to $10°$ below the nose of the orbiter, residual atmosphere was unlikely to impact directly on the crystal panels and it was deemed safe to begin sky-looking observations.

A sky-looking observation consisted of nine or ten back-and-forth scans of the spectrometer. Hence, the sky-looking times are often referred to as "scan" times. For the Starboard instrument, nine scans were used before orbit 51 and ten after; For the port, eight and nine, respectively. The reason for the increase in the number of scans will become apparent below. After the scan period, the instruments were rotated so that the entrance apertures were closed and the cal tube was run again. Then the instrument was left on until shut down by high particle rates or turned off by the operators. In retrospect, it would have been nice to run the cal tube again at the end of (or at least part way though) the post-scan background period. This would have given a more complete picture of the behavior of the gas gain in each orbit. As it was, the average of the two gas gains measured for each orbit was used to correct the pulse heights for that orbit.

2.4.1 The Problem of Breakdown

Proportional counters subject to very high counting rates ($>10^4$ s^{-1}) are at risk of entering a state called "breakdown." Breakdown occurs when the gas around the main anodes injects a continuous flood of electrons into the high field region. The resulting high count rates saturate the instrument telemetry and can cause permanent damage to the anode wires. High count rates in low Earth orbit are common in proportional counter experiments because of intense charged particle background over certain parts of the Earth due to concentrations of the Earth's magnetic field. One such region is the South Atlantic Anomaly, or SAA.

Each DXS proportional counter was designed to internally monitor its count rate and turn itself off when the count rate climbed above 4000 counts s^{-1}. The specific monitor chosen was the "Lower Veto Monitor," which counted the number of events detected by the veto

anodes that passed the veto anode lower level threshold criterion. A separate system, the radiation monitor, was supposed to independently measure the radiation that was causing the high count rate in the proportional counters and signal for them to be turned back on when the count rate dropped below the rate that had triggered them to be turned off. The radiation monitors were small Geiger tubes that, it turns out, were more sensitive to solar X-rays than the charged particle background. Thus, it was possible for radiation monitor system to signal the proportional counters to turn on even when there was still a high particle background.

Had the insensitivity of the radiation monitors to the charged particle background been the only unexpected factor, the DXS proportional counters may have been able to self-regulate their count rates using the "Lower Veto Monitor" system and breakdown may have been avoided. However, the "Lower Veto Monitor" rate monitor was subject to a dead time saturation effect so that as the actual count rate in the proportional counters increased beyond $\sim 2 \times 10^4$ counts s^{-1}, the rate reported by the "Lower Veto Monitor" *dropped*. With the radiation monitors turning on the proportional counters at essentially random times, it was possible for the proportional counters to be turned on *and stay on* when the charged particle rates were $>10^4$ s^{-1}. Such an event happened in orbit 10 for the Starboard instrument and orbit 11 for the Port. In both cases, the orbiter was over the Pacific Ocean near Ecuador. There is an enhancement in the particle background near this location seen in Figure 84.

Orbits 11 through 26 were spent diagnosing the problem with the particle detectors and the proportional counters. After orbit 27, discrete points, called "hot spots" in the Starboard counter would spontaneously generate high count rates. The count rate in this counter was controlled somewhat by heating the counter and flushing gas through it. Other than one hot spot in orbit 27, the Port counter showed no such behavior. Because hot spots show up directly as spectral features it is essential that none be present in the data used to created the final spectra. Section 4.6 discusses the nature of hot spots in more detail and the data analysis techniques used to remove the effects of the hot spots.

Another source of anomalous background, consisting of events with main anode pulse height information but no ground plane signals, was also detected throughout the flight. These events are easily removed from the data because of their GOF and SR-GOF values are always 63. These events are thought to be caused by breakdown in the high-voltage potting in the end cavities of the proportional counters.

2.5 Modeling the Spectrometer Response

This section presents the model of the DXS spectral response. The presentation is in two parts. Section 2.5.1 gives an analytic calculation of the resolving power of the instrument. Section 2.5.2 discusses the equation used to calculated the area-solid angle product, or total efficiency of the instrument. These two sections also describe the proportional counter collimator and its effect on the resolving power of the spectrometer. §2.5.3 describes a set of computer programs that has been used to calculate the area-solid angle product of the instrument as a function of wavelength and position in the dispersion direction on the proportional counter. The product of these programs is a two dimensional matrix in photon energy and position called the response matrix of the instrument. Section 2.5.4 gives the resolving power of the instrument as a function of wavelength (energy) as calculated by the spectrometer modeling program.

2.5.1 Analytic Calculation of Spectral Resolving Power

As described in §2.1, the collimator and the curve of the crystal panels work together to spatially separate the X-rays input to DXS. The precise shape of the crystal panels was chosen so that, to first order in reflection angle, the wavelength of light incident at a particular position on the proportional counter does not depend the opening angle of the collimator. Furthermore, it was desired that the crystals be continuous and have a continuous derivative. The shape that satisfies this constraint is cylindrical.

Figure 20 shows the path of two X-ray photons (bold lines) as they reflect from different points on the crystal panel and into the same point of the proportional counter. Because they land in the same point on the proportional counter, they appear to the instrument to be the same energy, however, the reflection angles α and α' are not the same, and, by the Bragg relation, the energy of the photons cannot be the same. Thus, the necessity of accepting photons over a finite range in angles around the perpendicular to the proportional counter introduces some additional spectral smearing.

For the photon not entering the proportional counter on a perpendicular to the window, call the angular coordinate of the point of reflection γ. The angle between the photon paths as they enter the proportional counter is ϕ. It is a property of cylindrical geometry that $\gamma = \alpha$ when ϕ

Crystal Panel

α′

α

δ

sin γ

φ

γ

α

cos γ

Proportional Counter Window

Crystal Panel Center of Curvature
R = 1
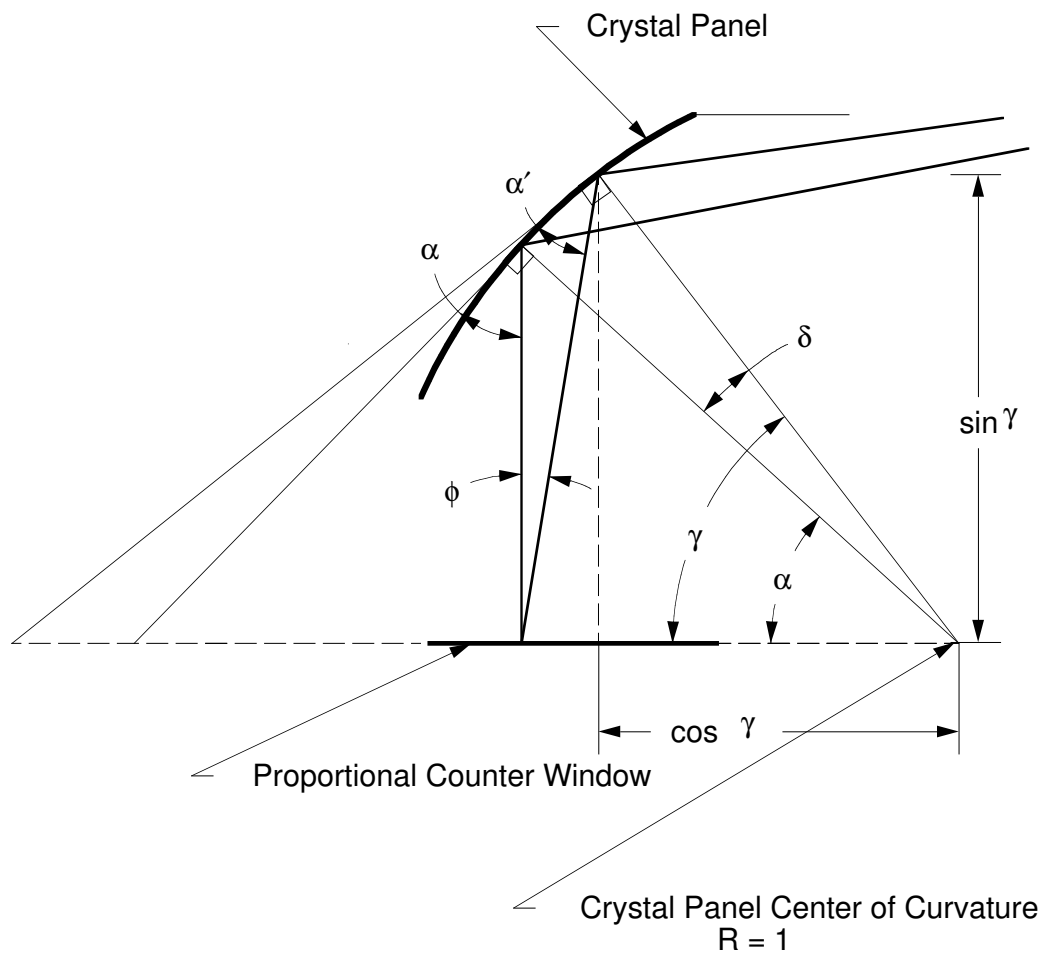
Figure 20: Dispersion Direction Geometry.

= 0. By considering the triangles in Figure 20, it is easy to show that:

$$\gamma = \phi + \alpha' = \alpha + \delta \tag{2.2}$$

By eliminating γ and taking the cosine of both sides of the equation, one arrives at:

$$\cos\alpha' = \cos(\alpha + \delta - \phi) \tag{2.3}$$

which, after several expansions and cancelations leads to the relation:

$$\cos\alpha' = \cos\alpha\cos\phi \tag{2.4}$$

Thus, to first order in ϕ, $\alpha' = \alpha$. Similarly, it can be shown that for the cross-dispersion direction (out of the page in Figure 20)

$$\sin\alpha' = \sin\alpha\cos(\arctan(\tan\psi\cos\phi)) \tag{2.5}$$

where ψ is the angle of incidence of the ray in the cross-dispersion direction.

Equations 2.1, 2.4, and 2.5 can be combined to derive the contribution of the collimator opening angle to the instrument resolving power ($\lambda/\Delta\lambda$) in the dispersion and cross-dispersion directions, respectively:

$$R_d = \frac{\lambda}{\Delta\lambda} = \frac{2\tan^2\alpha}{1 - \cos\phi_{FWHM}} \tag{2.6}$$

$$R_{cd} = \frac{\lambda}{\Delta\lambda} = \frac{2}{1 - \cos\psi_{FWHM}} \tag{2.7}$$

where ϕ_{FWHM} and ψ_{FWHM} are the collimator FWHM angles in the dispersion and cross-dispersion directions, respectively. The factor of two enters into the expressions because equations 2.4 and 2.4 do not depend on the sign of the collimation angles.

Setting Equations 2.6 and 2.7 equal to the empirical function for the resolving power of the Henke #2 crystal plotted in Figure 11 and solving for collimator opening angle, one arrives at the functions plotted in Figure 21. For the cross-dispersion collimator FWHM opening angle (ψ in the figure) the crystal resolving power is well matched by a constant value of $\sim$15 degrees. On the other hand, some improvement in resolution may have been gained by varying the dispersion direction collimation as a function of spectral position in the proportional counter. However, for ease of construction and higher throughput, a constant value of $\sim$15 degrees was used for the dispersion direction collimator FWHM angle as well. The explicit dependence of the instrument throughput on collimation angle is shown in Equation 2.9.

Figure 21: Plot of collimator FWHM angles in the dispersion and cross dispersion direction that match the crystal resolving power as a function of energy.

2.5.2 Area Solid-Angle Product ($A\Omega$)

The area solid-angle product, or $A\Omega$, of the DXS spectrometer can be calculated as a function of energy by the following integral:

$$A\Omega(E) = T_{win}(E) \int O(\phi, \psi, x, y) R_{xtl}(E, \alpha') d\phi d\psi dx dy \qquad (2.8)$$

The x axis points in the dispersion direction, along the proportional counter window starting from the crystal panel center of curvature (to the left, parallel to the page in Figure 20). The y axis is the cylindrical axis of the crystal panels. The angles ϕ and ψ are the dispersion and cross-dispersion angles also defined above. $T_{win}(E)$ is the transmission of the proportional counter window as a function of energy. This quantity has been taken out of the integral under the assumption that ϕ and ψ never get large and the window is uniform as a function of position. R_{xtl} is the reflectivity of the crystal panel as a function of energy, E, and reflection angle α', modeled in §2.2.1. As shown in §2.5.1, the angle α' is itself a function of x, ϕ, and ψ. The function O is 0 or 1 depending on whether or not the infinitesimal patch of the proportional counter at position (x,y) can look in direction (ϕ, ψ) and see out of the instrument, including the reflection off of the crystal panel.

A major contributor to the function O is the proportional counter collimator, which is

composed of two sets of thin metal strips. The 88 strips that provide the dispersion direction collimation are shown as a set of short lines in Figure 5. These strips run the length of the proportional counter. One of the strips of metal that compose the cross-dispersion direction collimator is shown face-on in Figure 5 above the dispersion-direction collimator. Because the dispersion direction strips cast regular shadows that can be easily detected by the proportional counter (see Figure 32), they are mounted on a slight diagonal, so that their effects, when integrated in the y direction, are spread uniformly across the counter. This allows the function O to be approximated as:

$$O(\phi, \psi, x, y) = (1 - \frac{|\phi|}{\phi_{FWHM}})(1 - \frac{|\psi|}{\psi_{FWHM}})O'(\phi, \psi, x, y) \qquad (2.9)$$

where $\phi_{FWHM} = \psi_{FWHM} = 15°$, as determined in §2.5.1. The remaining contributions to the function O, indicated here as O', are: an additional collimation factor for the electron rejection magnets, located at the entrance aperture of the instrument (see §2.3.2); logic tests to see if, for a particular direction (ϕ, ψ), a ray *starting* at point (x, y) on the proportional counter will bounce off of the crystal panel and exit the instrument aperture; a logic test for obscuration by the proportional counter gain-monitoring "cal tube" (see §2.3.3); and a factor known as the "open area fraction." The open area fraction is necessary because the transmission of the collimators are assumed to be 1 for light with normal incidence. In fact, the transmission of the proportional collimator to normal incident light is 83.0% and the electron rejecting magnets at the entrance aperture of the instrument transmit 93% of the normal incident light. Thus, the total transmission of the collimating systems at normal incidence is 77%. Note that this does not include the transmission of the support mesh on the proportional counter window, which is discussed in §3.1.1.

2.5.3   Spectrometer Modeling Program

The integral in Equation 2.8 gives the total response of the DXS spectrometer as a function of energy. Carrying out the integral over only the y, ϕ, and ψ axes results in a two dimensional function in energy and position, x. This two dimensional function is the position response matrix of the instrument.

During the design phase of DXS, a program called `SPCMOD` was written that carried out the integral in Equation 2.8. The program calculates a matrix that has 1000 energy points ranging

from 100 eV to 2000 eV and 240 position points corresponding to the 240 POS channels described in §2.3.1. The integration over each of the ϕ and ψ collimation angles is done in 101 steps from -15 to 15 degrees. Because of the cylindrical symmetry, there is no explicit integral in the y direction, rather the length of the line segment at the exit aperture of the instrument for each x, ϕ, and ψ is calculated. The collimation due to the magnets at the entrance aperture of the instrument and the shadowing of the cal tube are also taken into consideration.

A separate program, called RSPMATRIX, calculates the quantity T_{win} using a model of the proportional counter window transmission given the thickness of the materials used to make the window and the equation:

$$tranmission(E) = e^{-\tau(E)} \tag{2.10}$$

$$\tau(E) = \sum thickness_i \mu_i(E) \tag{2.11}$$

The thicknesses of the materials used to make the window are determined in the post-flight calibration phase described in §3.1.1 and the μ_i are from Henke *et al.* (1982).

RSPMATRIX also calculates the efficiency of the proportional counter at detecting photons. Once past the window, X-ray photons below 277 eV are absorbed within a few hundred microns, so for rough calculation, in a proportional counter that is several centimeters deep, this efficiency is 100%. However, the amount of secondary charge produced by each photoelectron event is statistically determined. This charge eventually produces a voltage pulse at the output of the main anode amplifier by the processes described in §2.3. The amplifier generates noise on its output as well, so to reduce the number of spurious events, a discriminator is set in the post-amplifier electronics. This discriminator also cuts out real pulses that happen to fall on the low-amplitude tail of the charge distribution. In order to correct for this loss in efficiency, an accurate model of the expected pulse height distribution of the proportional counter is needed.

Jahoda & McCammon (1988) have generated a model that describes the pulse height distribution as a function of energy in proportional counters. The details of the adaptation of this model to the DXS proportional counters are discussed in §3.1.4. In brief, the result of the pulse height model is presented in the form of a response matrix similar to the response matrix generated by SPCMOD, except that the matrix axes are not energy and position, but energy and pulse height.

Pulse Height Efficiency Correction
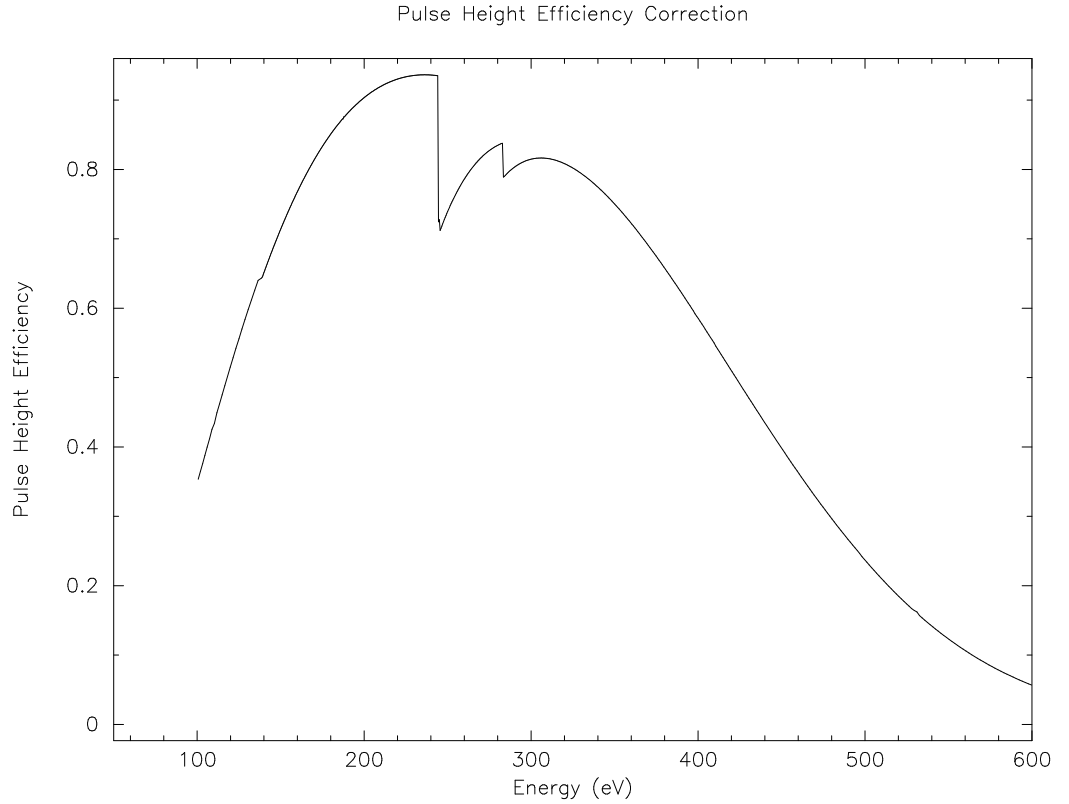
Figure 22: Pulse height efficiency correction for the Port instrument appropriate for processing of the flight data.

To understand the application of this pulse height response matrix to the problem of correcting the efficiency of the *position* response matrix, picture the pulse height response matrix as a series of pulse height distributions, one for each row on the energy axis. The pulse height response matrix is normalized so that the full integral of each pulse height distribution (energy row) is one. The efficiency correction factor *at each energy* is then simply the integral of each pulse height distribution (response matrix row) between the lower and upper pulse height cuts set in hardware, and/or software. In order to ease calculation, the energy axes of the position and pulse height response matrices are identical, so there is no need for interpolation.

Figure 22 shows the pulse height efficiency correction in the Port counter for the lower and upper pulse height cuts that were made in the flight data (see §4.7) to generate the spectra presented in §5.6.

It is important to note that improvement in the signal to background ratio is possible by

varying the upper and lower discriminator values as as function of position on the proportional counter, accepting a constant percentage (i.e., 70–90%) of the events expected at each position. The original calculation of the background rate due to un-vetoed cosmic ray events showed that the background would have a flat pulse height distribution and a magnitude of $\sim$25% of the diffuse X-ray background. Thus, limiting the background with the sliding pulse height discriminator technique would have been an important step in the data analysis process. The pulse height spectrum of the DXS background is indeed flat, but the counting rate is only $\sim$17% of the diffuse X-ray background. Thus, the sliding pulse height discriminator technique is not as important for basic data analysis. Furthermore, selecting events by this technique would have involved substantial modification to the program `hist`, described in §4.5.

The program `RSPMATRIX` reads in the efficiency response matrix generated by `SPCMOD`, integrates the matrix along each energy row and normalizes each row by the integral. The result is a two dimensional redistribution matrix file (RMF) which is the position response of the instrument per detected photon. The integrated instrument response as a function of energy determined by `SPCMOD` is then multiplied by the window transmission and pulse height efficiency as a function of energy to form the total instrument area solid-angle product ($A\Omega$). This information is stored in a separate file called the ancillary response file (ARF). Both files are (FITS) files (Hanisch *et al.* 1993) formated for use with the X-ray spectral analysis system `XSPEC` (Arnaud 1996). The programs `SPCMOD` and `RSPMATRIX` are themselves run from a script called `makersp.ksh`. All of these programs are kept in revision control on the DXS workstation.

2.5.4   Model Calculations of Resolving Power

Section 2.5.1 presented the analytic equations used to calculate the contributions of the crystal panel rocking curve and collimator opening angles to the resolving power of the DXS instrument. In order to accurately model the resolving power of the instrument, it is necessary to use the response matrix presented in §2.5.3 and the X-ray analysis package `XSPEC` (Arnaud 1996).

The program `XSPEC` generates model X-ray photon spectra and convolves them with an instrument response function, creating model count spectra that can be directly compared with measured data. Using zero-width Gaussians (functions with all their flux in one energy resolution element) as input photon spectrum models, the instrument response to delta-functions

Figure 23: Spectrometer Modeled Resolving Power $\lambda/\Delta\lambda$. X-axis is in units of wavelength, with energy increasing to the right.

is determined. The instrument resolving power, $\lambda/\Delta\lambda$ is the FWHM of the delta-function at each wavelength after it has been folded through the instrument response function. Figure 23 shows the resolving power as a function of wavelength.

Chapter 3

Calibration

This chapter presents the calibration of the DXS spectrometers. As described in Chapter 2, the two most important components of each spectrometer are the X-ray reflecting crystal panels and the position-sensing proportional counters. The calibration of these two sets of components will be considered separately in this chapter, beginning with the proportional counter in §3.1. With the proportional counter well understood, the reflectivity of the crystal panels is inferred from the calibration of the instrument as a whole, or the end-to-end calibration, covered in §3.2. The results of the chapter are summarized in §3.3.

3.1 Proportional Counter

As described in §2.3, a thin plastic window covers one face of each position-sensing proportional counter. Accounting accurately for the transmission of this window is a critical step in the absolute calibration of the instrument and is discussed in §3.1.1. Section 3.1.2 presents the calibration of the proportional counters' position-sensing capabilities. A discussion of the pulse height gain variation as a function of position in the detectors is presented in §3.1.3 and a model for fitting pulse height distributions is discussed in §3.1.4.

3.1.1 Window Transmission

The transmission of the Formvar/UV24 flight windows and the windows used in the post-flight calibration phase were measured as part of the post-flight calibration exercise. The windows were removed from the proportional counters and measurements were made at 32 distinct places on each window, except the Port flight window, which had broken during one of the post-flight calibration exercises. The Port flight window was measured in 21 places. The transmission at each location was measured at four different energies: zirconium M-ζ, boron K-α, carbon K-α, and fluorine K-α. For each window and at each energy, the standard

Table 2: Window Transmissions

Window (ID)	Formvar Thickness (μg cm^{-2})	UV24 Thickness (μg cm^{-2})
Port Flight (92.54)	66.0	20.0
Port Post-flight (92.55)	59.0	20.0
Starboard Flight (88.05)	60.0	20.0
Starboard Post-flight (92.106)	63.0	20.0

deviation for the set of measured transmissions at the 21 locations is less than 4%. There is no evidence of systematic variation in the window transmission, such as stripes or gradients greater than this level in any of the windows.

The chemical formula of Formvar is $C_5H_7O_2$ and the formula of UV24 is $C_{14}H_{12}O_4$. Equations 2.10 and 2.11 were used to find best-fit values for the thickness in Formvar and UV24 in μg cm^{-2}. These calculations are complicated by the fact that the constituent materials of Formvar and UV24 are the same. Although for some of the windows, lower χ^2 values are obtained with models containing no UV24, a minimum UV24 value of 20 μg/cm^2 was adopted, based on the construction of the windows. Table 2 shows the values for thickness adopted for the various windows. Figure 24 shows the measured and modeled window transmission vs. energy for the Port flight window. The appropriate model for each flight and post-flight window was generated by the program `RSPMATRIX`, as described in §2.5.3.

The proportional counter windows are supported between the 88 slats of the collimator structure by a 100 line per inch nickel mesh. This mesh has also been carefully mapped and found to have an average transmission of 65.4±1%. This figure is also incorporated into the program `RSPMATRIX`.

3.1.2 Flat-Field

In order to interpret the DXS data as a statistical ensemble, a position spectrum of the data is formed by dividing the proportional counter into bins and counting the X-rays recorded in each bin. The bin widths are measured in integral multiples of detector position channel (POS). The response matrix described in §2.5 determines how POS are mapped to photon energy. Section 2.3.1 describes an algorithm that can determine the position of a single event to an accuracy of a fraction of a detector channel (POS), or less than 0.01 inch. This accuracy
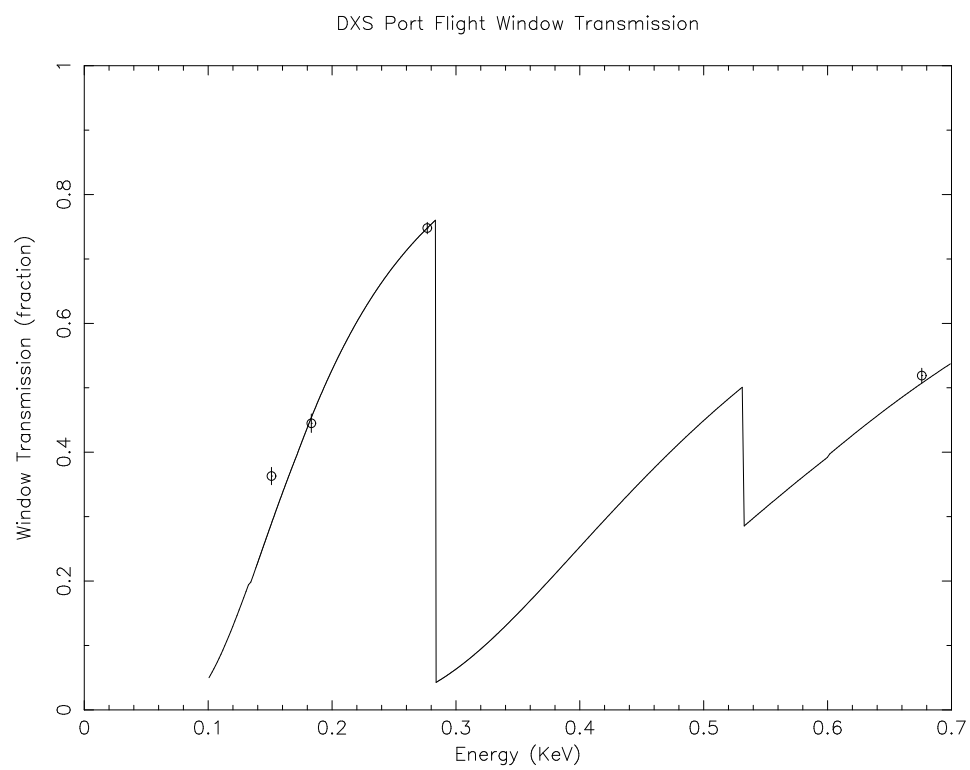
Figure 24: Measured (data points) and modeled (solid line) Port flight window transmission as a function of energy. The other Formvar/UV24 windows used have similar transmission curves.

is about a factor of 10 better than the narrowest expected line profile (at the higher energy end of the instrument).

Unfortunately, when the positions of individual events are collected together to form a position *spectrum*, slight differences in the width of the detector channel can cause systematic differences in the counting rate as a function of position. This effect, known as "differential non-linearity" is also seen when using a successive approximations analog-to-digital converter as a pulse height analyzer (Horowitz & Hill 1989). In the DXS proportional counters, the variation in bin widths remains fixed over time. Thus, the pattern induced in the data can be easily removed.

To remove the pattern in the data caused by differential non-linearity, each proportional counter is illuminated by a large, uniform (or "flat"), extended source of X-rays. The spectrum of this flat source (the flat-field spectrum) is then divided out of the final DXS spectra. This procedure is known as "flat-fielding."

X-ray Source

In the DXS flat-field experiment, the extended source of X-rays was a large piece of polypropylene ($\sim$1 foot by 2 feet) bombarded by α-particles from two $\sim$2 foot by 1 inch, line-like ^{210}Po sources, as shown in Figures 25 and 26. The X-ray source was placed above the proportional counter collimator and oriented with its long axis perpendicular to the long axis of the proportional counter. A movable mask was applied to the counter running along the position-sensing direction and centered in turn on each of the 14 anode wires, allowing the flat-field spectra for each anode wire to be obtained individually. These spectra were combined as described below to produce the final flat-field spectra. This procedure allowed small strips of the counter to be exposed to the extended source of X-rays to check for uniformity in the position sensing response.

Source Non-Uniformity

Preliminary reduction of the data showed that either the source of X-rays or the response of the proportional counter in the dispersion direction was not uniform. At high and low position coordinates (POS–see §2.3.1), there was a pronounced dip in the measured count rate. In order to find the source of this large scale non-uniformity (which turned out to be the source
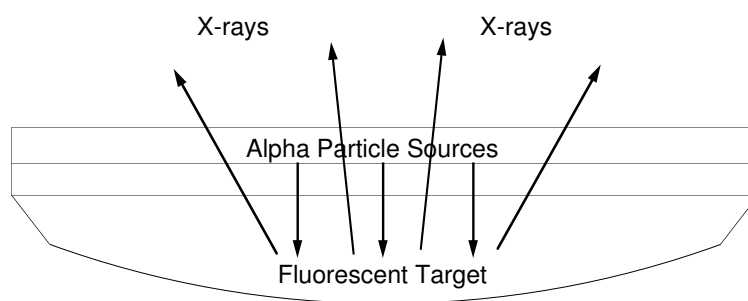
Figure 25: Fluorescent source side view. Alpha-particles emitted at the top edges of the apparatus (see Figure 26) bombard curved target. Fluorescent X-rays escape from the top of the apparatus. The apparatus is ∼20 inches long.
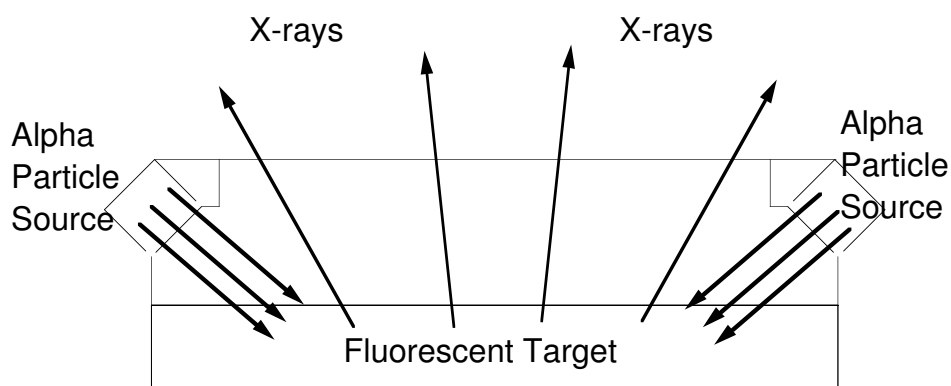
Figure 26: Fluorescent source end view. Alpha-particles emitted at the top edges of the apparatus bombard curved target (see Figure 25). Fluorescent X-rays escape from the top of the apparatus. The apparatus is ∼14 inches wide.

46

shape), the X-ray source was pushed to its extreme position in the vacuum tank (toward high POS). This dataset is referred to as the "CUC" data. Another measurement was taken with the source rotated 180 degrees about the axis perpendicular to the proportional counter window and pushed to the other side of the vacuum tank. This is the "CLC" data. It is important to note that this procedure mapped both sides of the proportional counter but only one side of the source.

In order to more easily study the source of the large-scale non-uniformity, the data were binned in tens of POS. With this binning, spectra of the data clearly show a sine wave of 32.8 POS period and approximately 2.2±0.2% amplitude (see Figure 27). The peaks in these spectra are coincident with the positions of the veto anodes shown in Figure 18. This behavior is caused by the slight distortion the veto anodes create in the electric field of the main anode section of the proportional counter. For the purposes of tracking down the large scale non-uniformity, this veto pattern was divided out of each of the position spectra used in the proceeding analysis.

With the veto pattern removed, the data taken with the source pushed to its extremes in the vacuum tank was overlayed for a direct comparison of the two sides of the proportional counter. The relative normalization of the two datasets and the peak channel were allowed to vary until the residuals between the data were minimized. Points on an even grid of POS/10 were calculated using the original data and parabolic interpolation. As shown in Figure 28, the response of the two sides of the proportional counter do not differ by more than 3%. As discussed in §3.1.1, the 3% difference is comparable to the variations in the proportional counter window.

Source Shape Removal

With the evidence that the proportional counter response was uniform, a method was designed to use the CUC and CLC data to remove the large scale non-uniformity (the source shape). With the assumption that the two halves of the large X-ray source are equivalent, the CLC and CUC spectra were spliced together in a method similar to the CUC, CLC′ fit in order to match the over-all pattern in the data (see Figure 29). At first, the normalizations and offsets of the CLC and CUC spectra were both allowed to float to achieve the best fit to the data. As the data were processed, however, it was clear that there were more features in the data than simply the source shape.
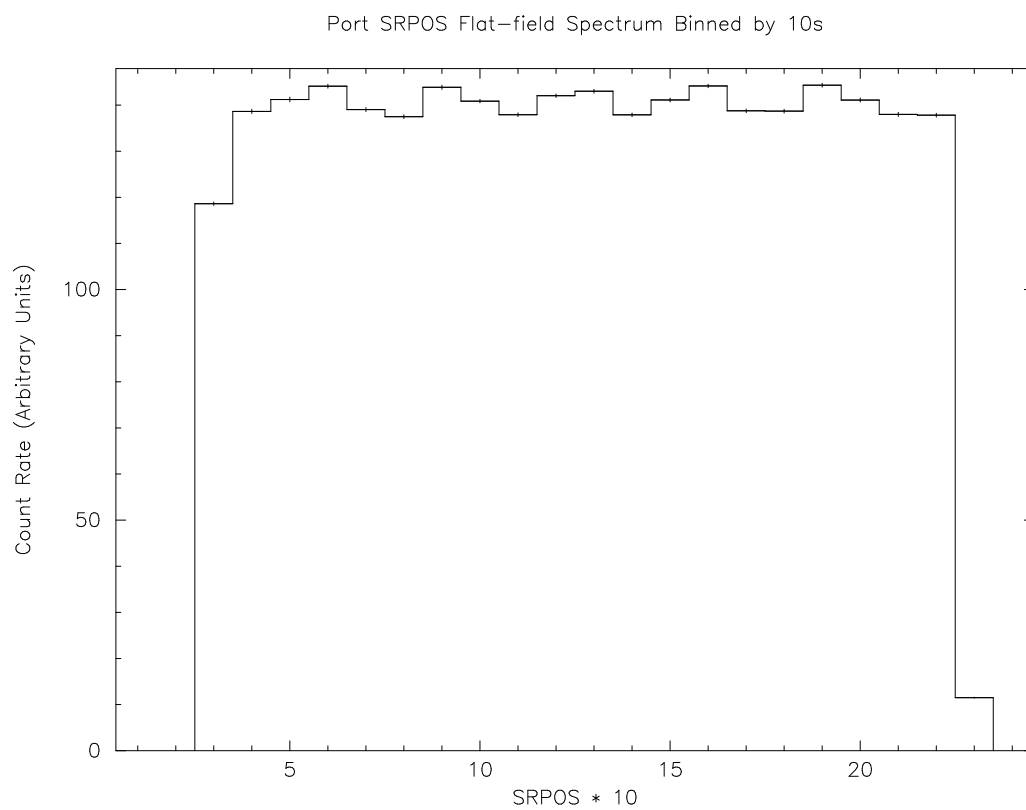
Figure 27: Port instrument KU telemetry (SRPOS) flat-field spectrum binned by tens to show the veto pattern of amplitude 2.2% and period 32.8 POS.

Figure 28: Comparison of the upper and lower position channels (POS) of the proportional counter with the extended source off center. CLC′ means that the X-axis of the CLC data has been plotted as (241–POS)/10.

As described in Mark Mulligan's post-flight calibration memo (Mulligan 1993), aluminum foil was used to mask off the proportional counter so that only the area above one anode wire would be exposed at a time. Instead of having a single mask cut from one piece of foil, two separate sheets of foil were used. It is clear from looking at the data that these sheets were not always parallel (particularly wire02, starboard counter). This effect has been corrected by fitting a sloped line to each wire spectrum individually and dividing out a normalized representation of this line (see Figure 31).

After the removal of the mask problem from the data, a systematic shape was still evident in the residuals (compare Figures 29 and 30, channels 15-19). The shape resembles a triangle, 4-5% in amplitude, 4 POS/10 wide (FWHM), centered in most of the spectra at POS/10 of ~ 17. In some of the individual datasets, the triangle appeared at a position of POS/10 ~ 7, the same distance from the center of the counter but on the other side. This feature has been attributed to the non-uniformity between the two halves of the large X-ray source. Recall that the CLC and CUC data were images of the same side of the source. The source itself is composed of a set of ^{210}Po alpha-particle sources arrayed in two lines aimed at a large sheet of polypropylene. The lines of the alpha-emitters are parallel to the long axis of the target. The triangular non-uniformity can result if the ^{210}Po sources on one end of the target are 4-5% weaker than the sources in the same position on the other end of the target. Figure 31 shows the triangular non-uniformity as the curve labeled "Right to Left Source Variation."

With both the linear correction due to the misalignment of the aluminum mask and the triangular correction due to the side-to-side source variation, the composite CLC/CUC spectrum could be used to fit the individual wire spectra, binned by ten, with veto pattern divided out, with good results (see Figure 30). The largest variation between the model source shape and an individual wire spectrum was 4%. The RMS differences were below 2%.

In the final processing of the flat-field dataset, the source shapes derived by the procedure outlined above were divided into the individual (unbinned) wire spectra. Figure 32 is an example of such a spectrum. Note that neither the ten channel POS period described in §2.3.1 nor the 32.8 channel veto anode period are dominant. Rather, a "hash" with a period of ~ 2 channels dominates. This is readily understood as the shadow of the dispersion direction collimator. Recall from §2.5.2 that the collimator for the dispersion direction has 88 thin leaves mounted on a slight diagonal so that no regular shadow would be cast in the dispersion direction. Thus, each individual wire spectrum has a hash in a slightly different place so that

Figure 29: Example source shape construction for flat-field exercise, wire04, port counter. The normalized source shape is constructed from the CUC and CLC data pictured in Figure 28.

Figure 30: Example source shape construction for flat-field exercise, wire04, port counter. The normalized source shape is constructed an in Figure 29 except that a triangle of amplitude -4% and FWHM 40 POS centered at POS/10 = 17 multiplying the data (see Figure 31).

Figure 31: Multiplicative factors applied to the CUC and CLC data in order to best fit the wire04 spectrum shown in Figure 30.
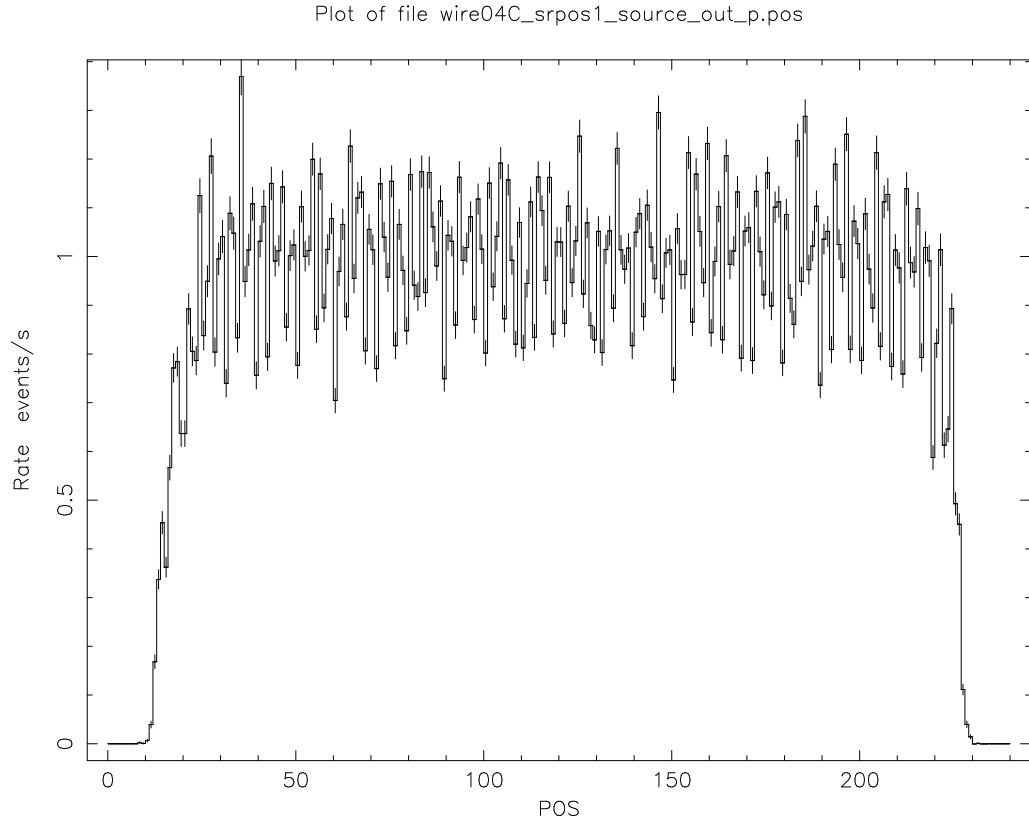
Figure 32: Single wire flat-field. Note "hash" caused by shadow of the collimator in the dispersion direction.

when added together (in rate), as in Figures 33–36, the collimator pattern disappears.

It should be noted that totaling the wire spectra with equal weighting, as described above, is not strictly correct. There is an additional collimation effect due to the finite instrument aperture in the cross-dispersion direction which applies an unequal weighting to the exposure of the main anode wires (see §2.3.2). However, as shown by the lack of the collimator "hash" in the combined end-to-end calibration spectra shown in Figure 63, this effect is small compared to the statistical error of all the combined post-flight calibration data.

Summary: Final Flat-Field Spectra

To summarize, this section has described how narrow strips of the DXS proportional counters above each main anode wire were illuminated by a large fluorescent X-ray source. By viewing one end of the source with both sides of a proportional counter, the source was found to have a

large scale non-uniformity. The source non-uniformity was constructed from the two views of the end of the source and was divided out of each wire spectrum individually. The individual wire spectra, which show the effects of the veto anodes, collimator shadow, and any other proportional counter non-uniformities were then combined to form the final flat-field spectra.

Recall from §2.3.2 that the DXS instrument uses two telemetry streams, a higher bandwidth KU and a lower bandwidth PCM stream. The PCM stream contains X-ray positions determined by the on-board processors, whereas the KU stream contains all of the ground plane signals for each event so that the full two-step algorithm described in §2.3.1 can be used to determine event positions. The processing for these two telemetry streams was kept separate through the flat-field exercise, thus, there are two final flat-field spectra for each instrument. Figures 33 and 34 show the flat-field spectra of the KU telemetry stream of the port and starboard instruments. The port flat-field has a pattern with a 10% amplitude repeating every ten channels. It is not clear what is causing the pattern. Processing the ground plane data with a completely independent algorithm (fitting with Gaussians) results in a KU spectrum with the same pattern, suggesting the pattern is caused by variation in the ground plane or main anode signal. However, the pattern is very stable, including the larger peak at 185 POS, so its effects can be removed simply by dividing by the flat-field spectrum.

Figures 35 and 36 show the PCM flat-field spectra for both instruments. Every tenth channel in these spectra is ∼20% low. The reason for this is that one of the bins defined in the first step of the algorithm described in §2.3.1 is too small. Thus, not enough events are assigned these positions. The boundaries can be changed to minimize this effect for future DXS missions. Like the pattern in the port KU flat-field, the PCM pattern is stable so its effect can be removed by dividing it out of the spectra from this mission.

3.1.3 Position Dependent Gain Correction

Because of the noticeable effect of the veto wires on the flat-field data shown in Figure 27, it was suspected that the pulse height gain would also vary in a pattern that reflects the presence of the veto anodes. To test this hypothesis, pulse height distributions were made from events that had positions above the veto anodes and from events that have positions between the veto anodes. The resulting pulse height spectra are overlayed in Figure 37.

The function governing the distortion in the pulse height as a function of position was assumed to be a simple sinusoid, with a period equal to the spacing between the veto anodes

Plot of file flatfield_kuonly_p.pos
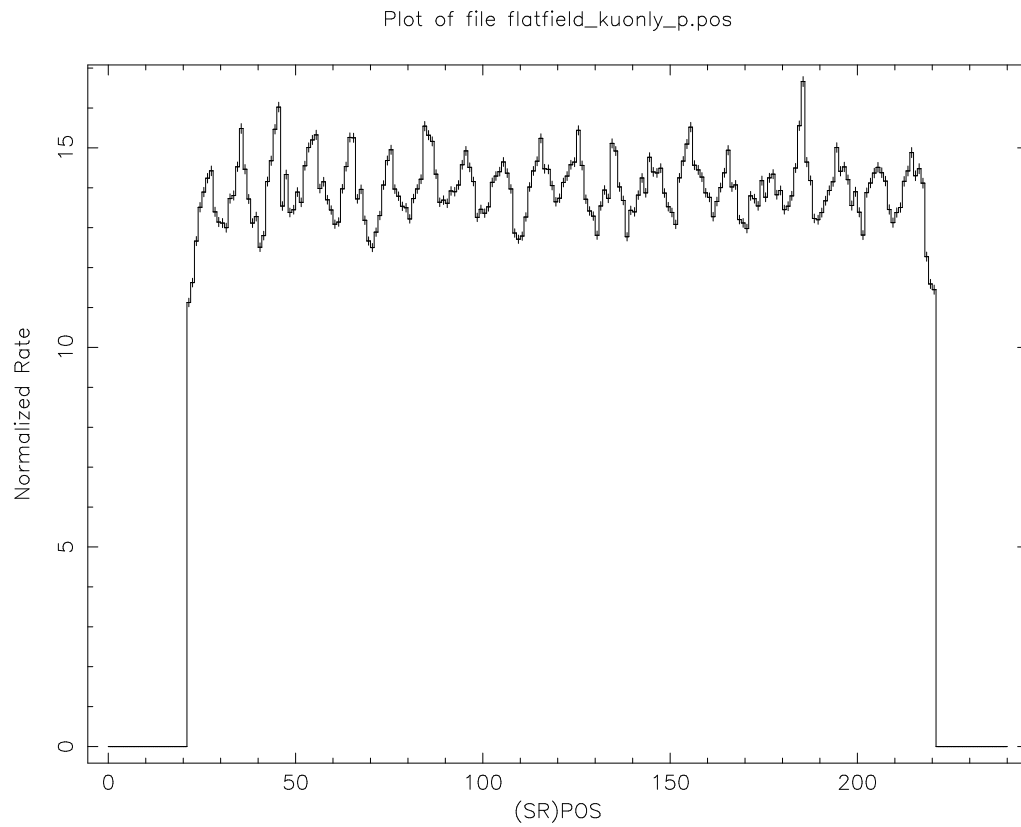
Figure 33: Flat-field spectrum for the KU (SRPOS) data, port instrument.

Plot of file flatfield_kuonly_s.pos
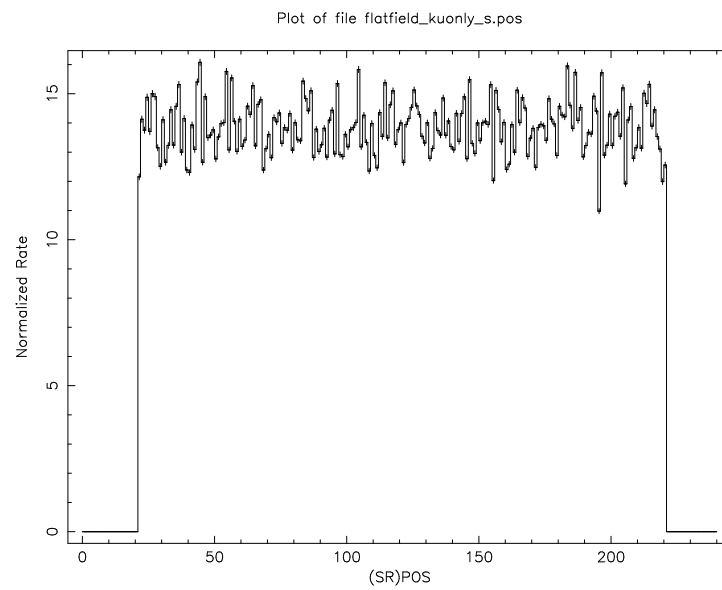
Figure 34: Flat-field spectrum for the KU (SRPOS) data, starboard instrument.
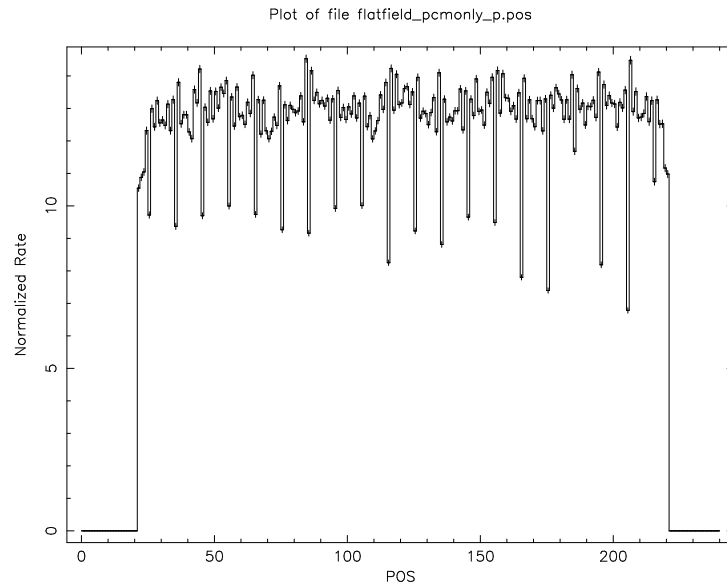
Figure 35: Flat-field spectrum for the PCM (POS) data, port instrument.
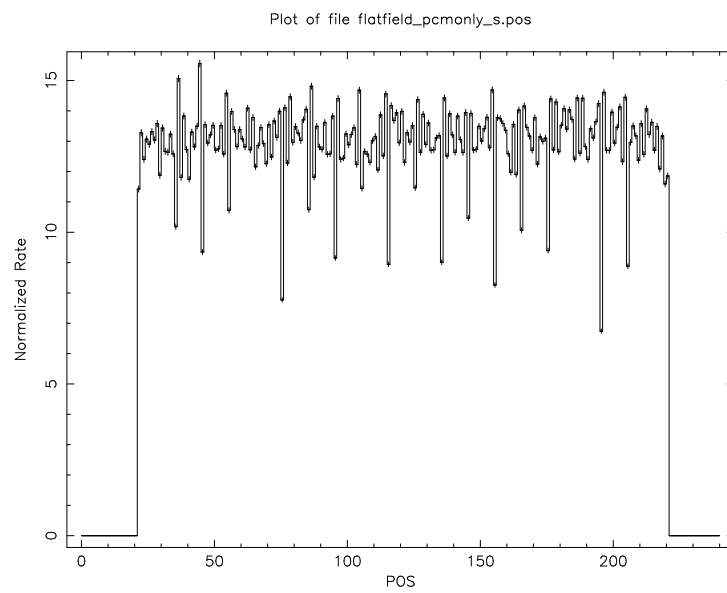
Figure 36: Flat-field spectrum for the PCM (POS) data, starboard instrument.
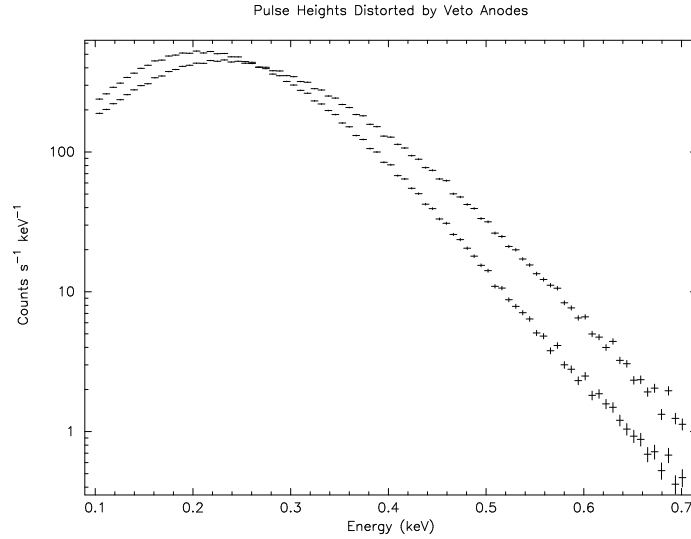
Figure 37: Pulse height distributions above (peaking at higher energies) and between (peaking at lower energies) the veto anodes.

(32.8 POS) and an amplitude that corresponds to the fractional deviation from the nominal pulse height. The phase of the sine wave is such that the distortion is the greatest (negative) over the veto anodes. The amplitude of the sine wave was adjusted until the two pulse height distributions became indistinguishable to the eye, as shown in Figure 38. The results are the same for both proportional counters (Port is shown). The final amplitude of the sine wave was 10%.

3.1.4   Pulse Height Response Matrix

In order to gain the best possible spectral information from earlier proportional counter experiments, the Wisconsin space physics group has generated an accurate model of the shape of the proportional counter pulse height distribution as a function of energy (Jahoda & McCammon 1988). The model described in the Jahoda & McCammon paper has been implemented in a program called `PHMODEL` (Bloch 1988).

   `PHMODEL` generates a two-dimensional matrix called a pulse height response matrix. One axis of the matrix represents the energy of an incoming photon, the other, the proportional counter pulse height. `PHMODEL` has been modified to generate an `XSPEC` compatible (Arnaud 1996) redistribution matrix file (RMF) similar to the DXS position response matrix described
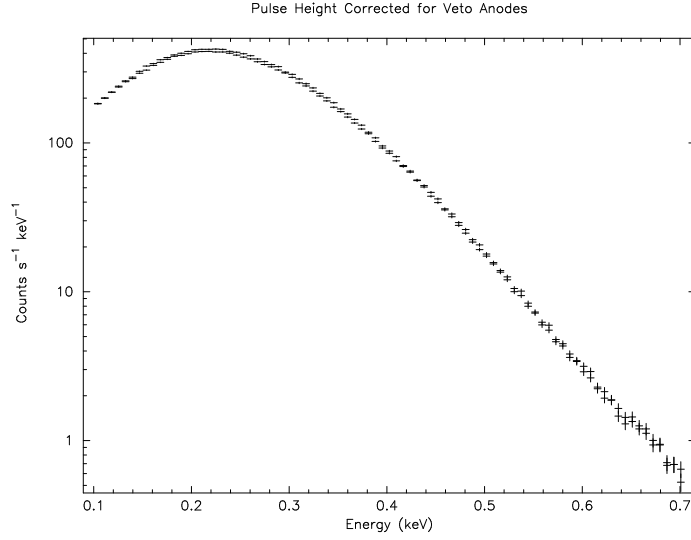
Figure 38: Flat-field pulse height corrected for veto anode distortion.

in §2.5.3. The ancillary response file (ARF), which gives the instrument area solid-angle product, $A\Omega$, as a function of energy is the same in the position and pulse height cases.

The input photon distribution functions determined by fits to the DXS position spectra described in §3.2, and pulse height spectra taken from the same data, were used to determine how well a particular pulse height response matrix generated by PHMODEL described the DXS pulse height response. The initial inputs for PHMODEL were drawn from the Jahoda & McCammon paper. It became immediately apparent that the DXS proportional counters were operating at a much higher gas gain than the proportional counters used by Jahoda & McCammon (by a factor of ∼4). Furthermore, the apparent gas gain decreased with increasing energy. This is suggestive of a charge saturation non-linearity. Thus, two pulse height response matrices were generated, the "High Gain" one, which best describes the zirconium M-ζ, and boron K-α pulse height distributions, and the "Low Gain" one which best fits the carbon K-α pulse height distribution. The gas gain is often characterized in terms of the total charge collected at the anode per secondary electron. Thus, a gas gain of 1.6 fC corresponds to a charge multiplication factor of 10^4.

In addition to having higher gas gain, the DXS pulse height distributions were wider than those of Jahoda & McCammon, resulting in a lower Polya width parameter, and the low energy tail of the carbon pulse height distribution was much more pronounced, implying a much

Table 3: Pulse Height Response Matrix Parameters

Parameter	Jahoda & McCammon Value	Low Energy Fit Value	High Energy Fit Value
Gas Gain (fC)	1.6	6.4	6.2
Polya Width	1.42	1.20	1.25
D/w (μm)	12	120	120

higher ratio of the diffusion constant to drift velocity, D/w. Table 3 lists the parameters that changed between the three response matrices. Figures 39 through 42, show the DXS pulse height data fit with the low gas gain response matrix and Figures 43 through 46 show the data fit with the high gain response matrix. Note that the aluminum K-α gain monitoring line at 1.4 keV is not well described by either response matrix. The gas gain implied by this pulse height distribution is 5.4 fC.

In principle, it would be possible to model the charge saturation non-linearity and incorporate it into the pulse height response matrix. However, the primary purpose of the pulse height response matrix is to provide accurate pulse height *efficiency* information for use in the position response matrix (see §2.5.3) and the difference in calculated pulse height efficiency between the high and low gain cases for energies of interest (151 eV to 284 eV) is only 2%. Therefore, this effect has been ignored and one of the response matrices (the high gain one) was used to generate the pulse height efficiency correction.

3.2 End-to-End Calibration

In addition to the characterization of the DXS proportional counters, the post-flight calibration phase also included a thorough measurement of the functioning of each instrument as a whole. Each instrument was exposed to each of the three sources listed in Table 4. An exposure of each source was taken as it was positioned across the entrance aperture of the instrument at 19 separate locations in order to simulate a continuous, diffuse source that completely filled the DXS field of view. The calibration of the surface brightness of these sources is discussed in §3.2.1. Section 3.2.2 shows how the DXS area-solid angle product ($A\Omega$) was measured using the sources and compares pre-flight and post-flight $A\Omega$ measurements. Section 3.2.3 presents the DXS position spectra obtained from the three sources and discusses fits of X-ray

60
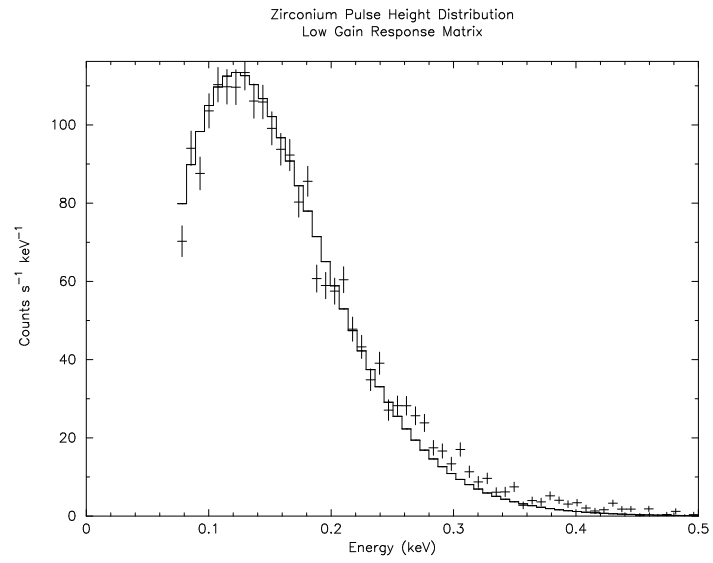
Figure 39: Pulse height spectrum of the zirconium calibration source, Port instrument, low gain response matrix.
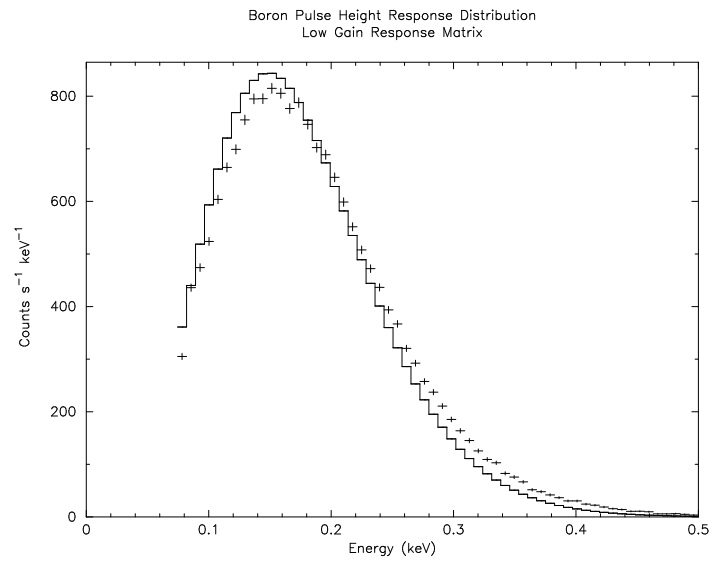
Figure 40: Pulse height spectrum of the boron calibration source, Port instrument, low gain response matrix.
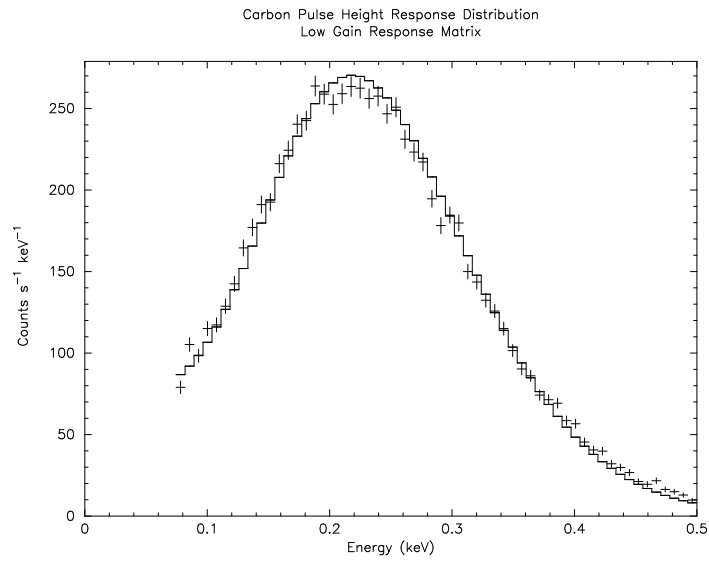
Figure 41: Pulse height spectrum of the carbon calibration source, Port instrument, low gain response matrix.
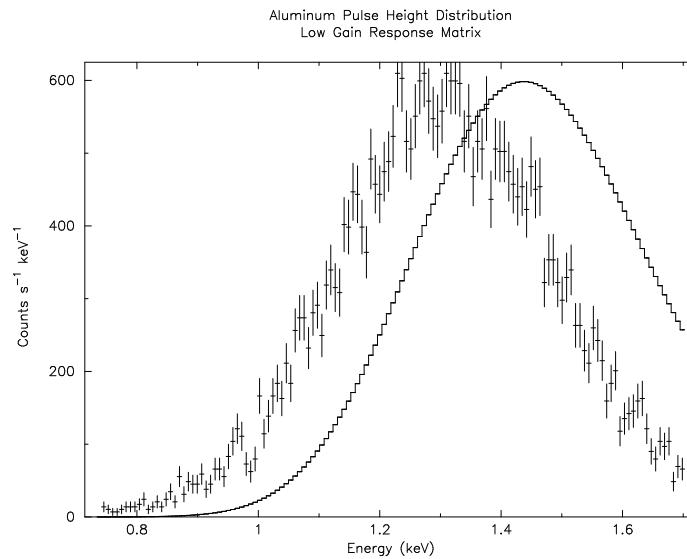
Figure 42: Pulse height spectrum of the on-board aluminum source, Port instrument, low gain response matrix.
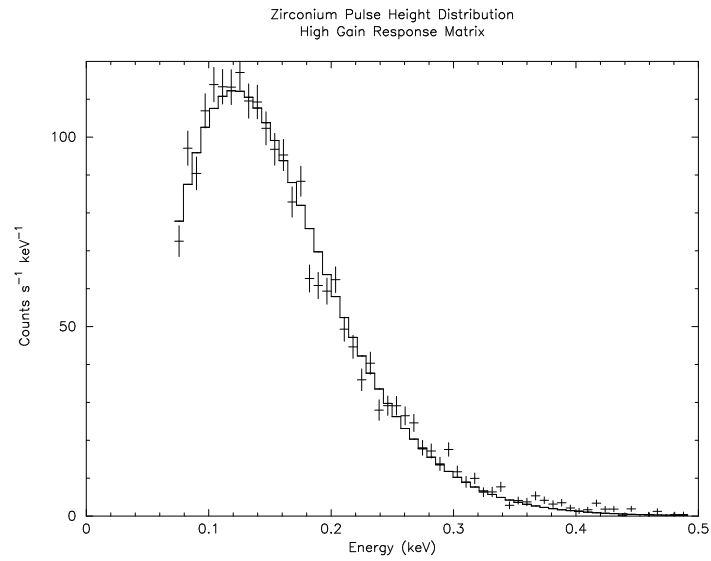
Figure 43: Pulse height spectrum of the zirconium calibration source, Port instrument, high gain response matrix.
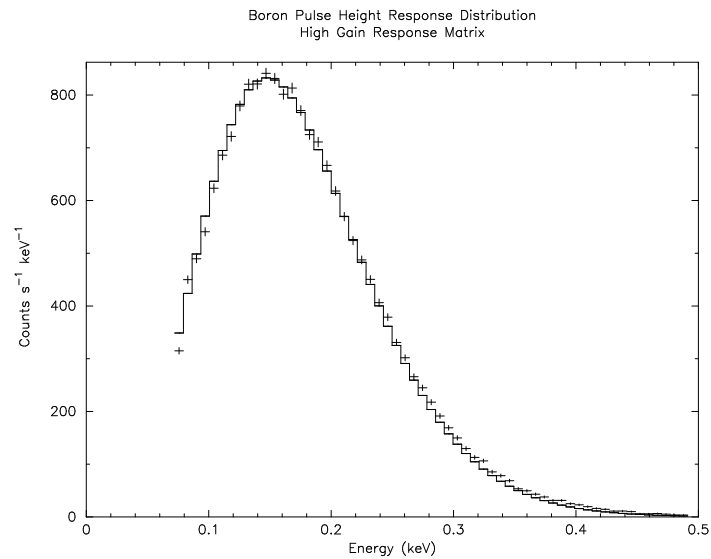
Figure 44: Pulse height spectrum of the boron calibration source, Port instrument, high gain response matrix.
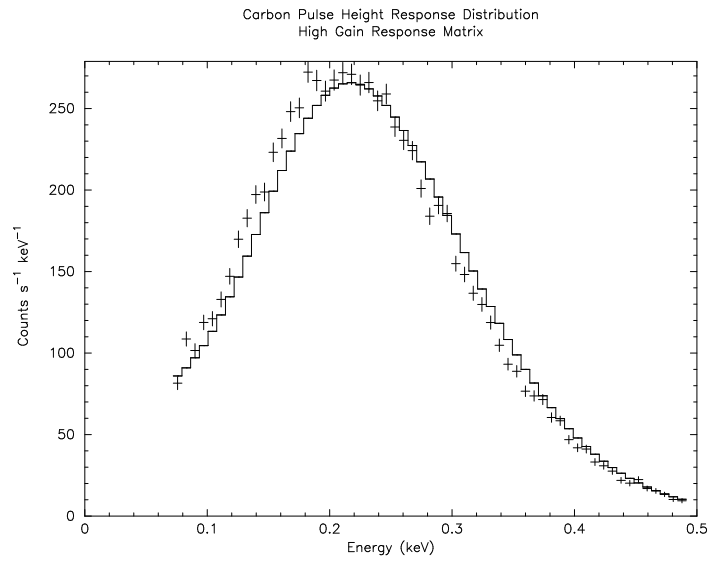
Figure 45: Pulse height spectrum of the carbon calibration source, Port instrument, high gain response matrix.
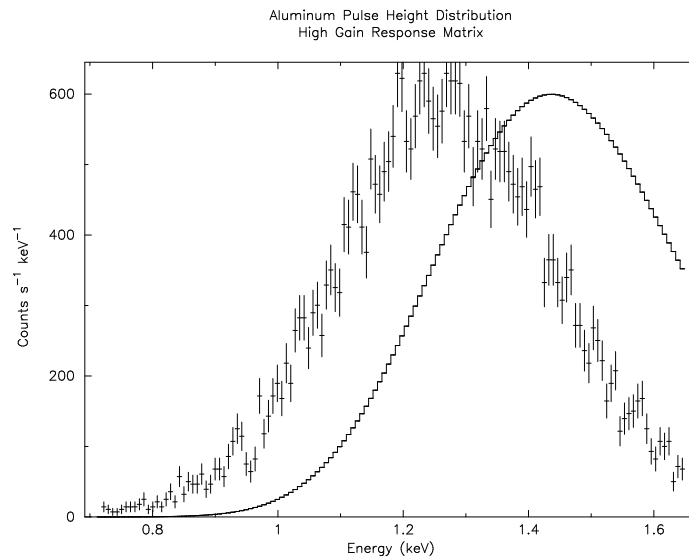
Figure 46: Pulse height spectrum of the on-board aluminum source, Port instrument, high gain response matrix.

Table 4: Alpha-Particle Excited X-ray Sources

Target Material	Primary Line	Energy (eV)	Wavelength (Å)
Zirconium	M-ζ	151	82.1
Boron	K-α	183.3	67.6
Carbon (Polypropylene)	K-α	277	44.8

spectra found in the literature to the data. The pulse height distributions of these sources were discussed in §3.1.4.

3.2.1   Source Calibration

The first step in area-solid angle ($A\Omega$) determination of DXS was to measure the surface brightness of the three test sources. This was done in a vacuum tank with a pressure below 10^{-4} torr, low enough to make the correction due to X-ray absorption of the residual gas negligible. One of the sources was the carbon K-α X-ray source described in §3.1.2. The other sources were of similar construction with different target materials. One source was a sheet of metallic zirconium, producing zirconium M-ζ radiation, and the other source was a polypropylene sheet coated with boron powder, producing boron K-α radiation. The linear surface brightness of each source was measured by sequentially masking off one centimeter wide strips of each source and measuring the flux coming from the slit at several angles with a small proportional counter. After correction for the foreshortening of the slit there was no systematic variation in the counting rates as a function of angle, nor was there any systematic variation in the counting rates as a function of with slit position. However, the standard deviation of the ensemble of measurements was large compared to the expected Poisson deviations. Table 5 summarizes these data.

The source surface brightnesses were normalized to the same day using the decay rate of the ^{210}Po alpha-particle sources and the formula:

$$I = I_0 2^{-T/\tau} \tag{3.1}$$

where T is time difference between 1/1/93 and the date the source was measured and τ is the half-life of ^{210}Po (138.4 days).

Table 5: X-ray source count rate. No correction has been made for the transmission of the entrance window of the small proportional counter used to measure these rates.

Target Material	Average I $\left(\frac{cts}{s \times cm \times sr}\right)$ normalized to 1/1/93	Standard Deviation of Ensemble	Poisson Error of Typical Measurement
Zirconium	3798	8%	2%
Boron	31511	2%	1%
Polypropylene (carbon)	64006	10%	1%

Table 6: Small Proportional Counter Window Transmission

Line	Energy (eV)	Measured Transmission	Theoretical Transmission
Zr M-ζ	151	0.158	0.109
B K-α	183.3	0.204	0.210
C K-α	277	0.400	0.433
F K-α	676.8	0.230	0.229

In order to obtain the absolute linear surface brightness of these X-ray sources (units of photons s^{-1} cm^{-1} sr^{-1}), the window transmission of the small proportional counter needed to be divided out of the count rates listed in Table 5. The small proportional counter window material was 0.5μm Mylar coated with DAG, a carbon compound that increases the surface conductivity of the Mylar. The mesh was the same 65.4% transmission mesh used in the DXS proportional counter windows. The window transmission was measured in much the same way as the DXS window transmission, described in §3.1.1, except that the size of the window (1 cm diameter circle) limited the effective number of measurement points to one. The transmission measurements were compared with theoretical transmissions based on the window material thicknesses in a method similar to that outlined in §3.1.1. It was not possible to justify the zirconium transmission measurement to the transmissions measured at other energies. This is most likely due to carbon contamination in the zirconium source (see below). Discarding the zirconium transmission value, the best-fit value for the thickness of the DAG coating was 75 μg cm^{-2} of carbon. The measured and fit transmissions are shown in Table 6.

66

Table 7: Zirconium Target Weighted Throughput

Line Energy (eV)	151	155.3	161.7	177	277
Norm (cts s^{-1} cm^2 sr^{-1})	753.8	71.2	101.1	55.0	43.5
Line Fraction	0.746	0.069	0.098	0.052	0.035
DXS Model 16					
$\quad A\Omega$ (cts photon^{-1} cm^2 sr)	0.0119	0.0141	0.0159	0.0176	0.0081
$\quad$ Weighted Throughput	0.0089	0.0010	0.0016	0.0009	0.0003
$\quad$ (cts photon^{-1} cm^2 sr)	Total:	0.0126			
Small Prop. Counter					
$\quad$ Window Transmission	0.109	0.122	0.141	0.190	0.433
$\quad$ Weighted Transmission	0.081	0.008	0.014	0.010	0.015
	Total:	0.128			

Zirconium Source

The DXS spectrum of the zirconium source (Figure 54) shows that its flux is distributed over several lines across the DXS pass band, including some carbon contamination. Since the small proportional counter used to measure the absolute surface brightness of the source could not resolve the flux in these individual lines, the effective area solid-angle product (throughput) of the small proportional counter and DXS instrument have been calculated for this source in order to compare results. The construction of these throughput values is shown in Table 7. "Norm" gives the XSPEC fit values to the DXS zirconium spectrum discussed in §3.2.3. The line fractions are calculated by dividing the total of the "Norm" row by each element in the row. These fractions are then multiplied by the DXS response matrix (model 16) $A\Omega$ at each energy to arrive at the weighted throughput for each individual line. The sum of the weighted throughput values is the total weighted throughput of the instrument for the zirconium source. For the Port instrument, this sum is 0.0126 counts photon^{-1} cm^2 sr. The weighted window transmission of the small proportional counter is calculated in a similar way and is used in the calculation of the "Source Surface Brightness" value for the zirconium target in Table 8.

It is important to note that the calculation of the DXS weighted throughput and small proportional counter window transmission for the zirconium lines is dependent on the model 16 response matrix. Neither the absolute flux ratios of the individual lines in the zirconium source nor the carbon contamination are known *a priori*, and fit values to the line fluxes derived using the model 16 response matrix must be used.
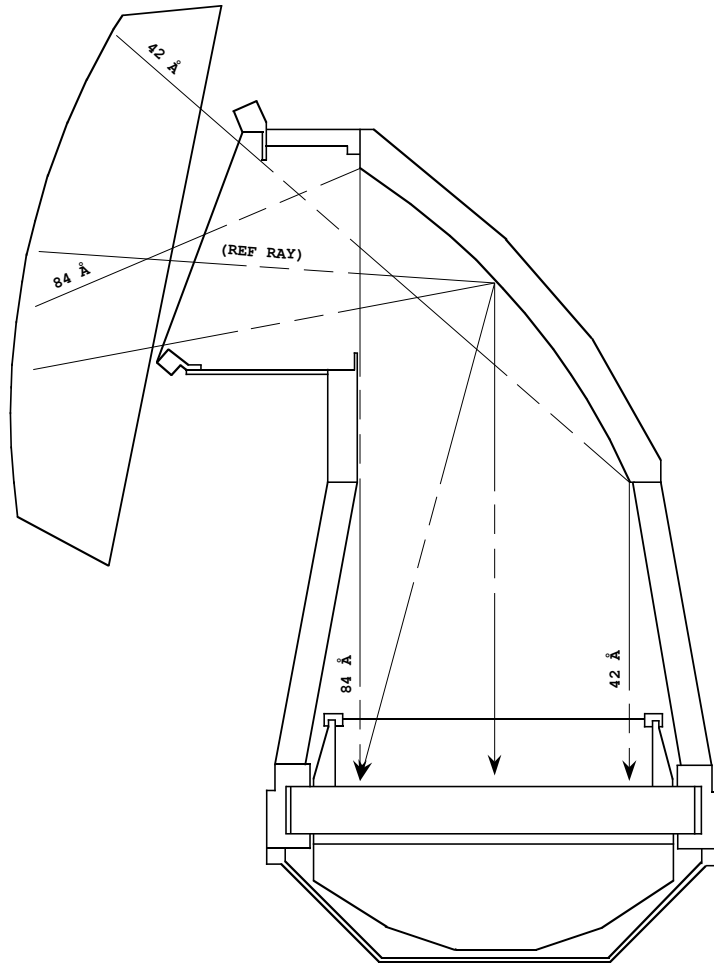
Figure 47: DXS end-to-end calibration geometry.

3.2.2   Area-Solid Angle Product ($A\Omega$)

The area-solid angle product ($A\Omega$) at each of the energies listed in Table 4 was measured by placing the instrument and corresponding source into a vacuum tank in the orientation shown in Figure 3.2. The sources were mounted with their long axes perpendicular to the long axis of the DXS entrance aperture, assuring uniform source exposure in the dispersion direction. The sources were mounted on a track (not shown) so that they could slide back and forth in front of the instrument (in and out of the page in Figure 47).

Data were taken with the source in 19 evenly spaced positions along the track. The counting rates in the instruments as a function of these position are shown in Figures 48 through 50. The statistical error in the counting rate is small compared to the size of the data points. The

Figure 48: Instrument Counting Rate vs. Zirconium Source Position.

variation the the counting rate with position is caused by the fact that the DXS proportional counter sits at the end of a long tube. This variation is easily calculable given the spectrometer geometry and the energy of the incident photons and is shown fit to the data as the solid lines. The difference between the integrals of the data and model curves is less than 1%.

The total count rate in all 19 positions (subtracting 19 times the average rate in positions 00 through 02 as background) for each source is given in Tables 8 and 9 as "DXS whole instrument response." This is the total counting rate for all good POS (20–220) in the DXS instruments as if they were viewing an extended source with a surface brightness equal to the product of the spacing between two of the 19 source positions (6.34 cm) and the linear surface brightness of the source (listed in Table 5). The calculated surface brightnesses for all three sources are listed as "Source Surface Brightness" in Tables 8 and 9. These have been corrected for the decay of the ^{210}Po source by equation 3.1. The "Surface Brightness Error" values are from Table 5, except for the zirconium value, which is added in quadrature with an estimate of the error in the effective efficiency (the standard deviation of the port and starboard effective efficiency values). The measured $A\Omega$ is simply the ratio of the DXS whole instrument response to the source surface brightness.

Figure 50: Instrument Counting Rate vs. Carbon Source Position.

70

Table 8: Area Solid-Angle Product ($A\Omega$) Calculation (Port)

Target Material	Zr (*weighted)	B	C
Date Measured	9/16/93	8/26/93	9/2/93
DXS whole instrument response (counts s^{-1})	15.06	130.62	54.59
Source Surface Brightness (photons s^{-1} cm^{-2} sr^{-1})	1223*	7224	6855
Surface Brightness Error	9%*	2%	10%
Measured $A\Omega$ (Post-flight) (counts photon^{-1} cm^2 sr)	0.0124*	0.0181	0.0080
Measured $A\Omega$ Error	9%*	2%	10%
$A\Omega/(T_wT_m)$ (Post-flight) (counts photon^{-1} cm^2 sr)	0.0535*	0.0571	0.0159
$A\Omega/(T_wT_m)$ (Pre-flight) (counts photon^{-1} cm^2 sr)	–	0.0598	0.0169
Pre-flight/Post-flight $A\Omega/(T_wT_m)$	–	1.05	1.07

$A\Omega$ measurements were made in a similar manner in November-December 1985 (Snowden 1986). In order to compare between the pre-and post-flight $A\Omega$ measurements, the transmissions of the DXS proportional counter window (T_w) and supporting mesh (T_m) used at the time of measurement are divided out of the $A\Omega$ measurements. Rows $A\Omega/(T_wT_m)$ of Tables 8 and 9 show good agreement (within 7%) between the pre- and post-flight $A\Omega$ measurements. This is important evidence that the DXS crystal panels did not degrade significantly during flight.

Model 16 Response Matrix

The DXS instrument response matrix described in §2.5 has been used to compare the pre-installation flight crystal panel integrated reflectivity values shown in Table 1 to the total instrument $A\Omega$ measurements shown in Tables 8 and 9. The response matrix was generated using the the original Henke #2 integrated reflectivity function. Next, the ratios between the $A\Omega/(T_wT_m)$ values predicted by this model and each of measured $A\Omega/(T_wT_m)$ values were computed. These ratios, together with the ratios of the pre-installation flight crystal panel reflectivity measurements to the Henke #2 integrated reflectivity function, are plotted as a function of time in Figure 51. Note that the zirconium K-α line was used only the post-flight

Table 9: Area Solid-Angle Product ($A\Omega$) Calculation (Starboard)

Target Material	Zr (*weighted)	B	C
Date Measured	11/17/93	11/27/93	11/11/93
DXS whole instrument response (counts s^{-1})	10.37	87.46	45.36
Source Surface Brightness (photons s^{-1} cm^{-2} sr^{-1})	894*	4534	4828
Surface Brightness Error	9%*	2%	10%
Measured $A\Omega$ (Post-flight) (counts photon^{-1} cm^2 sr)	0.0116*	0.0193	0.0094
Measured $A\Omega$ Error	9%*	2%	10%
$A\Omega/\left(T_w T_m\right)$ (Post-flight) (counts photon^{-1} cm^2 sr)	0.0510*	0.0632	0.0190
$A\Omega/\left(T_w T_m\right)$ (Pre-flight) (counts photon^{-1} cm^2 sr)	–	0.0609	0.0187
Pre-flight/Post-flight $A\Omega/\left(T_w T_m\right)$	–	0.96	0.99

calibration.

Figure 51 shows that the pre-installation, pre-flight, and post-flight calibrations all show comparable values at each energy studied. There is a trend, however, for the flight crystals to be more reflective at carbon and less reflective at zirconium than the Henke #2 crystal. As a result, the integrated reflectivity function in the response matrix generating program, SPCMOD, has been modified to fit the Port post-flight calibration data. This function has been multiplied by 1.082 in order to fit the Starboard post-flight data. The resulting response matrix (model 16) predicts the DXS post-flight $A\Omega$ values shown as the solid lines in Figures 52 and 53. The measured post-flight calibration $A\Omega$ values are plotted as the data points with error bars.

In order to minimize the potential for systematic errors in the response matrix calibration procedure, the instrument, telemetry, and data processing procedures were duplicated as much as possible between the flight and post-flight calibration with two important exceptions. First, the proportional counter windows used during the flight were replaced. This was necessitated by an accident which broke the port flight window. The new windows were of similar construction and fully calibrated, as discussed in §3.1.1. Second, when on the ground, the gas gains of the DXS proportional counters vary predictably on a daily cycle, with the majority of the day spent at the nominal value. Thus, time dependent gain correction was not necessary.

Figure 51: Flight crystal panel reflectivity at the three calibration energies listed in Table 4 vs. time, relative to Henke #2 sample crystal reflectivity. Data points from the same calibration line and instrument are connected with a line to aid identification. Formal error bars, calculated for the post-flight calibration data are 10% for zirconium and carbon and 5% for boron.

Figure 53: Comparison of $A\Omega$ of best-fit response matrix (model 16) to post-flight $A\Omega$ data (Starboard instrument).

This allowed the software lower level discriminator to be run at a lower level than the flight case (see §4.7). Both of these changes were incorporated into the response matrices used to analyze the post-flight calibration data.

3.2.3   Spectral Response to Mono-Energetic Sources

This section presents the position spectra DXS recorded of the three post-flight calibration sources and discusses model fits to these data.

The spectra of the three post-flight calibration sources were created from the data used to measure the instrument $A\Omega$, discussed in §3.2.2. The data from all 19 source positions were added together to create a single spectrum of each source. The spectra (formed from the KU data) were then flat-fielded using the procedure described in §3.1.2. The resulting spectra for the Port instrument are shown in Figures 54 through 56 as the points with error bars.

The solid lines in Figures 54 through 56 are models of the individual sources folded through the "model 16" response function by the X-ray spectral analysis package XSPEC (Arnaud 1996). When allowed to vary as a free parameters, the peak energies of the source models (excluding the smaller peaks in the zirconium spectrum) do not vary more than 0.3 Å from their nominal values. Agreement between model and data at this level has been made possible by careful choice of input functions, $2D$ (twice the spacing between the planes of lead atoms in the synthetic lead stearate crystals). Modifications to the crystal panel rocking curves are also considered.

Choice of Input Functions

Emission from fluoresced solid-state targets is often subject to chemical broadening, an effect in which the electronic orbits participating in the X-ray emission are distorted due to the presence of chemical bonds. This effect can result in complicated structure in the X-ray emission and even a shift in the peak energy. Thus, early in the DXS post-flight calibration exercise, an effort was made to find high-resolution spectra of sources similar to those used in the DXS post-flight calibration exercise for use as empirical source models.

The literature contains few high resolution X-ray spectra of sources similar to those used in the DXS post-flight calibration. Holliday (1967) is the most fruitful source uncovered so
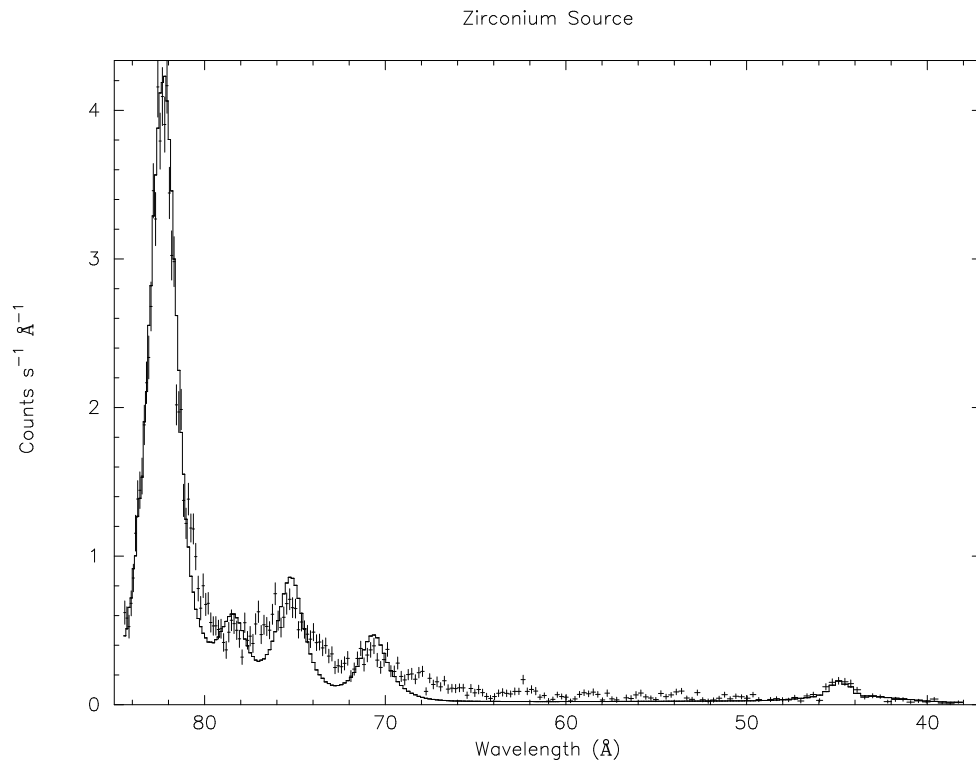
Figure 54: Spectrum of the zirconium calibration source, Port instrument. Solid line is five zero-width Gaussians, whose energies are listed in Table 7, folded through the post-flight model 16 response matrix.
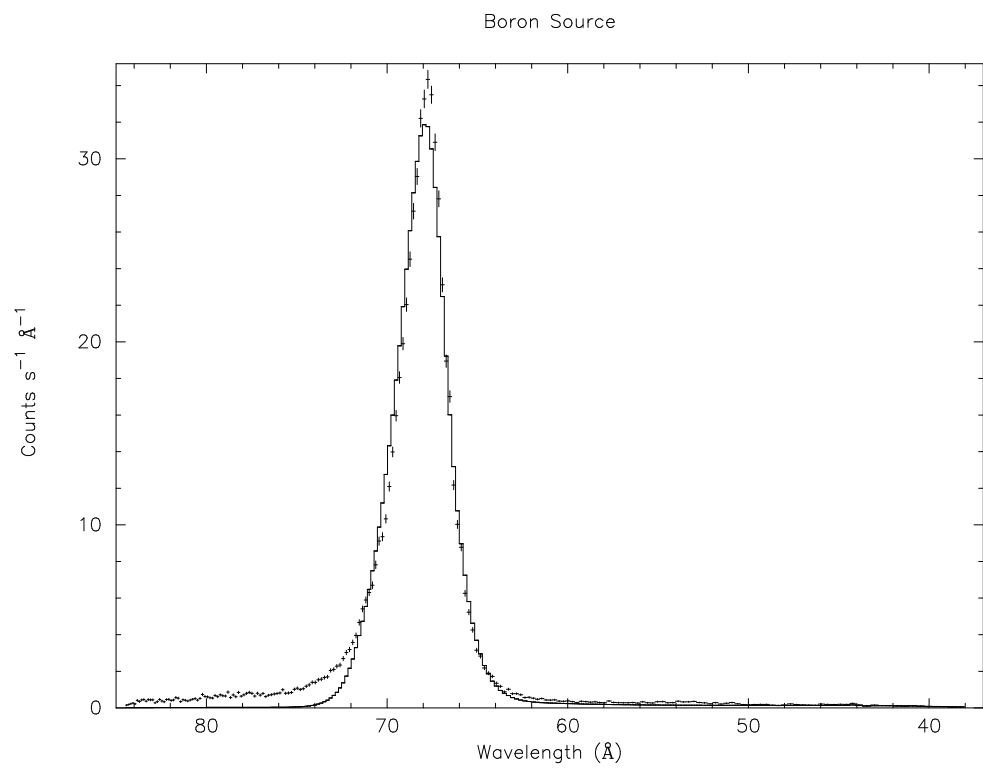
Figure 55: Spectrum of the boron calibration source, Port instrument. Solid line is the measured boron spectrum from Holliday (1967) folded through the post-flight model 16 response matrix.
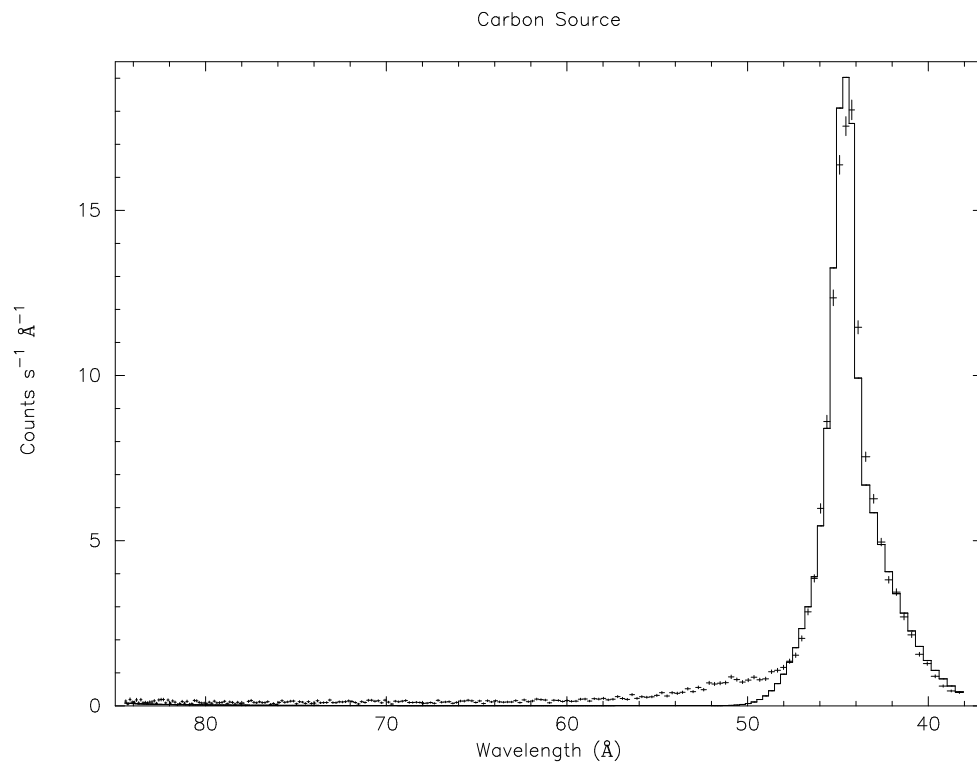
Figure 56: Spectrum of the carbon calibration source, Port instrument. Solid line is the measured TiC spectrum from Holliday (1967) folded through the post-flight model 16 response matrix.

far. This article contains several high resolution spectra of electron-excited boron and carbon-containing sources. R. J. Edgar hand-digitized all of the relevant spectra in the article and formatted them for use as input models to `XSPEC`, version 8 (Arnaud 1996). The elemental boron and TiC spectra were used directly as input models for the boron (Figure 55) and carbon (Figure 56) data, respectively. The Holliday TiC, ZrC, and HfC spectra are all essentially identical, and, after folding through the DXS response matrix, appear identical to a zero-width Gaussian at 277 eV. The Holliday graphite and "carbon contamination" spectra are significantly wider and their peaks are shifted more than 1 eV lower in energy that the TiC family. Other boron spectra found in the literature (e.g. Landolt-Börnstein 1955) all showed the extended tail toward lower energies seen in the data, but were even broader than the Holliday elemental boron spectrum.

No spectra of elemental zirconium sources have been found in the literature. Four zirconium M-line energies in the DXS pass band are listed, without line strengths, in Bearden (1967). These line energies, together with carbon K-α have been used as the input energies for five zero-width Gaussians which are fit with free normalization parameters to the zirconium data. As seen in Figure 54, it is evident that simple zero-width Gaussian lines do not fit all of the lines well. The primary zirconium M-line, and the carbon line, however, do fit well and have best fit energy values within 0.2% of nominal.

$2D$ Spacing of Lead-Stearate

The precise position of the model peak relative to the data depends sensitively on the value assumed for the spacing between the planes of lead atoms in the synthetic lead stearate crystal. For ease of use with the Bragg law (Equation 2.1), twice this spacing is often reported (i.e. $2D$). Henke *et al.* (1982) list the lead stearate $2D$ as 100 Å. This is in conflict with data collected by the Wisconsin Space Physics group. Recall from §2.2.1 that an X-ray monochromator at the Physical Sciences Laboratory (PSL) in Stoughton, Wisconsin was used to measure the rocking curves of sample lead stearate crystals. Using the monochromator output energy, the measured position in angle of the reflected X-ray peak, and the Bragg law, it is possible to solve for $2D$. For the PSL measurements, the average $2D$ was 101.0 Å. Also described in §2.2.1 was a simpler system, installed in the Space Physics Laboratory, that measured the peak and integrated reflectivity of crystal samples. This system also had an accurate angular scale. Using several different Bragg reflection orders of aluminum and oxygen the Space Physics

Table 10: Lead Stearate $2D$ Determination

	Line	Energy (eV)	Implied 2D (Å)	Comments
Space Phys.	Al	1486.7	101.5	Multi-order
Space Phys.	O	524.9	>101.10	Multi-order
Holliday	TiC, etc.	277	101.5	Good fit
Holliday	Graphite	276	<103	Too wide
Holliday	Boron	183.3	102	Too wide
Gaussian	Zr	151	101.5	Good fit
PSL lines		Various	101.0	Bad λs
Charles (1971)			100.4	
Henke (1982)			100	

system measured the lead stearate $2D$ as greater than 101.1 (see Table 10). Furthermore, the data from the three large fluorescent sources used in the DXS post-flight calibration exercise can be used to measure $2D$ by varying the value of $2D$ assumed by the program, SPCMOD, which generates the DXS response matrix. The results for the zirconium, boron, and carbon sources are shown in Table 10. In the case of the carbon target, the best-fit value of $2D$ depends on the choice of input function, with the Holliday (1967) graphite profile resulting in a significantly different $2D$ value from the TiC family of profiles.

The body of evidence assembled in Table 10 suggests that for the synthetic lead stearate crystals used in DXS, $2D = 101.5$ Å. Of particular importance is the value determined by the aluminum multi-order Bragg reflection measurement. According to the Bragg law (Equation 2.1), reflection peaks for a given energy, are equally spaced in $\sin(\theta)$. Thus, any potential zero-point error in the angular scale used to make the measurements can be measured by fitting a line through the peak angle vs. angle plot. Such an analysis reveals that the zero-point error of the space physics Bragg reflection system was small (less than 0.2°). The Henke value is clearly low compared to all of the other values and can be discarded. The PSL lines result in a low value of $2D$ probably because the X-ray monochromator wavelength scale is not accurate. Some hysteresis in the tuning mechanism was necessary for proper functioning of the monochromator (see §A). The oxygen multi-order measurement is a lower limit because carbon K-α radiation emitted from the same sample produces another peak in the spectrum not far from the oxygen peak. This results in a shift in the peak position of the oxygen line to a higher angle, thus decreasing the measured $2D$. The boron $2D$ determination by DXS is high

because when folded through the response matrix, the Holliday (1967) boron input function is too wide and the model peaks at a slightly lower energy than the data. The electron-excited graphite input profile from Holliday (1967) results in a large value of $2D$, presumably because it is a poor approximation to the profile produced by α-particle excited polypropylene. The Holliday TiC family of profiles fit the DXS data much better.

Rocking Curve Lorentzian Wings

Figure 57 shows a plot of the measured boron spectrum described in Figure 55 with a logarithmic Y-axis. The dashed line is the Holliday (1967) boron spectrum folded through the model 5 response matrix, which uses the original Henke #2 rocking curve. Note the clear discrepancy between the data and model in the wings. This discrepancy has two possible causes: the fluorescent source used for the DXS post-flight calibration has much broader wings than the Holliday (1967) boron source, or the flight crystal panel rocking curve has much broader wings than the Henke #2 crystal.

In an attempt to determine which of these two causes is the more correct, a new response matrix was generated (model 6) which is identical to model 5 except that a Lorentzian wing component was been added on the high angle (low energy) side of the Bragg peak and the low angle Lorentzian wing was modified so as to best fit the extended wings in all three of the post-flight calibration sources. The solid line is the Holliday (1967) boron spectrum folded through the model 6 response matrix.

The change in the Lorentzian wings is a clear departure from the original Henke #2 rocking curve data, as seen in Figures 58 through 60. Perhaps more importantly, the addition of the Lorentzian wings increased the predicted area solid-angle product ($A\Omega$) of the instrument by $\sim10\%$. The good agreement between the pre-installation crystal panel reflectivity and the pre-flight, and post-flight $A\Omega$ measurements using the original Henke #2 model shown in Figure 51 is evidence against such a change.

The evidence discussed above suggests that the fluorescent X-ray source used in the DXS post-flight calibration exercise has broader wings than the source measured by Holliday (1967). Therefore, The final response matrix (model 16) uses the unmodified Henke #2 rocking curve. However, given that the formal errors of the $A\Omega$ measurements are $\sim10\%$ the possibility still exists that the Lorentzian wings are caused by the crystals. In order to show the effect of the variation of the rocking curve Lorentzian wings on the interpretation of astrophysical models,

Comparison of Original and Modified Lorentizian Wings
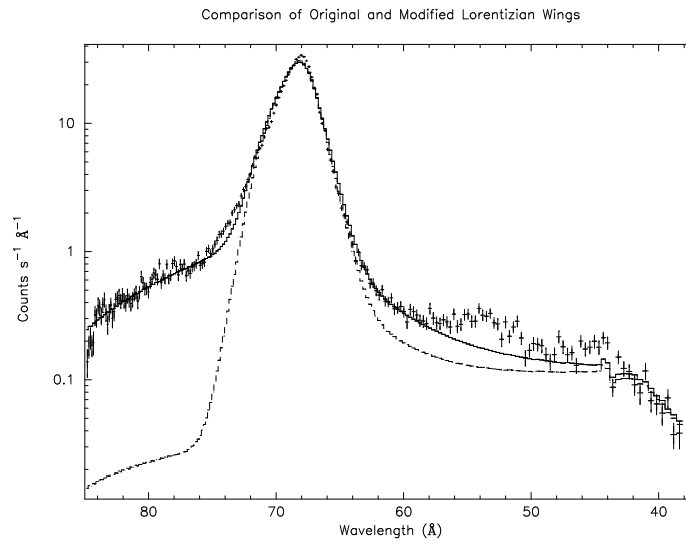
Figure 57: Comparison of response matrices models 5 and 6, using the Henke #2 (dashed line) and modified Lorentzian wings (solid line), respectively. Data is from the Port detector, boron source.

Lead Stearate Reflectivity at 151 eV
Post−Flight Calibration Fit
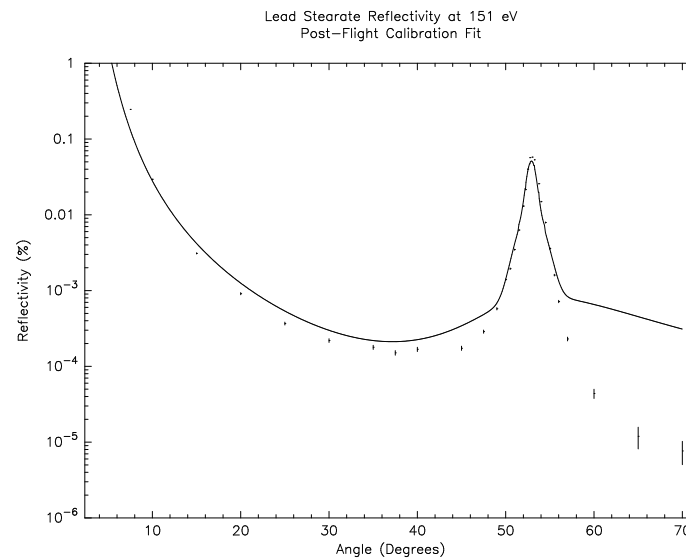
Figure 58: Henke #2 reflectivity as a function of angle at 151 eV (data points) with model 6 rocking curve (solid line).
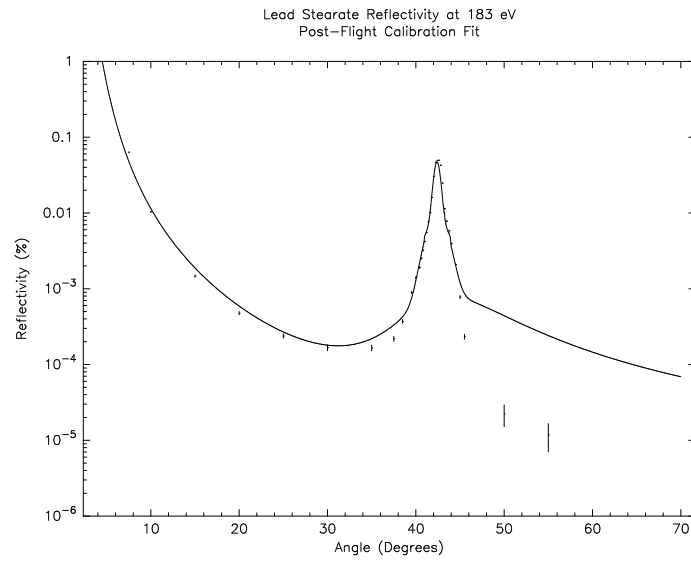
Figure 59: Henke #2 reflectivity as a function of angle at 183 eV (data points) with model 6 rocking curve (solid line).
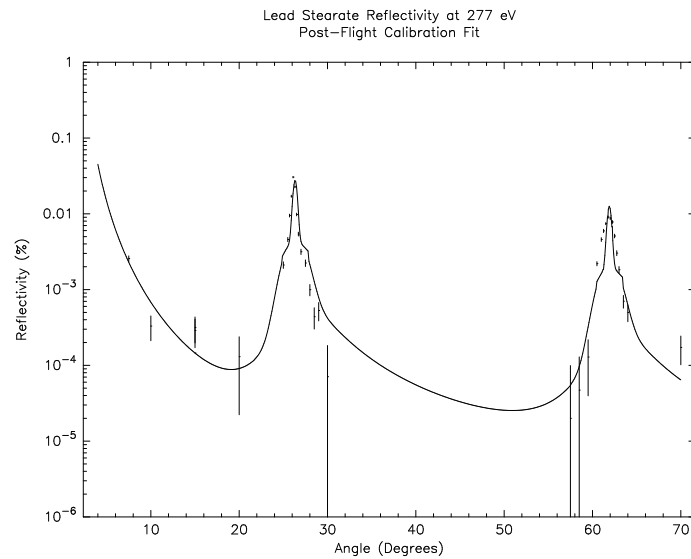
Figure 60: Henke #2 reflectivity as a function of angle at 277 eV (data points) with model 6 rocking curve (solid line).
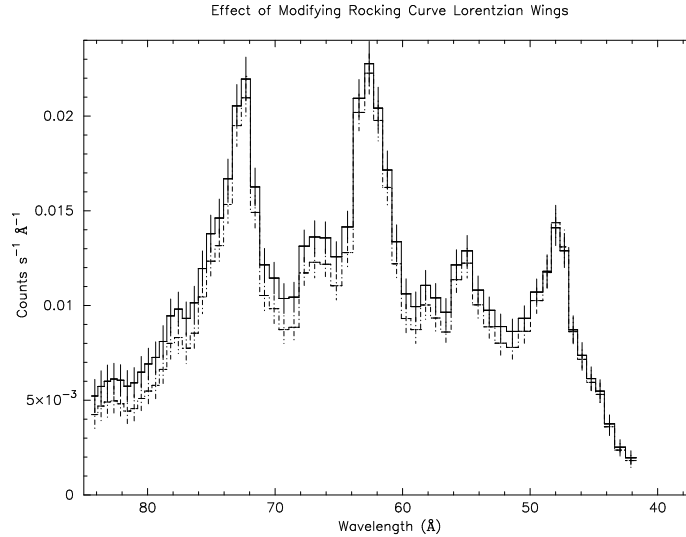
Figure 61: Comparison of Henke #2 (dash-dot line) and modified Lorentzian wings (solid line) in an astrophysical spectrum. The error bars are simulated, based on the counting statistics of the DXS HISM spectrum (see §5.6).

the "VMEKAL" model described in §6.2.3 has been folded through the model 5 and model 6 response matrices, as shown in Figure 61. Because there are so many lines that make up the "VMEKAL" spectrum, the addition of broader wings to the rocking curve raises the pseudo-continuum level. The effect is the greatest at low energies (∼20%).

Rocking Curve Full-Width-Half-Max (FWHM)

Recall from §2.2.1 that the rocking curves of the flight crystal panels were never measured with the narrow line synchrotron source. Rather, the response matrix generating program depends on an empirical fit to a sample crystal (Henke #2). It is possible that the flight crystal rocking curve parameters vary significantly from those of Henke #2. Thus, the rocking curve full-width-half-max (FWHM) has been varied in the program SPCMOD in an attempt to achieve better fits between the input functions from Holliday and the post-flight calibration data. For the Holliday elemental boron and graphite spectra, the best fit rocking curve FWHM values are 1/2 the FWHM value of Henke #2.

The rocking curves of several other sample crystals were measured at the same time as the Henke #2 crystal. Variations of up to a factor of two were seen in FWHM, however, the

Henke #2 crystal had one of the *narrower* FWHM values. Thus, it is unlikely that the flight crystals could have a FWHM half as wide as the Henke #2 crystal and so the original Henke #2 value is used in the final model 16 response matrix. However, without further measurements, it is impossible to completely rule out this possibility.

In order to show the effect that a change of a factor of two in the rocking curve FWHM might have in the scientific interpretation of the DXS data, the "VMEKAL" model from §6.2.3 has been folded through two versions of the DXS response matrix, which differ only in rocking curve FWHM (models 6 and 7). The resulting simulations of the DXS response are shown as the solid and dash-dot curves in Figure 62. The dash-dot curve (model 6) uses the FWHM of the Henke #2 crystal; the solid curve (model 7) uses a FWHM a factor of two smaller. The error bars are simulated, based on the counting statistics of the DXS HISM spectrum (see §5.6). It is evident from the figure that the change in the FWHM only effects the shape of shaper peaks in the model spectrum, and that only by $\sim$10% at the peak value.

Geometric Considerations

As discussed earlier in this section, the model of the crystal panel reflectivity has been modified in order to better fit the post-flight calibration data. One of the implicit assumptions allowing this modification is that other factors affecting the instrument performance are known to high accuracy. In particular, the precise shape and position of the crystal panel relative to the proportional counter are important in determining the wavelength scale. The accuracy of the function O' in Equation 2.9 is important in determining the instrument's area-solid angle product.

The shape and position of the crystal panel relative to the proportional counter were measured for the Port instrument in a laser reflection experiment. The measurement verified that the crystal panel center of curvature was within 0.030 inches of its nominal position relative to the mounting surface of the proportional counter. However, a slight deviation from cylindrical was found at the edges of the crystals, e.g., near the first and last proportional counter position channels. The response matrix generating program, SPCMOD, was modified in order to model the distortion in the crystal panel. During the modification process, several minor errors were found and corrected in the calculation of the geometric factor, O', in Equation 2.9. None of these modifications resulted in any significant change in the final response matrix.

A small systematic difference was found between the Port and Starboard proportional

Effect of Varying Rocking Curve FWHM by a Factor of 2
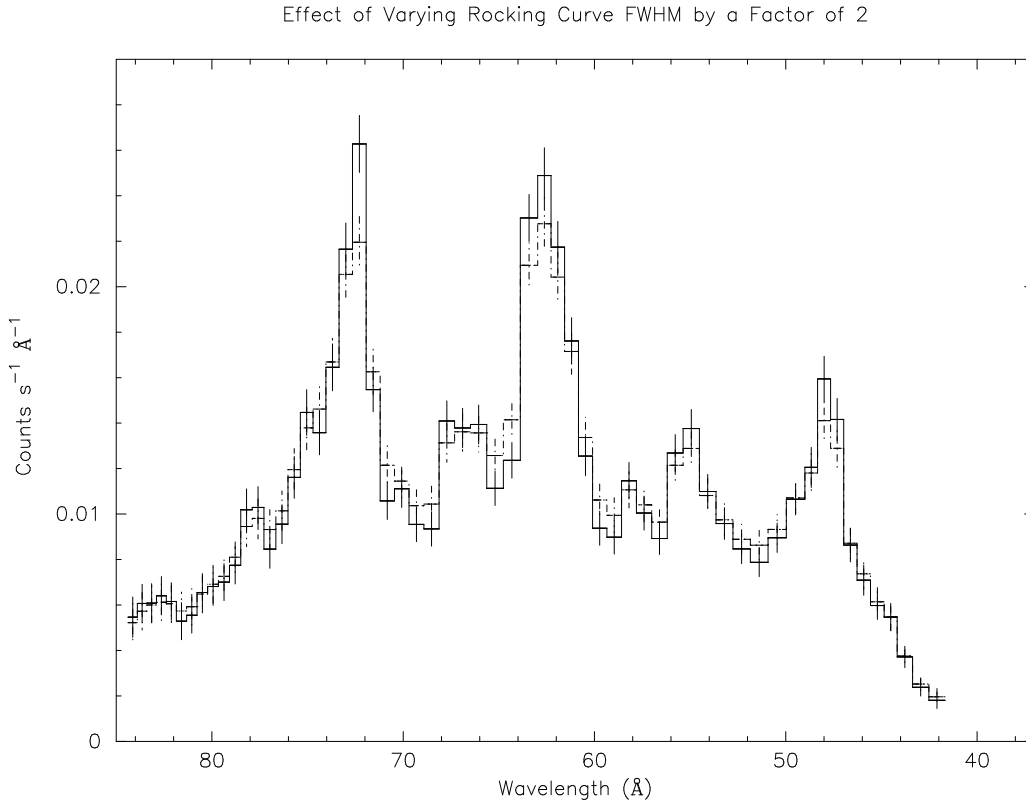
Figure 62: Effect of varying rocking curve FWHM by a factor of 2. The response matrix that produced the solid (model 7) has a rocking curve FWHM that is a factor of two smaller than the rocking curve used in the response matrix that produced the dash-dot line (model 6). The error bars are simulated, based on the counting statistics of the DXS HISM spectrum (see §5.6).

counter positions measured for the zirconium, boron, carbon Bragg reflection peaks. Since the line energies and crystal panel $2D$ values are the same for the Port and Starboard instruments, the most likely cause of the shift in peak position was a difference in the proportional counter positions relative to their respective crystal panel centers of curvature. The difference amounts to a relative shift of 0.020 inches. To achieve the best overall wavelength scale, the final response matrices are constructed assuming that the Port proportional counter is shifted 0.010 inches toward the Port crystal panel center of curvature, and the Starboard proportional counter 0.010 inches away. Given that there are six mechanical joints with nominal tolerances of 0.005 inches between the ground plane wires, which are responsible for the position detection (see §2.3.1), and the crystal panel assembly, the magnitude of these shifts is reasonable.

3.3   Summary and Conclusion

This chapter has discussed the calibration of the DXS spectrometers. Section 3.1 discussed the proportional counter detection efficiency and position determination accuracy. The proportional counter detection efficiency is primarily determined by the transmission of the thin plastic window (§3.1.1) and secondarily by the pulse height detection efficiency (§2.5.3 and §3.1.4). The effect of differential non-linearity in the proportional counter position detection has been corrected by the process of flat-fielding (§3.1.2).

With the proportional counter well understood, the performance of the rest of the spectrometer could be inferred from the whole instrument's response to laboratory X-ray sources of known brightness. Section 3.2.1 discusses the determination of the surface brightnesses of the three calibration sources. The DXS counting rate is divided by the surface brightnesses for each source, yielding the measured area-solid angle product ($A\Omega$) as a function of energy (the three points in Figures 52 and 53). These measurements compare well to pre-flight $A\Omega$ measurements and the pre-installation integrated reflectivity measurements shown in Figure 51.

Figure 63 shows the sum of the post-flight spectral data for the Port instrument. The point-to-point smoothness of the data shows that the flat-field procedure has removed all significant systematic variation with periods of 10 channels or less. The three major peaks are shown to be well fit by the combined source model (solid line), though upon close inspection, the modeled boron peak (at 67.6 Å) is too wide and the small peaks in the 75–78 Å region are too narrow. As discussed in §3.2.3, it is likely that the poor fits in these lines are the fault of
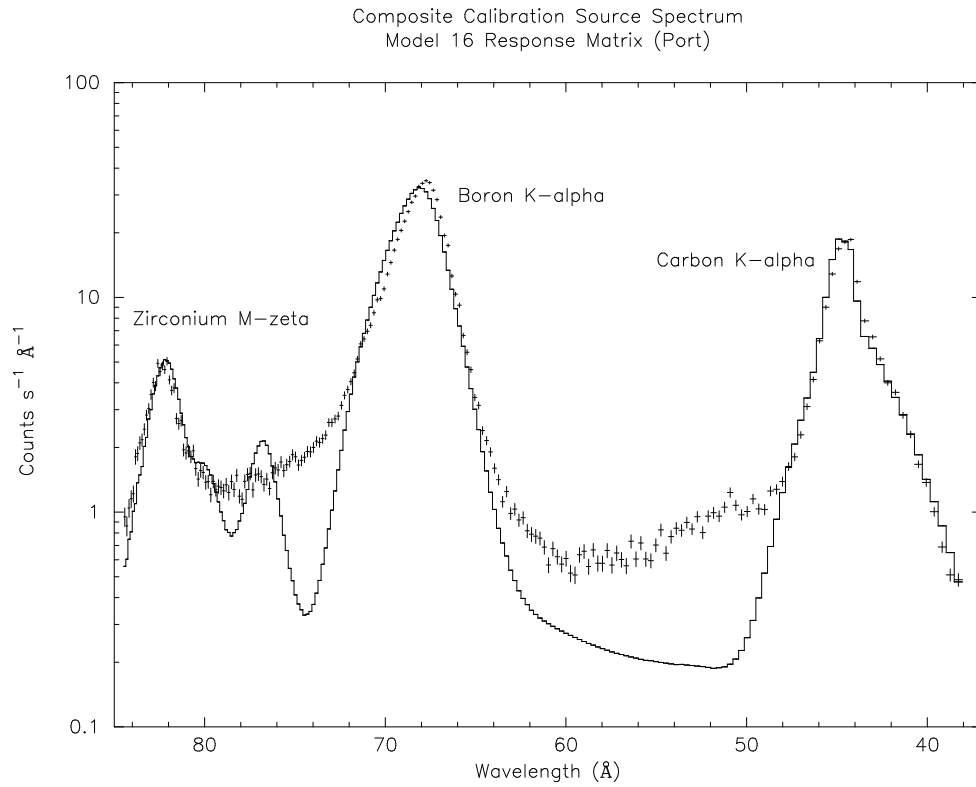
Figure 63: Model fits to the three DXS post-flight calibration sources using the model input functions discussed in §3.2.3. Plot is shown with a linear Y-axis in Figure 3.

the assumed line profiles for the α-particle excited calibration sources, and not the response matrix.

Finally, the DXS wavelength scale is well determined, as seen by the good relative positions of the data model peaks in Figure 63. When allowed to vary as a free parameter, the peak wavelengths differ by less than 0.3 Å from their nominal values.

Chapter 4

Data Reduction

This chapter outlines how the raw DXS telemetry was processed in order to produce useful end products, such as photon event lists, housekeeping records and final spectra. The flow chart shown in Figure 64 shows the general scheme of the system. First, the raw telemetry is converted to Flexible Image Transfer System (FITS, Hanisch *et al.* 1993) binary tables by the programs `ledt2fits` and `sedt2fits`. Then the FITS records are ordered by time and duplicates removed by the programs `dsort` and `skew`. Both these steps are discussed in §4.1. Next, missing time segments in the telemetry, or "dropouts" were fixed, wherever possible, as described in §4.2.

With a complete set of telemetry recorded in the FITS files, the programs `fast`, `slow`, and `sci` were run. These programs transformed the raw telemetry into completed housekeeping records and photon event lists. These transformations are discussed in §4.2 and §4.4. After the completion of these tasks, the FITS files are said to be in "reduced" form. At this point, the program `hist` (see §4.5) was run in order to inspect many of the important quantities contained in the FITS files. In particular, the pulse height distributions of the on-board gas gain monitoring source (described in §2.3.3) were plotted showing that the gas gain varied significantly during the flight. This gain variation was removed by the program `phgain`, as described in §4.4.1.

Another quantity easily found in the output of `hist` was the anomalously high counting rate, or "hot spots" of the Starboard counter explained in §2.4.1. In an effort to preserve as much of the Starboard dataset as possible, a procedure, outlined in §4.6, was developed for removing the hot spots on a statistical basis. The result of this procedure was a "hotmap," indicating times and positions of anomalously high counting rate in the Starboard counter. The "hotmap" was used by `hist` during the production of the final flight spectra to remove the effects of the hot spots. Section 4.7, describes how `hist` and the programs `specflatten`, `specarith`, and `grppha` were used to produce the final DXS spectra.
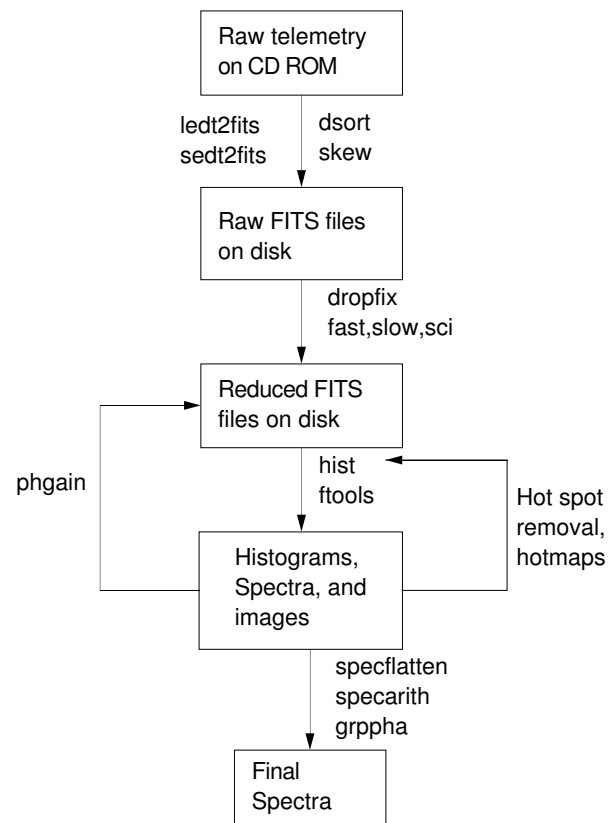
Figure 64: This flow chart shows the major components of the DXS data analysis system including the names of some of the programs and packages responsible for the transformations. A similar flow chart applies to the post-flight analysis.

90

Table 11: FITS File Contents

Example File Name	Contents	Rate
orbit07_orb.fits	Orbiter Attitude and Position	One per second
orbit07_cmd_p.fits	Up-linked Commands	Occasional
orbit07_fast_p.fits	Fast Housekeeping	One per second
orbit07_slow_p.fits	Slow Housekeeping	One per 4 seconds
orbit07_sci_p.fits	Science Events	Up to ~ 100 s^{-1}
orbit07_spoc_p.fits	Spoc Plate Housekeeping	One per 2 seconds
orbit07_time_p.fits	Telemetry Frame Monitoring	One per 4 seconds

4.1 Creating FITS Files from Telemetry

As discussed in §2.3.2, there are two telemetry bands for each instrument, a higher bandwidth "KU" band, and a lower bandwidth "PCM" band. Each telemetry band was recorded in a separate stream of records that were eventually written onto CD-ROMs and kept in a safe place at the Space Science and Engineering Center (SSEC) in Madison, Wisconsin. "SEDT" records contain the KU and PCM telemetry streams and "LEDT" records contain the PCM telemetry stream only. The programs ledt2fits and sedt2fits convert LEDT or SEDT records to records in Flexible Image Transfer System (FITS, Hanisch *et al.* 1993) binary tables, as indicated schematically in Figure 64.

For each shuttle orbit, as determined by a list of begin and end times in a separate database file, sedt2fits writes a number of FITS files. Each file contains a distinct type of information, as indicated in Table 11. "Housekeeping" or engineering data refers to all of the voltage level, temperature, and gas pressure data necessary to monitor the functioning of the instrument. Different housekeeping values are recorded at different rates, either once per second (fast) or once ever four seconds (slow). "Science" data refers to the proportional counter events. Items recorded in a science record include main anode pulse height, position as determined by the on-board processing algorithm (POS) and, if the KU band is present, the 24 ground plane signals. A full database of housekeeping values is available in SSEC document (Sanders & Richards 1990).

The program ledt2fits appends the PCM information from LEDT records to the files created by sedt2fits. Because the telemetry streams are independent, the resulting list of

FITS records in each file is not necessarily in time order. The program `dsort` sorts the records and the programs `skew` and `dsort` work together to remove PCM records that duplicate the more complete KU records.

4.2   Telemetry Dropouts

As discussed in §2.3.2, the KU band did not have complete coverage in each orbit. The result of this was missing ground plane information in ∼50% of the science records. Because of the on-board processing of the ground plane signals, no critical information was lost. Occasionally, the PCM telemetry stream was interrupted, which resulted in a loss of exposure time. There was another telemetry stream, included in the PCM stream that would occasionally have interruptions at times uncorrelated with the PCM or KU dropouts. This third telemetry stream contained the orbiter position and attitude information and was provided as part of the Shuttle Payload of Opportunity standard telemetry. In order to preserve as much of the DXS data as possible, the dropouts in the orbiter attitude telemetry stream had to be reconstructed.

The original orbiter attitude telemetry has three fields for the X, Y, and Z position of the orbiter, relative to the center of the earth, and four fields specifying the orbiter orientation in the form of an M50 quaternion (NASA 1985). Because of the simple circular orbit of the shuttle, the X, Y, and Z coordinate values could be fit with sinusoids. The entire flight was fit with 19 five-orbit segments, with the boundary between segments placed in such a way as to avoid sky-looking, or "scan" times. The X, Y, and Z values determined by the sinusoids were written to new fields in the orbiter attitude telemetry binary tables. New rows were added to the tables for the missing times during dropouts.

Because the orientation of the shuttle was not predictable, filling in the missing quaternion values is more difficult. Most of the orbiter attitude dropouts occured during times when the instrument was collecting background and not looking at the sky. Some of the dropouts occured during sky-looking, or "scan" times, but since the orientation of the orbiter was nearly fixed during these times, the last quaternion value before the dropout was a reasonable estimate for the orientation of the orbiter during the dropout times. However, for three orbits, the orbiter was making large-scale maneuvers just before a "scan" time when a dropout occured. Thus, the scheme of using the last quaternion value before the dropout is not valid. For these times, it would be better to fill in missing values with the first quaternion after the dropout. However,

this has yet to be done. The result is an incorrect pointing direction for 0.8% of the sky-looking DXS dataset used in subsequent analysis.

4.3   Engineering Data Processing and Corrections

Several programs were responsible for cleaning up the engineering telemetry data and adding useful quantities to each engineering record. The programs `fast` and `slow` scanned the fast and slow FITS files for noisy data and, wherever possible, filled in bad values by interpolation. No new records were added by these programs. The program `mag` calculated the McIlwain L and B parameters (McIlwain 1961, Hassitt & McIlwain 1967), which describe the Earth's magnetic field at the position of the orbiter for each second in the mission and added these values to each "fast" engineering record. The program `deadtime` corrects the dead-time value of the proportional counter. Dead-time is the percentage of of time that the proportional counter electronics spend processing events. Since the time to process each event is fixed (a few hundred milliseconds), the dead-time rises with increasing count rate. The program `deadtime` simply set the dead-time to 100% for times when the main anode voltage was turned off. The original telemetry entry for these times was 0%.

4.4   Science Event Processing and Corrections

This section describes how science event records were processed to maximize the useful information in each record. Two main programs were used: `sci` and `phgain`. A third program, `fburst` was used to remove duplicate events that were not removed during the `dsort` and `skew` procedures.

Only certain three orbits in the Port dataset were found to have duplicate events that were not removed with the `dsort` and `skew` programs: orbits 11, 27, and 80. In the post-flight calibration flat-field procedure, duplicate events of this type were more prevalent. The reason for these duplicate events is not clear: they have distinct times (which is why `dsort` and `skew` don't remove them), but have the same pulse height, position, ground-plane, etc. values as one or two of their neighbors. This effect may be triggered by high count rates, since the count rate during orbits 11, 27, and the post-flight calibration flat-field procedure was very high relative to other times.

Assuming that each event is caused by an X-ray that entered the proportional counter on

a path perpendicular to the entrance window, `sci` calculates the direction origin, the "look direction" of each event given the orbiter attitude, spectrometer rotation angle, and position of the event in the proportional counter. The look direction is expressed in three coordinate systems: Galactic coordinates; altitude and azimuth with respect to the local zenith; and the angle χ, which is the angle of the path of the incident photon to the vector extending perpendicular to the shuttle roll and pitch axes (i.e. the vector straight up out of the shuttle cargo bay). The program `sci` also scans the science records for KU events and applies the two step position determination algorithm described in §2.3.1 to the ground plane signals.

4.4.1 Pulse Height Gain Correction

As described in §2.3.3, a small X-ray tube that produces aluminum K-α radiation was mounted close to the window of each proportional counter. Section 2.4 describes how these X-ray sources were turned on twice per orbit to measure the gas gain in the proportional counter. Figure 65 shows the pulse height distribution from a typical calibration. The pulse height distribution is fit with a Gaussian distribution to determine its center channel in ADUs. The center channel at nominal gain is 2950 ADUs.

The proportional counter gas gain changed noticeably during the flight, as shown in Figure 66. As shown in §3.1.3, the gas gain also varies as a function of position in the proportional counters. These gain variations pose a problem in calculating to the overall efficiency of the DXS instrument. For instance, when the gas gain is low, the hardware lower level discriminator (LLD) in the pulse height circuitry cuts off more counts than when the gas gain is high. Thus, with all other conditions identical the count rates for the times are different.

The solution to the pulse height efficiency problem is a three step process. First, the pulse heights for each orbit were adjusted to nominal value by multiplying them by the ratio of the nominal pulse height of the Aluminum K-α calibration line with the average pulse height of the line measured for that orbit (Equation 4.1). An additional factor is included to convert the pulse height from hardware units to approximate electron Volts.

$$GCPH = \frac{PH * NominalPH_{Al}}{This\,orbit PH_{AL} * 1.985} \tag{4.1}$$

Next, the pulse height values were adjusted for the gain variation induced by the field of the veto anodes. Equation 4.2 shows how this correction is applied. POS is the position in the
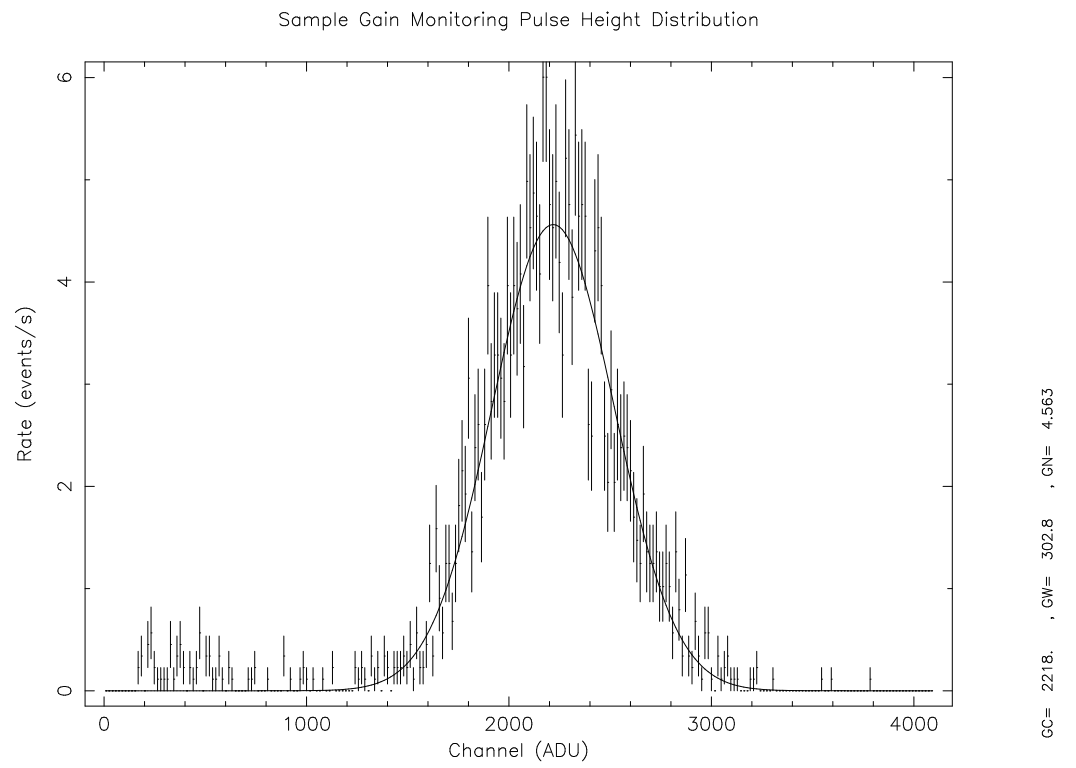
Figure 65: Pulse height distribution of the second cal run of orbit 50 fit with a Gaussian distribution.

Figure 66: Time history of gas gain. Nominal pulse height of 2950 ADUs.

detector, as defined in §2.3.1. The distance between veto anodes is 32.8 POS. The amplitude of the sine wave (10%) was determined in §3.1.3.

$$GCPH(POS) = GCPH * (1 + 0.10\cos(2\pi\frac{(POS - 120.0)}{32.8}))\qquad(4.2)$$

The final next step in solving the pulse height efficiency problem was defining a lower cut value in corrected pulse height so that all orbits and all POS had equal exposure in pulse height. This cut value is 10% more than the corrected pulse height value of the hardware lower level discriminator at the lowest gain orbit, or 116 eV (in corrected pulse height units) for the Port instrument.

It is important to note that because the pulse height energy scale is non-linear, as determined in §3.1.4, the values of corrected pulse height in electron Volts are only correct at Aluminum energies. The high gain pulse height response matrix described in §3.1.4 can be used to determine a more accurate energy scale at lower energies. As a result, the actual energy of the Port LLD is 100 eV. Figure 67 shows the deviation of the measured peak in the pulse height distribution vs. energy for the three calibration sources and the Aluminum K-α gain monitoring source.

Figure 67: Pulse height non-linearity. The high gain pulse height response matrix described in §3.1.4 was used to fit the pulse height distributions at four known energies. The "Fractional Deviation of Gain" is the ratio of the measured pulse height to the actual line energy.

Another ramification of the pulse-height energy scale non-linearity is the potential for inaccuracy in the gain correction for each orbit. However, this is only a problem if the gain changes enough to affect the `shape` of the non-linearity. The 30% change in gain seen in the flight is unlikely to cause such a change.

4.5   HIST

Because housekeeping information is essential for much of the processing of the photon events, a special program was written, called `hist`, that is capable of reading all of the FITS files for each orbit simultaneously and creating one or two dimensional histograms of counting rate, counts, or exposure as a function of housekeeping variables.

The axes of the histograms output by `hist` can be nearly any recorded variable in the

FITS files. Spectra, for example, are one dimensional histograms of the counting rate versus position in the detector. The program `hist` can also be used to calculate the total counting rate in the proportional counter as a function of Galactic longitude, as in Figure 80, or time, as in Figure 81.

In order to measure exposure time `hist` steps through the fast engineering FITS files one record at a time. Each record represents 1 s of mission elapsed time (MET). The program reads in a row of the appropriate slow engineering table every four seconds. Filter criteria can be specified to reject exposure time on the basis of the engineering data. For instance, during the production of the final spectra, all times for which the dead-time was above 30% were discarded. If the engineering data of a particular second of MET pass all engineering filter criteria, `hist` increments exposure time by one times the dead-time correction:

$$exposure = 1s \times \frac{(100 - deadtime)}{100} \qquad (4.3)$$

After incrementing the exposure time, `hist` reads the science event records that were recorded during that second. Additional filter criteria, such as pulse height, and goodness of fit can be specified to discard science events. These filter criteria do not effect the exposure time.

Some histograms, such as the final spectra and the plot of counting rate versus Galactic longitude, need to have special exposure calculations made because different parts of the proportional counter views different parts of the sky at the same time. When such a histogram is specified, `hist` calculates the look direction in Galactic coordinates, altitude–azimuth coordinates, and the coordinate system of the orbiter (the angle χ defined above) of each POS on the detector. This information is used to generate a special exposure histogram internal to `hist`, appropriate for the axes of the desired histogram. For the count rate versus Galactic longitude plot in Figure 80, for instance, the exposure histogram has one degree bins in Galactic longitude and tallies one second of exposure for each POS on the detector viewing a particular bin. Because the first and last 20 POS of the proportional counter do not look out on the sky, exposure is usually only calculated for the central 200 POS.

Finally, when all of the counts and exposure time are tallied, `hist` produces a FITS file containing a binary table with the desired histogram. The table usually has three columns: the histogram axis (such as position in counter, or Galactic longitude), the quantity histogrammed (usually the average counting rate per channel for the histogram bin in question), and the

statistical error of the histogrammed quantity. Because the results of `hist` are expressed in the standard FITS file format, it is easy to use other programs, such as "ftools" (available by anonymous ftp from `heasarc.gsfc.gov`) for subsequent processing.

4.6   Hot Spots

As described in §2.4.1, the two systems that were supposed to shut the proportional counters off during times of enhanced count rate did not function as anticipated. As a result, the count rate in the proportional counters rose to the point were the gas near the anode wires began to break down. Break-down in the gas results in a high rate of change transfer to the anode and count rates of thousands of counts per second. Count rates this high saturate the telemetry, which has a maximum rate of 85 events per second (PCM, greater for KU). After the initial break-down event, areas of high count rate, called "hot spots," are seen to spontaneously appear and disappear in the Starboard counter.

Figures 68 and 69 show the background count rates in each instrument as a function of *position* in the counters (X-axis) and *time* (Y-axis). The highest count rates in each instrument occurs in POS channels 0–4 between orbits 10 and 26. Because this is the period when the original problem with the particle detectors was being diagnosed, all the data recorded during this period is usually ignored. Also easily seen in Figures 68 and 69 is the enhanced count rate in the first and last 20 POS of the proportional counters. The count rate is higher here because of limited veto coverage. Section §5.2 discusses potential uses for the events in these regions, but for the analysis discussed here, they have been ignored.

After ignoring data from the sky-looking part of orbit 11 through the end of orbit 26, the Port dataset can be cleaned simply by ignoring the channels in orbit 27 with background count rates significantly higher than the average count rate for POS 20–220. Also, data from orbit 59 is discarded because of inadequate background exposure time. Figure 70 shows the cleaned background count rate in the Port instrument. The rest of this section discusses the cleaning of the Starboard dataset.
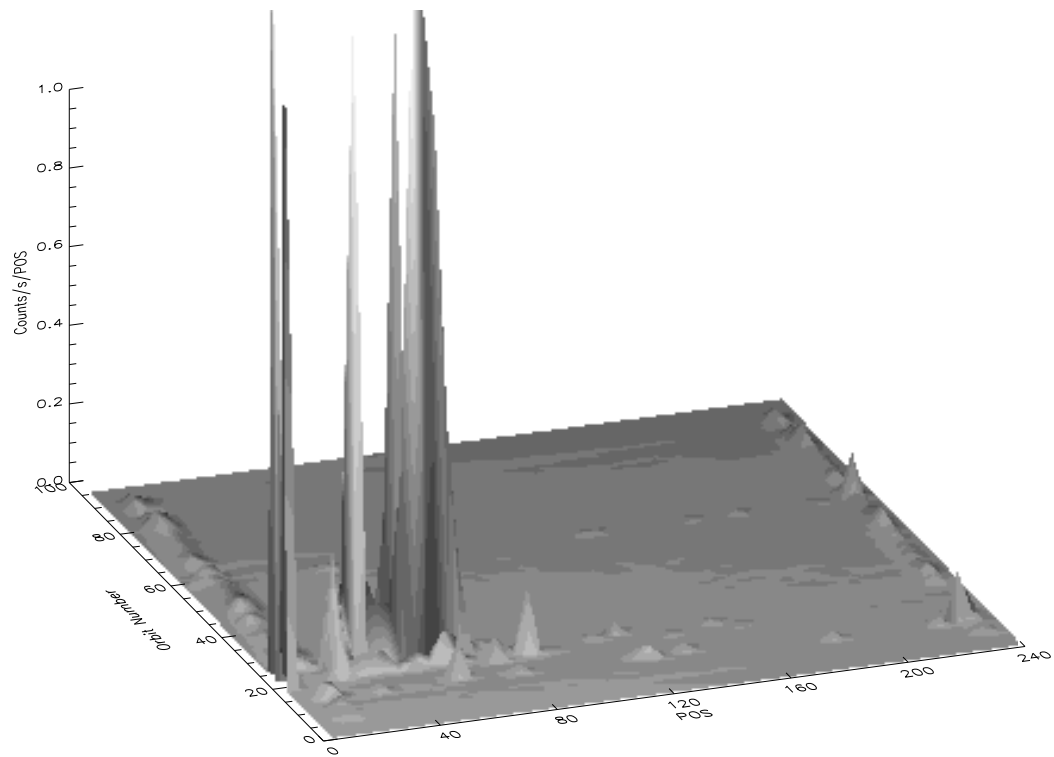
Figure 68: Background count rate in Port proportional counter as a function of position channel, POS (X-axis), and time (Y-axis). Data with corrected pulse heights below 106 eV and above 500 eV have been discarded. Also data with goodness of fit values higher than 20 have been discarded.
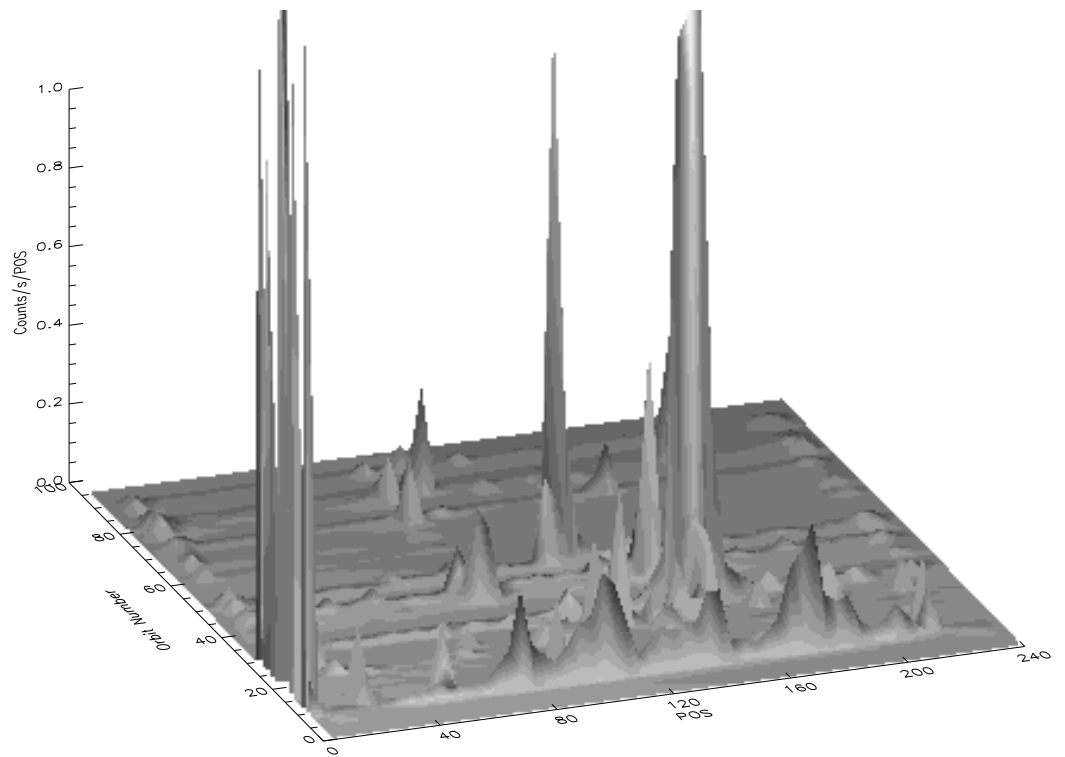
Figure 69: Background count rate in Starboard proportional counter as a function of position channel, POS (X-axis), and time (Y-axis). Data with corrected pulse heights below 89 eV and above 500 eV have been discarded. Also data with goodness of fit values higher than 20 have been discarded.
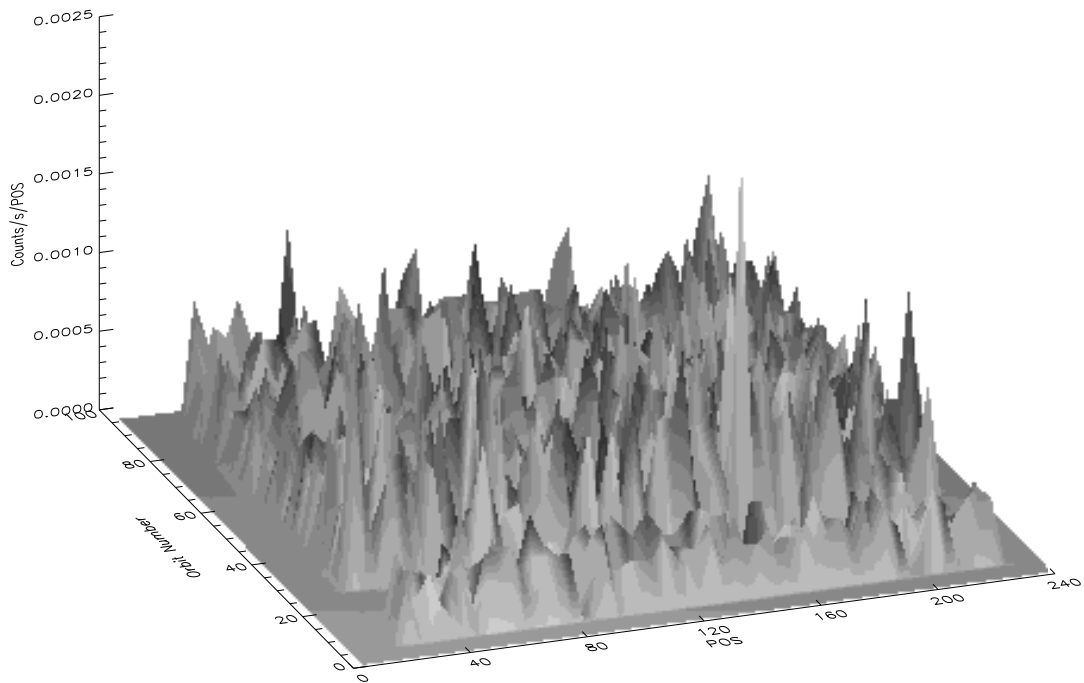
Figure 70: Background count rate in Port proportional counter as a function of position channel, POS (X-axis), and time (Y-axis), after cleaning. Spectrum averaged over time is seen in Figure 86, count rate averaged over position is seen in Figure 83. Data with corrected pulse heights below 116 eV and above 500 eV have been discarded. Also data with goodness of fit values equal to 63 have been discarded.

4.6.1 Goodness of Fit Parameter (GOF)

Eugene Moskalenko has studied the various forms of background in the DXS proportional counters (Moskalenko 1994). He found that the goodness of fit (GOF) parameter, described in §2.3.1, is one of the most important tools for identifying the different types of background in the DXS proportional counters.

The goodness of fit parameter varies from 0 to 63, with 0 representing a perfect fit to the nominal distribution of charge on the ground plane wires. Figures 71 and 72 show the goodness of fit distribution for the Port and Starboard proportional counters as a function of time. Moskalenko found that most of the events with a GOF of 63 had no ground plane signals at all. He called these "electronic events," postulating that they arise outside the main volume of the counter, for instance in the potted high voltage cavities on the sides of the proportional counters. Events with GOF=63 have already been rejected from the data that formed Figures 68 and 69.

Unfortunately, the goodness of fit parameter does not fully differentiate between normal X-ray events and hot-spot events. Hot spot events do tend to have higher GOF values, but this is probably due to the fact that they have low pulse height values. Simply because of the signal to noise in the ground plane change amplifiers, events with low pulse heights tend to have higher GOF, as shown in Figure 73. This figure was produced from Port sky-looking (scan) data.

4.6.2 Pulse Height Analysis

When a proportional counter enters break-down, there is a continuous discharge on the high voltage anode wire. The discharge produces a very high count rate and may cause the proportional counter electronics to malfunction. Figures 74 and 75 show the aperture closed background pulse height distributions as a function of time in both instruments. Notice that between orbits 10 and 27, the pulse height distribution is sharply peaked at ∼100 eV. For both instruments, during the worst breakdown, the recorded pulse heights are actually *below* the hardware lower level discriminator, which can be seen as the line at ∼100 eV in the other orbits. If the electronics are functioning properly, no events with pulse height below the hardware lower level discriminator would be registered.

Sections B.1 through B.2 show how hot spots can be isolated on the basis of statistical
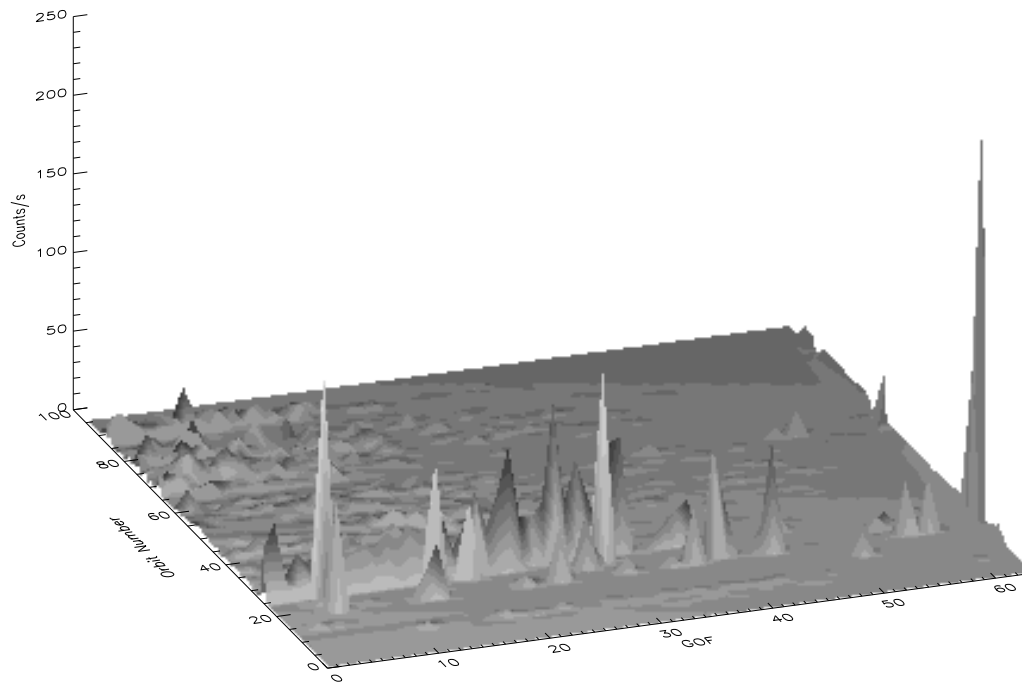
Figure 71: Goodness of fit distribution in the Port proportional counter as a function of time for aperture closed background data, POS=20–220 and corrected pulse heights=106–500 eV.
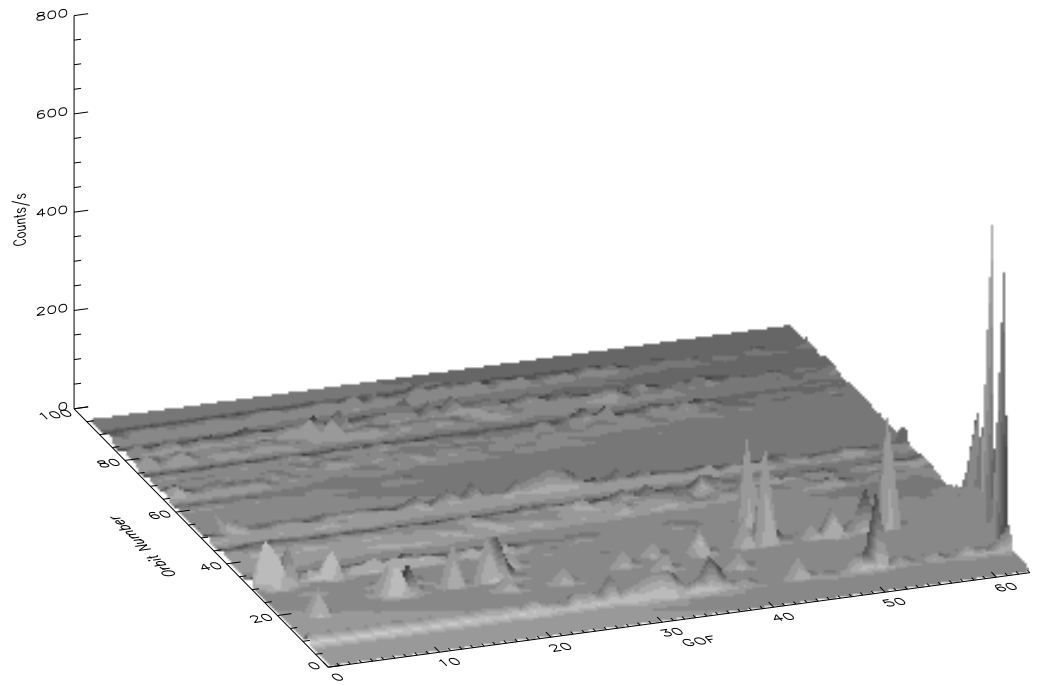
Figure 72: Goodness of fit distribution in the Starboard proportional counter as a function of time for aperture closed background data, POS=20–220 and corrected pulse heights=89–500 eV.
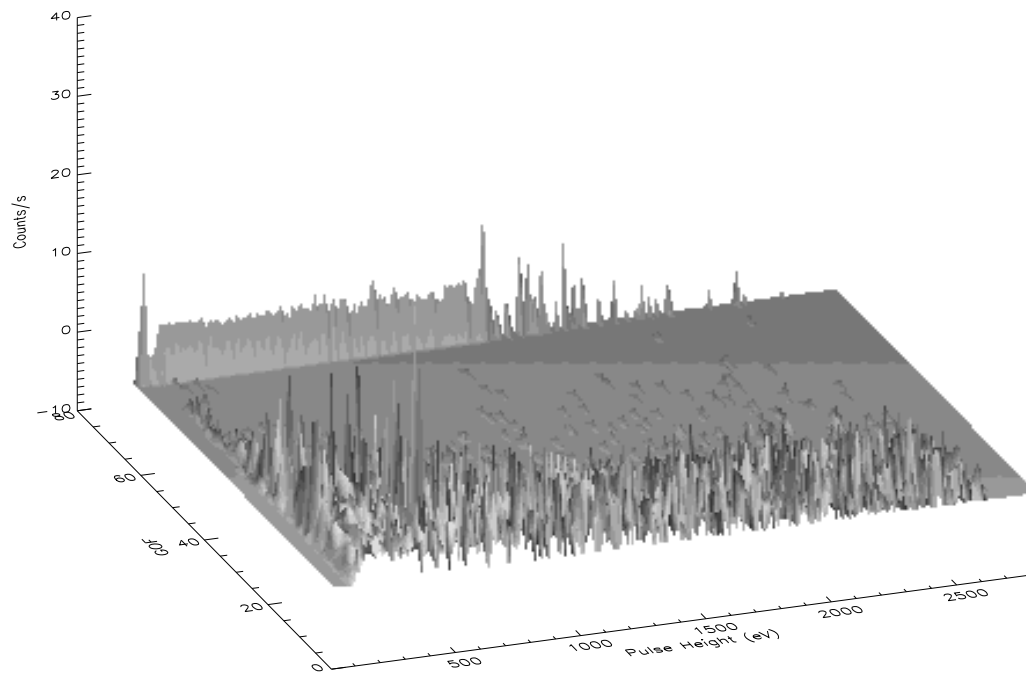
Figure 73: Pulse height vs. GOF in the Port proportional counter during sky-looking (scan) times, POS=20-220, excluding orbits 11–27. Events with low pulse height tend to have higher GOF values.

106
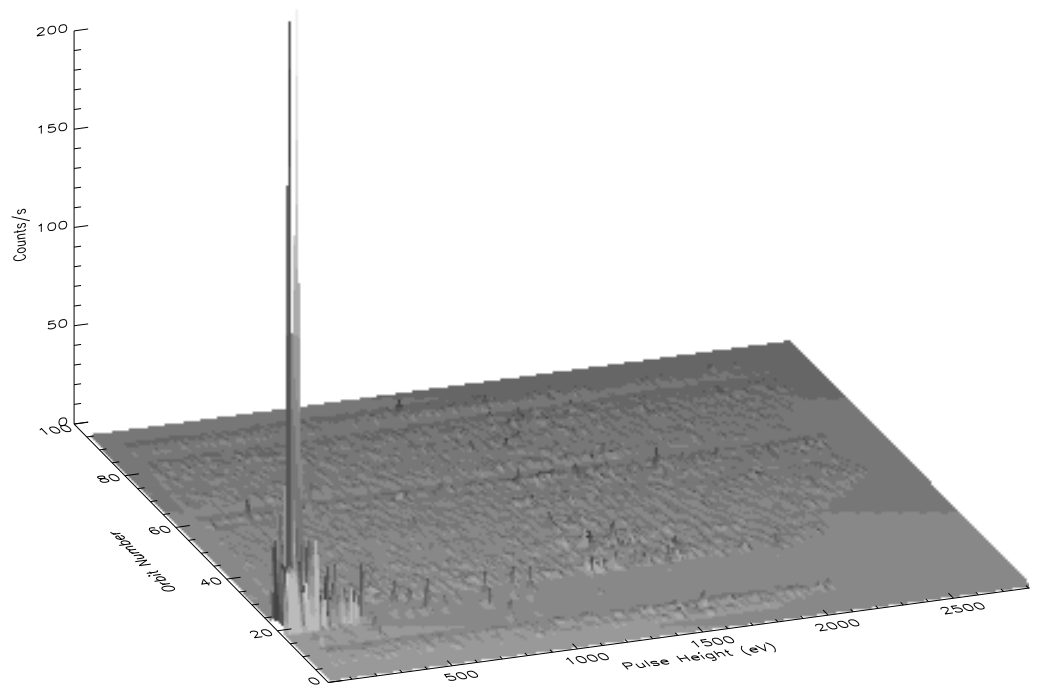
Figure 74: Aperture closed background pulse height distribution in the Port proportional counter as a function of time for POS=20–220, GOF=0=20.
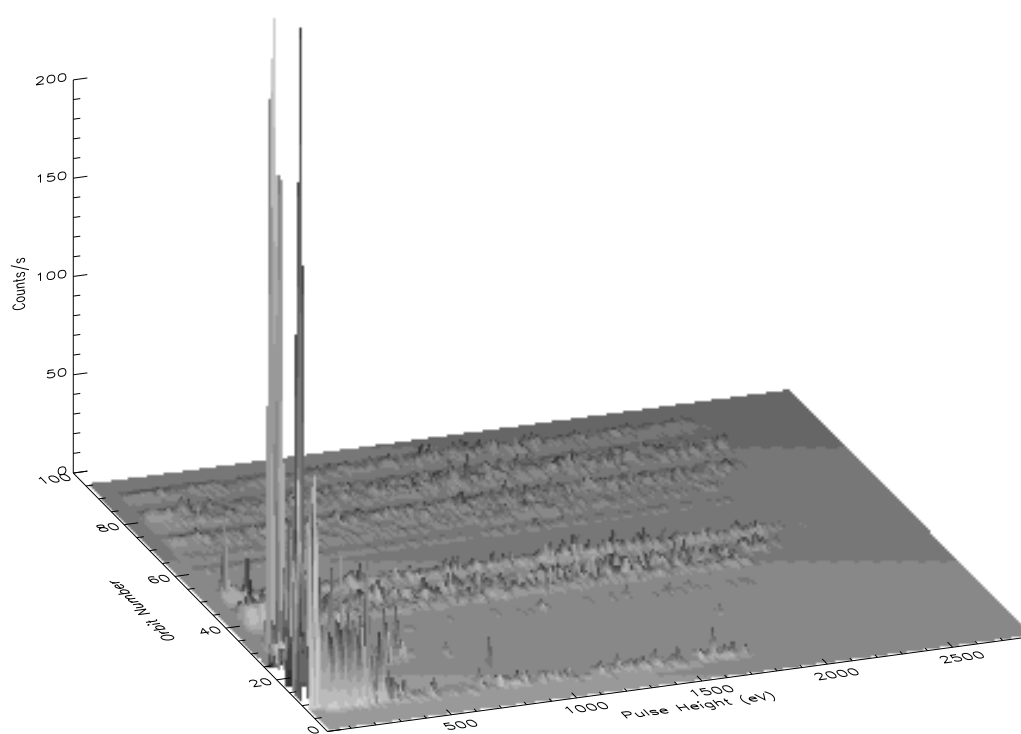
Figure 75: Aperture closed background pulse height distribution in the Starboard proportional counter as a function of time for POS=20–220, GOF=0-20.
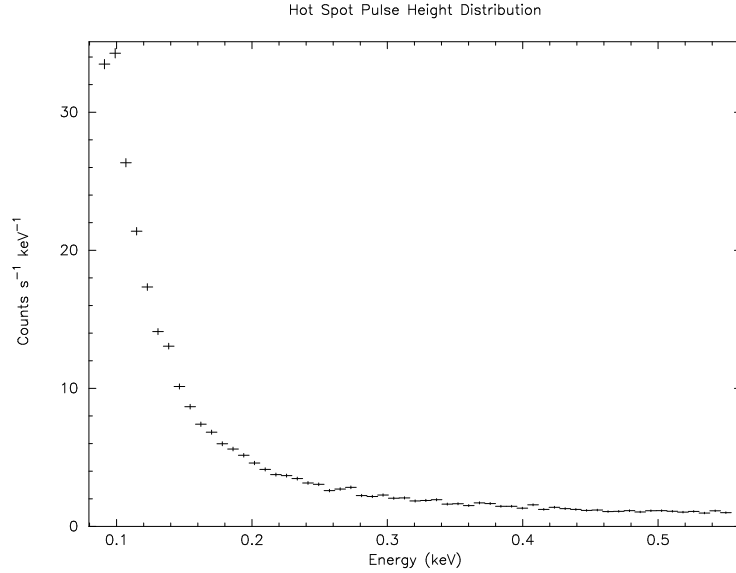
Figure 76: Histogram of the pulse heights for the regions identified as hot spots in the Starboard counter (scan data).

arguments. Figure 76 is the pulse height distribution formed from the hot spots in the Starboard dataset during sky-looking times. Compare this pulse height distribution to the Port pulse height distribution shown, for example, in Figure 121. The hot-spot pulse height distribution peaks at a much lower value.

4.6.3 Preliminary Cleaning

The first method used to attempt clean the Starboard dataset was simply to subtract the aperture closed background position spectrum from the sky-looking position spectrum with no correction for hot-spot contamination. If the hot-spot contamination did not change between the sky-looking and aperture closed background collection times, this method would have resulted in a reasonable spectrum. Unfortunately, this spectrum, shown in as the dashed data points in Figure 77, has large negative values in several channels, indicating that for many
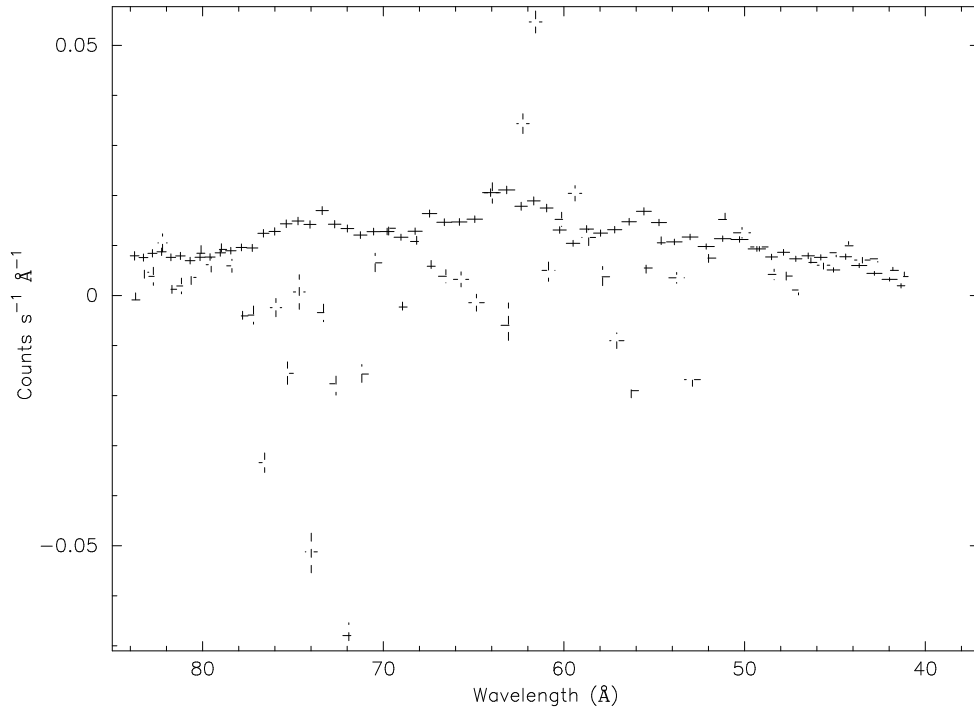
Figure 77: Comparison of Port (solid) and Starboard (dashed) spectra for all look directions. Both spectra have been background subtracted. Hot spots have not been removed from the Starboard data used in this Figure.

positions in the counter, the hot-spot activity during background collection times was higher than during scan times. Thus, it is essential to minimize the effect of the hot-spots.

Because the hot-spot pulse height distribution peaks at a lower value than the sky-looking pulse height distribution, as shown in §4.6.2, discarding events with low pulse heights removes most of the hot spot events. Figure 78 shows the background subtracted position spectra of both the Port and Starboard for the sky-looking data discarding all events with corrected pulse heights lower than 191 eV and higher than 382 eV. Except for a few wavelength regions, most notably between 70 Å and 75 Å where the Starboard count rate is higher than the Port, the Port and Starboard spectra are very similar. This is the most direct evidence that the Port and Starboard instruments were viewing the same source and, except for some wavelength regions, were not dominated by contaminating instrument background.
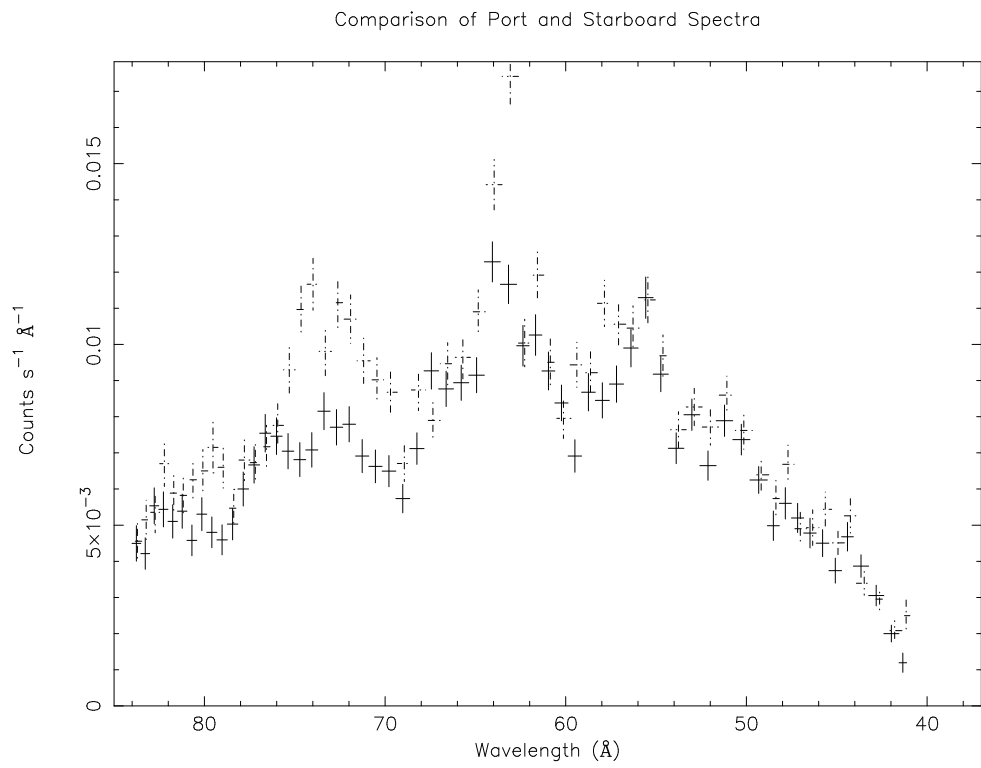
Figure 78: Position spectra of events with pulse heights between 191 eV and 382 eV. Spectrum from the Port instrument is shown with solid lines, the spectrum from the Starboard instrument as dotted lines.

4.6.4 Other Cleaning Attempts

After providing redundancy in the event of instrument failure, and complementary wavelength coverage at extreme scan angles, the purpose of flying two detectors was to double the exposure time to the X-ray background. Had the Starboard data not been contaminated, they could have been processed in the same way as the Port, in particular with the same pulse height limits. Then the counts and exposure time of the two instruments could have been added together and divided to form a single spectrum. Because of the contamination shown in Figure 77, this was not possible. Figure 78 shows that if events below about 200 eV are discarded, this concatenation of the Port and Starboard data could have been performed for at least some wavelength regions of the Starboard dataset. However, this cut in pulse height discards about half of the Port data. The exposure time on the Starboard instrument is less than that of the Port, so there would be a net loss in total number of events used in the final spectrum over discarding the entire Starboard dataset and forming a spectrum from the full Port dataset.

An alternative method for cleaning the Starboard dataset was to use two dimensional histograms similar to Figure 69 to find regions in position-time space that had intense hot spot activity and remove the events *and exposure time* for these regions. It was hoped that regions of hot spot activity could be identified by their excessive contribution to the aperture closed background counting rate. Early analysis showed that hot spots are limited to regions of single anode wires (Moskalenko 1994). Thus, analysis was conducted separately on the "odd" and "even" anode wires and the spectra later combined (see §4.7). Also, because high counting rates can saturate the dead-time correction (§4.5), times for which the dead-time was above 30% were rejected from analysis. Except for orbits 11–27 in the Port dataset, there is no orbit for which the deadtime is greater than 30%.

As shown in Figures 103 and 86, the Port instrument aperture closed background count rate, after cleaning is roughly constant between detector channels (POS) 20 and 220. This is expected based on the uniform exposure to cosmic ray events. If unusually high count rates were were found at particular positions in the background data of a particular orbit, background and sky-looking ("scan") data from those positions could be rejected for that orbit. Rejecting scan data on the basis of background data minimizes the chance that the statistical removal of events could bias the sky-looking count rate.

While looking for hot-spots, only events with corrected pulse height between 89 eV and 248 eV were considered. This maximized the effect of the hot spots. Also, orbits that did

not have adequate background exposure (at least 1000 s), were discarded. Thus, the orbits considered for analysis in the Starboard dataset were orbits 7 through the the first background collection of orbit 10, orbit 38, orbits 48–50, and orbits 61-92. When the final spectra were produced, the upper and lower pulse height limits were set to 89 eV and 500 eV, respectively, in the hope of diluting the effect of the hot spot events.

Section B.1 and §B.2 show that neither of the two statistical methods tried could remove all of the hot-spots in the scan data simply by removing the hot-spots from the background data. In order to arrive at spectra that compared well to the Port spectra, *scan* data had to be analyzed for hot-spots. Even though the resulting spectra compare well to the Port spectra, as shown in Figures 134, and 138, there can be no guarantee that the spectra are free of the bias effects that result from cutting out the statistical outliers.

As a result of the failure of the statistical methods at removing hot-spot contamination without potential bias effects, a hybrid technique, using a higher cutoff in pulse height and statistical identification of hot-spots in the the *background* data was used. This method, described in §B.3, determines which lower level pulse height cut off in the Starboard data results in a spectrum most similar to the Port spectrum. The best value ends up being 200 eV, which is very similar to the cutoff used to create Figure 78. Unfortunately, as described in the first paragraph of this Section, such a high cutoff in pulse height makes the use of the Starboard data awkward. It is possible to create separate response matrices that describe the Port and Starboard spectra and use the X-ray spectral analysis program XSPEC (Arnaud 1996) to simultaneously fit a model to the two spectra. Unfortunately, given the lack of good model fits to the Port spectra, shown in Chapter 6, and the large amount of Starboard data cut out in the cleaning procedure (more than half) it is unlikely that the Starboard data would significantly alter the constraints on the models and is therefore not used for further analyses in this document.

4.7   Production of Final Spectra

This section describes how the program hist and associated programs were used to process the "reduced" FITS files (described in the introductory Section of this chapter) to produce the final DXS spectra. Two types of spectra were produced: position spectra and pulse height spectra. The position spectra, in conjunction with the response matrix described in §2.5 are

used in the principal scientific analysis described in Chapter 6. The pulse height spectra, in conjunction with the response matrix described in §3.1.4 are used primarily as a check of the instrument function and the data analysis procedure. Some astrophysical interpretation of the pulse height spectra is possible (see §6.3.2), but the spectral resolution is much poorer than the position spectra.

In order to generate the best possible position spectra, events that were recorded by the higher bandwidth KU telemetry (about half of the total number of events, see 2.3.2) were processed separately from events that were recorded only when the PCM telemetry band was available. The subsequent treatment and combination of these spectra will be discussed below.

In order to demonstrate the repeatability of the DXS result and compliment the hot spot removal system, the data recorded with the "even" anodes were processed separately from the data recorded with the "odd" anodes (see §2.3.2 for a complete description of the "even" and "odd" anodes). Also, the data recorded during the first half of the flight (up to orbit 51) were kept separate from the data in the second half of the flight. As explained in §5.1, there were additional motivations for making this division in time.

As shown in §5.1, there were seven natural divisions in the DXS data along the coordinate of Galactic longitude. An eighth "division" in the data was also defined, which had no restriction in Galactic longitude. Although this eighth cut did not cover the whole sky (only ~3%, in fact), it is referred to as the "Allsky" region, since it covers all of the sky that DXS looked at.

Because of optimizations programmed into `hist`, all eight of the spectra corresponding to the regions on the sky could be generated at once. However, the position and pulse height spectra has to be generated in separate runs of `hist`. Also, `hist` had to be run separately for each division in time and anode type, as well as each telemetry type. To coordinate the input and output of `hist`, two programs were written. One of the programs, `clean_sky_spectrum` uses `hist` to generate a spectrum of each region on the sky for a particular subset of the DXS data. The program `clean_sky_spectrum` is called by `clean_spectra`, which systematically loops through the various divisions in the data and coordinates subsequent processing, such as flat-fielding, addition, and comparison of the spectra. The programs `clean_spectra` and `clean_sky_spectrum` are given verbatim in Appendix C. The rest of this section describes what `hist` and these programs do.

4.7.1 Running `Hist`

To create each set of spectra, the program `hist` steps through the "reduced" FITS file database one second at a time, as discussed is §4.5. The engineering data for that second (for instance the mission elapsed time or dead-time value) are examined to see if they fall within acceptable ranges. For the Port dataset, only orbits 11–26 and part of orbit 27, and orbit 59 were rejected using these criteria. For each acceptable second, the science events that occured during that second are read in and the science filter criteria are applied. An example of a science filter criterion is the condition that the goodness of fit parameter (see §2.3.1) must be greater than or equal to 0 and less than 63.

In most cases science filter criteria reject individual events and do not affect exposure time. However, there are two special cases in which the exposure time was modified based on the value of a science filter quantity. The first case is the removal of the hot spot regions. For each event, `hist` checks to see if the corresponding pixel in the "hotmap" is below the acceptable limit (the "hotcut"–see, e.g. §B.1). If not, the events are discarded. The exposure time corresponding to this time and position in the proportional counter is also discarded so that the final counting rate in each position channel can be calculated properly. Thus, the "hotmap" is also checked when the exposure time histogram is incremented.

The second case where both counts and exposure time need to be simultaneously rejected is in eliminating the effect of the shadow of the space shuttle cargo bay. Since the DXS proportional counters have 15° collimators, look directions closer than 15° from the top the shuttle cargo bay are likely to be shadowed. The angle χ, defined in §4.4 gives the look direction in the frame of reference of the shuttle. For both instruments the edges of the shuttle cargo bay fall at $\chi = \pm 80°$. In the same way that `hist` simultaneously rejects events and exposure time that fall in identified hot spots, `hist` rejects events and exposure time that fall within 15° of either cargo bay edge. It is important to note that because the collimator response is well known, it is possible to calculate what fraction of the sky is occulted by the orbiter for each look direction and correct the exposure time accordingly rather than reject all look directions that have some occultation. This would increase the total exposure to the X-ray background by ∼20%.

In this way, `hist` correctly calculates the exposure time and tallies the counts for each position channel in the proportional counter. To create the final spectra, `hist` divides the exposure time of each position or pulse height channel into the counts recorded in this channel.

The statistical error is the square root of the counts divided by the exposure time. Then `hist` writes a special FITS file that is suitable for use with the X-ray analysis package `XSPEC` (Arnaud 1996). The FITS file is a three column binary table. The three columns are: channel, rate, and statistical error. Position spectra have 240 rows, (POS 0–239). Pulse height spectra have 256 rows, which represent a binning of 16 ADU channels in the original 0–4095 ADU scale at nominal gas gain. In gain-corrected pulse height units (see §4.4.1), this corresponds to a binning of 8.05966101694 "eV."

4.7.2 Flat-Fielding and Grouping

After using `hist`, `clean_sky_spectrum` runs the program `specflatten` on each position spectrum. The program `specflatten` divides the raw spectrum by the appropriate flat-field spectrum (KU or PCM–see §3.1.2). In order to assure that this division does not not induce any change in the net counting rate, the flat-field spectra were normalized between channels 30 and 210, which are well away from the edges of the proportional counter field of view. The random and systematic error estimates of the flat-field spectra were added in quadrature and included in a fourth column in the `XSPEC` compatible spectral files, reserved for systematic errors.

At this point in the processing a program called `grppha` was used to mark bad channels and indicate how the position channels should be binned. This program is part of the suite of programs called "ftools," which is available by anonymous ftp from `heasarc.gsfc.nasa.gov`. The program `grppha` adds a column, called "QUALITY," to the position and pulse height FITS binary tables. This QUALITY column is used to mark bad channels. For position spectra, channels 0-20 and 200-220 are simply marked as "bad." When read into `XSPEC`, these channels can be ignored by issuing the "ignore bad" command. For the Port instrument, pulse height spectra have channels 1–10 marked as bad, since they fall below the lowest pulse height corrected value of the lower level discriminator. However, users fitting models to DXS pulse height spectra may wish to ignore `XSPEC` channels 1–14 and 56–256. These limits are within a few "eV" of the limits imposed on the position data by the `hist` processing filters. The `XSPEC` channels do not line up precisely with the pulse height limits since the corrected pulse height boundary selected to solve the pulse height efficiency problem (§4.4.1) do not fall precisely on a corrected pulse height bin boundary.

The program `grppha` adds another column to the position spectral files, called "GROUP-ING." This column indicates to XSPEC how the channels are to be binned in the internal XSPEC representation. Using the GROUPING column eliminates the need to create a new response matrix every time a spectrum is rebinned. The spectrum can be stored in natural detector units and it, together with the response matrix, will be rebinned by XSPEC according to the prescription set forth in the GROUPING column. The final DXS spectra are binned such that there are approximately two bins per resolution element, as determined by the calculations that produced Figure 23.

4.7.3   Final Addition

The various spectral files of each piece of the dataset were then combined using the program `specarith`. First the flat-fielded PCM and KU spectra were added together, then the first and second half of the flight and finally the "odd" and "even" halves of the counters. The addition was also done exchanging the order of the "odd" and "even" halves of the counters and first and second half of the flight. These two different sums compare exactly, thus verifying proper bookkeeping of all the photons. Also, when ignoring the appropriate XSPEC pulse height channels (1–14 and 56–256 for the Port instrument), the difference in the counting rates between the corrected pulse-height spectra and the position spectra is less than 5%. The slight difference is due to the fact that XSPEC channels of the corrected pulse height spectra do not line up precisely with the corrected pulse height limits used to filter the position data.

Chapter 5

Data Analysis

Chapter 4, particularly Figure 70, shows that after discarding less than one percent of the Port data, there is no evidence of excessive instrument background. Unfortunately, even with this cleaning, there is still a 20% drop in total sky-looking count rate over the course of the flight (§5.1). The flux of X-rays from the diffuse X-rays background should be very steady. Therefore, there must have been some other, variable source of contamination. Sections 5.2 and 5.3 show that this contamination was most likely *not* produced inside the instrument. In §5.4, the lowest Port counting rate is shown to be within 20% of that determined from the ROSAT all-sky survey, suggesting that the contamination is no more than 20% of the diffuse X-ray background count rate seen by DXS. An analysis of the likely sources of the 20% change in counting rate is presented in §5.5. The conclusion reached in §5.5 is that the Port DXS data set is contaminated by a time-varying source located near the Earth (probably inside the orbit of the moon). Contamination at this level has also been seen in the other soft X-ray all-sky survey data (Snowden *et al.* 1995).

Spectra of the various regions on the sky observed with the Port DXS instrument are shown in §5.6 and a quantitative analysis of the differences between these spectra is presented in §5.7. Section 5.7 also compares spectra from the first half of the flight (when the contaminating flux was most evident) to spectra from second half of the flight and shows that after the difference in average count rate is divided out, these spectra are not statistically different.

5.1   Introduction

DXS observed a swath of the sky 15° wide and ∼150° long roughly aligned with the Galactic plane and centered at a Galactic longitude of 230°. This scan path covers regions of the sky typical of the diffuse X-ray background as well as the Vela and MonoGem supernova remnants. Figure 79 shows this scan path superimposed on the C-band map of the ROSAT

118
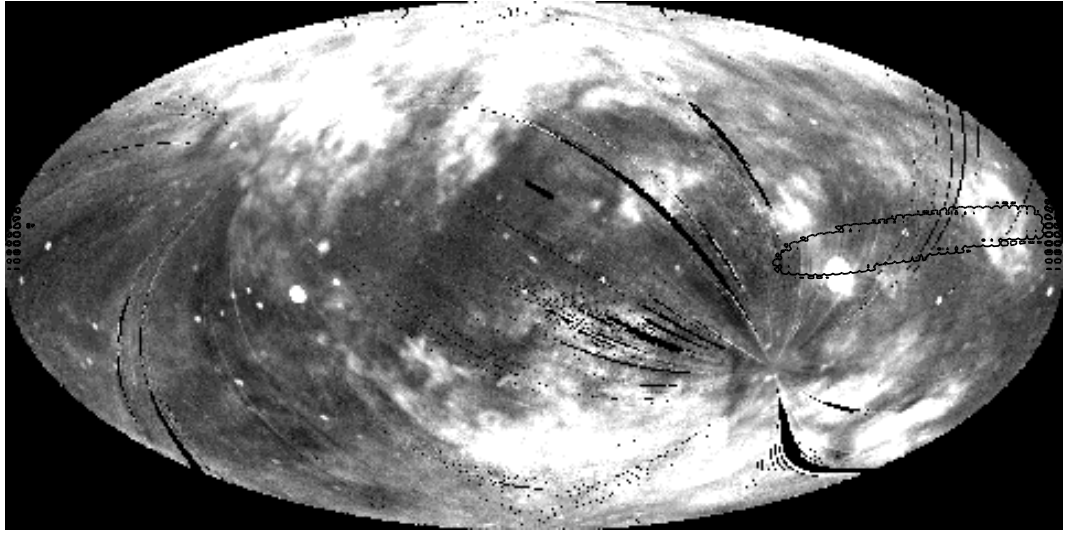
Figure 79: C-band map of the ROSAT all-sky survey (Snowden 1995) showing the DXS field of view. Projection is Aitoff, centered at 0∘ Galactic Longitude. The Vela supernova remnant is the bright disk toward the left side of the DXS scan path and the MonoGem supernova remnant is the ring-like structure toward the right side.

all-sky survey (Snowden *et al.* 1995). Figure 80 shows a plot of the counting rate (including background) in the Port DXS proportional counter versus the Galactic longitude of the center of the DXS field of view.

Figure 80 was produced by the program `hist`, described in §4.5. The rate in each one degree bin is the ratio of the total number of counts coming from that direction divided by the total number of seconds DXS spent looking in that direction. This calculation assumed that all wavelengths observed by the instrument were equally exposed to all directions on the sky. For look directions with Galactic longitudes between $280°$ and $180°$, this is a reasonable approximation. For look directions outside of this range, the rate in Figure 80 is up to 40% too high. Subsequent calculations of counting rate presented here properly weight exposure time as a function of wavelength and do not suffer from this problem.

Another effect not corrected in the creation of Figure 80 is occultation by the shuttle cargo bay. The effect of the occultation can be seen in the drop in the counting rate for Galactic longitudes greater than $300°$ and less than $160°$. The count rate in these regions falls to levels comparable to the non X-ray background counting rate measured when the instrument was stowed with its aperture covered. The aperture-closed count rate is indicated by the dotted line on the figure.
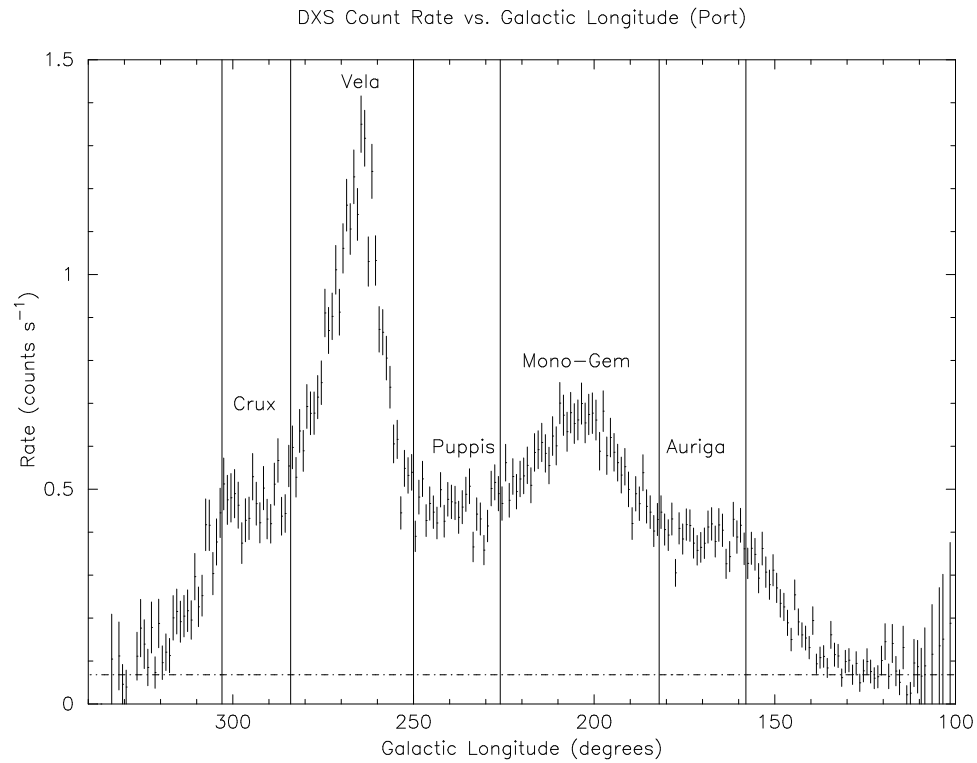
Figure 80: The counting rate in the port DXS instrument as a function of Galactic longitude in one-degree bins. Instrument background is included, with the background rate inferred from instrument closed measurements indicated with the dotted line. Divisions in the data set are indicated by the vertical lines. Because of incomplete spectral coverage, the rates in the Crux and Auriga regions are not accurate in this figure.

The vertical lines in Figure 80 indicate the divisions in Galactic longitude adopted for spectral processing of the DXS data set. A spectrum of each region and the non-X-ray background was produced following the procedure outlined in §4.7. Table 12 gives the net (background-subtracted) counting rates and statistical errors of these spectra. The counting rates in Table 12 are calculated by summing the rate in all channels with significant exposure time. Similarly, the statistical errors are the quadrature sum of the errors in the counting rate in each channel. This method of determining counting rate correctly accounts for exposure time differences as a function of energy in the instrument.

Correction for the effect of shuttle occultation in the spectra was accomplished in two ways. First, the divisions in the data were drawn (by eye) at the point at which the occultation began to take effect as a function of Galactic longitude (see Figure 80). The second and more accurate method involved the calculation of the nominal look direction of each spectral channel in the instrument in the coordinate system of the shuttle orbiter. This angle was defined in §4.4 as χ. The actual direction of an incident photon can vary by up to 15° from this nominal ray because of the finite opening angle of the proportional counter collimator (see §2.1). Thus, any look direction within 15° of the top of the shuttle cargo bay is subject to shadowing effects. The percentage of the shadowing effect can be calculated and the exposure time for these look directions adjusted accordingly. However, in order to simplify calculations and guarantee no contamination due to this effect, all data for which χ is within 15° from the top of the shuttle cargo bay are discarded. As discussed in §4.7.1, as a future enhancement to the data reduction process, the vignetting function of the cargo bay could be included, resulting in a $\sim$20% increase in exposure to the X-ray background.

Three more spectra were formed from the data with partial or no restriction in Galactic longitude (though still discarding data occulted by the shuttle cargo bay). The first two are Centarus (Galactic longitude greater than 303°) and Camelopardalus spectra (Galactic longitude less than 158°). A final spectrum, the "Allsky" spectrum, was created with no restriction on Galactic longitude. The arithmetic sum of the seven other spectra equals the "Allsky" spectrum, an important check of the self-consistency of the data reduction software.

Figure 81 shows the time history of the sky looking count rate in the Port instrument. Each point is the "Allsky" spectrum count rate in that particular orbit, thus the effect of varying exposure time as function of position in the instrument is properly considered. For the Port instrument, the sky exposure for each orbit is made up of eight or nine back-and-forth scans

Table 12: DXS Observation Boundaries and Total Count Rates. Counting rates are calculated from spectra which correctly account for exposure variations as a function of wavelength.

Region	Longitude Range (degrees)	Net Count Rate (cts/s)	Statistical Error (cts/s)	Statistical Error (%)
Allsky	$\sim$158$\sim$303	0.512	0.004	0.8
Crux	284–303	0.285	0.010	3.5
Vela	250–284	0.760	0.009	1.2
Puppis	226–250	0.387	0.008	2.1
MonoGem	182–226	0.502	0.007	1.3
Auriga	158–182	0.321	0.008	2.6
Background		0.068	7×10^{-4}	1.1

of the sky. Eight scans were used before orbit 51 and nine during and after orbit 51. The important feature to notice in Figure 81 is the $\sim$20% variation in the count rate over the course of the flight. Table 13 shows the background-subtracted counting rates in the first and second half of the flight (using orbit 51 as the dividing line). To aid in the interpretation of Table 13, Table 14 shows the ratio and difference of the values in Table 13. As discussed in §2.3.2, the "even" and "odd" anode groups act as independent proportional counters in the Port instrument. Thus, it is significant that for the "Allsky" region, the ratio of the first half to the second half of the flight is $\sim$20%, with a 1σ uncertainty of 3% for *both* anode groups. The following sections discuss possible causes for this behavior.

5.2 Background

As discussed in §2.4, the Port and Starboard instruments were turned on before each sky-looking (or "scan") period and left on for up to several thousand seconds after each sky-looking period. During these times, the instrument aperture was closed, so no X-ray background photons could enter the instrument. The veto system (§2.3.2) essentially eliminates the background rate due to charged particles that pass directly through the proportional counter. However, high energy charged particles can convert to high energy γ-rays in the materials surrounding the proportional counter. These γ-rays can then Compton scatter off of electrons in the proportional counter gas. Usually, these Compton electrons have a large amount of

DXS Sky Looking Count Rate vs. Time (Port)
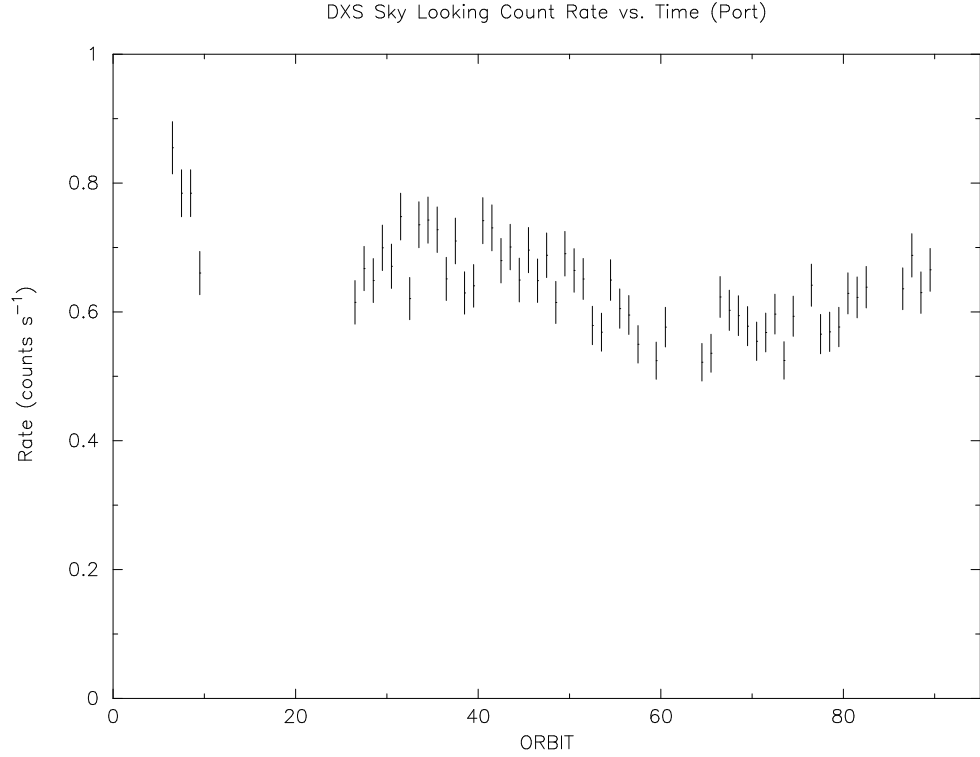
Figure 81: Time history of the "Allsky" count rate in the Port instrument. Instrument background is included. The division between the first and second half of the flight discussed in §5.5 and §5.7.2 is made at orbit 51.

Table 13: Background subtracted rates in the subdivisions of the port data set. These rates are calculated for spectra as in Table 12.

Region	Even Anode First Half Rate (cts/s)	Even Anode Second Half Rate (cts/s)	Odd Anode First Half Rate (cts/s)	Odd Anode Second Half Rate (cts/s)
Allsky	0.297±0.004	0.242±0.004	0.266±0.004	0.227±0.004
Crux	0.228±0.017	0.203±0.014	0.198±0.016	0.189±0.013
Vela	0.452±0.010	0.357±0.008	0.387±0.010	0.336±0.008
Puppis	0.228±0.009	0.180±0.007	0.200±0.008	0.172±0.007
MonoGem	0.285±0.007	0.234±0.006	0.269±0.007	0.224±0.006
Auriga	0.178±0.009	0.162±0.008	0.169±0.009	0.136±0.008
background	0.033±0.001	0.033±0.001	0.035±0.001	0.034±0.001

Table 14: Rate comparison of the subdivisions of the port data set. These are ratios and differences between the rates in Table 13.

Region	Even Anode 1st/2nd	Even Anode 1st–2nd (cts/s)	Odd Anode 1st/2nd	Odd Anode 1st–2nd (cts/s)
Allsky	1.23±0.03	0.055±0.006	1.17±0.03	0.039±0.005
Crux	1.12±0.11	0.025±0.022	1.05±0.11	0.009±0.021
Vela	1.26±0.04	0.095±0.013	1.15±0.04	0.051±0.013
Puppis	1.26±0.07	0.047±0.011	1.16±0.07	0.027±0.011
MonoGem	1.22±0.04	0.051±0.009	1.20±0.05	0.046±0.009
Auriga	1.10±0.08	0.017±0.012	1.24±0.09	0.033±0.012
background	0.99±0.03	0.000±0.001	1.05±0.03	0.002±0.001
Region	1st Half Even/Odd	1st Half Even–Odd (cts/s)	2nd Half Even/Odd	2nd Half Even–Odd (cts/s)
Allsky	1.12±0.02	0.031±0.006	1.07±0.02	0.015±0.005
Crux	1.15±0.12	0.030±0.023	1.07±0.10	0.014±0.019
Vela	1.17±0.04	0.065±0.014	1.06±0.04	0.021±0.012
Puppis	1.14±0.07	0.028±0.012	1.05±0.06	0.008±0.010
MonoGem	1.06±0.04	0.016±0.010	1.04±0.04	0.010±0.009
Auriga	1.06±0.08	0.009±0.012	1.19±0.09	0.026±0.011
background	0.94±0.03	-0.002±0.001	1.00±0.03	0.000±0.001
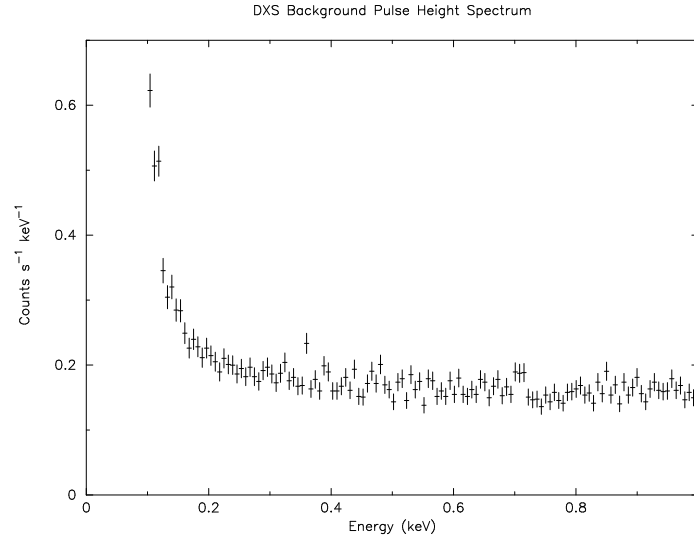
Figure 82: DXS Port instrument aperture-closed background pulse height spectrum.

energy and would not be confused with X-ray background photons. However, if the Compton electron is produced near the proportional counter window, it only deposits a small amount of its energy. Assuming that a random amount of energy is deposited by each Compton electron that ends up escaping through the window, the resulting pulse height distribution should be flat. As shown in Figure 82, this is indeed the case for pulse heights above 300 eV. The predicted background count rate in the DXS proportional counter due to this mechanism is 0.27 counts s^{-1} keV^{-1} (McCammon 1998). The actual rate was somewhat lower ($\sim$0.2 counts s^{-1} keV^{-1}).

Figure 83 shows the time history of the non-X-ray background count rate in the Port proportional counter. The average rate is 0.068 counts s^{-1} (over the entire counter from $\sim$100 eV to $\sim$450 eV, but there are excursions in the rate of 0.02 counts s^{-1}. These excursions appear periodic, with a period of 15$\sim$16 orbits. The variation is most likely due to to enhanced particle background over a particular part of the Earth. Since the shuttle orbits the Earth every $\sim$90 minutes, it passes over the same location on the Earth every $\sim$16 orbits. Figure 84 shows a plot of the aperture-closed count rate as a function of Earth coordinates. Because of the limited number of orbits, coverage is not good. However, an enhanced count rate near the South Atlantic Anomaly (SAA) is clearly visible.

Because the sky-looking observations were executed during the same 1/4 of each orbit,
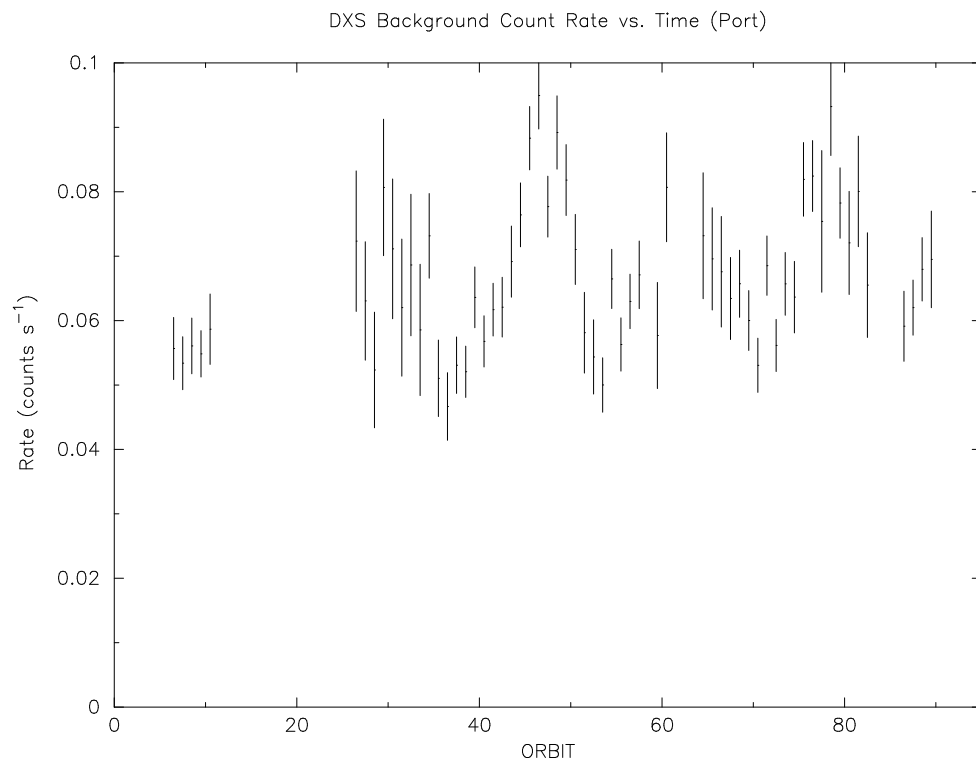
Figure 83: Time history of the background in the Port proportional counter.
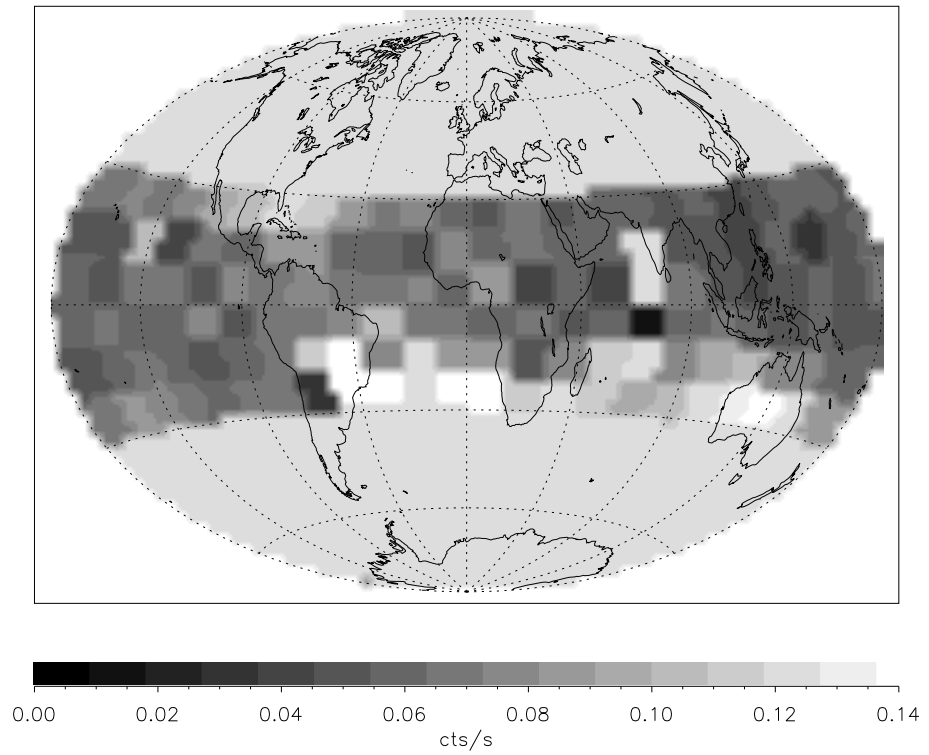
Figure 84: Aperture-closed background count rate in Earth Coordinates. Pixel size is 15°x15°. There is no exposure above South Western India or in the middle of the South Atlantic. The other pixels in the South Atlantic have very little exposure time and count rates greater than 0.25 counts/s.

and the particle background is highly variable with position over the Earth, it is possible that the average particle background recorded during the aperture closed times is significantly different than the particle background during sky-looking times. Furthermore the periodic variation might have a significantly different amplitude. Periodic variation with amplitudes above $\sim$0.1 counts s^{-1} would be evident in the sky-looking count rate history shown in Figure 81. The fact that none are seen suggests the contribution to the sky-looking background by such periodic enhancements is within a factor of two of the contribution seen during aperture closed times.

As an interesting side note, it is possible to estimate the magnitude and variation in the particle background during sky-looking (or "scan") times by considering the count rate in the edges of the proportional counter (position channels 1–20 and 220–240). These channels of the proportional counter are shadowed from the sky by the support structure at the edge of the proportional counter window. Also, there is limited veto coverage in this area (see §2.3.2), so the count rate in these channels is several times higher than that of the background level in the sky-looking channels. During aperture-closed background observations, however, the count rate in the edge channels is roughly correlated with the count rate in the central channels. Assuming that this correlation holds during scan times, we can use the count rate in the edge regions to estimate the contribution of the particle background during scan times. Figure 85 shows the count rate in the edge regions during scan times as a function of Earth coordinates. The average count rate in Figure 85 is about 20% lower than that of that the edge channels of aperture-closed observation times. Notice that the highest count rate occurs above the North Pacific, though because of the observation geometry (see §2.4), no scan observations were taken at the low latitudes where the bright spot in the aperture-closed observations was seen. This is most the likely reason for the lower average count rate in the edge events of the scan observations versus the edge events of the aperture-closed observations. Using these observations, it may be argued that the background count rate of 0.068 counts s^{-1} quoted in Table 12 is $\sim$20% too high. However, the lack of strong correlation between the edge and sky-looking spectral channels in the aperture-closed data suggests that un-vetoed charged particles are not the only source of background in the proportional counters. Thus, to be conservative, the full count rate from the aperture-closed observations is used as the instrument background.

The count rate in the extreme Galactic longitudes of Figure 80 shows that the average non-X-ray background is not significantly different between the sky-looking (or "scan") times
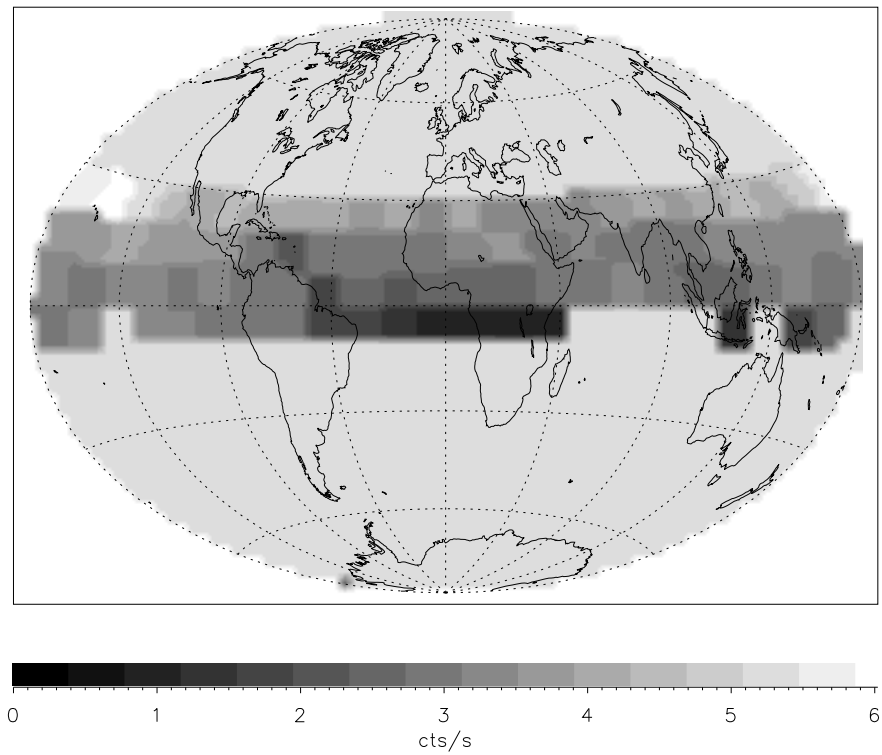
Figure 85: Counting rate in the edges of the Port counter as a function of Earth coordinates during scan times. Background counting rate in the main volume of the counter may follow a similar trend. Pixel size is $15° \times 15°$.

and the aperture-closed times. The count rate at both extremes of Galactic longitude, where occultation by the shuttle cargo bay is complete, is consistent with the average aperture-closed background level of 0.068 counts s^{-1} over the entire proportional counter.

Additional evidence that the average non-X-ray background counting rate is similar in the aperture-closed and open cases comes from the comparison of Figures 86 and 87. Figure 86 is the position spectrum of the aperture-closed background. Position channels 1–20 and 220–240, which are shadowed by the support structure of the proportional counter entrance window have been omitted because of high counting rates. The average rate per channel is shown as a dotted line. Figure 87 is the aperture-open non-X-ray background. The events and exposure time contributing to this histogram had values of the angle χ (defined in §4.4) more than 15° below the top edge of the orbiter cargo bay, thus, the entire field of view was occulted by the orbiter. Because of the limited rotation of the instrument, position channels 100–200 never became fully occulted. Discarding these channels, the average count rate per channel in Figure 87 is $3.5 \pm 0.4 \times 10^{-4}$ counts s^{-1} channel^{-1} (between $\sim$100 eV and $\sim$450 eV. This is consistent with the average count rate of $3.40 \pm 0.04 \times 10^{-4}$ counts s^{-1} channel^{-1} in the aperture-closed background spectrum shown in Figure 86. Figures 103 and 104 show the background spectra with coarser binning on a wavelength scale for comparison to the region-by-region spectra.

In conclusion, the non-X-ray background rate in the Port DXS instrument is 10∼15% of the total sky-looking rate. Though 30% variations in time are seen due to increased particle background over the Pacific ocean, the non-X-ray background shows no sign of variation large enough to cause the $\sim$20% variation in the sky-looking instrument counting rate.

5.3   Spectral Self-Consistency Test

By using the proportional counter pulse height information recorded for each X-ray event, it is possible to show that the majority of the events recorded came from outside the instrument and bounced off of the crystal panel. This is accomplished by checking for self-consistency between the position and pulse height information of each event. Specifically, the proportional counter was divided up into a few spatial bins and pulse height spectra of the events in these bins were created.

The spatial bins chosen for the spectral self-consistency test are shown in Figure 88. The
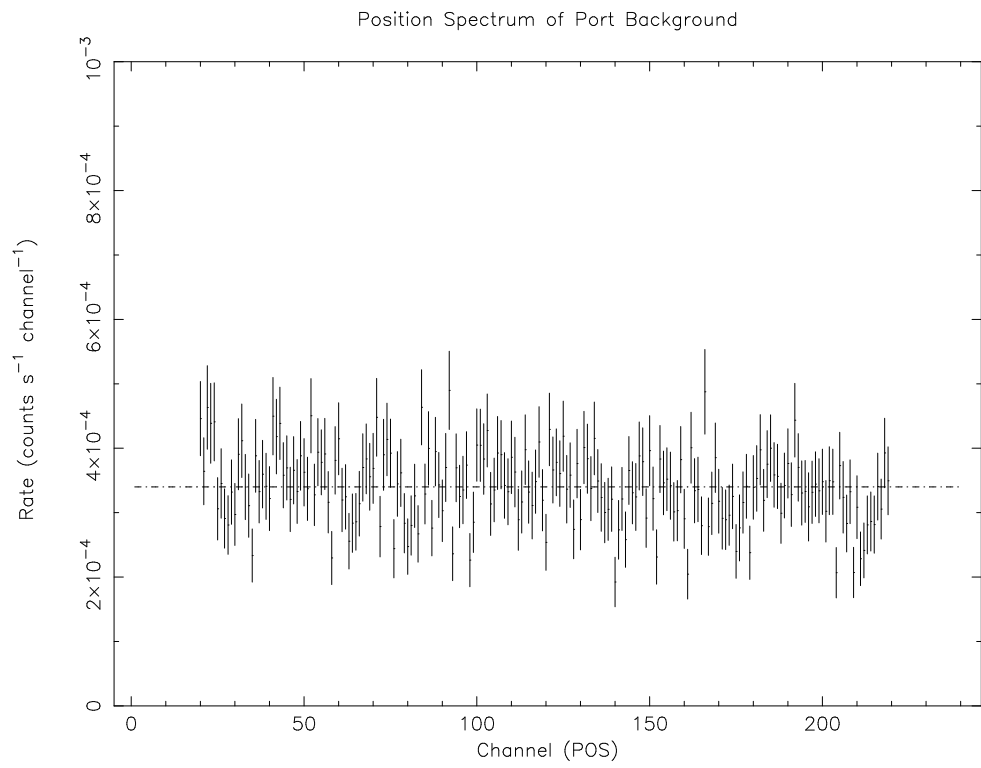
Figure 86: The position spectrum of the non-X-ray background of the Port instrument, collected when the instrument was stowed and the aperture closed. The average rate per channel is shown as dotted line.
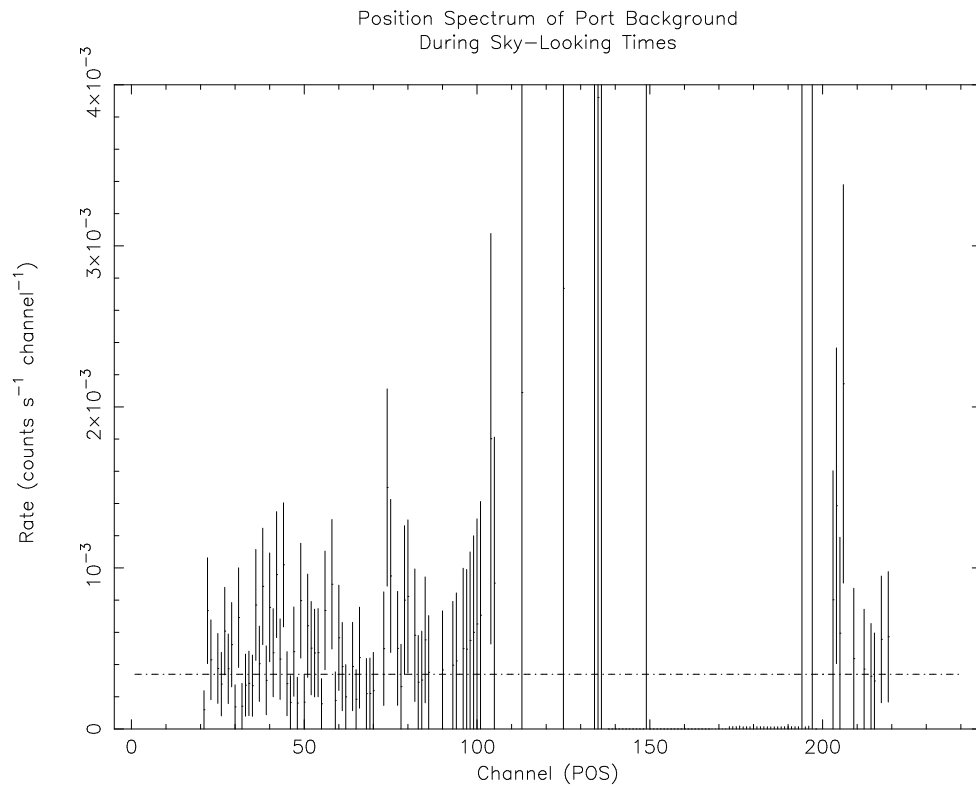
Figure 87: Position spectrum of the non-X-ray background of the Port instrument during sky-looking times, collected when the instrument was not stowed, but the field of view was fully occulted by the orbiter. The average aperture-closed background rate per channel of the Port instrument is shown as dotted line. Channels 100–200 are not occulted enough by orbiter cargo bay to allow a significant measurement.
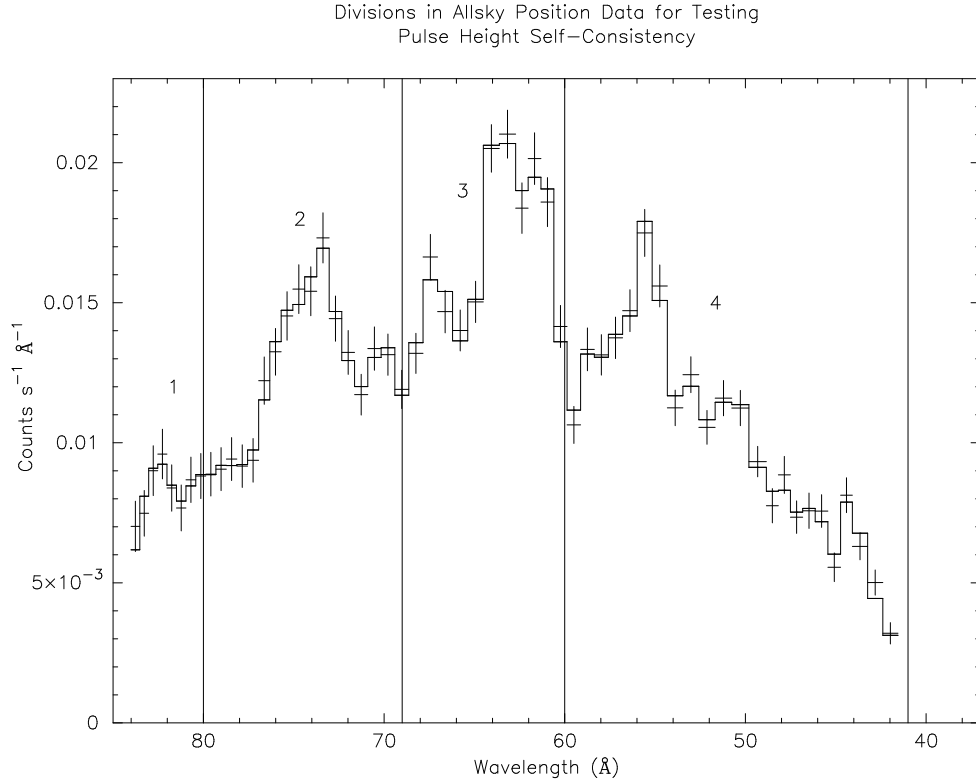
Figure 88: DXS Allsky spectrum with the divisions made for the spectral self-consistency test. The solid line is model composed of 50 Gaussians, two per resolution element.

bin boundaries were drawn in the valleys between the major spectral features. Table 15 gives the precise bin boundaries in raw proportional counter channels (POS), wavelength and energy.

The next step in the spectral self-consistency test was to form a pulse height spectrum of the events from each region. To do this, the program `hist` (see §4.5) was run on the Port data with the position channel (POS) filters indicated in Table 15. The resulting background-subtracted pulse height distributions are shown in Figures 89 through 92. Note that the pulse height distributions peak at successively higher energies as the wavelength decreases. This is evidence that the majority of the events recorded in the Port instrument are X-rays that have Bragg reflected off of the crystal panel. This is the fundamental result of this exercise.

An additional outcome of the spectral self-consistency test is the confirmation of the variation with energy of the input parameters to the Jahoda & McCammon (1988) pulse height model described in §3.1.4. In order to show this result, a model was fit to the position data in

Table 15: Spectral Regions of Port "Allsky" Position Spectrum

Spectral Range	Channel Range (POS)	Wavelength Range (Å)	Energy Range (eV)
1	20-52	84-80	147-155
2	53-116	80-69	155-179
3	117-161	69-60	179-208
4	162-220	60-41	208-301
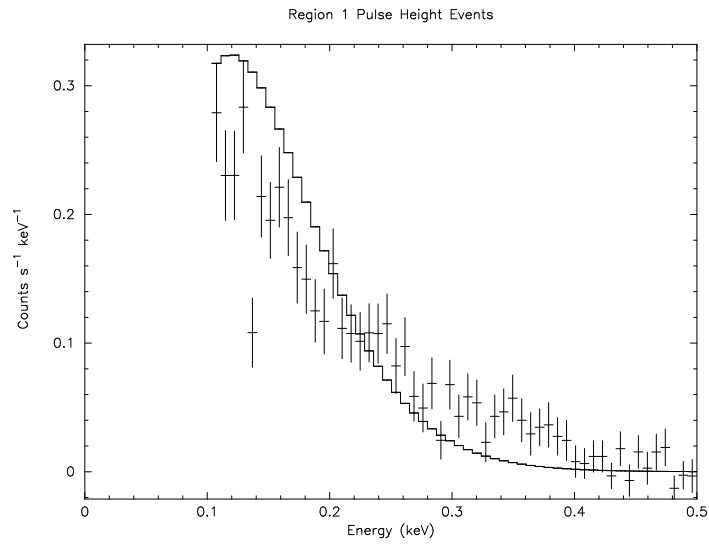
Figure 89: Pulse height spectrum of spectral region 1. Model, described in text is convolved with the high gain pulse height response matrix.
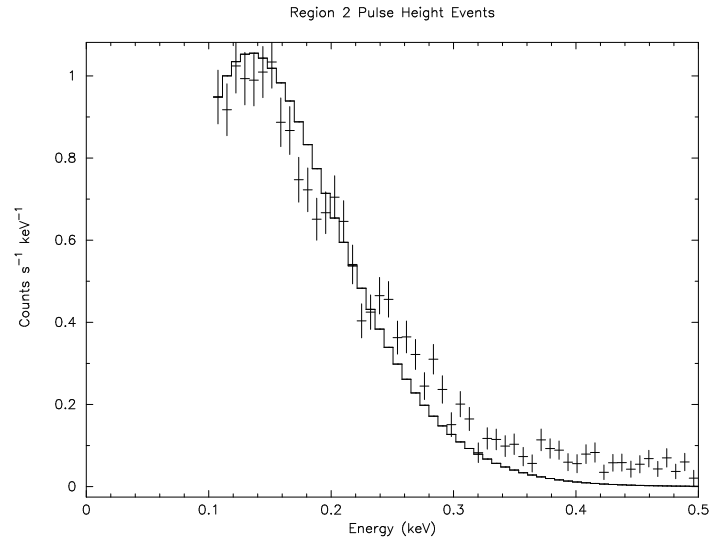
Figure 90: Pulse height spectrum of spectral region 2. Model, described in text is convolved with the high gain pulse height response matrix.
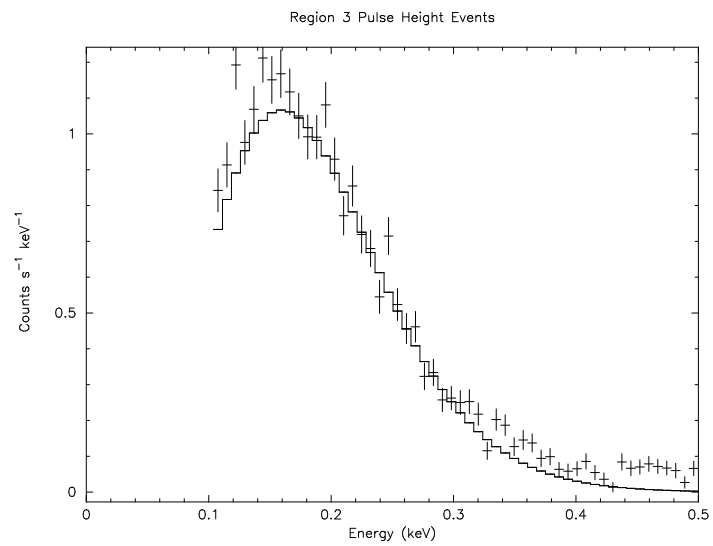
Figure 91: Pulse height spectrum of spectral region 3. Model, described in text is convolved with the high gain pulse height response matrix.
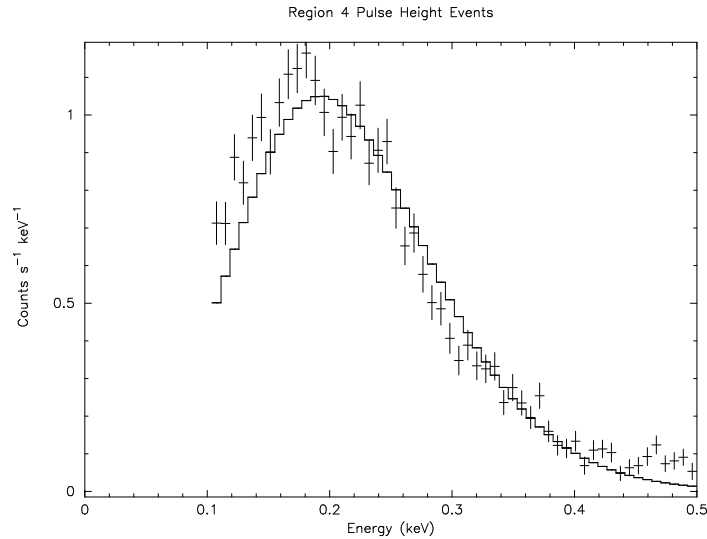
Figure 92: Pulse height spectrum of spectral region 4. Model, described in text is convolved with the `low` gain pulse height response matrix.

Figure 88. The model consists of 50 zero width Gaussians with energies ranging from 149 eV to 284 eV. The Gaussians are spaced so that there are ∼2 Gaussians per instrument resolution element, as determined by the calculations that produced Figure 23. The model, convolved with the instrument *position* response function described in §2.5, is shown as the solid line in Figure 88. The reduced χ^2 of the model fit is 1.9 for 9 degrees of freedom.

Next, the instrument response for each of the four spectral regions in Figure 88 was generated. Section 2.5 describes the general scheme of creating the DXS position response matrix. One of the parts of the response matrix is a normalized redistribution matrix file (RMF), which gives the position probability distribution for recording a photon of energy. A similar matrix has been generated for the pulse height response of the instrument (§3.1.4). For regions 1-3, the low gain In this case it has been the *low gain* pulse height response matrix that has been used. The other part of the response matrix is a one dimensional vector which gives the area solid-angle product of the instrument as a function of energy (the ancillary response file, or ARF). It is the ARF which has been uniquely generated for each of the spectral regions in Figure 88. To do so, the `SPCMOD/RSPMATRIX` system described in §2.5 was run with the instrument response set to zero for the channels outside of the POS range in question.

Each of the four unique response matrices have been convolved with the model of 50 zero-width Gaussians described above. The resulting pulse height distributions are the solid lines in Figures 89 through 92. Notice that for spectral regions 2, 3 and 4, the agreement between model and data is not bad, but becomes progressively worse toward spectral region 4, with the data appearing at lower energies than the model predicts. This behavior, also seen in the post-flight data as described in §3.1.4, may be due to a pulse height non-linearity caused by the high gas gain of the DXS proportional counters.

For spectral region 1, the convolved model does not resemble the data: there is an excess of counts in the 200–400 eV range and a lack of counts at 150 eV relative to the model. It is unlikely that the poor fit of the model to the data here is caused by the non-X-ray background of the Port instrument. Figure 82 shows the pulse height spectrum of the non-X-ray background, observed during times when the instrument was stowed and the aperture was closed. The position spectrum of these data is shown in Figures 86 and 103. The pulse height spectrum of the non-X-ray background observed during the sky-looking, or "scan" times (position spectrum shown in Figures 87 and 104) looks similar but with much poorer counting statistics. These pulse height spectra are flat at energies higher than 300 eV. Thus, it would be difficult to form the shelf-like feature in the spectral region 1 pulse height spectrum (Figure 89) with this background. Instead, events with energies near 300 eV are needed.

A more likely cause for the poor fit of the model to the data in spectral region 1 is the presence of strong lines near $\sim$300 eV that are seen in second order Bragg reflection. Photons of $\sim$300 eV Bragg reflecting in second order appear in the same place in the proportional counter as photons with energies of $\sim$300 eV ($\sim$80Å). Figure 93 shows the region 1 pulse height spectrum together with a model that was the result of a simultaneous fit of the region 1 pulse height spectrum and the Allsky position spectrum with a modified version of the 50 Gaussian model described above. The 50 Gaussian model was modified by moving one of the Gaussian components that was not contributing to the flux at first order energies to 300 eV. The best fit value of the flux in the 300 eV line is 31 counts s^{-1} keV^{-1} sr^{-1} which is $\sim$20 times that of typical Gaussian line fluxes in the 150–284 eV range. The presence of such a strong line, or collection of a few lines is not unreasonable given that most of the astrophysical models fit to the data in Chapter 6, have strong lines near 300 eV.

Because of the potential confusion between first and second order Bragg reflection in spectral region 1, all of the fits in Chapter 6 have been computed twice: once with the data in
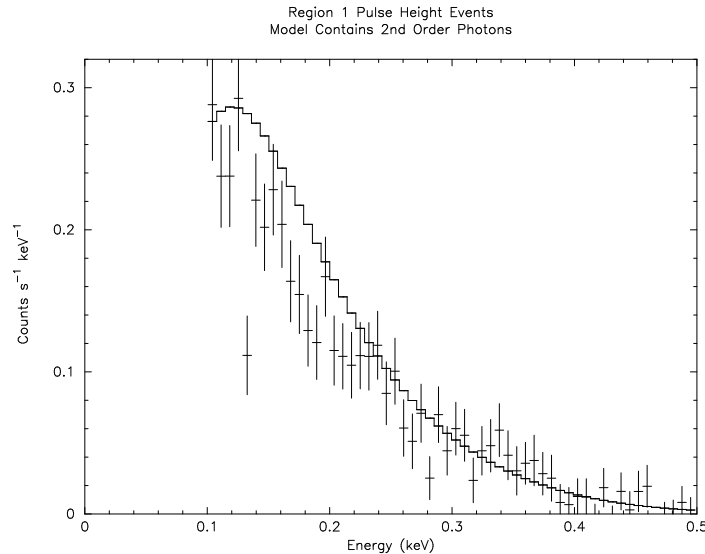
Figure 93: Pulse height spectrum of position region 1. Solid model curve is the the 50 zero with Gaussian model described in text plus one line at 300 eV.

spectral region 1 and once without. None of the models discussed in Chapter 6 show significant difference between the two cases. Thus, in the work to date, there seems to be no major difference in the DXS results whether or not the data from spectral region 1 (first order wavelengths longer than 80 Å) are included. However, this does not rule out the possibility that order confusion may affect future work: fits should always be done twice, with and without data longward of 80 Å (XSPEC channels 20-27).

5.4 Comparison with ROSAT All-Sky Survey

This section describes in detail how the counting rates in the regions observed with DXS were compared to the counting rates of the ROSAT 160–284 eV band (C–band) surface brightness map (Snowden *et al.* 1995). The results of this exercise, summarized in Table 16, show that the ∼20% decrease in the DXS counting rate between the first and second halves of the flight is not due to the slight changes in the shuttle attitude between the two halves of the flight. An additional result of this exercise is an *absolute* comparison of the DXS counting rate to the ROSAT observed counting rate. Because of the difference in the shapes of the instrument energy response functions, however, this comparison is model-dependent.
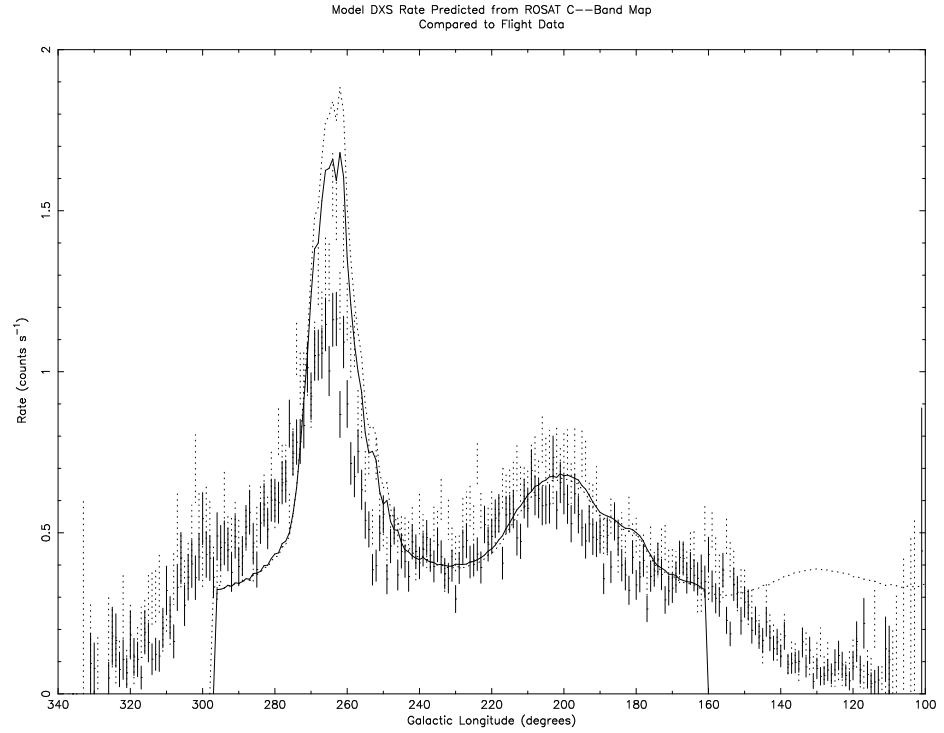
Figure 94: DXS count rate vs. Galactic longitude for the first half (dotted error bars) and second half (solid error bars) of the flight. Lines are results of the modeled DXS counting rate based on the ROSAT C–band all-sky map. Instrument background of 0.068 counts s^{-1} is included in the model calculations between 160° and 300∘. Exposure between 100° and 160° in the first half of the flight is due to telemetry errors discussed in §4.2.

The basic scheme of the ROSAT-to-DXS comparison was to use the ROSAT C–band surface brightness maps as a synthetic sky. A map in Galactic coordinates of the DXS exposure was used together with successively more accurate models of the DXS footprint on the sky to create model histograms of DXS count rate versus Galactic longitude. An example of model histograms from the first and second half of the flight are shown overlayed on the DXS count rate data in Figure 94.

The model calculations transform the ROSAT C–band map into raw DXS counts using the ratio of the DXS to ROSAT responses. The ratio of responses was established by taking the same equilibrium plasma model and folding it through the ROSAT C–band response matrix and the DXS "model d 16" response matrix using the program XSPEC (Arnaud 1996). For

the solar abundance Mewe and Kaastra model described in §6.2.3, the ratio of ROSAT to DXS response in surface brightness units is 1301. The other equilibrium plasma models discussed in Chapter 6 give results varying by less than 1% from this value.

Two models of the DXS collimator response were used to check how sensitive the predicted DXS counting rates are to the exact collimator shape. The simplest model of the collimator response is a $15° \times 15°$ square pyramidal pattern, with a transmission of 1 in the center and 0 at the edges. This is the transmission pattern of the proportional counter collimator described in Chapter 2. The true DXS view of the sky, however, is affected by the reflection off of the curved crystal panel. Recall the nomenclature of Figure 20. The photon that enters the proportional counter perpendicular to the proportional counter window has collimation angles $\phi = \theta = 0$. The reflection angle of this reference ray from the crystal panel is α. Deviations of the incoming ray in the cross-collimation, or θ direction do not affect the collimation pattern: the angle of the incoming ray will be the same with respect to the normal ray before and after the reflection off the crystal panel. However, because of the curve in the crystal panel, rays entering the proportional counter at an angle in the dispersion direction, ϕ, with respect to the reference ray will have a different angle ϕ' with respect to the reference ray outside the detector. The relation of ϕ', ϕ, and α is:

$$\phi' = 2[\alpha - \cos^{-1}(\cos \alpha \cos \phi)] + \phi \tag{5.1}$$

This relation results in a shift of up to $6°$ in the collimation pattern in the dispersion direction. Because the distortion depends on the bounce angle, α, which depends on energy, the distortion in the collimation pattern also depends on the input spectrum. Rather than calculate the effect using an assumed input spectrum, a typical bounce angle was chosen ($38°$). Predicted counting rates using the extreme bounce angles of $26°$ and $54°$ vary by no more than 2%.

Table 16 show the details of the ROSAT-to-DXS comparison. The first section of the table gives rates in counts per second measured by DXS and calculated from the ROSAT C–band rate map by the method described earlier in this section for the first and second halves of the flight. The calculation of the DXS counting rate based on the ROSAT data in the Crux region has been adjusted for incomplete spectral coverage.

The important result of this exercise is that in all sky regions, the DXS rate changes significantly between the first and second halves of the flight, but the DXS rates predicted from the ROSAT maps only change by 1–2%. This slight predicted change is due to a small change

Table 16: Comparison of measured and predicted (background subtracted) DXS count rates based on ROSAT C–band count rate map. DXS counting rates are the sum of the rates in the individual spectral channels. The ROSAT rate in the Crux region has been corrected for the incomplete spectral coverage in the DXS data.

Region	DXS 1st Half Count Rate (cts/s)	ROSAT 1st Half Count Rate (cts/s)	DXS 2nd Half Count Rate (cts/s)	ROSAT 2nd Half Count Rate (cts/s)
Crux	0.301 ± 0.017	0.250	0.274 ± 0.014	0.250
Vela	0.840 ± 0.014	0.972	0.694 ± 0.014	0.958
Puppis	0.428 ± 0.012	0.375	0.352 ± 0.012	0.366
MonoGem	0.554 ± 0.010	0.495	0.458 ± 0.010	0.497
Auriga	0.347 ± 0.012	0.327	0.298 ± 0.012	0.329
Region	1st Half DXS–ROSAT (cts/s)	1st Half DXS/ROSAT	2nd Half DXS–ROSAT (cts/s)	2nd Half DXS/ROSAT
Crux	0.053 ± 0.017	1.21 ± 0.07	0.024 ± 0.014	1.10 ± 0.06
Vela	-0.132 ± 0.014	0.86 ± 0.01	-0.264 ± 0.014	0.72 ± 0.01
Puppis	0.053 ± 0.012	1.14 ± 0.03	-0.014 ± 0.012	0.96 ± 0.03
MonoGem	0.059 ± 0.010	1.12 ± 0.02	-0.039 ± 0.010	0.92 ± 0.02
Auriga	0.020 ± 0.012	1.06 ± 0.04	-0.032 ± 0.012	0.90 ± 0.04

in orbiter attitude over the flight.

The second portion of Table 16 shows the difference and ratios of the measured DXS rates to the rates predicted by the ROSAT C–band map. For all table entries except the second half of the Vela observation, the measured and predicted rates are within ∼15% of each other. The predicted counting rate in the Vela region probably does not agree well with the measured rate because the Vela spectrum is not well fit by an equilibrium plasma emission model at $T \sim 10^6$ K.

Ignoring the Vela region, the average ratio between the DXS measured rates and the rates predicted by the ROSAT C–band map in the first half of the flight is 1.133. For the second half of the flight, the average ratio is 0.97. This suggests that there was excess emission in the first half of the flight. It is important to note, however, that Snowden *et al.* (1995) have proposed a 10% reduction in the ROSAT C–band effective area in order to reconcile the results of the ROSAT all-sky survey with the surveys of SAS-3 (Marshall & Clark 1984), HEAO-1 (Garmire *et al.* 1992), and Wisconsin (McCammon *et al.* 1983). This correction *increases* the predicted rates in Table 16 by 10%. With this correction applied, the average ratios for the first and second half of the flight (ignoring Vela) are 1.033% and 0.87%, respectively.

5.5   The Long-Term Enhancement Hypothesis

The plot of the time history of the sky-looking Port instrument count rate shown in Figure 81 and the count rates presented in Table 14 clearly show that there is a ∼20% *decrease* in the count rate over the course of the DXS observation. Section 5.2 demonstrate that there is no evidence for a long-term time-varying background produced *inside* the Port DXS instrument of this magnitude. Electron trapping magnets at the entrance aperture of the instrument shield the proportional counter from low energy electrons that have been responsible for variable background in other missions (see §2.3.2). Furthermore, the self consistency of the proportional counter pulse height and position spectra presented in 5.3 demonstrate that the majority of the events detected by DXS were X-rays that bounced off of the Bragg crystal panels. I have identified three other possible sources for the total count rate variation: a change in the instrument sensitivity, unexpected occultation of the instrument aperture, or the presence of a contaminating flux of X-rays.

If a change in instrument sensitivity were the true cause of the 20% variation in DXS counting rate, the natural culprit would be degradation in the crystal panel reflectivity. However, as shown in Figure 51 and §2.2.2, there is no evidence for any such degradation. Furthermore, if the residual atmosphere was the cause of crystal panel degradation (see §2.4), the rate of degradation, or the slope of the count rate vs. time graph in Figure 81 would become more negative after orbit 51, when the number of scans per orbit was increased from eight to nine. However, after orbit 60, the counting rate actually increases slightly. For these reasons, we can rule out the possibility that the crystal panel reflectivity changed during flight.

The instrument sensitivity also depends on the shape of the proportional counter pulse height distribution and dead-time correction. As discussed in §4.4.1, the effects of the changes in pulse height *gain* have already been removed. However, if the pulse height `shape` had become broader and flatter over the course of the flight, more X-ray events would have been filtered out by the software lower level discriminator (LLD), thus dropping the instrument efficiency during the second half of the flight. Figure 95 shows that the "Allsky" pulse height distributions from the first and second half of the flight show no shape difference of the significance needed to change the total flux by ~20%. An error in the proportional counter electronics dead-time correction would effect the total counting rate, however, the dead-time correction for the Port instrument was only a few percent.

Unaccounted-for occultation of the instrument aperture during observation is unlikely because visual inspection of the instrument was made throughout the flight. No unusual material was reported in the vicinity of the instruments while they were operating. Absorption by the atmosphere at the orbital altitude of the shuttle is negligible, even for the extreme look angles. Using the 1972 COSPAR model atmosphere with a high exospheric temperature (2200 K), photons at $100°$ zenith angle with energies above 150 eV have transmissions higher than 99% for altitudes above 210 km. During the DXS mission, the shuttle was at an altitude of ~300 km.

With changes in the instrument sensitivity, occultation of the instrument aperture, contamination by soft electron flux and changes in the high-energy charged particle flux ruled out, the most likely explanation for the difference in behavior between the first and second halves of the flight appears to be variation in a non-cosmic X-ray background. Several such sources have been detected during the ROSAT all-sky survey (Snowden *et al.* 1995). These include
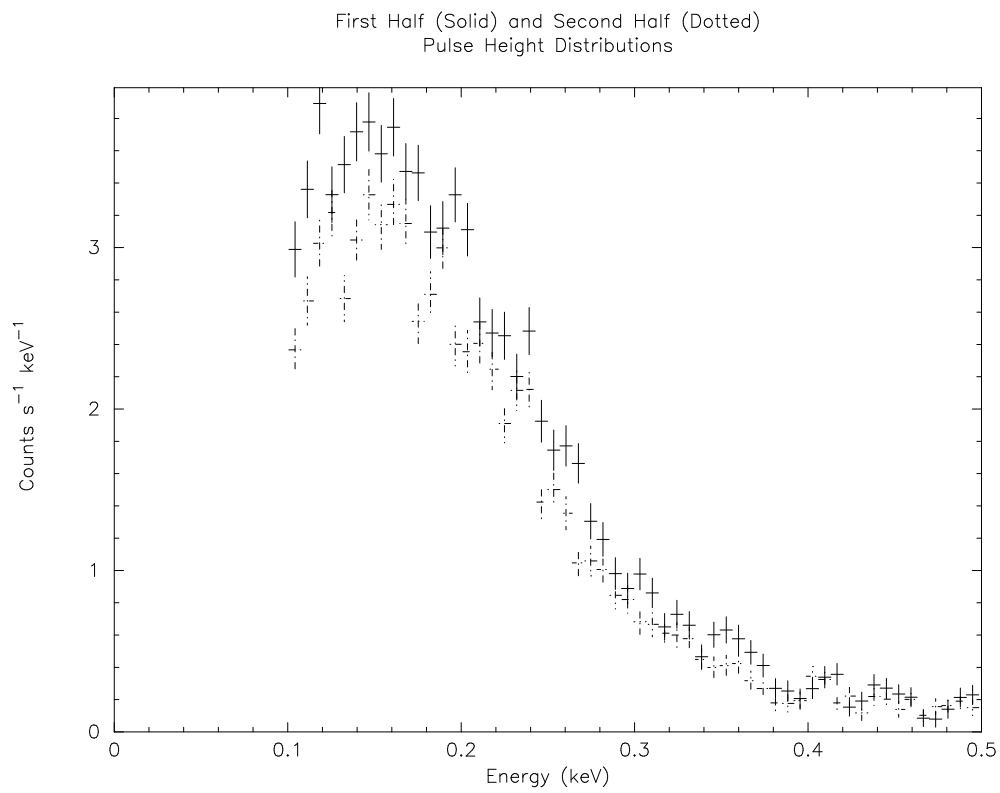
Figure 95: Comparison of the "Allsky" pulse height distributions from the first and second half of the flight.

short-term enhancements (STEs), scattered solar X-rays and a mysterious source of contamination called long-term enhancements (LTEs). STE contamination occurred in the ROSAT data over times scales much shorter than the variation seen in the DXS data. Because DXS observed in the anti-solar direction, the DXS data are not contaminated by scattered solar X-rays. LTEs, however, are a likely source of contamination. LTEs have been shown to be X-rays coming from somewhere between low Earth orbit and the Moon (Snowden *et al.* 1995). The count rate attributable to LTE contamination in the ROSAT all-sky survey often reached 20% or more of the typical diffuse X-ray background count rate in the C–band (160–284 eV). Unfortunately, LTE flux does not seem to be reliably correlated to any geo-magnetic or solar parameter (Snowden *et al.* 1995). Since ROSAT observed the same part of the sky repeatedly over long periods of time, the minimum observed rates could be taken as most probably free from contamination. With the DXS data recorded to date, we do not have such a luxury; the total DXS count rates quoted in Table 12 may be high by 10% or more.
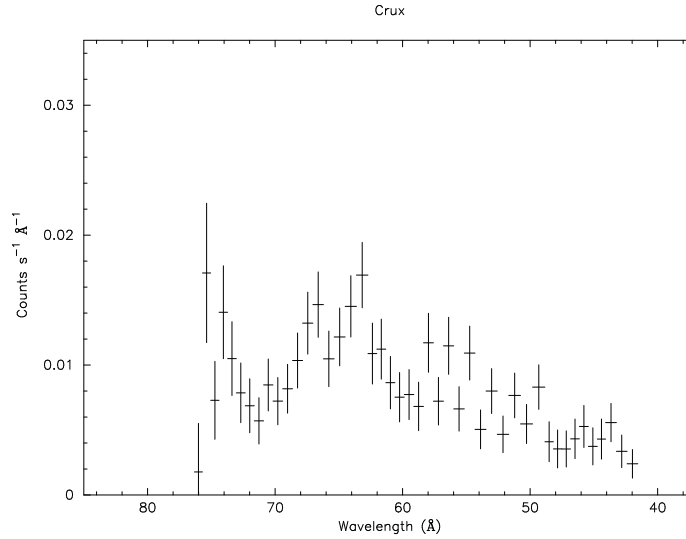
Figure 96: DXS spectrum of the Crux region. The Port instrument could not detect X-rays longward of 76 Å coming from this region.

5.6   Region-by-Region Spectra

The boundaries of the regions shown in Figure 80 and Table 12 were drawn in order to isolate the photons likely to be coming from the diffuse X-ray background from those known coming from the Vela and MonoGem supernova remnants. Figures 96–100 show the background-subtracted spectra of the individual regions as recorded by the Port DXS instrument. As discussed in §5.1, the Crux region did not receive full spectral coverage from the Port instrument. Also, the exposure time changes as a function of energy in the Auriga region, with the higher energies receiving less exposure. Because the exposure time and number of counts are tabulated separately for each spectral channel (see §4.5), the rate in each channel is correct, regardless of exposure time. Channels with small exposure time have large error bars, and channels with no exposure time are excluded from analysis.

In order to simplify spectral analysis of the diffuse X-ray background data, the Crux, Puppis, and Auriga spectra have been added together to form a Hot Interstellar Medium (HISM) spectrum, shown in Figure 101. The spectral addition is done by totaling counts and exposure time for each spectral channel individually and then re-calculating the counting rate and Poisson error for each channel in the total spectrum. Because of its relatively large exposure time, the contribution from the Puppis region dominates the HISM spectrum. Section 5.7.3
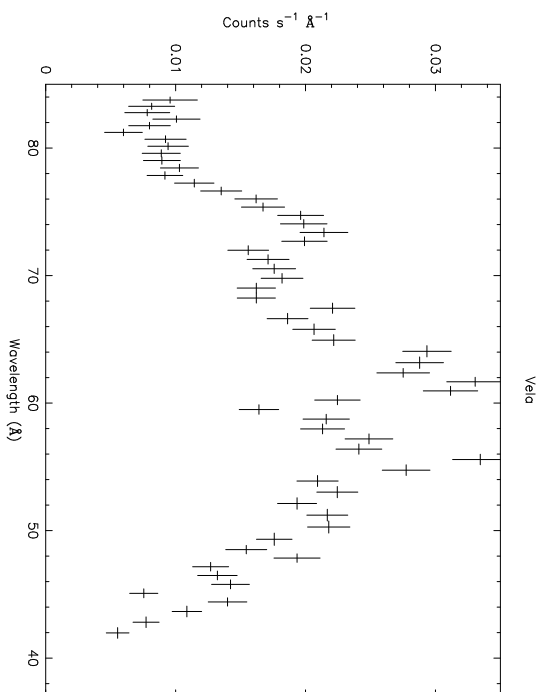
Figure 97: DXS spectrum of the Vela region.
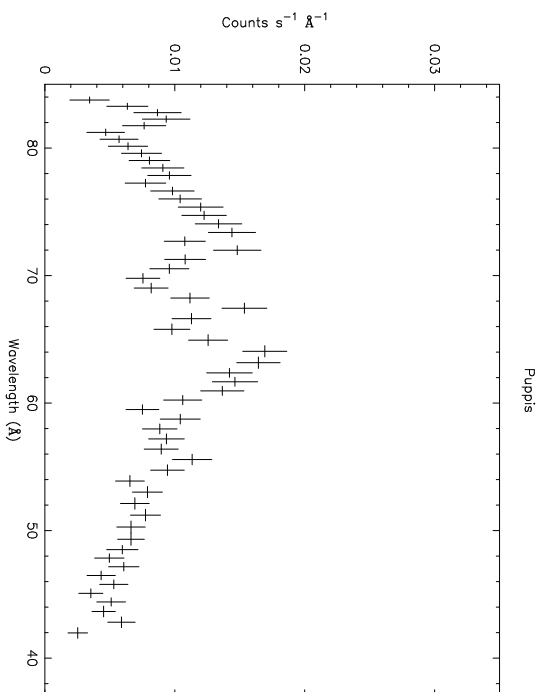
Figure 98: DXS spectrum of the Puppis region.
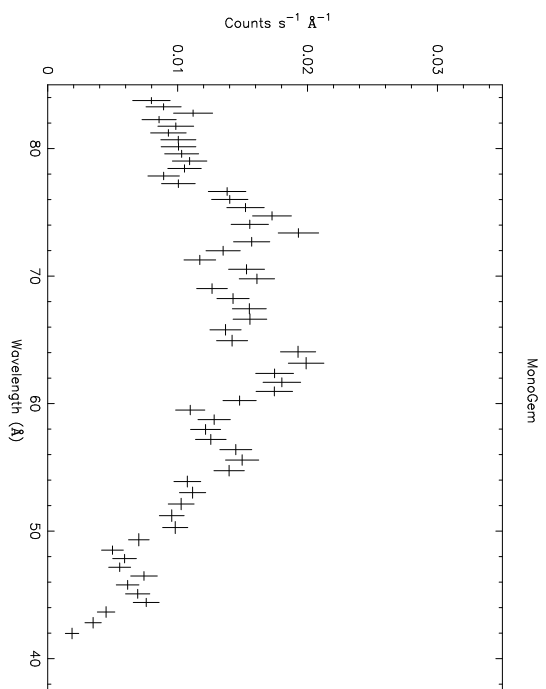
Figure 99: DXS spectrum of the MonoGem region.
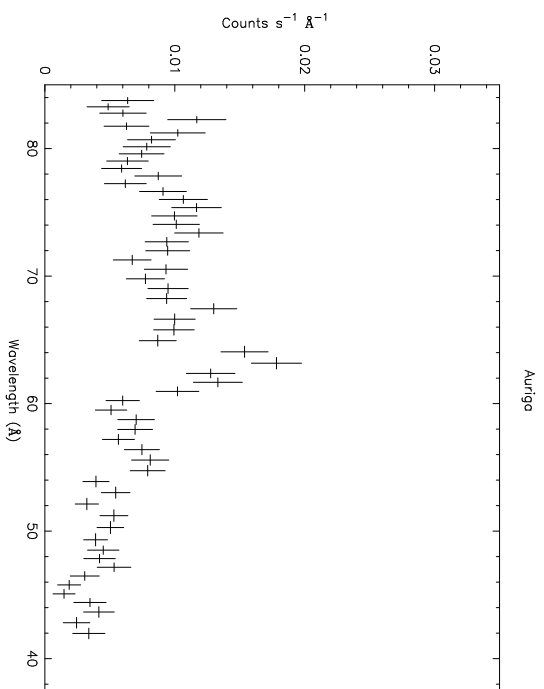
Figure 100: DXS spectrum of the Auriga region.
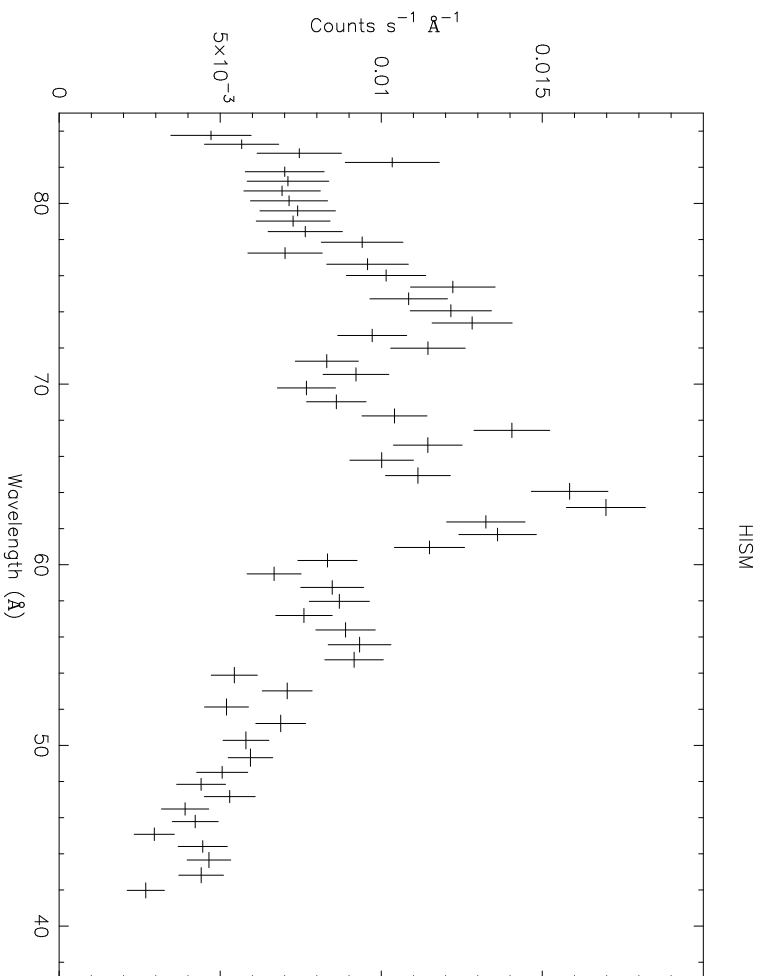
Figure 101: The Spectrum of the Hot Interstellar Medium (HISM).

discusses the comparison of the individual spectra of these regions.

The combined spectrum of all of the regions, the so-called "Allsky" spectrum is shown in Figure 102. Because of the high counting rate in the Vela region, the Allsky spectrum is dominated by Vela supernova remnant.

Figures 103 and 104 show the detector stowed (aperture covered) and detector scanning background spectra, respectively. Figure 103 is the background spectrum subtracted from Figures 96–102.

All of the spectra, as created by the program hist (see §4.5) have 240 channels, corresponding to the 240 position channels of the position sensing proportional counters (see §2.3.1). As discussed in §5.2, the first and last 20 channels of the position spectra, which are not exposed to the sky, are highly contaminated by particle events, so they are discarded. The remaining 200 channels are binned for display purposes into roughly two bins per detector resolution element, resulting in spectra with 60 spectral bins. Figure 23 shows how the number
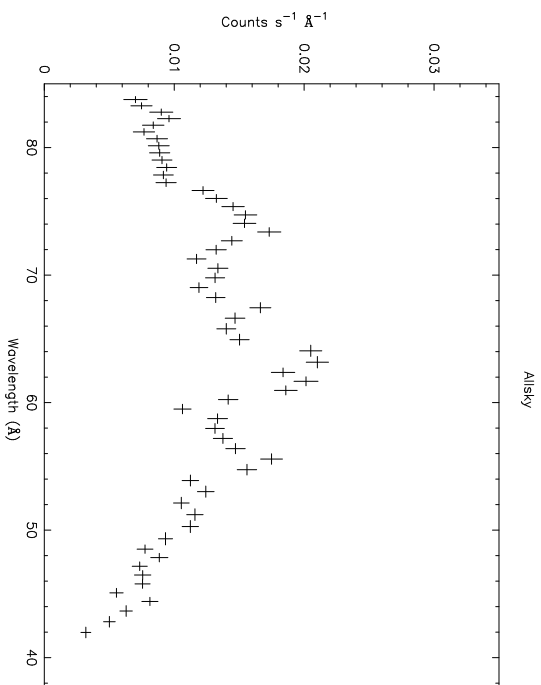
Figure 102: DXS "Allsky" spectrum, with coverage from Galactic longitude ∼130° to ∼320° in a 15° swath near the plane of the Galaxy.

Allsky

Counts s^{-1} Å^{-1}
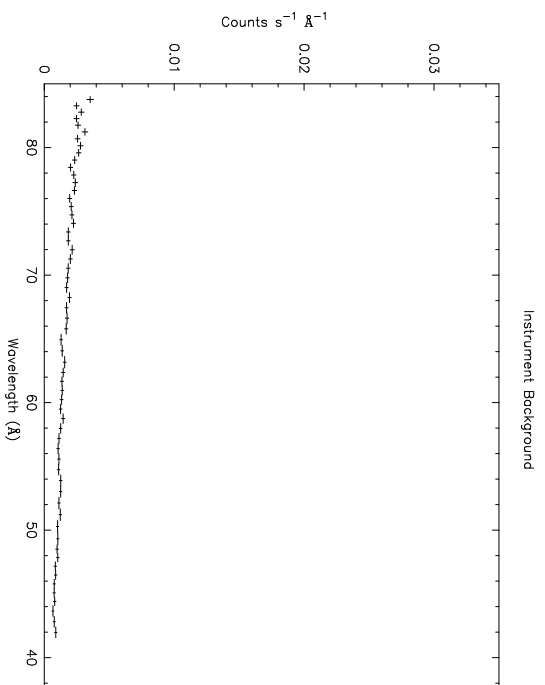
Wavelength (Å)

Figure 103: DXS background in wavelength units.

Instrument Background

Counts s^{-1} Å^{-1}
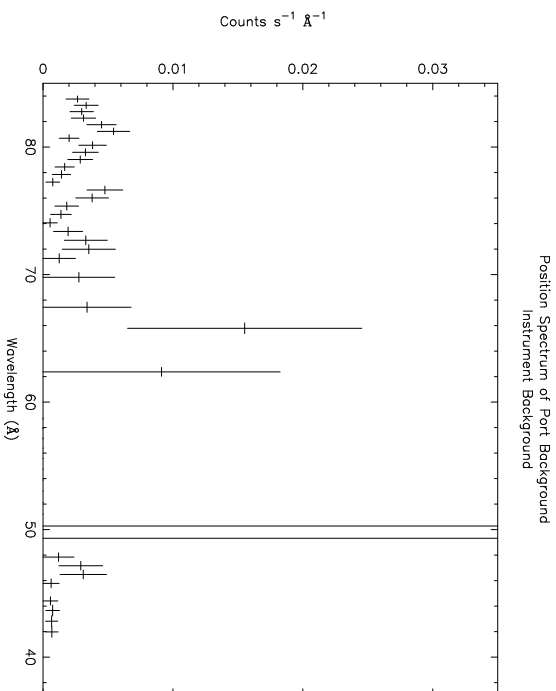
Wavelength (Å)

Figure 104: DXS occulted background in wavelength units. These are the same data as are shown in Figure 87.

of detector channels in each resolution element changes across the detector.

It is important to note that no correction for the variation in count rate discussed in the previous sections has been made to these spectra.

5.7 Spectral Comparison

This section presents a quantitative analysis of the differences between the spectra obtained by the Port DXS instrument. The difference between two spectra is quantified by using the χ^2 statistic to calculate the probability that the two spectra are drawn from the same parent population. In comparisons between two spectra where a difference in total count rate contributes significantly to χ^2, the second spectrum is multiplied by a parameter that is allowed to vary until a minimum in χ^2 is reached. In this way, the χ^2 parameter is used to gauge whether or not two spectra have the same shape. The specifics of this calculation are discussed in §5.7.1. Section 5.7.2 compares the spectra of the subdivisions of the Port dataset described in §4.7 (first and second half of the flight, and "odd" and "even" anode groups). Section 5.7.3 compares the spectra from the different regions on the sky.

Position Spectrum of Port Background
Instrument Background

5.7.1 χ^2 Probability

This section details the computation of the χ^2 probability that two spectra are the same. I adopt the following notation: $RS1_i$ is the raw counting rate (counting rate including background) in the ith channel of the first spectrum, $R\sigma1_i$ the raw statistical error of the ith channel, B_i is the background counting rate in the ith channel, and $B\sigma_i$ is the statistical error of the ith channel of the background counting rate, $RS2_i$, the raw counting rate in the ith channel of the second spectrum, etc. The first step in the calculation is to subtract the background from each spectrum. This is done channel by channel, resulting in background-subtracted spectra $S1_i$ and $S2_i$. The calculation for the first spectrum looks like this:

$$S1_i = RS1_i - B_i.$$

(5.2)

The statistical errors of the raw and background spectra are added in quadrature to calculate the counting rate error for each channel:

$$\sigma1_i = \sqrt{R\sigma1_i{}^2 + B\sigma_i{}^2}.$$

(5.3)

The χ^2 of the two spectra is defined as:

$$\chi^2 = \sum_{i=1}^{n} \frac{(S1_i - S2_i)^2}{\sigma1_i{}^2 + \sigma2_i{}^2},$$

(5.4)

where n is the number of channels in each spectrum. The quantity χ^2 is often used to compare a model spectrum to a measured spectrum. When this is done, the reduced χ^2, or $\chi^2{}_\nu$ is used as a measure of the goodness-of-fit:

$$\chi_\nu = \frac{\chi^2}{n - p},$$

(5.5)

where p is the number of free parameters in the fitting function. In the calculation of the χ^2 of two spectra, described above, $p = 0$, because there is no adjustable parameter.

In order to determine whether or not spectra with different total count rates had underlying spectral differences, a normalization parameter N is introduced which multiplies each channel of the second spectrum:

$$S2'_i = NS2_i. \tag{5.6}$$

N is varied and χ^2 recalculated until a minimum in χ^2 is reached. The reduced χ^2 is then:

$$\chi_\nu = \frac{\chi^2}{n-1}, \tag{5.7}$$

since there is one free parameter.

The χ^2 *probability* is computed using the incomplete gamma function, Q, described in *Numerical Recipes* (Press *et al.* 1992) and the degrees of freedom, ν. In the notation above,

$$\nu = n - p \tag{5.8}$$

All DXS spectra have 240 channels, corresponding to the 240 position channels in the position reduction algorithm (see §2.3.1). However, the first and last 20 channels are always discarded, since these channels do not see the sky. Thus, for must of the DXS spectral comparisons, $n = 200$. Channels below POS = 82 of Crux spectra have negligible or zero exposure time. So, whenever a Crux spectrum is one of the pair of spectra being analyzed, these channels are discarded in both spectra, and $n = 138$.

5.7.2   Internal Comparison

The Port DXS data set was divided into regions (e.g. Crux, Vela, etc.) on the basis of Galactic longitude, as indicated in Figure 80 and Table 12. Recall from §4.7 that the data from each region in the Port dataset was further subdivided into eight independent subdivisions for processing purposes ("even" and "odd" anode groups, first and second halves of the flight, PCM and KU telemetry streams). Thus, there are 8 independent spectra of each region. The spectra from the two telemetry streams were combined in order to simplify analysis, resulting in four independent spectra: "even" and "odd" anode groups for the first and second half of the flight. These spectra were combined to form the first half of the flight spectra and second half

Table 17: Spectral comparison of the subdivisions of the Port instrument. Table entries are χ^2 probabilities that the two spectra of a particular region (indicated at the left) formed from two subdivisions of the data (indicated at the column head) are the same shape, as determined by the minimum χ^2 procedure described in §5.7.1. Probabilities below 5% (a confidence level of 2σ) are indicated in boldface.

Region	1st to 2nd Half	"Even" 1st Half to 2nd	"Odd" 1st Half to 2nd
Allsky	0.58	0.12	0.97
Crux	0.09	0.31	0.40
Vela	0.43	0.44	0.45
Puppis	0.12	0.21	0.76
MonoGem	0.68	0.05	0.92
Auriga	0.06	0.36	0.34
background	0.55	0.78	0.43
HISM	0.12	0.41	0.81

Region	"Even" to "Odd"	"Even" to "Odd"	1st Half "Even" to "Odd"	2nd Half "Even" to "Odd"
Allsky	**0.00**	**0.00**	**0.00**	**0.02**
Crux	0.19	0.61	0.27	
Vela	**0.00**	0.06	**0.01**	
Puppis	0.49	0.64	0.69	
MonoGem	**0.00**	**0.02**	**0.01**	
Auriga	0.93	0.93	0.72	
background	**0.03**	0.26	0.18	
HISM	0.73	0.70	0.98	

of the flight spectra and the "even" and "odd" spectra. Various parings of these spectra were then compared using the minimizing χ^2 technique described above. Table 17 summarizes the results of these calculations. For the region indicated in the leftmost column and the pairing indicated at the column head, each number in the table is the χ^2 probability that the two spectra have the same shape. χ^2 probabilities less than 5%, which indicate that the spectra are not likely to have the same shape (at the 2σ confidence level), are indicated in boldface.

The important result shown in Table 17 is that none of the spectra show significant shape change between the first and second half of the flight. This suggests that whatever is causing the variation on count rate over the course of the flight does not significantly alter the shape

154
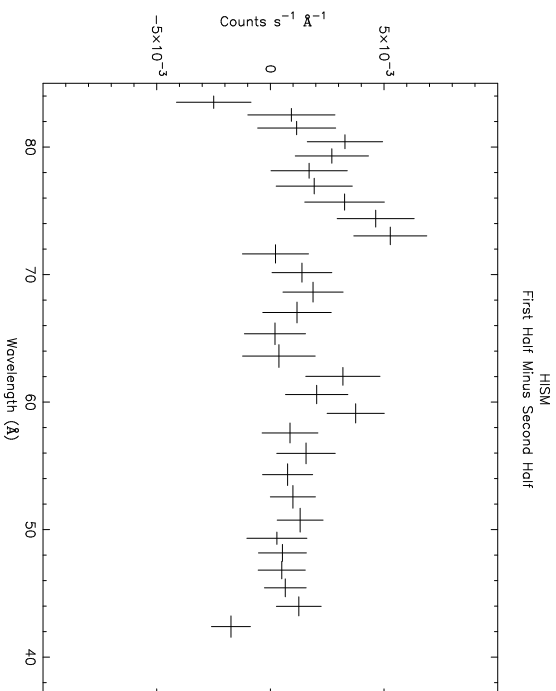
Figure 105: HISM spectrum from the first half of the flight minus the HISM spectrum from the second half of the flight. The χ^2 probability that the two original spectra are identical is 12%.

HISM
First Half Minus Second Half

of the X-ray spectrum significantly enough for DXS to detect. The second result is that regions comprising the HISM spectrum (Crux, Puppis, and Auriga) do show good "even"/"odd" agreement but the Vela and MonoGem regions do not. The fact that the Vela and MonoGem spectra show substantial spectral differences between the "even" and "odd" anodes may be related to the sensitivity of the odd/even ratio in the Port DXS instrument to gradients in the cross dispersion direction (see §2.3.2) and the fact that the Vela and MonoGem sources do not fill the DXS field of view. One difficulty with this hypothesis is the fact that the "even" anode count rate was than the "odd" count rate towards Vela (Table 14). Since Vela is on the southern side of the scan path, one would expect the "odd" anode count rate to be higher (§2.3.2). This effect has yet to be explained.

The difference between the first and second half HISM spectra is shown in Figure 105. The χ^2 probability that these spectra are the same (e.g. the difference is a flat line), as determined by the χ^2 minimization procedure in §5.7.1 is 12%. For display purposes, the bin size in Figure 105 has been increased by a factor of two over the bins of Figure 101. Figure 106 shows the difference between the background spectra for the "even" and "odd" anode groups, which were unexpectedly dissimilar. Note that the differences in the background spectra are small compared to the differences in the HISM spectra.
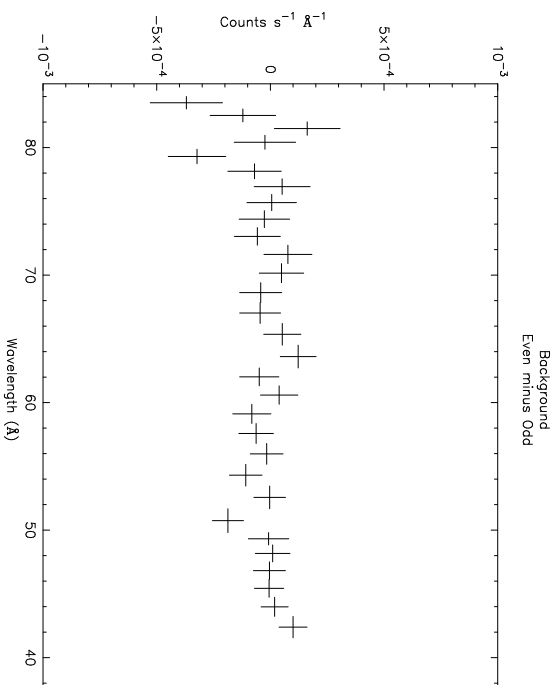
Figure 106: Background Spectra: "Even" anode group minus "odd" anode group. The χ^2 probability that the two original spectra are identical is 3%.

5.7.3 Region-to-Region Comparison

A χ^2 probability analysis similar to that outlined §5.7.1 was used to compare the region-by-region spectra presented in §5.6. The analysis was done according to the prescription in §5.7.1, with and without scaling the total rates. Table 18 summarizes the results. Only Vela appears to have a significantly different spectral shape.

Figures 107 through 111 show the channel-by-channel differences (without any scaling) between the spectra compared in Table 18. The bin sizes of these figures have been adjusted for display purposes; they are twice that of Figures 96–104. Vela clearly shows harder, brighter emission than the general diffuse X-ray background. The slight differences between the other spectra are not statistically significant as shown by the high values (more than 8%) of χ^2 probability in Table 18.

5.8 Conclusion

The counting rate in the Port DXS instrument changes by ~20% of the course of the flight. This change may be due to a long-term enhancements (LTE) as was seen in the ROSAT all-sky survey (§5.5). By comparing the shapes of the more contaminated and less contaminated

Table 18: Spectral Comparison of Region-by-Region Spectra. The first column indicates the χ^2 probability that the spectra have the same shape (as discussed in §5.7.1). The second column is the χ^2 probability the two spectra are identical, computed with no free normalization parameter.

Regions	χ^2 Probability (shape)	χ^2 Probability (identical)
Puppis–Auriga	0.08	0.00
Puppis–Crux	0.13	0.01
Auriga–Crux	0.09	0.09
Vela–HISM	0.00	0.00
MonoGem–HISM	0.46	0.00
Vela–MonoGem	0.00	0.00
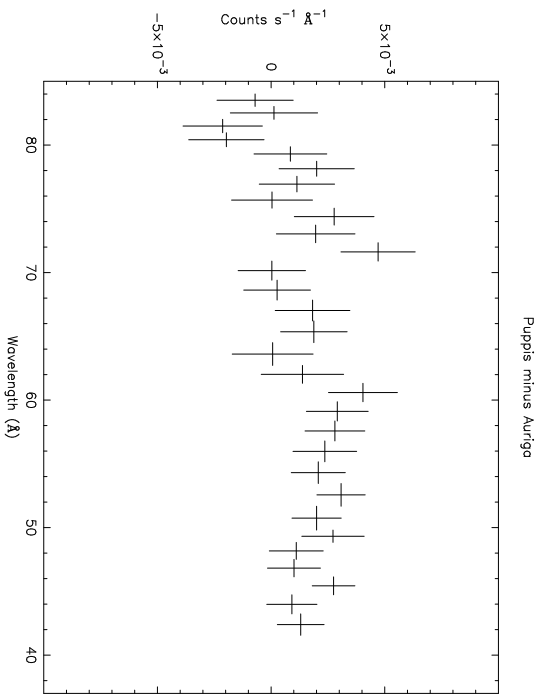
Figure 107: Puppis minus Auriga
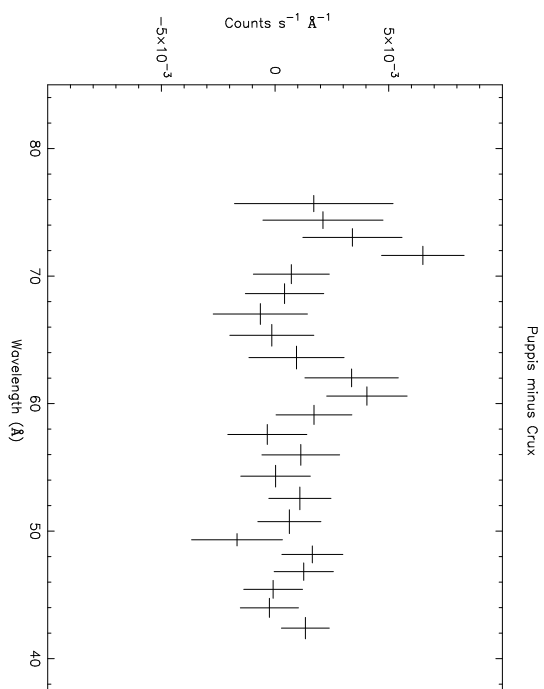
Figure 108: Puppis minus Crux
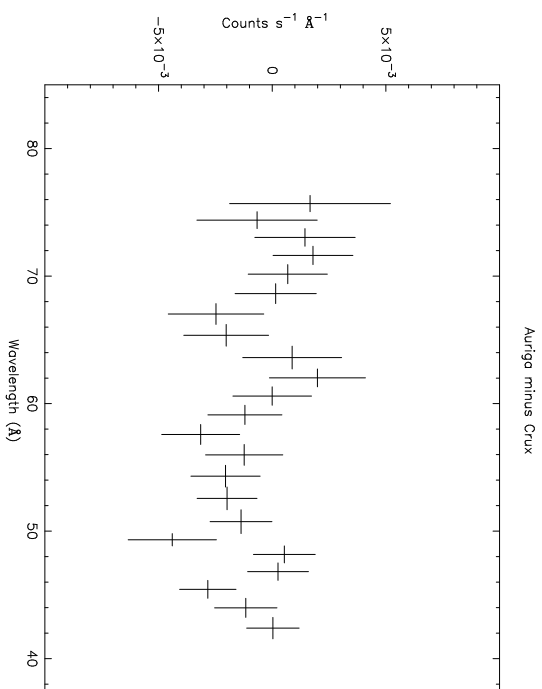
Figure 109: Auriga minus Crux
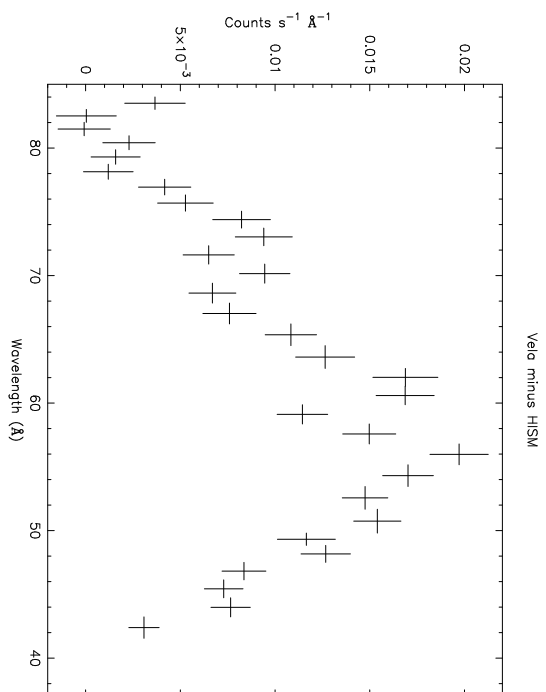
Figure 110: Vela minus HISM
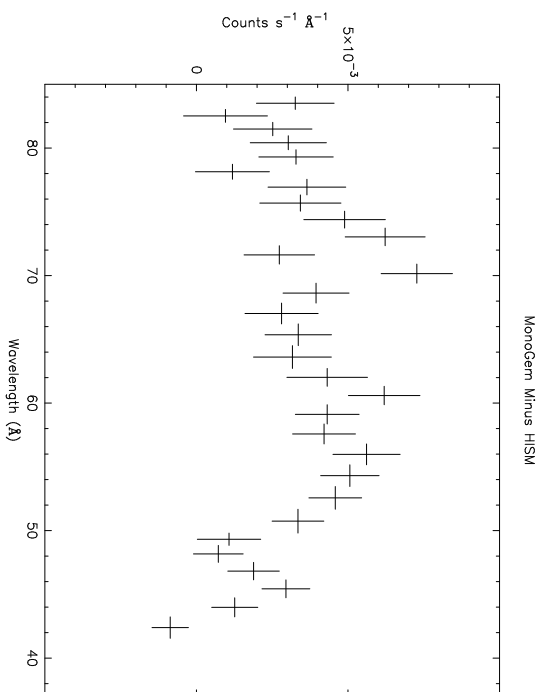
Figure 111: MonoGem minus HISM

spectra from the same region on the sky, the contamination is shown not to significantly affect the overall shape of the spectra (§5.7.2).

Section 5.7.3 compares the spectra from the regions of the sky typical of the diffuse X-ray background (Crux, Puppis, and Auriga), and concludes that there is no statistically significant shape difference between these spectra. The spectra from these regions have therefore been added together to form a single typical spectrum of the hot interstellar medium (HISM), which is shown in Figure 101. Because of contamination by the transient source (LTE or otherwise), the average count rate in the HISM spectrum is probably high by $\sim$10%, but the spectral shape is probably not significantly affected. The average ROSAT C–band surface brightness rate in the region covered by the HISM spectrum is 460 counts s^{-1} arcmin^{-2}.

Chapter 6

Astrophysical Analysis

This chapter discusses the scientific analyses of the X-ray spectra obtained by DXS. Following the results of the previous chapter, it is reasonable to assume that the DXS spectrum shown in Figure 101 is typical of emission from the Hot Interstellar Medium (HISM), at least in the region observed near the Galactic Plane. Chapter 3 presents evidence that the model of the instrument response is accurate, particularly in wavelength scale (see Figure 63). However, the instrument response matrix is not diagonal, so inverting the response and finding a unique solution for the input spectrum is not possible. Instead, a program called XSPEC (Arnaud 1996) was used to generate spectra from astrophysical models which were then folded through the instrument response matrix and compared with the measured spectrum. The astrophysical models had free parameters, such as power-law index, temperature, and emission measure (see following sections). XSPEC adjusts these variable parameters using a Levenberg-Marquardt minimization algorithm (Bevington 1969) to find the minimum in the χ^2 between the model and data spectra. XSPEC is maintained and distributed by the High Energy Astrophysical Science Archive Research Center (HEASARC), at NASA's Goddard Space Flight Center (http://heasarc.gsfc.nasa.gov/).

Section 6.1 shows how a power law, which is used to approximate synchrotron emission and inverse Compton scattering, does not fit the data well. This confirms the hypothesis of Williamson *et al.* (1974), summarized in §1.2, that these processes are unlikely to be the primary source of X-ray photons in the diffuse X-ray background. This is an important result of the DXS experiment. According to Williamson *et al.*, the most likely source of the diffuse X-ray background is hot gas in the interstellar medium. The rest of the models considered in this chapter are based on this hypothesis. Section 6.2 discusses equilibrium plasma emission models and §6.3 discusses non-equilibrium models. A multi-component model is considered in §6.4.

Unfortunately, none of the astrophysical models considered thus far fit the DXS data. As discussed in §6.2.4, the primary reason for poor fits is incomplete atomic emission spectra that

are used as inputs to the astrophysical models. In the absence of a good astrophysical model, up-to-date single-ion atomic spectra from Liedahl (1997) have been compared to the data in order to obtain upper limits on the *partial emission measure* for each of the ions likely to be contributing to the spectrum recorded by DXS. Partial emission measure is defined in § 6.5 by Equation 6.14. The results of these calculations are given in Table 27 and can be used for quick comparison to future theoretical work.

6.1 Power Law Model: Non-Thermal Processes

A convincing case for the need to include emission lines in the spectrum of the diffuse X-ray background can be made by fitting a power law of the form $A(E) = K(E/1keV)^{-\alpha}$ photons cm^{-2} s^{-1} keV^{-1} sr^{-1} to the DXS data. The power law model is a good approximation to non-thermal continuum processes, such as synchrotron emission or inverse Compton scattering, which were eliminated on the basis of astrophysical arguments summarized in §1.2 (Williamson *et al.* 1974). Indeed, the best fit power law model (convolved with the "model 16" DXS response matrix), shown as the solid line in Figure 112 does not describe the DXS HISM spectrum, shown as the points with error bars. The photon index (α) of the best-fit power law is 3.2±0.1 and the normalization is 1.1±0.2 photons cm^{-2} s^{-1} keV^{-1} sr^{-1}. The reduced χ^2 of the fit is 3.7, which translates into a probability of 1×10^{-19} that the model and spectrum are drawn from the same parent population. This suggests that emission lines are necessary to fully describe the DXS spectrum.

6.2 Equilibrium Plasma Emission Models

Low resolution spectral observations of the diffuse X-ray background (McCammon *et al.* 1983; Marshall & Clark 1984; Garmire *et al.* 1992) are consistent with emission from a plasma in thermal equilibrium at ~10^6 K as calculated by Raymond & Smith (1977). However, these observations have very poor spectral resolution and do not preclude non-thermal emission mechanisms (McCammon & Sanders 1990). As shown above, DXS has adequate spectral resolution to rule out the non-thermal processes. This section presents the fits of several thermal equilibrium plasma models to the DXS HISM spectrum.
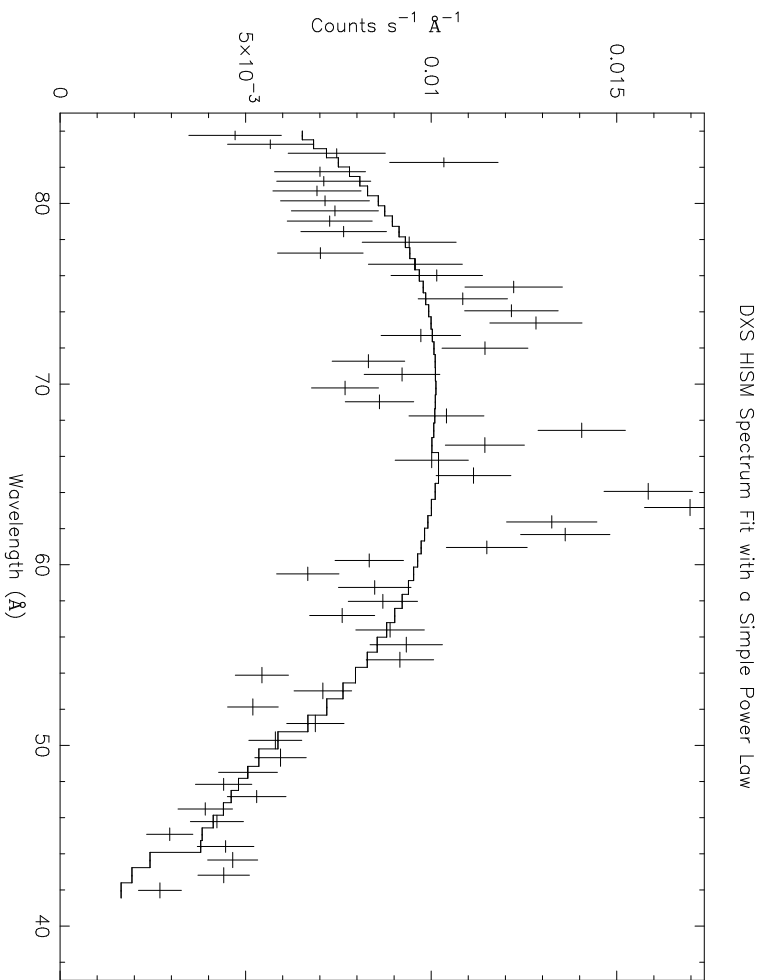
Figure 112: Power law spectrum fit to the DXS HISM spectrum. The reduced χ^2 of the fit is 3.7 and the χ^2 probability is 1×10^{-19}.

6.2.1 General Considerations

As discussed in §1.3 and §1.4, the Sun appears to be embedded in a region of the Galaxy relatively free from neutral material, called the "Local Bubble." Cox & Reynolds (1987) argue that this bubble is filled with gas at $\sim 10^6$ K with a density of $\sim 5 \times 10^{-3}$ cm^{-3}. Cox & Reynolds also argue that the bubble is about 10^7 years old and the gas is near thermal equilibrium. At this temperature, hydrogen and helium, the dominant elements in interstellar material (e.g. Anders & Grevesse 1989), are fully ionized. Most other elements present in the interstellar medium are partially ionized. The temperature and density are such that the electrons scatter elastically from each other and the protons but do not radiate much of their energy in the form of Bremsstrahlung. Instead, radiative cooling dominates. Radiative cooling occurs when inelastic collisions between electrons and ions excite the ions. The time between collisions is long, so the most probable method of de-excitation is photon emission. Also, because the plasma density is low, it is optically thin, so most of the photons escape. Thus, energy is pumped out of the plasma in the form of atomic emission lines.

Because the process of radiative cooling depends on the collision of electrons and ions, the energy radiated in an atomic line of a particular ionic species is proportional to the product of the number density of the electrons n_e and ions of that species, n_{ion}:

$$line \; emissivity \left(\frac{\mathrm{erg}}{\mathrm{cm^3 \; s}} \right) = \Lambda_{ion}(T, \lambda) n_e n_{ion}. \qquad (6.1)$$

$\Lambda_{ion}(T, \lambda)$, the constant of proportionality, is determined by the detailed physical processes of excitation and emission of the ion in question.

In equilibrium, the rate of ionization is balanced by the rate of recombination. Thus, at a given temperature, it is possible to calculate the fraction of each atomic species j in a given ionization state i. Call this fraction F_{ji}. The density of each atomic species j can be expressed as a fraction of the density of hydrogen at that location, A_j. Thus, the total emissivity of the plasma due to atomic emission can be written:

$$total \; emissivity \left(\frac{\mathrm{erg}}{\mathrm{cm^3 \; s}} \right) = \sum_{ji} A_j F_{ji} \Lambda_{ji}(T, \lambda) n_e n_H. \qquad (6.2)$$

The two plasma codes discussed in the next two section use different methods for calculating the F_{ji} and $\Lambda_{ji}(T, \lambda)$. What follows is a discussion of geometry and units which make explicit the definitions of the normalization constants used in these sections.

The total amount of energy radiated by a plasma is the integral of Equation 6.2 over the volume of the plasma. Let

$$\Lambda(T) = \int \sum_{ji} A_j F_{ji} \Lambda_{ji}(T, \lambda) d\lambda. \tag{6.3}$$

Thus,

$$total\ energy\ radiated \left(\frac{\text{erg}}{\text{s}} \right) = \int \int \Lambda(T) n_e n_H dV. \tag{6.4}$$

Now consider a plasma in which the temperature and abundances are constant throughout, so $\Lambda(T)$ can be brought out of the integral. The total flux of radiation received by an observer at the origin from such a plasma is:

$$flux \left(\frac{\text{erg}}{\text{cm}^2 \text{s}} \right) = \frac{\Lambda}{4\pi} \int \frac{1}{r^2} n_e n_H dV, \tag{6.5}$$

where r is the distance from the observer to volume element dV.

For many plasma sources, such as stars, compact objects, and distant supernova remnants, r does not change much over the integral, so it can be brought out of the integral as D, the distance to the source. Thus, Equation 6.5 can be written:

$$point\ source\ flux \left(\frac{\text{erg}}{\text{cm}^2 \text{s}} \right) = \frac{\Lambda}{4\pi D^2} \int n_e n_H dV. \tag{6.6}$$

The default plasma emission models provided with program XSPEC, several of which are used in this work, assume a point source flux of the form in Equation 6.6. The normalization constant, K, of these models is defined as:

$$K = \frac{10^{-14}}{4\pi D^2} \int n_e n_H dV. \tag{6.7}$$

where the factor of 10^{-14} is an arbitrary scaling factor. The units of K are cm^{-5}.

For diffuse interstellar plasmas, the point source approximation to Equation 6.5 is not appropriate. Rather, it is convenient to express dV in spherical coordinates: $dV = r^2 dr d\Omega$. Thus,

$$diffuse\ source\ flux \left(\frac{\text{erg}}{\text{cm}^2 \text{s}} \right) = \frac{\Lambda}{4\pi} \int n_e n_H dr d\Omega. \tag{6.8}$$

Assuming the diffuse plasma is uniform over the field of view, both sides of Equation 6.8 can be divided by solid-angle, Ω, resulting in:

$$diffuse\ source\ intensity \left(\frac{\text{erg}}{\text{cm}^2\ \text{s}\ \text{sr}}\right) = \frac{\Lambda}{4\pi}\int n_e n_H dr. \tag{6.9}$$

The factor $\int n_e n_H dr$ (cm^{-5}), is a measure of the emission of the diffuse plasma and so it is called the *emission measure*. Diffuse source emission measure is more commonly defined as:

$$emission\ measure = \int n_e^2 dl, \tag{6.10}$$

where n_e is expressed in units of cm^{-3} and dl, the distance along the line of sight from the observer, in units of parsecs (1 parsec = 3.085678×10^{18} cm). Thus, the units of emission measure defined in this way are cm^{-6} pc. In a plasma such as the HISM, where helium is fully ionized, $n_e = 1.194n_H$ (Anders & Grevesse 1989). Thus:

$$\int n_e n_H dr = 2.58432 \times 10^{18} \int n_e^2 dl, \tag{6.11}$$

Writing Equation 6.7 in a form suitable for diffuse sources yields:

$$K = \frac{10^{-14}}{4\pi} \int n_e n_H dr. \tag{6.12}$$

Substituting Equation 6.11 and solving for $\int n_e^2 dl$ results in:

$$\int n_e^2 dl\ (emission\ measure) = \frac{K}{2056}, \tag{6.13}$$

which is the formula used to convert XSPEC normalization constants to emission measure, as defined in Equation 6.10.

6.2.2 Raymond and Smith (1977 & 1993) Plasma Code

J. Raymond and B. Smith wrote a computer program that calculates the spectrum of a thin, diffuse plasma in thermal equilibrium (Raymond & Smith 1977). First, the computer code calculates ionic fractions, F_{ji} in Equation 6.2, by balancing the rate of collisional ionization with recombination. The F_{ji} depend on the temperature of the plasma and the ionization and recombination cross-sections of the ions. Next, the code calculates the $\Lambda_{ji}(T, \lambda)$, which can be thought of as single ion spectra (per hydrogen atom, per electron), from collisional excitation cross sections and oscillator strengths. As better data on the ionization cross-sections

Raymond and Smith Equilibrium Plasma Model
Best Fit Single Temperature Solar Abundance
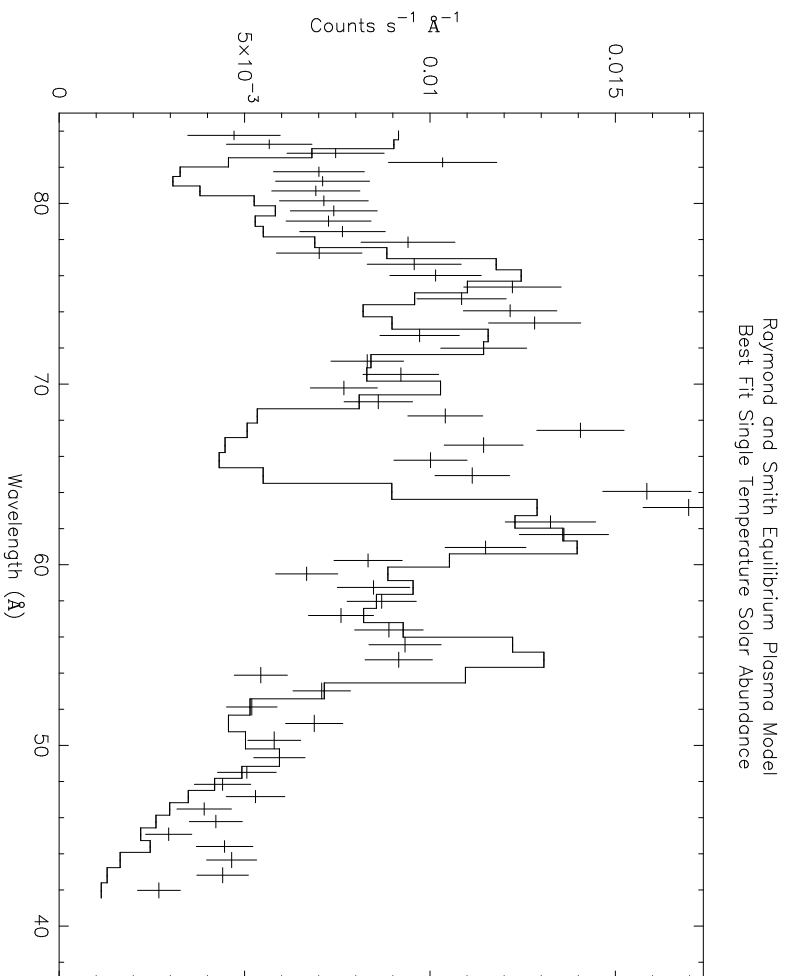
Figure 113: DXS HISM spectrum best fit to a single temperature Raymond and Smith (1993 code version) equilibrium plasma model, solar abundances (Anders & Grevesse 1989) at $1.1 \pm 0.1 \times 10^6$ K. $\chi_\nu = 9.5$, χ^2 probability is negligible.

and emission spectra have become available, the Raymond & Smith computer code has been updated. The most recent update of the code was in 1993 and will hereafter be referred to as "RS93." A sample equilibrium plasma emission spectrum unconvolved with any instrument response function is shown in Figure 1.

The DXS HISM spectrum has been fit using the RS93 model. The elemental abundances (A_j of Equation 6.2) were set according to Anders & Grevesse (1989) "solar abundances." Figure 113 shows the best-fit model, convolved with the "model 16" DXS response matrix, as a solid line. The best fit parameters are shown in the "Solar Abundance" column of Table 19.

The solar abundance RS93 model does not fit the DXS spectrum well. The reduced χ^2 of the fit is 9.5. The probability that these data are drawn randomly from a population whose mean values are the model spectrum is significantly less than 10^{-49}. Even the power law spectrum shown in §6.1 fits the data better.

Table 19: Raymond and Smith Equilibrium Plasm Model (1993) fit to HISM spectrum. Abundances are fraction of Solar (Anders & Grevesse 1989). Abundances of elements not listed were frozen at solar values. The fit is particularly sensitive to Si abundance as shown between variable abundance cases 1 and 2.

Parameter	Solar	Variable (1)	Variable (2)
Temperature ($\times 10^6$ K)	1.11±0.01	1.30±0.03	1.23±0.02
Mg Abundance	1	0.28±0.06	3.9±0.4
Si Abundance	1	0 (free)	1 (fixed)
S Abundance	1	0.05±0.02	0.2±0.2
Ar Abundance	1	0.38±0.12	6.3±0.9
Fe Abundance	1	0.04±0.02	0.9±0.1
Emission measure ($\times 10^{-3}$ cm^{-6} pc)	2.91±0.06	16.7±0.9	2.6±0.2
χ^2	541	158	351.6
Degrees of Freedom	57	52	53
χ_ν^2	9.5	3.1	6.6
χ^2 probability	$<10^{-49}$	1.2×10^{-12}	1.4×10^{-45}

What is wrong? The data and the RS93 model spectrum show spectral features, but the RS93 spectral features do not line up with the data's spectral features. In particular there is a pronounced gap in the RS93 model at ~66 Å, where the DXS spectrum clearly shows emission. Figure 63 shows that we can rule out the possibility that the instrument response function is incorrect by this much. Chapter 5 shows that, though the overall counting rate in the first half of the flight was ~15% higher than the counting rate in the second half of the flight, the first and second half HISM spectra are not significantly different if normalized to the same count rate. Furthermore, § 5.4 demonstrated that the DXS counting rate in the HISM regions is within 20% of the rate predicted by the ROSAT all-sky survey, thus ruling out the possibility that the emission observed by DXS is dominated by some source other than the X-ray background. Therefore we conclude that *the DXS spectrum of the hot interstellar medium is not well described by the Raymond & Smith equilibrium plasma emission model assuming solar abundances.*

The RS93 model fits the DXS data better if the abundances of the individual elements in the emitting plasma are allowed to vary as free parameters. Some variation in elemental abundances is expected because the presence of interstellar dust grains. Interstellar dust causes

the spectral reddening of stars at optical wavelengths. Spectral reddening in stars has been correlated with the depletion of certain elements, such as Si, Mg, and Fe. Sofia, Cardelli, & Savage (1994) report recent results on this topic. Dust is often detected around massive stars that produce large stellar winds. These stars are often precursors to supernova explosions, which, by energy considerations (McKee & Ostriker 1977), are the most likely source for the hot gas in the interstellar medium. So, the presence of dust, and hence depletion in a 10^6 K plasma is not unexpected (Smith 1996).

Thus, a fit was tried allowing *all* elemental abundances to vary. The result is that only the abundances of Si, S, Mg, Ar, and Fe were well constrained. It is not surprising that the fit is sensitive to these particular elements since, as will be shown in §6.5, certain ionization states of Si, S, Ne, Mg, and Fe are the significant contributors to the equilibrium plasma emission spectrum at 10^6 K. The lowest reduced χ^2 values are achieved if the abundance of Si is allowed to drop to zero. The solid line in Figure 114 shows the result of this fit. The parameter values are shown in the "Variable (1)" column of Table 19. Abundances that were not constrained were set to solar values. Even though the fit is a significant improvement from the RS93 solar abundance case, the χ^2 probability of 1.2×10^{-12} indicates that the variable abundance RS93 model is not a good description of the data. Furthermore, a Si abundance value of 0 is most likely unphysical. In order to ascertain the sensitivity of the RS93 parameters to the Si abundance value, the Si abundance was frozen at several values between 0 and 1 and the data re-fit. As the Si abundance is increased, the emission measure drops, the Mg abundance increases dramatically. The fit with the Si abundance value frozen at 1 is shown as the dotted line in Figure 114. The parameter values of this fit are given in the "Variable (2)" column of Table 19.

Figure 115 shows the predicted pulse height distributions of both of the variable abundance RS93 models. In the primary DXS pass band (150 eV–284 eV), the predicted pulse height distributions are nearly identical. The dramatic difference between the emission measures of the models is seen almost entirely at energies above 300 eV. Note that both models fall below the data in this energy regime. This is because above 500 eV, extragalactic sources and the Galactic halo begin to dominate the diffuse X-ray background. Section 6.4 presents a model which includes these sources.
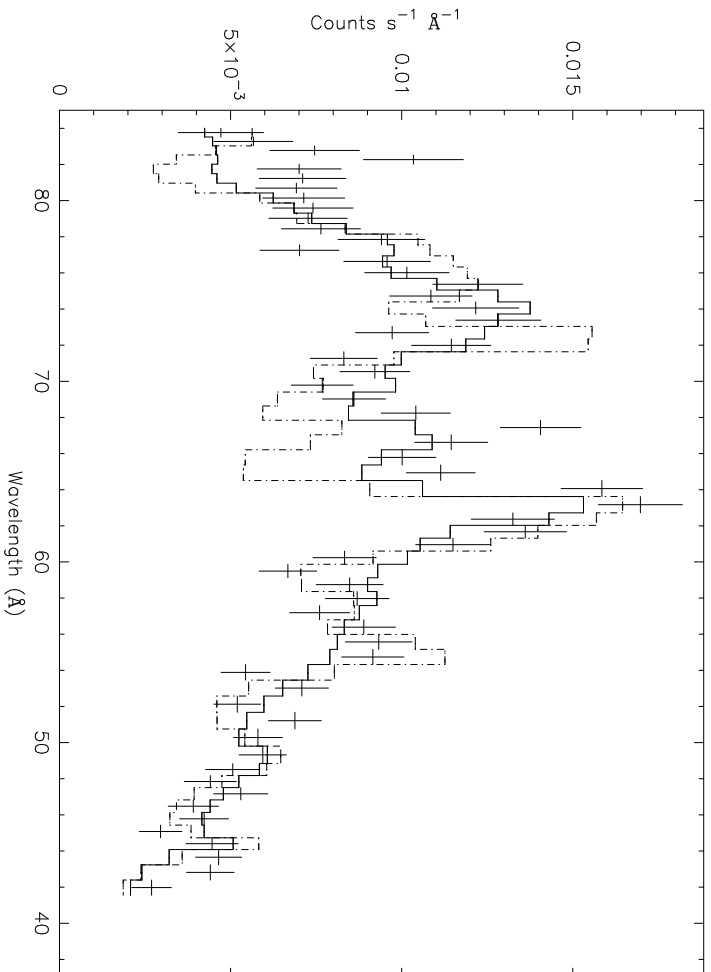
Figure 114: DXS HISM spectrum showing the fits by single temperature Raymond and Smith (1993 version) equilibrium plasma models. Solid line is fit allowing abundances of Si, S, Mg, Ar, and Fe to vary. Dotted line is fit with the same variable parameters, except the Si abundance is frozen at its solar value. Parameter values are given in Table 19.
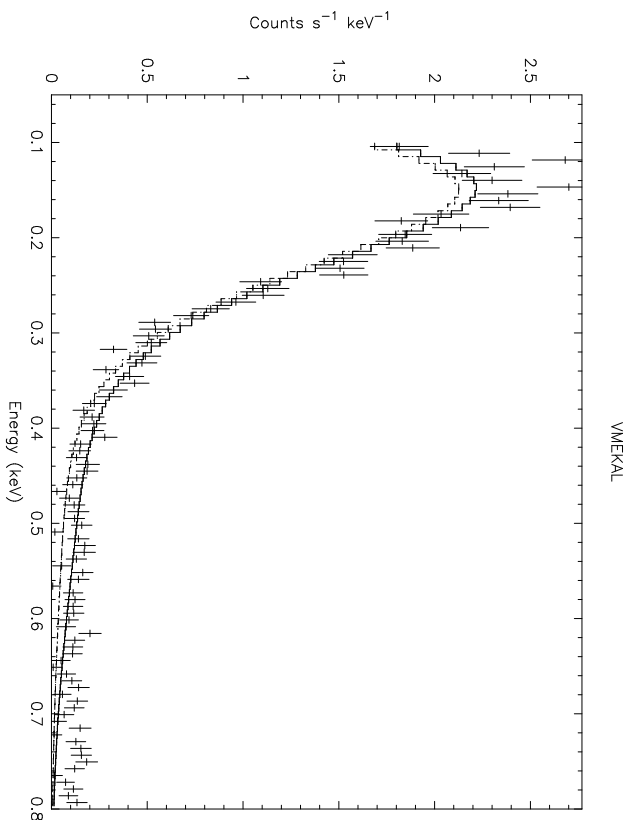
Figure 115: DXS HISM pulse height spectrum with predicted pulse height spectra from RS93 models shown in Figure 114.

6.2.3 Mewe and Kaastra (1985 & 1992) Plasma Code

Mewe, Gronenschild, & van den Oord (1985) have written a plasma emission code that produces different results from the Raymond & Smith (1977) code. J. S. Kaastra updated the Mewe, Gronenschild, & van den Oord code in 1992 (Kaastra 1992) and more recently, values for the Fe L lines, calculated by D. Liedahl, have been added. The resulting model is available in XSPEC version 9.00 as "MEKAL" (solar abundance) or "VMEKAL" (individually variable abundances).

Mewe, Gronenschild, & van den Oord (1985) use a similar approach to Raymond & Smith in calculating the emission from a hot plasma in equilibrium. First, the equilibrium ionization balance is calculated (the F_{ji}), then the X-ray spectrum is constructed from the individual ionic spectra, $\Lambda_{ji}(T, \lambda)$. The Mewe et al. code uses the equilibrium ionization balance calculations of Arnaud & Rothenflug (1985) (hereafter AR85). The AR85 calculations make use of different approximations for the ionization and recombination cross-sections, thus the equilibrium ion fractions of AR85 differ significantly from those of RS93 for the same temperature,

VMEKAL

Counts s^{-1} keV^{-1}

Energy (keV)

as shown in Table 20. For the ions thought to significantly to emission in the DXS passband, the AR85 calculations predict lower ionization fractions for the highly ionized states and higher ion fractions for the less ionized states. The Mewe, Gronenschild, & van den Oord and Raymond & Smith codes also differ in the treatment of multiplet and satellite emission lines (Raymond 1988).

Using Anders & Grevesse (1989) solar abundances, the MEKAL model fits slightly better than the RS93 solar abundance model ($\chi_\nu^2 = 9.3$). Figure 116 shows the model compared to the data. Note that the MEKAL model does not have as pronounced a gap at ~ 66 Å as the RS93 does, presumably because the MEKAL code includes more satellite emission lines. Also, the brightest peaks, caused by emission primarily from Fe and Mg ions, are much sharper than in the RS93 case. In spite of these differences, the best-fit plasma temperature and emission measure, given in the MEKAL column of Table 21 are similar to those of the RS93 solar abundance case.

When the abundances of all the elements are allowed to vary as free parameters (VMEKAL), only the abundances of Ne, Si, S, Mg, Ar, and Fe were well constrained, which is similar to the RS93 case. The fit allowing only these abundances and the temperature and normalization to vary as free parameters is shown as the solid line in Figure 117. The "Variable(1)" column of Table 21 shows the parameters of this fit. The VMEKAL model exhibits a sensitivity to the abundance of S that is very similar to the sensitivity of the RS93 model to Si. The dotted line in Figure 117 and the "Variable(2)" column of Table 21 shows the results of the fit when the S abundance is fixed at its solar value. The pulse height spectra predicted by these models are shown in Figure 118. Note that the poor agreement of the "Variable(2)" model at low energies is also reflected in the pulse height data.

In spite of the improvement in reduced χ^2 of the VMEKAL equilibrium plasma model over the RS93 model, the lowest χ^2 probability that the VMEKAL model and the DXS HISM data are drawn from the same population is 1.1×10^{-7}, is still too low to be formally a good fit. Furthermore, this fit requires the abundance of S to be negligible, which is likely to be unphysical.

172

Table 20: Comparison of the RS93 and AR85 ion fractions at $T = 10^6$ K.

Ion	RS93 Ion Fraction $T = 10^6$ K	AR85 Ion Fraction $T = 10^6$ K	Ratio RS93/AR85
Si XII	1.04×10^{-3}	7.08×10^{-5}	14.69
Si XI	2.38×10^{-2}	6.31×10^{-4}	37.72
Si X	1.90×10^{-1}	1.12×10^{-2}	16.93
Si IX	4.30×10^{-1}	1.51×10^{-1}	2.84
Si VIII	2.96×10^{-1}	4.37×10^{-1}	0.68
Si VII	5.64×10^{-2}	3.39×10^{-1}	0.17
Si VI	3.25×10^{-3}	6.17×10^{-2}	0.05
S XII	6.11×10^{-4}	2.29×10^{-6}	266.71
S XI	2.08×10^{-2}	3.98×10^{-4}	52.25
S X	1.88×10^{-1}	1.86×10^{-2}	10.10
S IX	4.53×10^{-1}	2.40×10^{-1}	1.89
S VIII	2.92×10^{-1}	4.79×10^{-1}	0.61
S VII	4.49×10^{-2}	2.40×10^{-1}	0.19
Ne VIII	6.74×10^{-2}	9.33×10^{-1}	0.07
Mg X	2.08×10^{-1}	2.09×10^{-1}	1.00
Mg IX	3.48×10^{-1}	2.24×10^{-1}	1.55
Mg VIII	2.24×10^{-1}	2.51×10^{-1}	0.89
Mg VII	4.65×10^{-2}	2.40×10^{-1}	0.19
Mg VI	2.84×10^{-3}	6.76×10^{-2}	0.04
Fe XVI	2.49×10^{-7}	0	–
Fe XV	2.96×10^{-5}	1.55×10^{-7}	191.11
Fe XIV	9.92×10^{-4}	1.15×10^{-5}	86.40
Fe XIII	1.01×10^{-2}	3.63×10^{-4}	27.82
Fe XII	5.37×10^{-2}	6.61×10^{-3}	8.13
Fe XI	2.36×10^{-1}	3.63×10^{-2}	6.50
Fe X	2.68×10^{-1}	1.41×10^{-1}	1.90
Fe IX	3.50×10^{-1}	2.69×10^{-1}	1.30
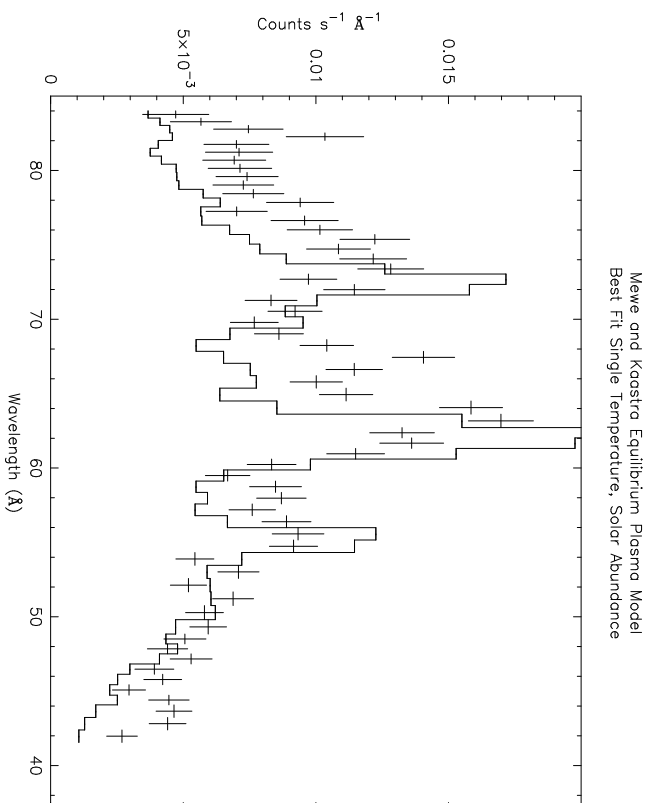
Figure 116: DXS HISM spectrum fit to a solar abundance (Anders & Grevesse 1989) single temperature Mewe and Kaastra equilibrium plasma model (MEKAL). Best fit parameters are given in Table 21.
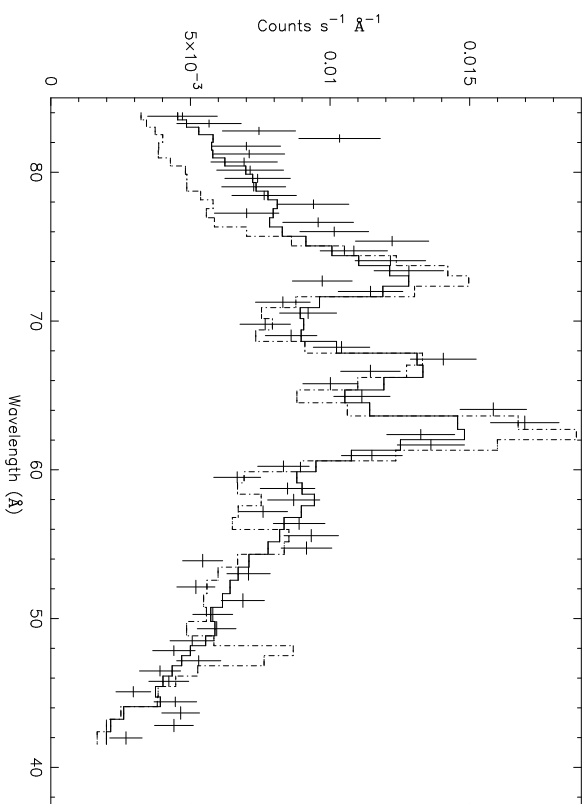
Figure 117: DXS HISM spectrum fit showing fits by single temperature Mewe and Kaastra equilibrium plasma models (VMEKAL). Solid line is fit allowing abundances of Ne, Si, S, Mg, Ar, and Fe to vary. Dotted line is fit with the same variable parameters, except the S abundance is frozen at its solar value. Best fit parameters are given in Table 21.

Table 21: Mewe and Kaastra equilibrium fit to HISM spectrum. Abundances are fraction of Solar (Anders & Grevesse 1989). Abundances of elements not listed were frozen at solar values. Fit is particularly sensitive to S abundance as shown between variable abundance cases 1 and 2.

Parameter	Solar	Variable (1)	Variable (2)
Temperature $(\times 10^6$ K)	1.23±0.02	1.27±0.05	1.31±0.03
Ne Abundance	1	0.5±0.1	2.8±0.4
Mg Abundance	1	0.09±0.03	0.5±0.08
Si Abundance	1	0.008±0.01	0.16±0.03
S Abundance	1	0.00±0.09	1 (fixed)
Ar Abundance	1	0.2±0.1	0 (free)
Fe Abundance	1	0.05±0.01	0.21±0.03
Emission measure $(\times 10^{-3}$ cm^{-6} pc)	3.24±0.05	21±1	8.4±0.5
χ^2	530	120	285
Degrees of Freedom	57	51	52
χ_ν^2	9.3	2.4	5.5
χ^2 probability	$<10^{-49}$	1.1×10^{-7}	1.1×10^{-33}
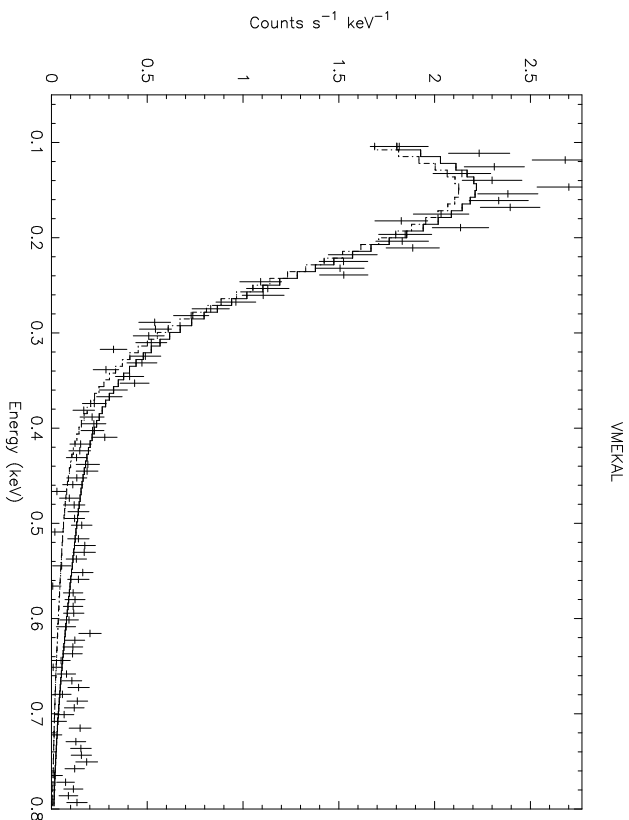
Figure 118: DXS HISM pulse height spectrum with predicted pulse height spectra from VMEKAL models shown in Figure 117.

6.2.4 Hybrid Raymond & Smith Model

Recent calculations of ionic spectra using the Hebrew University Lawrence Livermore Atomic Code (HULLAC; Klapisch 1971; Klapisch *et al.* 1977) by D. Liedahl find an order of magnitude more emission lines in the DXS pass-band than listed in the RS93 code (Liedahl 1997). In order to test the hypothesis that incomplete atomic physics calculations contribute to the poor fit in the RS93 model, R. J. Edgar of the University of Wisconsin, Madison (now at the Center for Astrophysics, Cambridge, Massachusetts) created a hybrid model using the RS93 equilibrium ionic concentrations as a function of temperature (F_{ij}) and Liedahl's ionic spectra, $\Lambda_{ji}(T, \lambda$ (see Equation 6.2). This model has been fit to the DXS HISM spectrum with fixed solar abundances (Allen 1973) and again with variable abundances. The best-fit models are shown as the solid lines in Figures 119 and 120. Figure 121 shows the predicted pulse height spectrum of the variable abundance hybrid model. Table 22 lists the best-fit parameters.

The variable abundance hybrid RS93 model fits the DXS HISM spectrum better than the other models considered here, though a χ^2 probability of 3.8×10^{-6} is still too low to be considered formally a good fit. The reduction in χ^2 of the variable abundance hybrid model

Hybrid Raymond and Smith Model
Best Fit Single Temperature, Solar Abundance
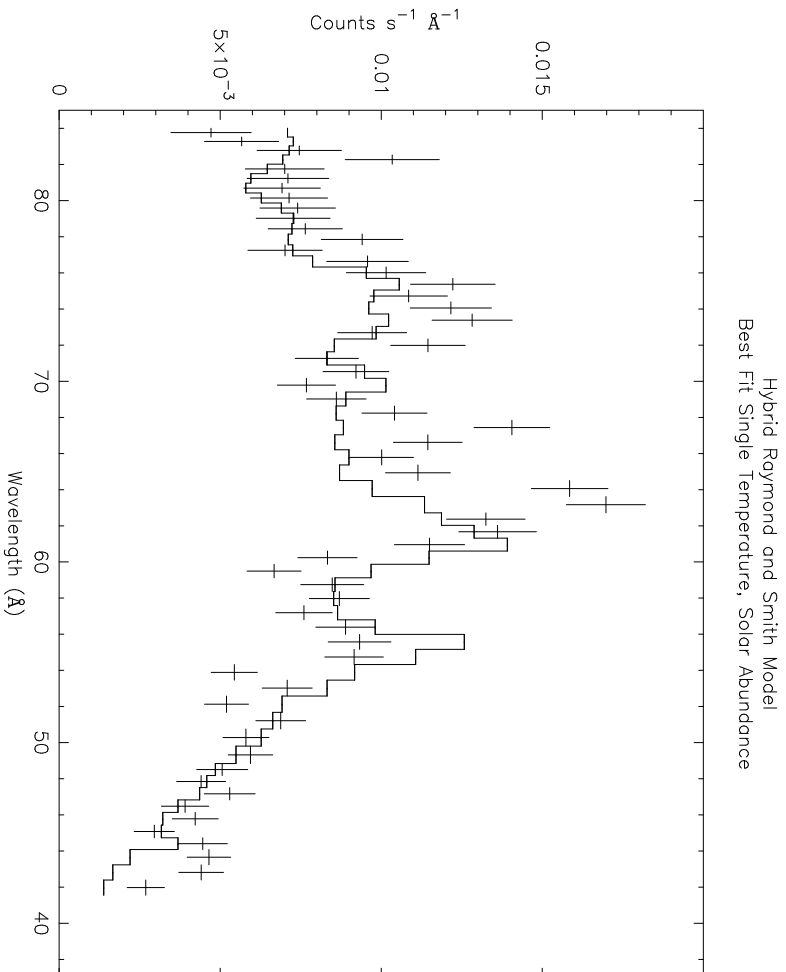
Figure 119: Hybrid RS93/Liedahl equilibrium model fit to HISM spectrum. Elemental abundances are fixed at solar values (Allen 1973).

(Figure 120) over the RS93 model (Figure 114) is evidence that the incomplete atomic emission line data in the RS93 code are the primary cause of the poor fit to the DXS data. As in the other models, one of the parameters, the abundance of Ni, is forced to zero by the fit, however, Ni is not a major contributor to the spectrum. Fixing the Ni abundance at its solar value raises the χ^2 to 111 and does not significantly change the other parameters.

6.3 Non-Equilibrium Plasma Models

As shown in §6.1, the features in the DXS HISM spectrum indicate the presence of lines. Section 6.2 shows that the current state of the art single-temperature equilibrium plasma models do not fit the DXS data well, even if elemental abundances are allowed to float. This section presents the fits of two particular non-equilibrium models to the DXS data.
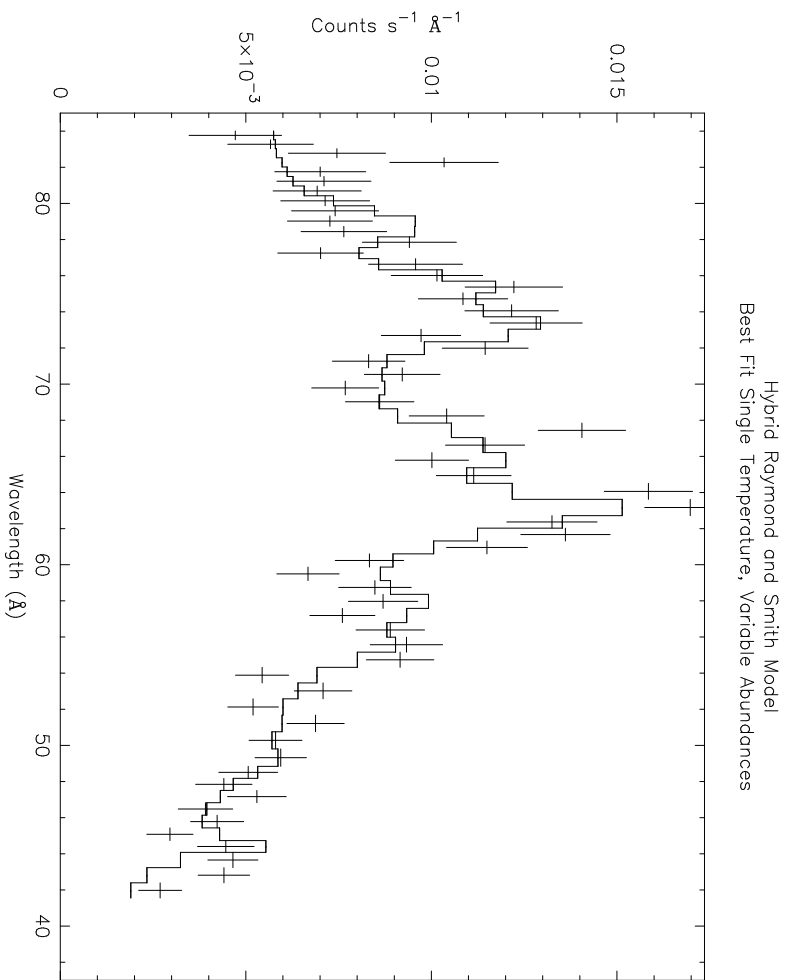
Figure 120: Hybrid RS93/Liedahl equilibrium model fit to HISM spectrum. Elemental abundances are fixed at solar values (Allen 1973) except for Mg, Si, S, Ar, Fe, and Ni, which were free parameters of the fit.
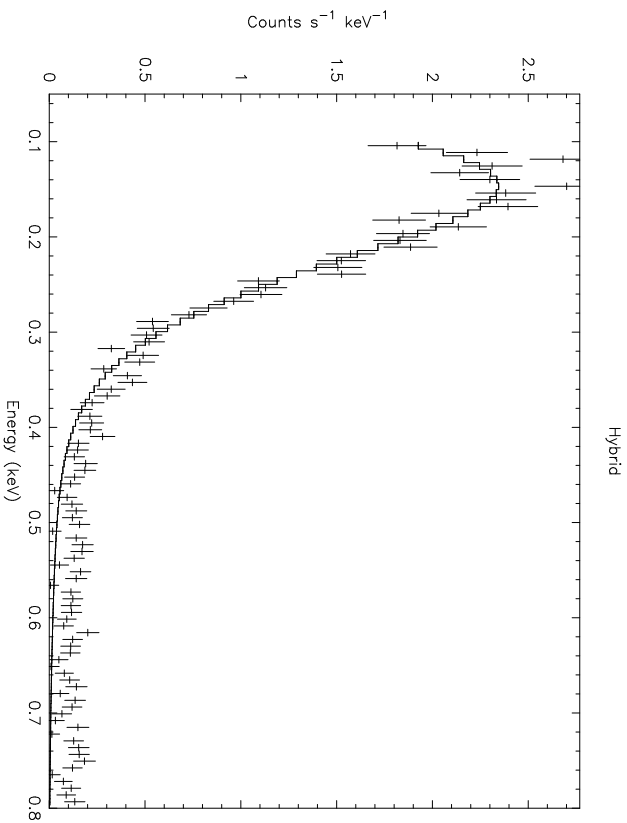
Figure 121: DXS HISM pulse height spectrum with predicted pulse height spectra from the hybrid RS93 model shown in Figure 120.

Table 22: Hybrid Raymond and Smith Equilibrium Model. Abundances are fraction of Solar (Allen 1973).

Parameter	Solar Abundances	Variable Abundances
Temperature ($\times 10^6$ K)	1.08 ± 0.03	1.23 ± 0.03
Mg Abundance	1	1.4 ± 0.4
Si Abundance	1	0.12 ± 0.07
S Abundance	1	0.03 ± 0.1
Ar Abundance	1	0.8 ± 0.3
Fe Abundance	1	0.1 ± 0.1
Ni Abundance	1	0 (free)
Emission measure (cm^{-6} pc)	$2.7 \pm 0.06 \times 10^{-3}$	$6 \pm 1 \times 10^{-3}$
χ^2	253	108
Degrees of Freedom	57	51
χ_ν^2	3.9	2.1
χ^2 probability	1.1×10^{-26}	3.8×10^{-6}

6.3.1 Smith and Cox (1998): Under-Ionized Plasma

The picture of the diffuse X-ray background discussed in §1.4 proposes that the Sun is inside a cavity, the "Local Bubble," which has been formed by one or more supernova explosions. Each supernova explosion shock heats the ambient gas in the interstellar medium and enlarges the boundary of the bubble. The equilibration time for the kinetic temperature in the gas is short compared to the ionization time, so the ionization state of the gas lags the kinetic temperature. Hence, the gas is said to be under-ionized. Edgar & Cox (1993) model the details of X-ray production in the single supernova explosion case and find that it is difficult to match observational parameters. Smith (1996) and Smith & Cox (2001) (hereafter SC98) have modeled emission from multiple supernova remnants. The supernova explosions are separated by a 1-2×10^6 years and the current epoch is 4-8×10^6 years after the first explosion. The models include thermal conduction in the gas, the effects of dust cooling and sputtering, and the possibility of spatially varying abundances. SC98 find that models consisting of two or three supernova explosions fit the Wisconsin all-sky survey B and C band rates (McCammon *et al.* 1983) and other observational parameters reasonably well.

Two of the more successful SC98 models have been fit to the DXS HISM data as shown in Figures 122 and 123. The models, as implemented here, have two free parameters: time since the first supernova explosion and an arbitrary normalization constant. The best-fit parameters and χ^2 values are shown in Table 23. Model A has two minima in χ^2 with significantly different parameter values. However, as shown in Figure 122, the resulting spectra are very similar.

The appearance and, unfortunately, goodness of fit of the SC98 models are similar to the equilibrium, solar abundance RS93 model shown in Figure 113, particularly the lack of emission near ~66 Å. This is because the atomic physics calculations used in the SC98 models are the same as those used in RS93. Also, several million years since the last explosion, the gas in the SC98 model is near equilibrium. Thus, it is possible that the poor fit of the SC98 models to the DXS data is due to the outdated atomic physics information used to generate the X-ray spectra and not any intrinsic shortfalls in the SC98 astrophysical model.

Smith & Cox Model A (Two Supernovae)

Counts s^{-1} Å^{-1}

Wavelength (Å)
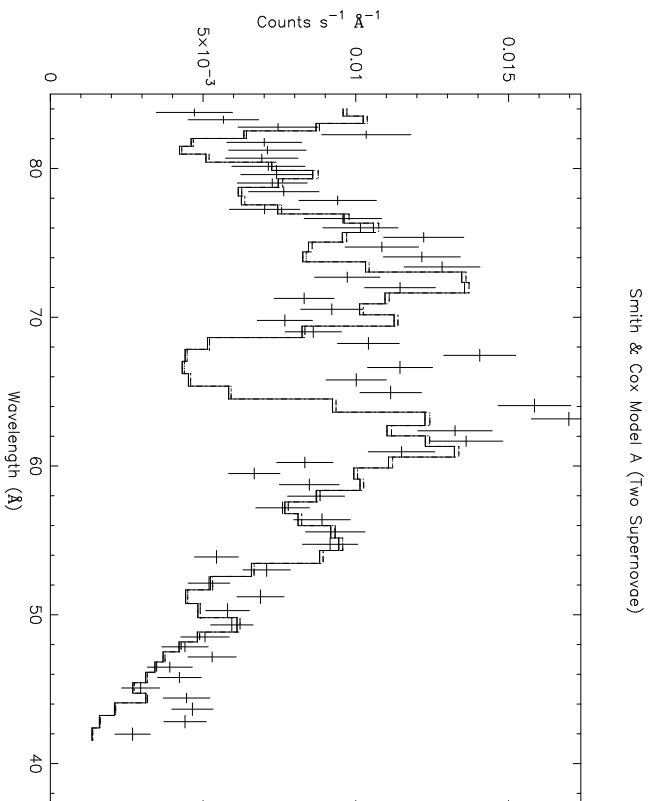
Figure 122: HISM spectrum fit with Smith and Cox (1998) model A. There are two χ^2 minima, one at $T = 3.6 \times 10^6$ yr (solid line) and one at 5.4×10^6 yr (dotted line).

Smith & Cox Model B (Three Supernovae)

Counts s^{-1} Å^{-1}

Wavelength (Å)
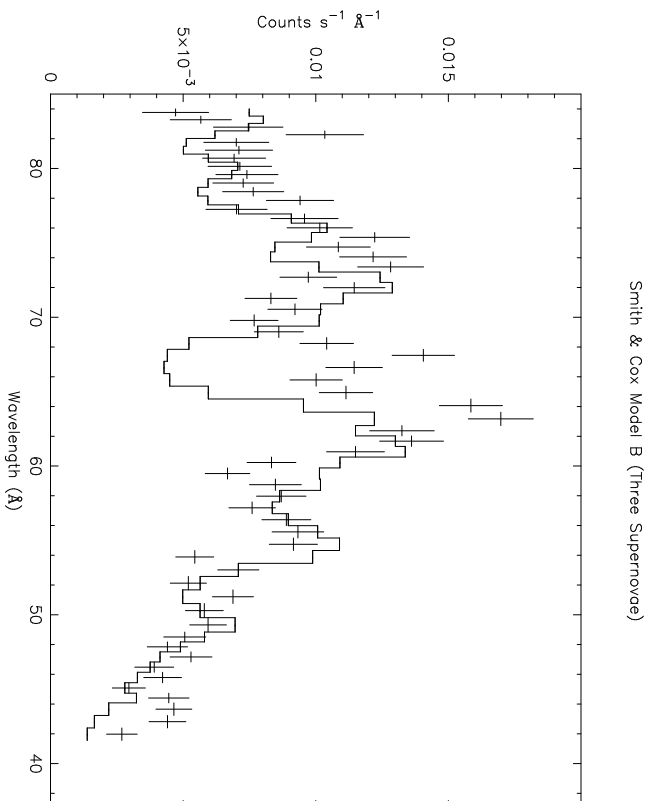
Figure 123: HISM spectrum with to Smith and Cox (1998) model B. The best fit time since the first supernova explosion is $T = 6.9 \times 10^6$ yr.

Table 23: Two Smith and Cox (1998) multiple supernova remnant models fit to HISM spectrum. The quantity $\beta_{Spitzer}$ is calculated in Spitzer (1956). The first supernova (SN) occurs at $T = 0$.

Parameter	Model A(1)	Model A(2)	Model B
Number of SN	2	2	3
T at 2nd SN ($\times 10^6$ years)	1	1	1
T at 3rd SN ($\times 10^6$ years)	-	-	3
Ambient n_H (cm^{-3})	0.2	0.2	0.4
Energy per Supernova ($\times 10^{51}$ ergs)	1	1	1
Magnetic Field (μGauss)	5	5	5
Thermal Conduction ($\beta/\beta_{Spitzer}$)	1/6	1/6	1/6
Best Fit T ($\times 10^6$ years)	3.6±0.3	5.4±0.8	6.9±0.2
Normalization (arbitrary)	6800±400	4000±1000	2500±100
χ^2	480	488	449
Degrees of Freedom	57	57	57
χ_ν^2	8.4	8.6	7.9
χ^2 probability	$<10^{-49}$	$<10^{-49}$	$<10^{-49}$

6.3.2 Breitschwerdt and Schmutzler (1994): Over-Ionized Plasmas

Breitschwerdt & Schmutzler (1994) (hereafter BS94) examine the results of the hypothesis that the local bubble is a cavity created by the stellar winds and supernova explosions of about 10 massive stars. They propose that the stars were initially embedded in a dense cloud, which allowed the bubble to reach a temperature of $\sim 10^7$ K. Next, the bubble "breaks out" of the dense cloud into a less dense medium and the $\sim 10^7$ K gas expands (and cools) adiabatically. Under these conditions, adiabatic cooling would dominate radiative cooling, therefore "freezing in" high ionization states. After about 4×10^6 years, the local bubble would reach its present size but, in contrast to the SC98 model, it would be filled with gas no hotter than 4×10^5 K. Furthermore, the X-ray spectrum of this gas consists almost entirely of recombination lines and recombination edges.

As a quick test of the BS94 model, R. J. Edgar of the University of Wisconsin, Madison (now at the Center for Astrophysics, Cambridge, Massachusetts) has written a program called `impulse`, which calculates the X-ray spectrum of a parcel of gas that is initially in collisional

equilibrium at a temperature, T_0. Instantaneously, the gas temperature is changed to a value, T_1. Given a fixed T_0, impulse uses the RS93 plasma emission code to calculate the X-ray spectrum emitted by the parcel of gas as a function of T_1 and fluence, $\int n_e dt$, where n_e is the electron density in the plasma and the integral is from instantaneous change in temperature to the present. The units of fluence are cm^{-3} s.

Using values for the initial and final gas temperature that were found by the BS94 model and allowing the fluence and normalization to vary, the impulse program produces spectra that are qualitatively similar to the spectrum shown in Figure 2b of the BS94 paper, but differ in detail. In particular, the shape of the impulse spectrum in the primary DXS pass-band differs from the shape of the BS94 spectrum. However, both the impulse and BS94 spectra have strong recombination features at energies above 300 eV resulting from the high ionization state of the gas. Such strong features are not consistent with the DXS or Wisconsin all-sky survey data. For instance, if the fluence of the impulse model is adjusted so that the Wisconsin B-band (130–188 eV) and C-band data (160–284 eV) are well fit, the model predicts counting rates in the M$_1$ (440–930 eV) and M$_2$ (600–1100 eV) and J (1100–2200 eV) bands that are an order of magnitude higher than the observed count rates. This effect is also seen when comparing the impulse model to the DXS pulse height spectrum, as shown in Figure 124. The solid line of this Figure is the impulse model folded through the high gain DXS pulse height response matrix discussed in §3.1.4. The model predicts too much emission above 400 eV and too little emission below 400 eV.

As an experiment, the final temperature T_1 in the impulse model was allowed to vary in order to attempt to achieve better fits. Using XSPEC, the DXS HISM position and pulse height spectra were fit simultaneously. In order to reduce the effect of the recombination lines from high ionization states contributing in the 300~800 eV range, the fitting program lowered the overall normalization. To make up for the emission lost in the primary DXS pass-band, XSPEC raised the final temperature of the plasma, arriving at a best-fit value much closer to 10^6 K than the Breitschwerdt & Schmutzler model predicts. Final fit values are summarized in Table 24. The resulting model is compared to the DXS HISM position spectrum in Figure 125. The implications of the impulse experiment are that over-ionized plasma tend to produce too much emission in the 300-600 eV range due to strong recombination features.

HISM Pulse Height Spectrum
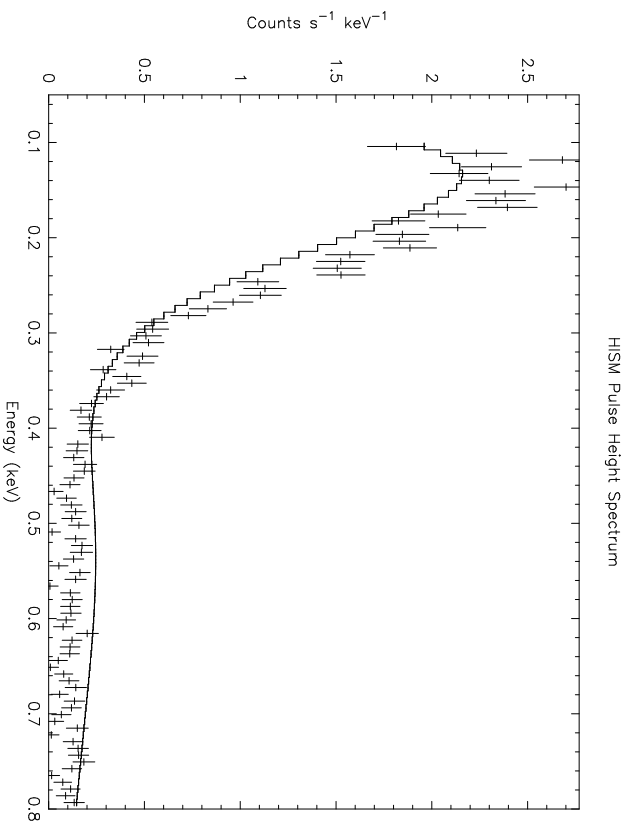
Figure 124: DXS HISM pulse height spectrum (data points with error bars) fit with an approximation to the BS94 over-ionized plasma model (solid line). In this fit, only the normalization was free to vary.

Table 24: Impulse model fit parameters. Best fit spectrum is shown in Figure 125.

Parameter	Value
Initial Temperature (T_0)	1.0×10^7 K
Final Temperature (T_1)	$6.72 \pm 0.06 \times 10^5$ K
Fluence (cm^{-3} s)	$1.82 \pm 0.03 \times 10^{11}$
Position Spectrum χ^2	391
Position Spectrum Degrees of Freedom	56
Position Spectrum χ_ν^2	7.1
χ^2 Probability	$<10^{-49}$
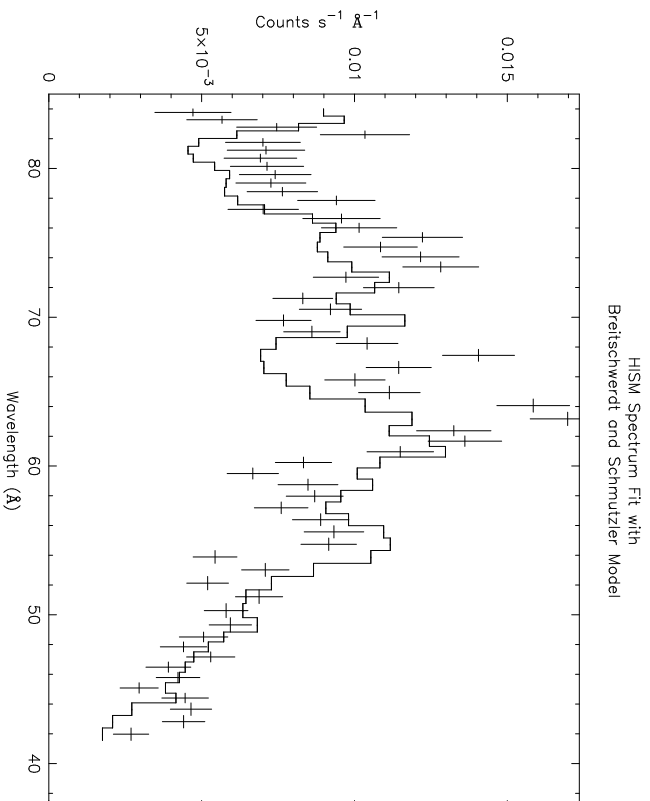
Figure 125: DXS HISM position spectrum fit by an approximation of the BS94 model. The final plasma temperature, T_1 and normalization were allowed to vary to achieve better fits to the data. The best fit value of the temperature is a factor of two higher than that predicted by the original Breitschwerdt and Schmutzler model.

6.4 Three-Component Model

The models discussed up to this point have been primarily concerned with the soft X-ray background below 284 eV. However, as shown by Figures 115, 118, and 121, the DXS pulse height distribution at energies between 300 eV and 800 eV are not well fit by the single temperature equilibrium plasma models discussed above. This is not surprising, since at these higher energies, extra-galactic sources and a mysterious source, possibly thermal in origin, begin to dominate (McCammon & Sanders 1990). This section describes a three-component model (extra-galactic power law, and two equilibrium plasma emission models at different temperatures) that has been simultaneously fit to the DXS position and pulse height spectra and the ROSAT all-sky survey data for the HISM region.

The contribution of extra-galactic sources to the diffuse X-ray background is discussed by Hasinger *et al.* (1993) using ROSAT observations in the direction of the lowest neutral hydrogen column density (the "Lockman Hole"). Hasinger *et al.* find that in the 0.5–2 keV range, at least 75% of the X-ray background at high Galactic latitudes can be resolved into discrete sources. These sources are thought to be active galactic nuclei, and therefore isotropic. Hasinger *et al.* have fit a power law to the photon spectrum of these sources which has the form $A(E) = KE^{-\alpha}$, where E is measured in keV, $K = 7.8$ keV^{-1} cm^{-2} s^{-1} sr^{-1}, and $\alpha = 1.9$.

Extra-galactic X-ray photons are absorbed by the neutral interstellar material in the Galaxy. The absorption cross-section varies as a function of energy and has been calculated by Balucinska-Church & McCammon (1992). In order to find the average column density of neutral material in the region of the sky observed by DXS, the DXS collimator pattern was "flown" across the 21 cm map of Dickey & Lockman (1990) using software similar to that described in §5.4. This software was also used to average each of the three ROSAT all-sky survey band maps in the regions observed by DXS. The average ROSAT counting rates and the HI column density are shown in Table 25. The ROSAT survey rates for the HISM region in Table 25 were converted into an XSPEC compatible spectrum. A ROSAT response matrix created by S. Snowden is used to compare model spectra to the ROSAT spectrum.

Figure 126 shows the Hasinger *et al.* power law model absorbed with the column density of neutral material found from the Dickey & Lockman survey (dotted lines) overlayed with the average ROSAT counting rates for the HISM region. As expected from previous results

Table 25: Average all-sky survey results by region. ROSAT C, M, and IJ rates have units of 10^{-6} counts s^{-1} arcmin^{-2}. The HI survey column densities have units of cm^{-2}.

Band Name	C	M	IJ	HI
Band Energy (keV)	1/4	3/4	1.5	
Allsky	748	184	168	3.13×10^{21}
HISM	450	124	146	3.26×10^{21}
Crux	370	198	219	5.75×10^{21}
Vela	1260	376	258	4.71×10^{21}
Puppis	486	120	129	2.50×10^{21}
MonoGem	653	111	135	2.21×10^{21}
Auriga	433	102	142	3.35×10^{21}

(McCammon & Sanders 1990), because the HISM region lies in the plane of the Galaxy, the absorbed extra-galactic spectrum falls short of the observed spectrum over the entire ROSAT pass band.

Section 6.1 argues that some form of thermal spectrum is needed to fit the DXS data. Initially a single MEKAL plasma model, similar to that described in §6.2.3, was added to the absorbed extra-galactic power law spectrum. The temperature and normalization of the MEKAL model were allowed to float as free parameters as the model was simultaneously fit to the ROSAT and DXS pulse height spectra and the DXS position spectrum for the HISM region. Satisfactory fits were not obtained: it was not possible to fit both the lower energy position data and the higher energy pulse height data.

In order to obtain a better fit for empirical comparison between the DXS and ROSAT pulse height spectra, a second thermal component was added to the model. The normalizations and temperatures of both equilibrium plasma models were allowed to float as the combined model was simultaneously fit to the ROSAT and DXS pulse height spectra and the DXS position spectrum. A solar abundance hybrid RS93 model was used for the lower temperature plasma model and the MEKAL model for the higher temperature model. Figure 127 shows the best fit model overlayed on the DXS and ROSAT pulse height spectra. Note the improved agreement between the model and measured DXS pulse height spectra over the single equilibrium plasma models shown in Figures 115, 118, and 121 for energies above 300 eV. Closer agreement in this energy range might be possible if the second and third order Bragg reflection efficiencies were better determined for the DXS lead-stearate crystals (see §2.2.1). The DXS HISM position spectrum is overlayed with the model in Figure 128 and the best fit parameters are shown
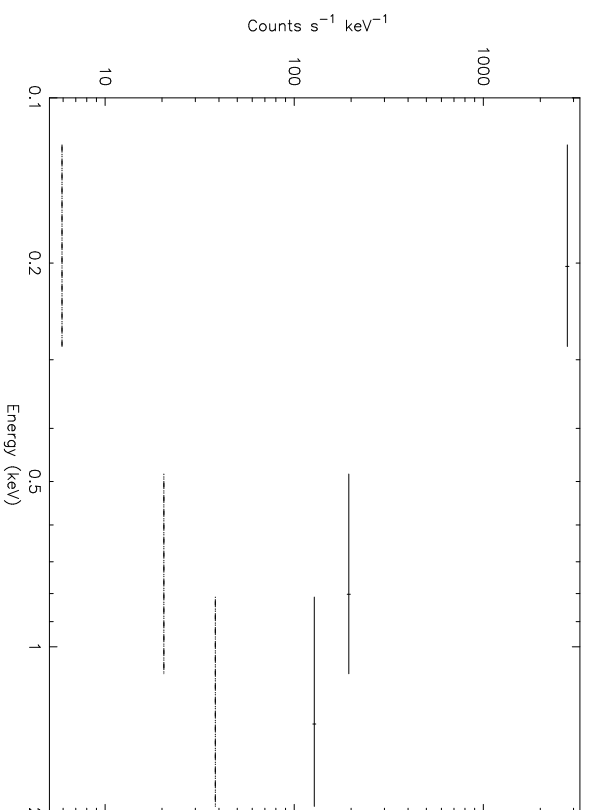
Figure 126: The solid lines show the ROSAT all-sky survey band rates averaged over the DXS HISM region. The absorbed extra-galactic source model from Hasinger *et al.* (1993) is shown as dotted lines.
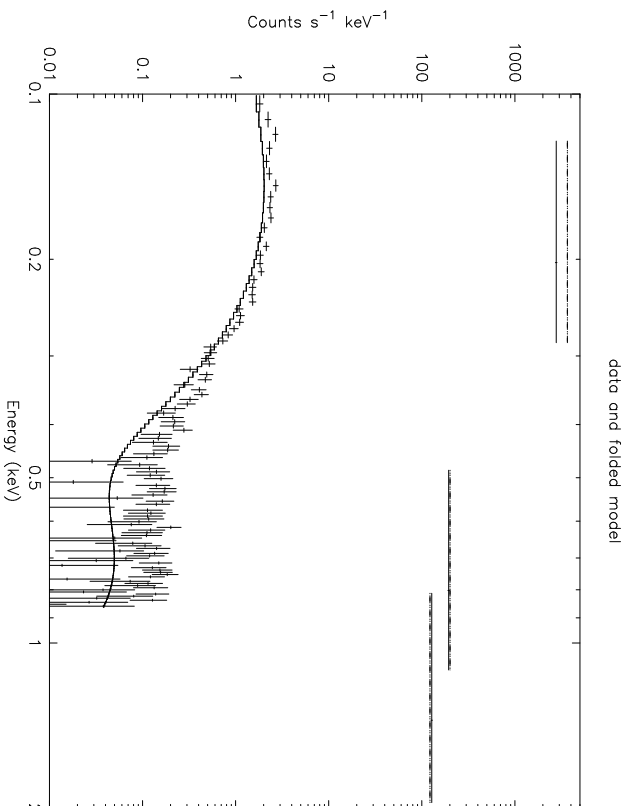
Figure 127: The ROSAT spectrum from Figure 126 and the DXS pulse height spectrum from the HISM region are compared to predictions of the three-component model described in the text.

in Table 26.

6.5 Partial Emission Measure Limits on Individual Ions

This section describes how the DXS HISM spectrum was used to set limits on the partial emission measure of each ion predicted by the RS93 model to be contributing to the DXS pass-band. Partial emission measure is defined as:

$$partial\ emission\ measure = \int n_e n_{ion} dl \qquad (6.14)$$

where n_{ion} is the volume density of the particular ion in question and n_e is the volume density of electrons. The integral is performed along the line of sight, dl.

The upper limit of the partial emission measure of a particular ion is obtained obtained by comparing the emission spectrum of that ion at an assumed temperature (in this case $T = 10^6$ K), to the DXS HISM spectrum. The ionic spectra, calculated by Liedahl (1997), are
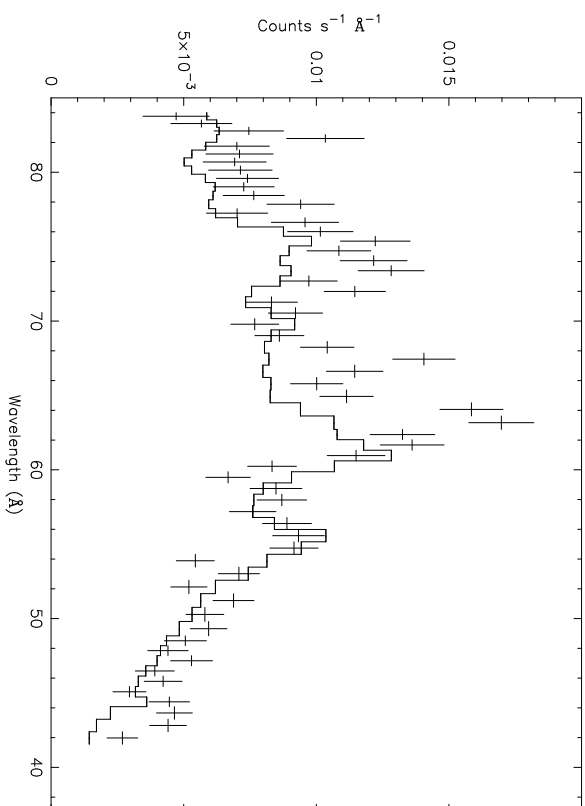
Figure 128: The data points are the DXS position spectrum from the HISM region and the solid line is the predicted spectrum for the three-component model described in the text.

Table 26: HISM spectra fit to three component model. The power law photon index and normalization are from Hasinger *et al.* (1993), the absorption from Dickey and Lockman (1990).

Parameter	Parameter Value
Power Law Photon Index	1.9
Power Law Normalization	7.8 photons keV^{-1} cm^{-2} s^{-1} sr^{-1}
Power Law Absorption	3.26×10^{21} cm^{-2}
MEKAL Temperature	$7.2 \pm 0.2 \times 10^{6}$ K
Halo emission measure	$4.2 \pm 0.1 \times 10^{-3}$ cm^{-6} pc
Hybrid Temperature	$1.00 \pm 0.02 \times 10^{6}$ K
Hybrid emission measure	$2.0 \pm 0.04 \times 10^{-3}$ cm^{-6} pc
χ^2	829
Degrees of Freedom	165
$\chi_\nu{}^2$	5.0
χ^2 probability	$< 10^{-49}$

the same as those used in the hybrid model described in §6.2.4. Using XSPEC version 9.00 (Arnaud 1996) and the "model 16" response matrix, the normalization of each ion spectral model was adjusted until the highest point on the model exceeeded the DXS HISM spectrum by 2–3σ. Figures 129–133 show the spectra of ions which contribute significantly to the equilibrium hybrid plasma model at their limiting emission measures. The limits on partial emission measure calculated in this section are given in Column two of Table 27. These numbers, together with the appropriate atomic physics calculations, can be used to set limits on the emission from an ion in any energy band.

In order to compare the limiting emission measures found here to the partial emission measures predicted by equilibrium models, Equation 6.14 can be rewritten:

$$equilibrium\ partial\ emission\ measure = \int A_j F_{ji} n_e n_H dl. \qquad (6.15)$$

where A_j is the atomic abundance for element j and F_{ji} is the fraction of element j in ion state i. For a plasma where helium is fully ionized,

$$\int n_e n_H dr = \frac{\int n_e^2 dl}{1.194}. \qquad (6.16)$$

Using Equations 6.15 and 6.16, the A_j from Allen (1973), and the F_{ji} calculated by RS93 for T = 10^6 K, the partial emission measures of the ions contributing to the hybrid RS93 model are calculated. The results are listed in Column three of Table 27. The ratio of the limiting emission measure to the hybrid model partial emission measure is shown in column four. For ions that contribute significantly to the hybrid model emission in the DXS pass band, the ratio is close to one.

The emission measure limits found here, together with the appropriate atomic physics calculations can be used to set limits on the emission from an ion in any energy band.

6.6   Conclusion

This chapter presents the results of various model fits to the DXS data. The most definitive result of the chapter, and the important result of the DXS experiment, is that the spectrum of the diffuse X-ray background shows evidence for the presence of atomic lines. This is demonstrated clearly by the deviation of the DXS data from a simple power law spectrum, shown in Figure 112. Detection of atomic lines is important confirmation of the hypothesis

Table 27: Limits on Emission Measure of Individual Ions for T = 10^6 K, Liedahl atomic physics.

Ion	Limiting Emission Measure (cm^{-6} pc)	Hybrid Model Partial Emission Measure (cm^{-6} pc)	Ratio Limit/Hybrid
Si XII	6.5×10^{-7}	8.6×10^{-11}	7500
Si XI	3.8×10^{-7}	2.0×10^{-9}	190
Si X	1.3×10^{-7}	1.6×10^{-8}	8.2
Si IX	6.5×10^{-8}	3.6×10^{-8}	1.8
Si VIII	4.5×10^{-8}	2.4×10^{-8}	1.8
Si VII	2.5×10^{-8}	4.7×10^{-9}	5.4
Si VI	4.5×10^{-8}	2.7×10^{-10}	170
S XII	1.2×10^{-5}	2.3×10^{-11}	5.2×10^{5}
S XI	9.7×10^{-7}	7.8×10^{-10}	1200
S X	3.7×10^{-7}	7.1×10^{-9}	52
S IX	1.2×10^{-7}	1.7×10^{-8}	7.0
S VIII	6.0×10^{-8}	1.1×10^{-8}	5.5
S VII	3.5×10^{-8}	1.7×10^{-9}	20
Ne VIII	7.0×10^{-7}	1.9×10^{-8}	36
Mg X	2.6×10^{-7}	1.8×10^{-8}	14
Mg IX	1.6×10^{-7}	3.1×10^{-8}	5.2
Mg VIII	5.0×10^{-8}	2.0×10^{-8}	2.5
Mg VII	4.0×10^{-8}	4.1×10^{-9}	9.7
Mg VI	9.0×10^{-8}	2.5×10^{-10}	360
Fe XVI	6.0×10^{-7}	2.7×10^{-14}	2.2×10^{7}
Fe XV	1.1×10^{-7}	3.2×10^{-12}	34000
Fe XIV	1.9×10^{-7}	1.1×10^{-10}	1800
Fe XIII	1.2×10^{-7}	1.1×10^{-9}	110
Fe XII	8.0×10^{-8}	5.9×10^{-9}	14
Fe XI	2.8×10^{-7}	2.6×10^{-8}	11
Fe X	2.2×10^{-7}	2.9×10^{-8}	7.5
Fe IX	1.3×10^{-7}	3.8×10^{-8}	3.4
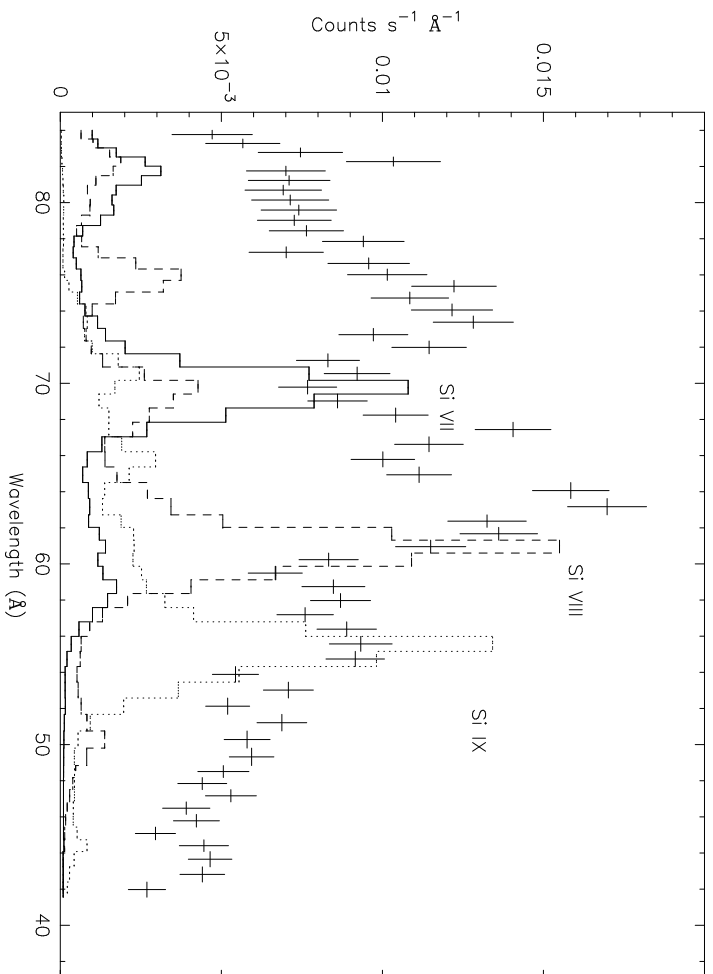
Figure 129: HISM spectrum with SiVII–IX single ion emission models at their limiting emission measures. The Si atomic levels are populated as they would be for a plasma in collisional equilibrium at 1×10^6 K.
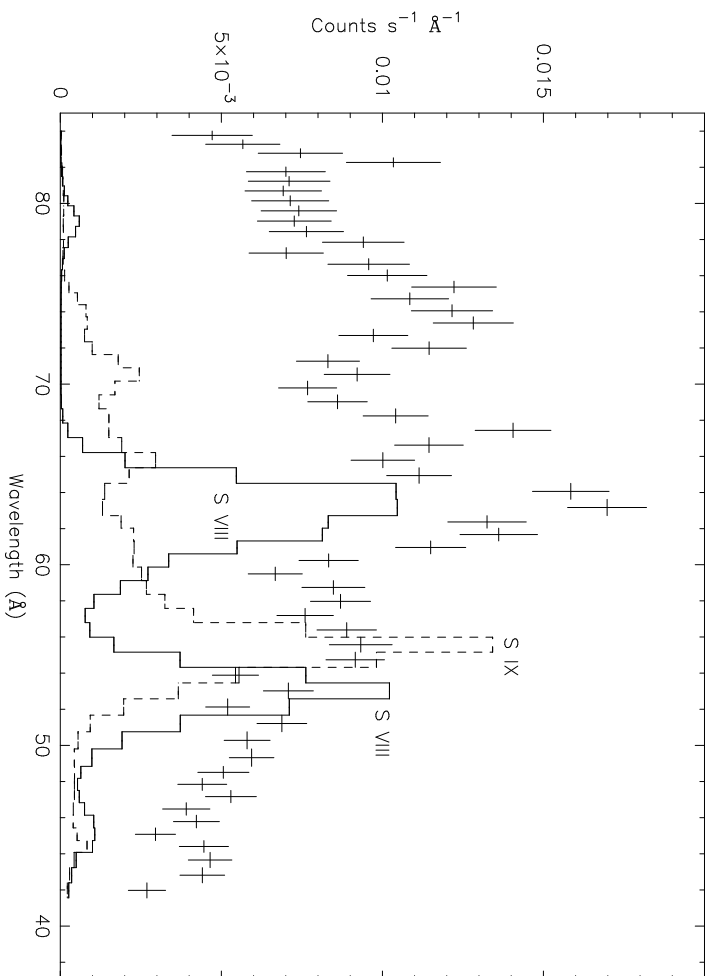
Figure 130: HISM spectrum with SVIII–IX single ion emission models at their limiting emission measures. The S atomic levels are populated as they would be for a plasma in collisional equilibrium at 1×10^6 K.
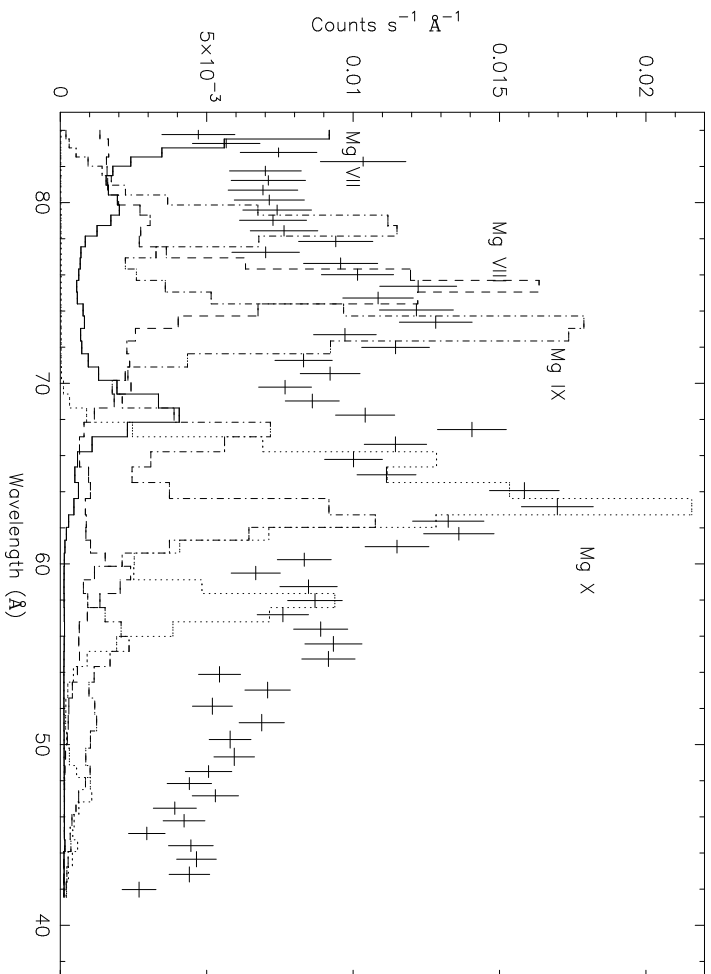
Figure 131: HISM spectrum with MgVII–X single ion emission models at their limiting emission measures. The Mg atomic levels are populated as they would be for a plasma in collisional equilibrium at 1×10^6 K.
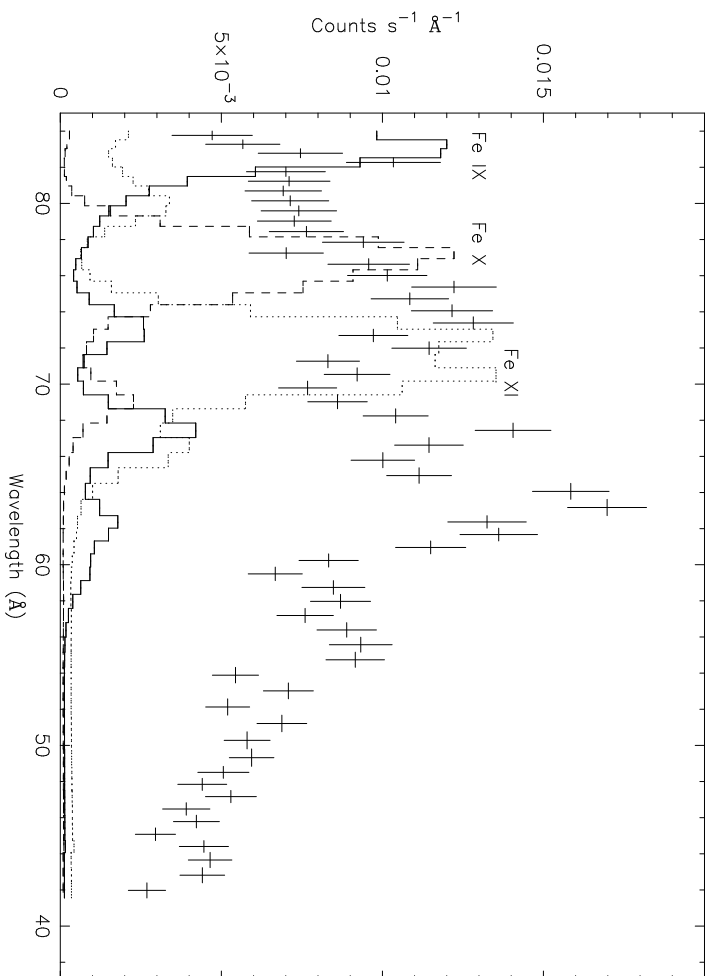
Figure 132: HISM spectrum with MgIX–XI single ion emission models at their limiting emission measures. The Fe atomic levels are populated as they would be for a plasma in collisional equilibrium at 1×10^6 K.
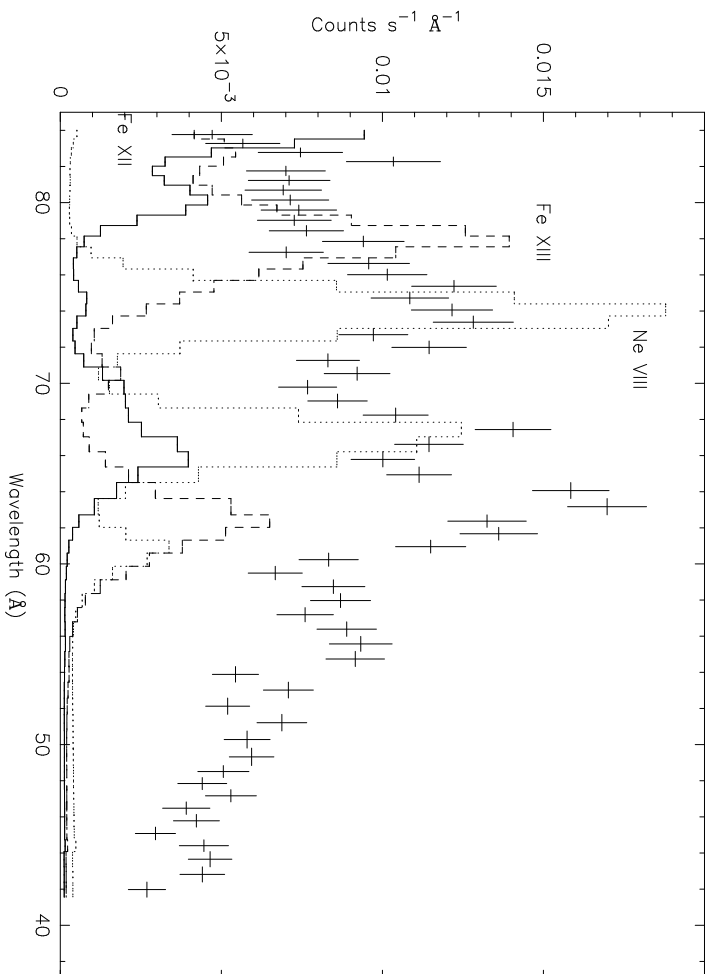
Figure 133: HISM spectrum with FeXII–XIII and NeVIII single ion emission models at their limiting emission measures. The Fe and Ne atomic levels are populated as they would be for a plasma in collisional equilibrium at 1×10^6 K.

presented in Williamson *et al.* (1974) that the X-ray background from ∼100 eV to 284 eV likely originates from "widely distributed regions of interstellar gas with temperatures in the region of 10^6 K," since radiation by collisionally excited ionic lines is the principle mechanism for cooling such gas.

The next question to ask is "what is the precise condition of the hot interstellar gas." Unfortunately, as of the writing of this document, this is a question that cannot be answered with any certainty. Among available models, the only progression toward better fits to the DXS data is in the direction of including more atomic physics. The relative success of the Mewe & Kaastra and hybrid Raymond & Smith/Liedahl models at fitting the data (§6.2) suggest that near equilibrium conditions may reign in the gas but atomic abundances may not be solar. Global models that treat the question of atomic abundances, multiple sources, possibly non-equilibrium conditions, *and* that include the latest atomic physics will be necessary to fully address the question of the precise condition of the hot gas in the interstellar medium.

Chapter 7

Summary and Conclusion

The essential and important result of DXS is the confirmation of the hypothesis, set forth in Williamson *et al.* (1974), that the 1/4 keV component of the diffuse X-ray background is composed largely of emission lines, most likely emitted from gas heated to temperatures near 10^6 K. This conclusion was reached relatively early on in the DXS data analysis process, when "bumps and wiggles" were seen in the data. The majority of the work that went into this thesis project concentrated on careful treatment of the DXS data to ensure that none of the "bumps and wiggles" seen in the final spectra were due to instrumental effects or un-accounted background.

Chapters 2 and 3 show that the response of the DXS instrument is calculated using the geometry of the instrument and empirical measurements of the Bragg crystal panel reflectivity. As shown in Figure 63, agreement between the calibration data and the model of the detector response is good, certainly good enough to rule out the possibility that the spectral features shown in Figure 112 are caused by the instrument's response to a spectrally featureless source.

The reduction and analysis of the DXS data is discussed in Chapters 4 and 5. The data were divided up into several sections and analyzed independently. The most important division was between the two physically independent instruments. Despite complications in the background of the Starboard detector, reasonable agreement between the two instruments' final spectra was achieved, as shown in Figures 78, 134, and 139–141. However, in order to ensure no contamination due to the starboard detector problems, the Starboard dataset was not used in further analysis.

Internal consistency checks on the Port instrument dataset reveal that there was a time-varying component to the observed flux. Over the course of the 5 day mission, the background subtracted DXS counting rate changed by $\sim$20%. Section 5.5 presents evidence that this change in counting rate was caused by an earth-local phenomenon known as "long term enhancements." Similar enhancements in the soft X-ray counting rate have been observed with other X-ray missions, such as ROSAT (Snowden *et al.* 1995). The lowest counting rate

observed by DXS is 5% above to 15% below the counting rate predicted using the ROSAT all-sky survey C–band surface brightness map of Snowden *et al.* (1995) and correcting for the apparent 10% overestimation in the ROSAT effective area in this energy range (see §5.4). This indicates that on average, the DXS data are not highly contaminated. Additionally, the variable source had no detectable spectral features, as shown by statistical analysis summarized in Table 17.

Section 5.7.3 presents a detailed statistical comparison between the spectra of different regions in the DXS dataset. After differences in counting rate are taken out, none of the spectra appear significantly different as measured by the χ^2 probability test described in §5.7.1, except for the spectrum of the Vela supernova remnant. Because of their association with known supernova remnants, data from the Vela and MonoGem regions were excluded from subsequent analysis. Data from the Crux, Puppis, and Auriga regions were co-added to form a single spectrum representative of the diffuse X-ray background (Figure 101) at low Galactic latitude. The average ROSAT C–band surface brightness rate in this composite region is given (460 counts s^{-1} arcmin^{-2}) so that, as a first approximation, the results of this thesis can be scaled and applied to any region of the sky dominated by the diffuse X-ray background.

Chapter 6 suggests a few of the astrophysical implications of the DXS data. Several global models have been constructed to attempt to model the HISM DXS spectrum. The most successful model is the 1993 revision of the Raymond & Smith equilibrium plasma emission code (Raymond & Smith 1977) modified to include ionic spectra calculated recently by Liedahl (1997). The reduced χ^2 of this model is 2.1 with 51 degrees of freedom. This translates into a χ^2 probability of 3.8×10^{-6}, which is not formally a good fit to the data.

Because of the poor model fits to the DXS data, the question of the precise condition of the hot gas that comprises the local interstellar medium is still open. As an aid to future theoretical research, upper limits on the partial emission measures of individual ionic species have been calculated for a temperature of 10^6 K using the calculations of Liedahl (1997). Also, the DXS spectra and response matrices will soon be made available either through the the High Energy Astrophysical Science Archive Research Center (HEASARC) or the National Space Science Data Center (NSSDC). The response matrices and spectra are also available from the author. Send email requests to jpmorgen@wisp.physics.wisc.edu.

Bibliography

Allen, C. 1973, Astrophysical Quantities (third ed.) (University of London, the Athlone Press), Ch. 3, 30

Anders, E., & Grevesse, N. 1989, Geochim. Cosmochim. Acta, 53, 197

Arnaud, K. 1996, in Astronomical Data Analysis Software and Systems V, ed. G. Jacoby & J. Barnes, ASP Conf. Ser. 101 (San Francisco: ASP), 17

Arnaud, M., & Rothenflug, R. 1985, A&AS, 60, 425

Balucinska-Church, M., & McCammon, D. 1992, ApJ, 400, 699

Bearden. 1967, Rev. Mod. Phys., 39, 78

Bevington, P. R. 1969, Data Reduction and Error Analysis for the Physical Sciences (McGraw-Hill), Ch. 11, 237

Bloch, J. J. 1988, Ph.D. thesis, University of Wisconsin, Madison

Bloch, J. J., Jahoda, K., Juda, M., McCammon, D., Sanders, W. T., & Snowden, S. L. 1986, ApJ, 308, L59

Borken, R. J., & Kraushaar, W. L. 1976, Space Science and Instrumentation, 2, 277

Breitschwerdt, D., & Schmutzler, T. 1994, Nature, 371, 774

Bunner, A. N., Coleman, P. L., Kraushaar, W. L., McCammon, D., Palmieri, T. M., Shilepsky, A., & Ulmer, M. 1969, Nature, 223, 1222

Burrows, D. N. 1982, Ph.D. thesis, University of Wisconsin–Madison

Charles, M. 1971, J. Appl. Phys., 42, 3329

Cox, D., & Tucker, W. 1969, ApJ, 157, 1157

Cox, D. P., & Reynolds, R. J. 1987, ARA&A, 25, 303

Dickey, J. M., & Lockman, F. J. 1990, ARA&A, 28, 215

Edgar, R. J., & Cox, D. P. 1993, ApJ, 413, 190

Field, G., Goldsmith, D., & Habing, H. 1969, ApJ, 155, L149

Garmire, G., Nousek, J. A., Apparao, K. M. V., Burrows, D. N., Fink, R. L., & Kraft, R. P. 1992, ApJ, 399, 694

Giacconi, R., Gursky, H., Paolini, F. R., & Rossi, B. B. 1962, Phys. Rev. Lett., 9, 439

Gould, R., & Sciama, D. 1964, ApJ, 140, 1634

Hanisch, R., Schlesinger, B., Brotzman, L., Kemper, E., Teuben, P., Van Steenberg, M., Warren, W. J., & White, R. 1993, Definition of the flexible image transport system (fits), Technical report, NASA/Science Office of Standards and Technology, Greenbelt, MD

Hasinger, G., Burg, R., Giacconi, R., Hartner, G., Schmidt, M., Trümper, J., & Zamorani, G. 1993, A&A, 275, 1

Hassitt, A., & McIlwain, C. E. 1967, Computer programs for the computation of b and l, Technical Report 67-27, NSSDC

Henke, B. L. 1964, Advances in X-ray Analysis, 7, 460

Henke, B., Gullikson, E., & Davis, J. 1993, Atomic Data and Nuclear Data Tables, 54

Henke, B. L., Lee, P., Tanaka, T. J., Shimabukuro, R. L., & Fujikawa, B. K. 1982, Atomic Data and Nuclear Data Tables, 27, 1

Holliday, J. E. 1967, The Norelco Reporter, XIV, 84

Horowitz, P., & Hill, W. 1989, The Art of Electronics (2 ed.) (Cambridge University Press), Ch. 15.16, 1035

Inoue, H., Koyama, K., Matsuoka, M., Ohashi, T., Tanaka, Y., & Tsunemi, H. 1979, ApJ, 227, L85

Jahoda, K., & McCammon, D. 1988, Nucl. Instrum. Methods Phys. Res., Sect. A, A272, 800

Juda, M. 1988, Ph.D. thesis, University of Wisconsin, Madison

Kaastra, J. 1992, An x-ray spectral code for optically thin plasmas, Technical Report 2.0, SRON-Leiden

Kahn, S. M., Gorenstein, P., F.R. Harnden, J., & Seward, F. D. 1985, ApJ, 299, 821

Klapisch, M. 1971, Comput. Phys. Commun., 2, 239

Klapisch, M., Schwab, J., Fraenkel, J., & Oreg, J. 1977, J. Opt. Soc. Am. A, 61, 148

Landolt-Börnstein, ed. 1955, Zahlenwerte und Funktionen (6 ed.), Vol. I/4 (Berlin: Springer-Verlag), 769

Levine, A., Rappaport, S., Halpern, J., & Walter, F. 1977, ApJ, 211, 215

Liedahl, D. 1997, private communication

Lyman Spitzer, J. 1956, Physics of Fully Ionized Gasses (New York: Interscience), 634

Marshall, F. J., & Clark, G. W. 1984, ApJ, 287, 633

McCammon, D., Bunner, A. N., Coleman, P. L., & Kraushaar, W. L. 1971, ApJ, 168, L33

McCammon, D., Burrows, D. N., Sanders, W. T., & Kraushaar, W. L. 1983, ApJ, 269, 107

McCammon, D., & Sanders, W. T. 1990, ARA&A, 28

McCammon, D. 1998, Private Communication

McIlwain, C. E. 1961, J. Geophys. Res., 66, 3681

McKee, C. F., & Ostriker, J. P. 1977, ApJ, 218, 148

Mewe, R., Gronenschild, E. H. B. M., & van den Oord, G. H. J. 1985, A&AS, 62, 197

Moskalenko, E. 1994, Background in the dxs counters, Technical Report 1, University of Wisconsin, Space Science and Engineering Center

Mulligan, M. 1993, Internal University of Wisconsin–Madison Space Science and Engineering Center (SSEC) Memo

204

NASA. 1985, Payloads mathematical specifications, Technical Report CSC/SD-85/6024, Contract NAS527888

Nousek, J., Cowie, L., Hu, E., Linblad, C., & Garmire, G. 1981, ApJ, 248, 152

Press, W. H., Teukolsky, S. A., Vetterling, W. T., & Flannery, B. P. 1992, Numerical Recipes (Cambridge University Press), Ch. 6, 215

Raymond, J. C. 1988, in Hot Thin Plasmas in Astrophysics, ed. R. Pallavicini, NATO ASI, series 249C (Dordrecht, NL: Kluwer)

Raymond, J. C., & Smith, B. W. 1977, ApJS, 35, 419

Sanders, W., & Richards, E. 1990, Dxs detector controller firmware requirements, Technical Report 5000-0609, University of Wisconsin Space Science and Engineering Center

Schmitt, J., Snowden, S., Aschenbach, B., Hasinger, G., Pfefferman, E., Predehl, P., & Truemper, J. 1991, Nature, 349, 583

Schnopper, H. W., Delvaille, J. P., Rocchia, R., Blondel, C., Cheron, C., Christy, J. C., Ducros, L., & Rothenflug, R. 1982, ApJ, 253, 131

Smith, R. K. 1996, Ph.D. thesis, University of Wisconsin–Madison

Smith, R. K., & Cox, D. P. 2001, ApJS, submitted

Snowden, S. 1986, Dxs area-solid angle calibration, Technical report, University of Wisconsin, Space Science and Engineering Center

Snowden, S. L., et al. 1997, ApJ, 485, 125

Snowden, S. L., Cox, D. P., McCammon, D., & Sanders, W. T. 1990, ApJ, 354, 211

Snowden, S. L., et al. 1995, ApJ, 454, 643

Sofia, U. J., Cardelli, J. A., & Savage, B. D. 1994, ApJ, 430, 650

Vanderhill, M. J., Borken, R. J., Bunner, A. N., Burstein, P. H., & Kraushaar, W. 1975, ApJ, 197, L19

Williamson, F. O., Sanders, W. T., Kraushaar, W. L., McCammon, D., Borken, R., & Bunner, A. 1974, ApJ, 193, L133

Appendix A

Response Matrix Versions

This appendix describes the development of the DXS response matrices chronologically. Sections 2.5 and 3.2 discuss the response matrix in its final form.

The original response matrix generating program, SPCMOD, was written by D. McCammon in the late 1970's to help with the design of the Bragg crystal spectrometer that became DXS. McCammon's program and sections of another program, PLOTMD, were ported to a VMS workstation by S. Snowden in the mid 1980s. From there, they were ported to the DXS Ultrix workstation from by D. Edgar in the early 1990s. Edgar created a new program, RSPMATRIX which used parts of PLOTMD and new code that output XSPEC (Arnaud 1996) compatible response matrices.

Edgar's early work on the response matrix (model 3) assumed a 2D spacing of 101 Å for lead stearate. This is the value indicated by the location of the peaks in the rocking curve data taken at PSL described in §2.5.3. Edgar also assumed that the alpha-particle excited polypropylene (carbon) source used for the DXS calibration produced radiation most similar to the "graphite" source in Holliday. With these assumptions, it is *not* possible to achieve reasonable fits to the data given the DXS detector geometry of the construction drawings (SSEC drawing series 5000). Edgar's method for achieving better fits was to change the geometry of the instrument as modeled in SPCMOD. In particular, he moved the positions of the first and last position channels (POS—see §2.3.1) relative to the crystal panel center of curvature. Because SPCMOD accepts the positions of the first and last POS in units of crystal panel radius of curvature, it was not immediately obvious what type of distortion Edgar was demanding of the proportional counter or DXS instrument.

I advanced Edgar's work on the wavelength scale by writing a Microsoft ® Excel spreadsheet that accepted as input the physical parameters of the proportional counter (length and position of center relative to the crystal panel center of curvature) in inches and output the values to use as input to SPCMOD. With these inputs, SPCMOD was able to generate a new DXS response matrix which was then used to fit the Holliday boron and graphite spectra and

the four Gaussian lines of the zirconium spectrum. The spreadsheet also recorded the final best fit parameter values of XSPEC fits for the curve normalization and the wavelength shift ("red-shift"). The normalization values of boron and graphite do not have physical meaning, however, they were recorded in order to track relative changes in the different versions of the response matrix.

Keeping the lead stearate $2D$ value of 101 Å, I found the best fit wavelength scale was one for which the entire proportional counter was shifted toward the crystal panel center of curvature by 0.1 inches (model 4). With this adjustment of the DXS geometry, the assumed input spectral models folded through the model 4 DXS response matrix produced a predicted output spectrum that agreed with the calibration data to within 0.5% in wavelength. The problem was that the mechanical engineers who had designed the DXS instrument assured me that 0.1 inches was an unphysically large deviation from the expected geometry given the quality of the design and machining. My own review of the drawings led me to the conclusion that there was no easy mistake that could been made on this scale. The quadrature sum of the six 0.005 inch tolerance joints between the crystal panel and proportional counter ground plane wires gives a root mean square error of 0.015 inches. The absolute maximum error is 0.030 inches. This response matrix (model 4) also has a polynomial approximation to the correct pulse height efficiency (PHEFF) calculation described in §2.5.3.

As an alternate approach, I tried fixing the DXS geometry as indicated by the construction drawings and investigated the effect of varying the lead stearate $2D$ spacing. Using the spreadsheet/SPCMOD method outlined above, I arrive at a best fit value of 102 Å for $2D$ assuming nominal geometry (model 5). The fit was actually weighted toward the value that gave the minimum red-shift for the boron calibration data. The zirconium data favored a $2D$ value of 101.5 Å, and graphite, 103 Å. When the assumed input spectra were folded through the model 5 response matrix, the largest excursion in wavelength between the predicted output spectra and the calibration data was 1% at carbon. At this point, inadvertently introduced an error in SPCMOD that severely underestimated the shadowing effect of the cal tube.

With the wavelength scale reasonably well understood, I began to modify the response matrix to fit the precise shape of the lines in the DXS data. This was most readily done by changing the lead stearate rocking curve modeled in SPCMOD. Many experiments were tried; the best results are shown in models 6 and 7. Model 6 is identical to model 5 except that a Lorentzian wing has been added on the high angle side of the rocking curve in order to fit the

low energy points of the carbon and boron spectra. The existing low angle Lorentzian curve was modified to better fit the high energy points of the zirconium and boron spectra. Figure 57 shows the difference between the modeled instrument response when an identical boron input spectrum is folded through the model 5 and model 6 response matrices. Reviewing Figures 8 through 60 reveals that the Henke #2 crystals do not show evidence for such large Lorentzian wings.

The model 7 response matrix is identical to model 6, except that the full width at half maximum (FWHM) of the Gaussian component of the rocking curve was reduced by a factor of two. This change resulted in good point-by-point agreement in the peaks of the boron and graphite spectra. One drawback was that the Lorentzian components joined the Gaussian in a curve with an unphysically small radius of curvature. A more important problem was the implication that the Henke #2 FWHM determination was erroneous by a factor of two. This implied either large crystal-to-crystal variations, which were not evident in the sample of crystals studied at the same time as the Henke #2 crystal, or a monochromator beam-width of 3 eV. Discussion with the PSL staff revealed some important facts about how the double grating "torpedo" monochromator used to study the lead stearate crystals worked. The design was thought to achieve beam widths significantly less than 1 eV, but there was a problem with the wavelength adjustment. A one-meter long screw was used to move the monochromator gratings, but no screw could be found that was straight enough to ensure smooth operation. If the screw was attached firmly to the grating shuttle mechanism, its wobble would cock the gratings relative to each other, thus severely degrading the monochromator beam width in energy. The solution to this problem was to loosen the nuts that attached the screw to the shuttle mechanism, thus sacrificing positioning (wavelength) accuracy, but assuring reasonable spectral performance. I saw evidence of wavelength hysteresis in test measurements of the PSL monochromator, so it appears the decision to sacrifice wavelength accuracy for beam width had been made in the case of the lead stearate crystal measurements.

With this understanding of the PSL monochromator, the rocking curve FWHM was set back to its original value and the poor fits to the boron and graphite data were attributed to the input functions rather than in incorrect response matrix. Secondly, a skepticism of the accuracy of the $2D$ determination based on the PSL data developed.

Table 10 shows the implied $2D$ spacing given experiments or input spectra at various energies. The "Al" and "O" lines refer to multiple order reflection measurements of aluminum

K-α and oxygen K-α radiation made with the Wisconsin Space Physics X-ray tube. The oxygen peak was colliding with another peak, so precise determination of the reflection angle was not made (hence the limit). The graphite, boron and zirconium $2D$ determinations were made with the DXS post-flight calibration data as described above. The "TiC, etc." is a family of curves found in Holliday (1967) that was originally rejected using chemical composition arguments. Using a $2D$ value of 101.5 Å, the zirconium and TiC input models fit the data well with red-shifts smaller than 0.1%.

At this point, I had an idea for how distortions in the crystal panel from its nominal cylindrical geometry might be responsible for problems in the wavelength scale. I designed and executed an experiment in which I shined a laser from a jig attached to the mounting surface of the proportional counter (the counter was removed). The system shined the laser to within a fraction of a degree of the perpendicular to the proportional counter window (had it been mounted). The laser bounced off of the crystal panel surface and shone on a screen placed a few feet away from the entrance aperture of the instrument. Given the distance to the screen (determined to within 1/8 inches), and about 60 measurement points, I could determine the relative position of the crystal panel radius of curvature to the center of the proportional counter mounting plane to within 0.030 inches and find any deviations from cylindrical geometry in the panel. Indeed, as the mechanical engineers had promised, the relative positions of the crystal panel and proportional counter were within 0.030 inches, *but* there were distortions in the crystal panel shape at the edges (near the first and last POS). I re-wrote most of the geometric calculations in SPCMOD in order to accommodate for my model of the distortions (simple chords of 1.75 degrees in angular extent) and found that the resulting response matrix was *identical* to the previous one! Only then did I really understand how the instrument worked. There is no way that small distortions in the crystal panel can affect the wavelength scale, since the large collimation angle causes each point of the proportional counter to look out on a large section of the crystal panel.

The model 8 response matrix uses these new geometric calculations, a $2D$ lead stearate crystal spacing of 101.5 Å, the original Gaussian components of the rocking curve, and the enhanced Lorentzian wings. A final subtlety incorporated into the wavelength scale of the model 8 response matrix is a correction for the relative shift of 0.020 inches between the positions of the Port and Starboard proportional counters relative to their respective crystal panel center of curvatures. The evidence for this shift comes from the systematic behavior of the

wavelength shifts of the assumed input spectra when they are folded through pre-model 8 response matrices and compared to the calibration data. These wavelength shifts, or "red-shifts" were converted to equivalent proportional counter offsets for each of the peaks in the carbon, boron, and zirconium spectra. Consistently, the difference between the Port and Starboard offset values for each peak was 0.020 inches. Consistently, the difference between the Port and Starboard offset value of the shift in either proportional counter, so the shift was taken to be 0.010 inches toward the crystal panel center of curvature for the Port instrument and 0.010 inches away from the crystal panel center of curvature for the Starboard. With this small shift, the red-shifts in the fits to the zirconium, boron, and carbon data using the four Gaussian zirconium method, and the Holliday boron and TiC models, are all less than 0.5%.

The model 9 response matrix is similar to model 8 but incorporates the correct cal tube shadowing and a different (though also inaccurate) PHEFF polynomial. In addition, the model 9 response matrix includes estimates of the response to second and third order Bragg reflections. The second and third order Bragg reflection rocking curve shapes are simply copies of the first order rocking curve peaks. As shown in Figure 60, this assumption significantly underestimates the width of the second order peak. The integrated reflectivity for the second and third order Bragg reflections was estimated by scaling the first order integrated reflectivities down by factors of 2.2 and 2.0, respectively. These values are based on an eyeball integration of the carbon, oxygen and aluminum multi-reflection data. In order to accommodate the larger wavelength scale necessary to model the second and third order reflections, several of the polynomials governing the shape of the rocking curve were modified, including the FWHM and the ratio of amplitudes of the two Gaussian components that make up the model Bragg peak. None of the new polynomial values deviate more than 5% from the old values in the critical range of 150–277 eV.

The model 10 response matrix is identical to the model 9, except that the integrated reflectivity of the lead stearate crystal panels is assumed to be lower by a factor of 1.123. In model 11, a height response matrix was incorporated into the pulse height efficiency determination procedure.

In the construction of the model response matrix 12, the crystal panel reflectivity was treated as a free parameter and a best fit value to the post-flight area solid-angle product measurements was used. The model 13 response matrix is like model 12 except that the pulse height upper level discriminator (ULD) value used in reducing the flight data was lowered

from 500 to 450 eV to match the the processing of the spectra in June 1997.

For Model 14 the pulse height response matrix was re-worked. The low gain response matrix of §3.1.4 was used. This work also included a more careful treatment of the precise location of the LLD and ULD values in terms of change channels, since the non-linearity in the gas gain makes the nominal value of 1.985 pulse height channels per eV based on the aluminum cal peak highly inaccurate at low energies.

After unearthing the pre-flight $A\Omega$ calibration memo (Snowden 1986), I discovered that the pre- and post-flight $A\Omega$ *measurements* where within 7% of each other. This was yet another piece of evidence that the crystal panel reflectivity had not changed during the flight. This, together with the fact that the original model 3 response matrix (before porting to UNIX) predicted the measured $A\Omega$ to within 6% (with one outlier at 15%), convinced me that I needed to re-evaluate my modification of the crystal panel integrated reflectivity.

Model 3 used the value of the flight crystal panel reflectivity measured in the Henke tube apparatus at the University of Wisconsin Space Physics Laboratory, described in §2.2.1 and correctly predicted $A\Omega$. Looking more carefully at the predicted value of $A\Omega$ as a function of model number, I found that between models 5 and 6, $A\Omega$ jumped by 15%: the enhanced Lorentzian wings were contributing significantly to the total instrument efficiency. To compensate for this and reach agreement between the predicted and measured $A\Omega$ values, I scaled the integrated reflectivity value used by SPCMOD down by 15-30% between models 9 and 14. This was the wrong thing to do, since this integrated reflectivity value is the integral of the rocking curve between $\pm 4°$, which from the earliest flight crystal measurements has shown no evidence of change. Thus, on the basis of the 15% increase in $A\Omega$, I can rule out the possibility that the flight crystal panel rocking curves have broad Lorentzian and thus conclude that these wings are caused by the calibration sources. The result is model 15, which uses the original Henke #2 rocking curve, scaled by 1.123, according to the flight crystal integrated reflectivity measurements.

Model 16 is a refinement of model 15. As discussed in §3.2.2, the function that defines the crystal panel reflectivity was modified to fit the Port post-flight calibration data. The Starboard crystal panel reflectivity uses the same function, but scaled by 1.082.

Appendix B

Hot Spot Removal

This appendix describes the details of the statistical methods used to attempt to clean the Starboard dataset. The cleaning procedures result in qualitative agreement between the Port and Starboard spectra, as shown in Figures 134, 138, and 139–141. The agreement of the spectra recorded from two independent instruments is important evidence that the diffuse X-ray background (or some other source external to the detectors) was being observed. However, none of the cleaning methods completely rid the Starboard data of the effects of the hot spots, the Starboard data have not been used in the scientific analysis of this project.

B.1 Sigma Method

The first method of hot spot identification was based on Gaussian statistics. Four histograms similar to those plotted in Figure 69, with the X-axis as position on the counter (binned by fours) and the Y-axis as time (in orbit number) where made using `hist`. The pixel value of one of the histograms was the number of aperture closed background counts collected in that orbit in that four POS bin. Another histogram's pixels contained the aperture closed exposure time in seconds. The other two histograms were counts and exposure of the sky-looking, or "scan" data. Also, spectra of count rate as a function of position (also called "rate spectra") were formed binned in the same sense as the X-axis of the images. Then, a "hotmap" image was formed using the program `hot_stat` with the following formula:

$$hotmap_{i,j} = \frac{counts_{i,j} - rate_i * exposure_{i,j}}{\sqrt{rate_i * exposure_{i,j}}} \tag{B.1}$$

where $rate_i$ is the ith spectral bin of the rate spectrum and j is the index of time.

This procedure produces a 2 dimensional image (the "hotmap") whose pixels represent the number of Poisson standard deviations (sigma) away from average the count rate at a particular time and place in the proportional counter.

Then the program `hot_iterate` was used create to a new, cleaned rate spectrum using the hotmap, an input parameter called "hotcut," and the original counts and exposure maps. Pixels in the hotmap that were larger than the hotcut parameter were rejected. The remaining counts and exposure pixels were totaled as a function of time and divided to form a new rate spectrum. This new rate spectrum was used as the input to equation B.1 to produce a new hotmap. The procedure was repeated keeping the hot cut value the same, until the rate spectra stopped changing. When working with the aperture closed background data, it was possible to make use of the additional constraint that the background was flat in detector coordinates (see §5.2). In contrast, each spectral bin of the sky looking, or "scan" data was treated independently.

The problem with this method for identifying hot spots in the background data was that the number of expected counts in each bin, $rate_i * exposure_{ij}$, was significantly less than one. Thus, the assumption that the hotmap pixel values measured standard deviations, as they would in the Gaussian limit was invalid. Even for the sky looking, or "scan" data, the number of expected counts in most bins was less than 10.

Without heed to the statistical problems, I used this method with hotcut values of 0.5 (that is, rejecting all pixels with rates 0.5 sigma above the mean counting rate) in three iterations to create hotmaps for both scan and background data for each anode group (odd and even) of the Starboard counter. I then formed two more hotmaps (odd and even) by taking the higher of the pixel values of the background and scan hotmaps. Using a these hotmaps and a hotcut value of 0.5, there was so little data left that the scan spectra were useless. It was, however, clear that the background spectra were flat and had rates similar to those in the Port counter. In order to include more data, I increased the hotcut parameter to 0.9. The resulting final spectrum, produced as per the procedure described in §4.7, is shown as the dotted line in Figure 134.

Unfortunately systematically cutting out bins with hotmap pixel values above 0.9 sigma results in a population of bins with an artificially low mean (assuming that this hotcut removes most of the contamination). This may be acceptable in the background data, which can be corrected with a single factor, but biasing the scan data in this way is is dangerous, because the effect of the hotcut on each channel is different and thus might induce spectral effects.
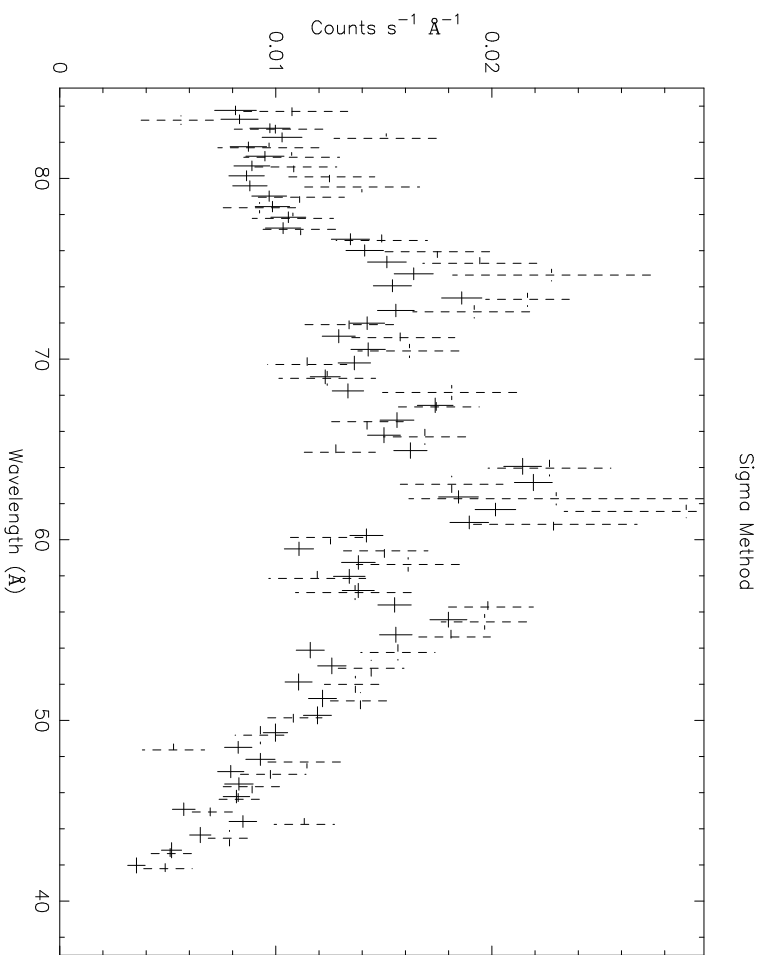
Figure 134: Cleaned Starboard Allsky spectrum (dotted) compared to port. The "sigma method" described in §B.1 was used to clean the Starboard data.

B.2 Integrated Probability Method

The other method used to try to clean the Starboard dataset was similar in design to the "sigma" method described above, but used the statistic of integrated Poisson probability instead. This allows for an estimation of the biasing effect of the hotcut parameter on final count rate. For each bin in the position, orbit number space, the program `hot_prob` calculates the expected number of counts, m_{ij}, based on the count rate of the input spectrum, $rate_i$, and the exposure time $exposure_{ij}$, where i and j are defined as above. The actual number of counts in each bin is x_{ij}. The integral from 0 to x_{ij} of the Poisson probability distribution of mean counts m_{ij} is then calculated for each pixel and stored in the hotmap. For high values of x_{ij} (in a hot spot), the integral is near 1. For average values of x_{ij}, the integral is near 0.5. Thus, the program `hot_iterate` could be used as above with a hot cut of, say, 0.95, to generate cleaned spectra for another iteration.

In both the "integrated probability" and "sigma" methods, a one dimensional histogram of the hot map was formed in order to better determine a hot cut value. The histogram in integrated probability was particularly striking, since so many pixels had improbably many counts, there was a large spike at the bin containing the integrated probability of 1, as shown in Figure 135.

One of the advantages of the integrated probability method over the sigma method is that the ideal distribution of the one dimensional histogram described in the previous paragraph can be calculated. The histogram represents the probability that a certain bin has that integrated probability. In the case of the Poisson distribution that probability is just the Poisson probability back again. There is an additional complication in the case of the background DXS data, since each orbit has a distinct background exposure, so there is not a single Poisson distribution describing the number of expected counts per bin, m_{ij}. However, the ideal Poisson histogram can be formulated by summing the individual Poisson distributions of each of the m_{ij} bins. The ideal Poisson histogram is shown for the data in Figure 135 in two cases. First, for the population of all bins (upper model curve), second, using only those bins that passed the hotcut criterion in the previous iteration (lower model curve).

The integrated probability method can also be used to calculate the effect of the hotcut parameter on the apparent background counting rate. This is done by using the ideal Poisson distribution as a sample population and calculating the average counting of the population as
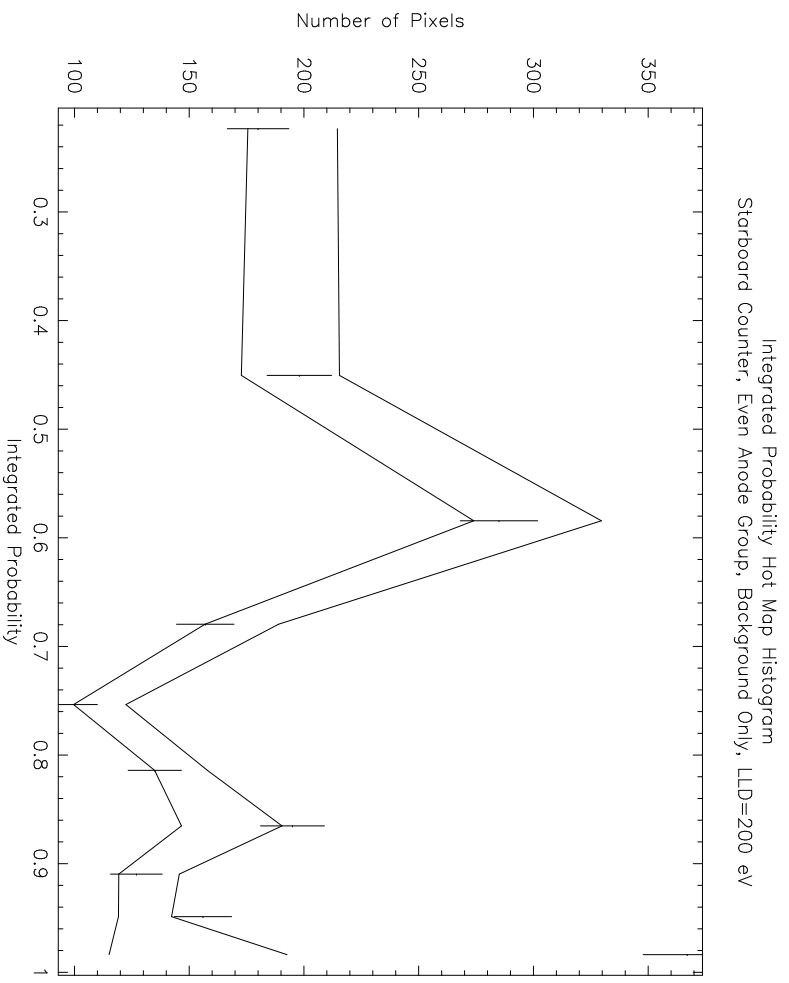
Figure 135: Histogram of integrated probability, Starboard instrument. Points are plotted near the center of each integrated probability bin. See text for description of the model lines. Bins are distributed exponentially.

a function of an upper cutoff in integrated probability. Equation B.2 is the equation used in this calculation.

$$average\ rate(ip) = \frac{\int_0^{n(ip)} x\, Poisson(m, x)\, dx}{\int_0^{up} Poisson(m, x)\, dx}$$

(B.2)

where $Poisson(m, x)$ is the Poisson probability of obtaining x counts if the expected number of counts is m, $n(ip, m)$ is the inverse of the integrated probability function (determined analytically), and up is the upper limit for the normalization integral. In the case that the population of all bins in the hotmap are being considered, the appropriate value of up is 1 and the numerator in Equation B.2 is 1. If the population of bins being considered is the subset of bins that passed the hotcut criterion in the last iteration, the appropriate value of up is $n(ip)$. This calculation is complicated slightly by the fact that for each orbit, there is a different expected number of counts expected in each bin because the background exposure time is different in each case. To accommodate for this, the average $rate(ip)$ for each population of bins considered is calculated.

The apparent counting rate as a function of upper integrated probability cutoff (hotcut) calculated from the ideal Poisson distribution above is compared to the measured average background rate of the previous iteration simply by dividing the former by the later. The results of this calculation for the the even anode Starboard data is shown in Figure 136. The lower curve is the ratio assuming the population of all bins in the hotmap are being considered, the lower curve is the ratio assuming the population of bins being considered is the subset of bins that passed the hotcut criterion in the last iteration. The difference in the apparent counting rate of the two populations is not significantly different in the region of hotcut used for these calculations (0.95).

B.2.1 Results of Integrated Probability Method

The goal of the hot spot removal scheme was to mark regions of high anomalous background activity in time versus counter position space so that the counts and exposure from these regions could be removed from consideration during the creation of the final spectra. As described in §B.1, both background and scan data had to be included in order to arrive at spectra that compared well to the Port spectra using the "sigma method." Figure 137 shows the result a similar scheme using the "integrated probability" method, looking at background
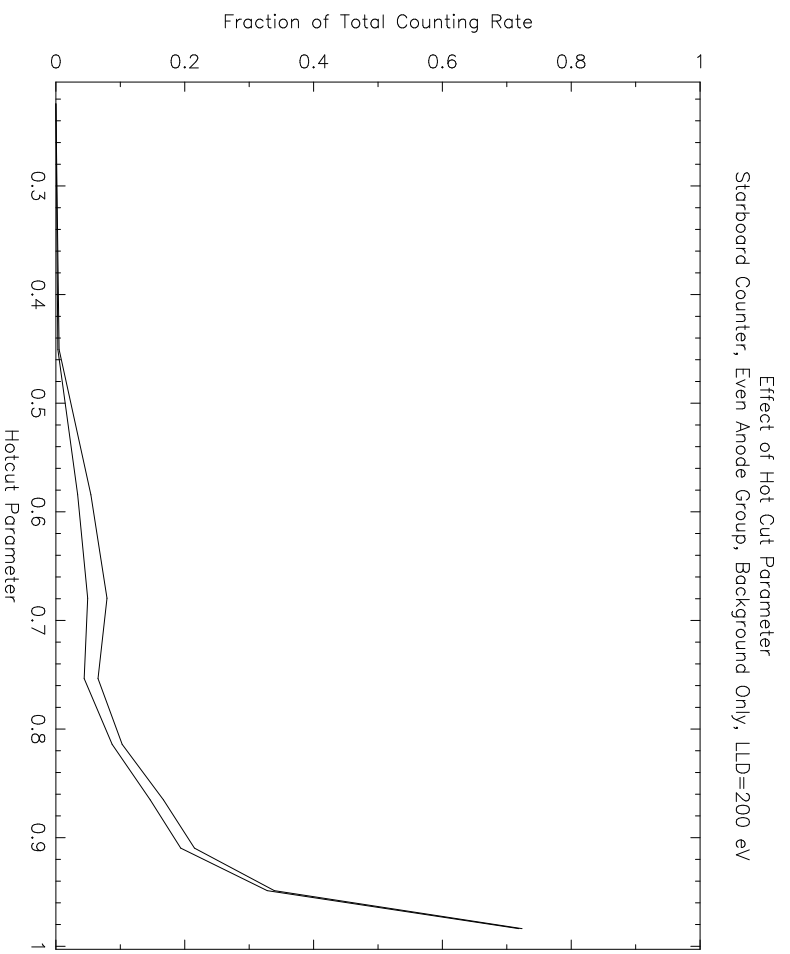
Effect of Hot Cut Parameter
Starboard Counter, Even Anode Group, Background Only, LLD=200 eV

Fraction of Total Counting Rate

Hotcut Parameter

Figure 136: Effect of hotcut parameter on final counting rate given ideal Poisson statistics.

Integrated Probability Method, background only

Figure 137: Cleaned Starboard Allsky spectrum (dotted) compared to port. The Starboard spectrum was produced using the "integrated probability method," described in §B.2, using background data only to find hot spots.

data only. Note the problems in the Port to Starboard comparison in the 74 Å and 63 Å regions. By including scan data in the statistical analysis in a manner similar to that outlined in §B.1, a better comparison between Port and Starboard is obtained, as shown in Figure 138. However, the need to include the scan data to obtain good Port to Starboard comparison represents a failure to clean the data as originally planned.

B.3 Hybrid Hot Spot Removal Technique

The hybrid hot spot removal technique cleans the Starboard dataset *looking at background data only*. This method takes advantage of the fact the the pulse height spectrum of the hot spots is very soft. Thus, by discarding events with low pulse heights, the effect of the hot
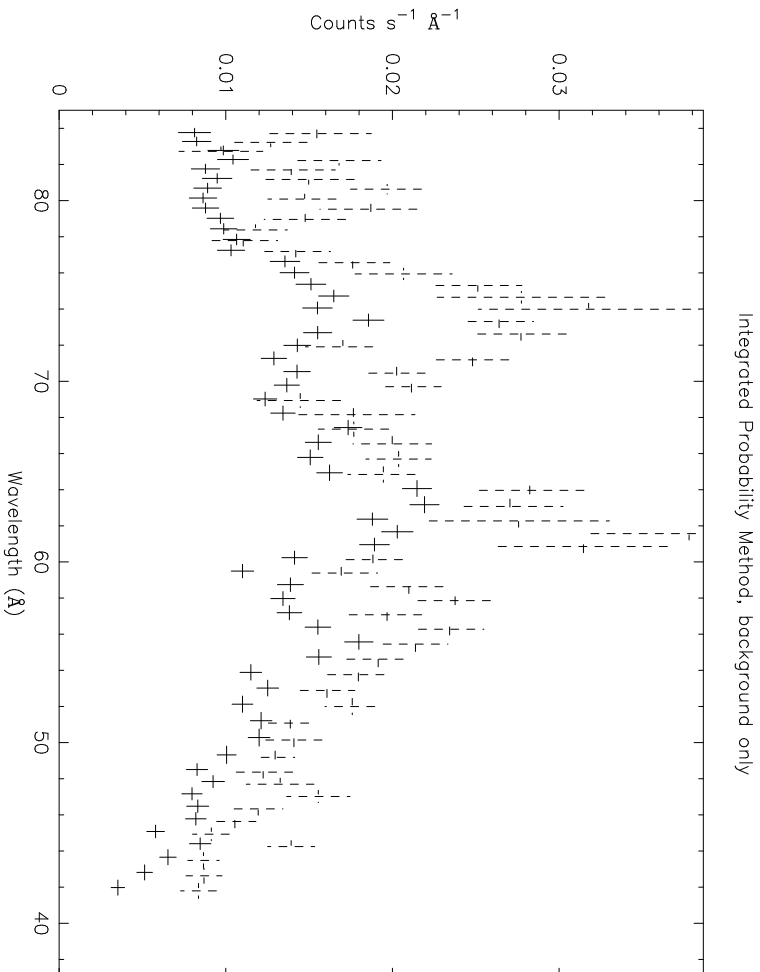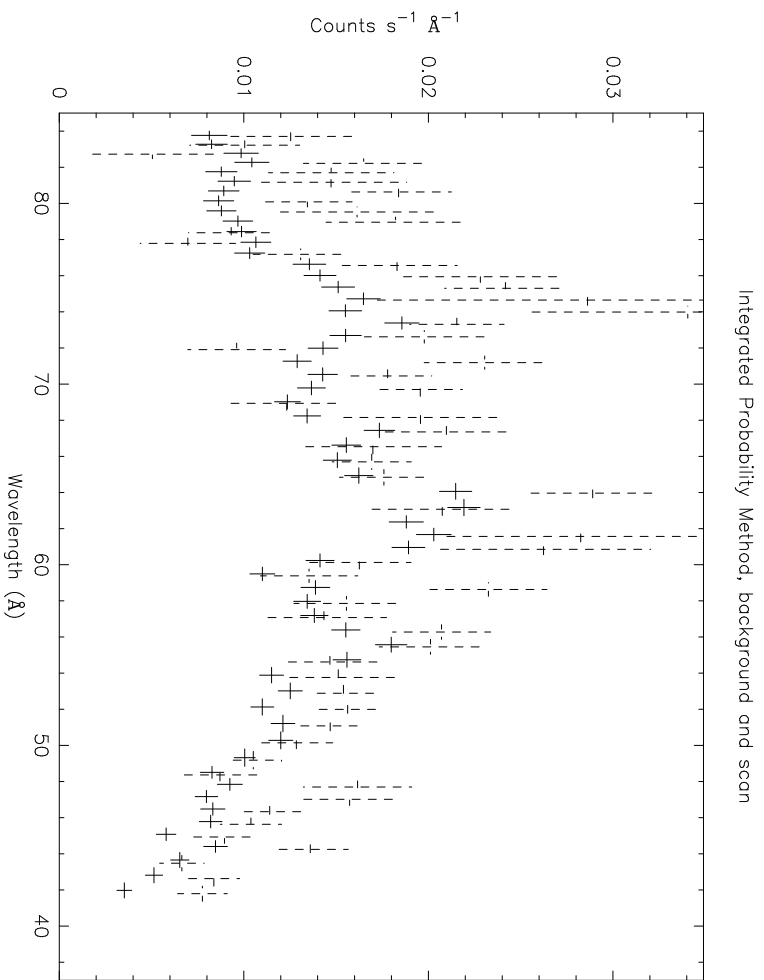
Figure 138: Cleaned Starboard AllSky spectrum (dotted) compared to port. The Starboard spectrum was produced using the "integrated probability method," described in §B.2, using background and scan data to find hot spots. Also, a lower cut in integrated probability was used.

Figure 139: Cleaned Starboard Allsky spectrum (dotted data points), LLD = 150 eV, compared to Port. Lower curve is model convolved with Starboard response. Reduced $\chi^2 = 5.9$.

spots could be minimized. Section 4.6.3 shows that this scheme will work. The only disadvantage is that direct comparison between the final Port and Starboard spectra is no longer possible, because of the different pulse height limits used. Instead, a model composed of 50 zero-width Gaussians spaced so that there are ~2 Gaussians per instrument resolution element, as determined by the calculations that produced Figure 23, is convolved through the instrument responses and simultaneously fit to both the Port and Starboard data. Three cases were considered, with lower level discriminator values set at 150 eV, 200 eV, and 250 eV. For each case, a different pulse height efficiency factor was calculated, using the method of §2.5.3. Also, in each case, two iterations of the "integrated probability" hotspot removal scheme were run on the data. Figures 139 through 141 show the resulting data and convolved models. The simultaneous fit with the lowest reduced χ^2 is the LLD=200 eV case.
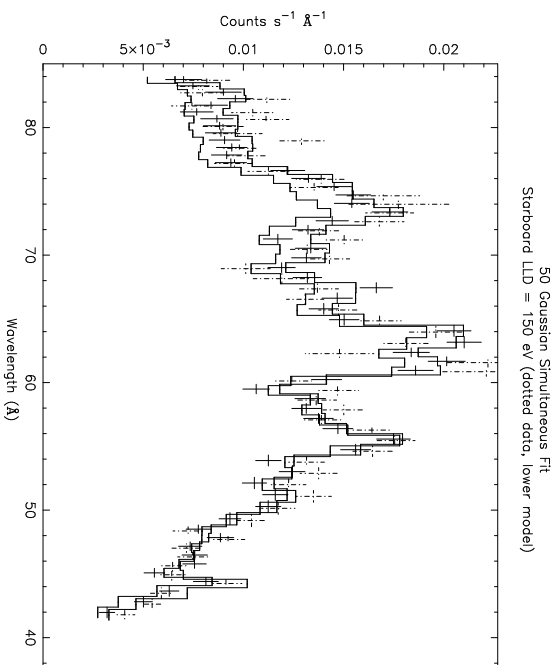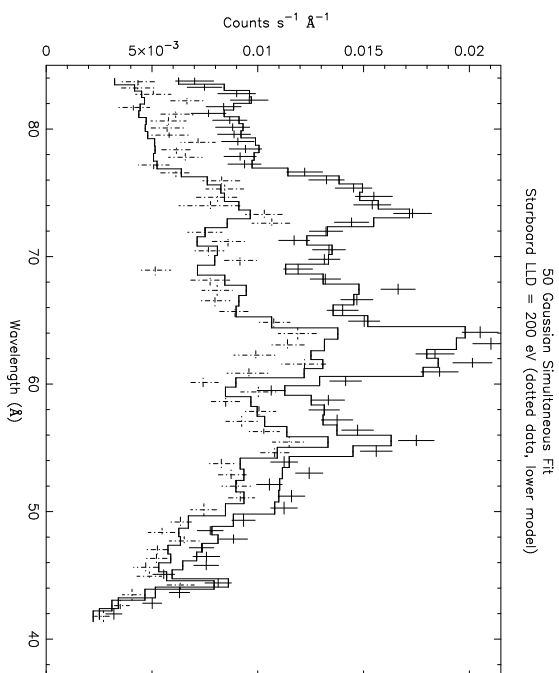
Figure 140: Cleaned Starboard Allsky spectrum (dotted data points), LLD = 200 eV, compared to Port. Lower curve is model convolved with Starboard response. Reduced χ^2 = 3.2.
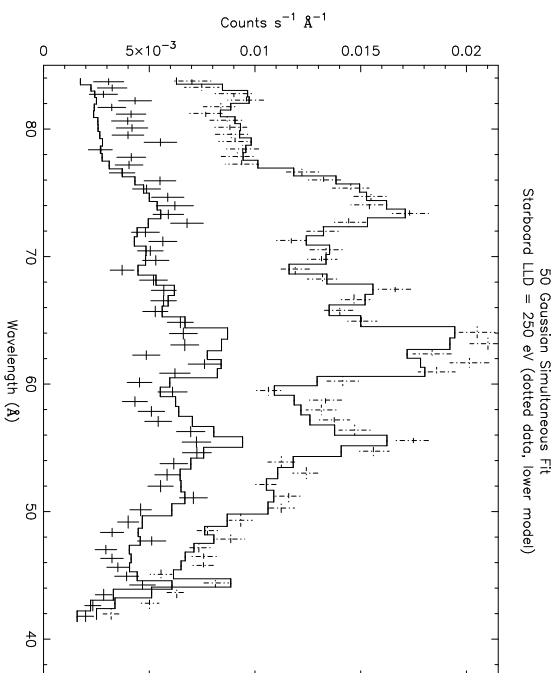
Figure 141: Cleaned Starboard Allsky spectrum (solid data points), LLD = 250 eV, compared to port (dotted data points). Lower curve is model convolved with Starboard response. Reduced χ^2 = 4.1.

Appendix C

Korn Shell Scripts

This Appendix presents the two major Korn shell scripts used to generate the final position and pulse height spectra. Korn shell is a programming language available in the UNIX operating system. A \ in the final column followed by a + in the first column of the next line indicates a line wrapped for display purposes.

C.1 Clean Spectra

```
#!/usr/bin/ksh
#  clean_spectra_ksh   "QCID SCCS @(#)clean_spectra.ksh\
+ 1.9 97/10/30  RCS $Header$"
#  clean_spectra_ksh

SRC=flight

#-------
# Loop through all the optional arguments.
#-------

while [ $# != 0 ]
do
    case $1
    {
      -SRC)
SRC="$2"
```

```
        shift; shift
        echo "-SRC = $SRC"
        ;;
    *)  break
        ;;
    }
done

if [ $1 = "p" ]
then
echo Proccessing for Port.
elif [ $1 = "s" ]
then
echo Proccessing for Starboard.
else
echo Side is a required parameter. $0 s or $0 p
exit -1
fi

# Where to put FITS files and the script log
ORBDEST=/dxsdata/${SRC}/reduced
H=/dxsdata/${SRC}/histogram/spectrum
DB=/dxsdata/${SRC}/db
LOGNAME=clean_spectra_$1.log
LOGPATH=/dxsdata/${SRC}/logs
LOG=`echo $LOGPATH/$LOGNAME`
BIN=/dxsdata/${SRC}/bin

# Echo commands as executed
set -x
```

```
#lock the logfile
cd $LOGPATH
rm -f  $LOGNAME

# Initialize the log file
echo > $LOG  $LOG
echo >> $LOG
echo >> $LOG  "Destination: $ORBDEST"
echo >> $LOG
echo >> $LOG  "Start Time:"
date >> $LOG
echo >> $LOG
echo >> $LOG
echo >> $LOG  "Script:"
# Put a copy of this script into the log
cat $0 >> $LOG
echo >> $LOG
echo >> $LOG  "Execution:"

cd ${H}

${BIN}/clean_sky_spectrum -SRC $SRC $1 even 1 >> $LOG
${BIN}/clean_sky_spectrum -SRC $SRC $1 even 2 >> $LOG
${BIN}/clean_sky_spectrum -SRC $SRC $1 odd 1 >> $LOG
${BIN}/clean_sky_spectrum -SRC $SRC $1 odd 2 >> $LOG

# Combine spectra to form HISM spectrum (all but MonGem and
# Vela)
for EXT in kuflat pcmflat flat pha
do
first=YES
```

```
for eo in even odd
do
    for half in 1 2
    do
        first=YES
        for Q in Cen Crux Pup Aur Cam
        do
            spec=${Q}_$1.${EXT}
            if [ $first = YES ]
            then
                first=NO
                ${BIN}/speccp ${eo}_${half}_${spec} \
                    ${eo}_${half}_HISM_$1.${EXT}  >>  $LOG 2>&1
            else
                ${BIN}/specarith -countadd \
                    ${eo}_${half}_HISM_$1.${EXT} \
                    ${eo}_${half}_${spec}       >>  $LOG 2>&1
            fi
        done
    done
done

CONSTELL="Allsky Cen Crux Vela Pup MonGem Aur Cam HISM"

echo Combining spectra >> $LOG
for EXT in kuflat pcmflat flat pha
do
    first=YES
    for Q in back $CONSTELL
    do
```

```
spec=${Q}_$1.${EXT}

if [ $Q = Crux ]
then
    IG_BELOW="-ig_below 82"
else
    IG_BELOW=""
fi

for eo in even odd
do

    echo Combining spectra to form ${eo}_${spec} >> $LOG

    rm -f ${eo}_${spec}

    ${BIN}/specarith -countadd \
        ${eo}_1_${spec} \
        ${eo}_2_${spec} \
        ${eo}_${spec} >> $LOG 2>&1

    if [ $EXT = flat ]
    then

        echo Combining spectra to form ${eo}_1_2_${Q}_$1.comp\
        >> $LOG

        if [ $Q != back ]
        then
            BACKFILE="-backfile ${eo}_back_$1.${EXT}"
        else
            BACKFILE=" "
        fi

        ${BIN}/speccomp -no_edge ${IG_BELOW} \
            ${BACKFILE} \
            ${eo}_1_${spec} \
            ${eo}_2_${spec} \
            ${eo}_1_2_${Q}_$1.comp  >> $LOG 2>&1

        ${BIN}/speccomp -no_edge ${IG_BELOW} -conorm \
```

```
${BACKFILE}                     \
${eo}_1_${spec} \
${eo}_2_${spec} \
${eo}_1_2_conorm_${Q}_$1.comp  >> $LOG 2>&1
      echo Combining spectra to form ${eo}_1-2_${Q}_$1.flat\
>> $LOG
         ${BIN}/specarith -sub \
${eo}_1_${spec} \
${eo}_2_${spec} \
${eo}_1-2_${Q}_$1.flat  >> $LOG 2>&1
         grppha ${eo}_1-2_${Q}_$1.flat \
\!${eo}_1-2_${Q}_$1.flat \
'reset group & group 1-20 1 21-148 16 149-196 12\
+ 197-219 8 220-240 1 & exit' \
chatter=0  >> $LOG 2>&1
         fparkey NONE \
${eo}_1-2_${Q}_$1.flat \
backfile add=yes >> $LOG 2>&1
fi
if [ $Q != back ]
then
         fparkey ${H}/${eo}_back_$1.${EXT} \
${eo}_${spec} \
backfile add=yes >> $LOG 2>&1
fi
    done
    for half in 1 2
    do
echo Combining spectra to form ${half}_${spec} >> $LOG
rm -f ${half}_${spec}
```

```
${BIN}/specarith -countadd2 \
even_${half}_${spec} \
odd_${half}_${spec} \
${half}_${spec} >> $LOG 2>&1

if [ $EXT = flat ]
then

        echo Combining spectra to form \
+ even_odd_${half}_${Q}_$1.comp >> $LOG
        then

if [ $Q != back ]
then

BACKFILE="-backscale 0.5 -backfile \
+${half}_back_$1.${EXT}"
        else

BACKFILE=" "
        fi

        ${BIN}/speccomp -no_edge ${IG_BELOW} \
${BACKFILE} \
even_${half}_${spec} \
odd_${half}_${spec} \
even_odd_${half}_${Q}_$1.comp  >> $LOG 2>&1

        ${BIN}/speccomp -no_edge ${IG_BELOW} -conorm \
${BACKFILE} \
even_${half}_${spec} \
odd_${half}_${spec} \
even_odd_${half}_conorm_${Q}_$1.comp  >> $LOG 2>&1

        echo Combining spectra to form\
+ even-odd_${half}_${Q}_$1.flat \
>> $LOG

${BIN}/specarith -sub \
even_${half}_${spec} \
odd_${half}_${spec} \
```

```
even-odd_${half}_${Q}_$1.flat   >> $LOG 2>&1
     grppha even-odd_${half}_${Q}_$1.flat \
\!even-odd_${half}_${Q}_$1.flat \
'reset group & group 1-20 1 21-148 16 149-196 12\
+ 197-219 8 220-240 1 & exit' \
chatter=0  >> $LOG 2>&1
     fparkey NONE \
even-odd_${half}_${Q}_$1.flat \
backfile add=yes >> $LOG 2>&1
fi
if [ $Q != back ]
then
     fparkey ${H}/${half}_back_$1.${EXT} \
${half}_${spec} \
backfile add=yes >> $LOG 2>&1
fi

done

     echo Combining spectra to form clean_${spec} >> $LOG
     rm -f clean_${spec}
${BIN}/specarith -countadd2 \
even_${spec} \
odd_${spec} \
clean_${spec}  >> $LOG 2>&1

     if [ $EXT = flat ]
     then
rm -f even_odd_${Q}_$1.comp
echo Combining spectra to form even_odd_${Q}_$1.comp \
>> $LOG
if [ $Q != back ]
then
```

```
BACKFILE="-backscale 0.5 -backfile \
+ clean_back_$1.${EXT}"
else
BACKFILE=" "
fi
${BIN}/speccomp -no_edge ${IG_BELOW} \
${BACKFILE} \
even_${spec} \
odd_${spec} \
even_odd_${Q}_$1.comp  >> $LOG 2>&1
${BIN}/speccomp -no_edge ${IG_BELOW} -conorm \
${BACKFILE} \
even_${spec} \
odd_${spec} \
even_odd_conorm_${Q}_$1.comp  >> $LOG 2>&1
echo Combining spectra to form even-odd_${Q}_$1.flat \
>> $LOG
${BIN}/specarith -sub \
even_${spec} \
odd_${spec} \
even-odd_${Q}_$1.flat  >> $LOG 2>&1
grppha even-odd_${Q}_$1.flat \!even-odd_${Q}_$1.flat \
'reset group & group 1-20 1 21-148 8 149-196 6 197-199 \
+ 3 200-219 4 220-240 1 & exit' \
chatter=0  >> $LOG 2>&1
fparkey NONE \
even-odd_${Q}_$1.flat \
backfile add=yes >> $LOG 2>&1
fi

if [ $Q != back ]
then
```

```
fparkey ${H}/clean_back_$1.${EXT} \
clean_${spec} \
backfile add=yes >> $LOG 2>&1
  fi

echo Combining spectra to form cleanc_${spec} >> $LOG
rm -f cleanc_${spec}
${BIN}/specarith -countadd \
1_${spec} \
2_${spec} \
cleanc_${spec}  >> $LOG 2>&1

if [ $EXT = flat ]
  then

rm -f 1_2_${Q}_$1.comp
echo Combining spectra to form 1_2_${Q}_$1.comp >> $LOG
if [ $Q != back ]
then

BACKFILE="-backfile clean_back_$1.${EXT}"
else

BACKFILE=" "
fi

${BIN}/speccomp -no_edge ${IG_BELOW} \
${BACKFILE} \
1_${spec} \
2_${spec} \
1_2_${Q}_$1.comp  >> $LOG 2>&1
${BIN}/speccomp -no_edge ${IG_BELOW} -conorm \
${BACKFILE} \
1_${spec} \
2_${spec} \
1_2_conorm_${Q}_$1.comp  >> $LOG 2>&1
```

```
echo Combining spectra to form 1-2_${Q}_$1.flat >> $LOG
${BIN}/specarith -sub \
    1_${spec} \
    2_${spec} \
    1-2_${Q}_$1.flat  >> $LOG 2>&1
grppha 1-2_${Q}_$1.flat \!1-2_${Q}_$1.flat \
  'reset group & group 1-20 1 21-148 8 149-196 6 \
  + 197-199 3 200-219 4 220-240 1 & exit' \
  chatter=0  >> $LOG 2>&1
fparkey NONE \
  1-2_${Q}_$1.flat \
  backfile add=yes >> $LOG 2>&1
fi

    if [ $Q != back ]
    then

fparkey ${H}/cleanc_back_$1.${EXT} \
  cleanc_${spec} \
  backfile add=yes >> $LOG 2>&1
then

    if [ $Q != HISM ]
    then

    if [ $Q != Allsky ]

        echo Adding 'clean[c]_'${spec} to \
        + 'clean[c]_'cAllsky_$1.${EXT} \
        >> $LOG
        if [ $first = YES ]
        then
            first=NO
            rm -f clean_cAllsky_$1.${EXT} \
            cleanc_cAllsky_$1.${EXT}
```

```
${BIN}/speccp clean_${spec} \
    clean_cAllsky_$1.${EXT}    >> $LOG 2>&1
${BIN}/speccp cleanc_${spec} \
    cleanc_cAllsky_$1.${EXT}   >> $LOG 2>&1
else
${BIN}/specarith -countadd \
    clean_cAllsky_$1.${EXT} \
    clean_${spec}    >> $LOG 2>&1
${BIN}/specarith -countadd \
    cleanc_cAllsky_$1.${EXT} \
    cleanc_${spec}   >> $LOG 2>&1
fi
fi
fi
done #Q

if [ $EXT != pha ]
then
echo Combining spectra to form ${EXT}_Pup_Aur_$1.comp\
    >> $LOG
${BIN}/speccomp -no_edge \
    -backfile clean_back_$1.${EXT} \
    clean_Pup_$1.${EXT} \
    clean_Aur_$1.${EXT} \
    ${EXT}_Pup_Aur_$1.comp  >> $LOG 2>&1
echo Combining spectra to form Pup-Aur_$1.${EXT}  >> $LOG
${BIN}/speccomp -no_edge -conorm \
    -backfile clean_back_$1.${EXT} \
```

```
echo Combining spectra to form Pup-Aur_$1.comp  >> $LOG
${EXT}_conorm_Pup_Aur_$1.comp  >> $LOG 2>&1
${BIN}/specarith -sub \
clean_Pup_$1.${EXT} \
clean_Aur_$1.${EXT} \
clean_Pup-Aur_$1.${EXT}  >> $LOG 2>&1
grppha clean_Pup-Aur_$1.${EXT} \!clean_Pup-Aur_$1.${EXT} \
'reset group & group 1-20 1 21-148 8 149-196 6 197-199\
+ 3 200-219 4 220-240 1 & exit' \
chatter=0  >> $LOG 2>&1
fparkey NONE \
clean_Pup-Aur_$1.${EXT} \
backfile add=yes >> $LOG 2>&1
echo Combining spectra to form ${EXT}_Pup_Crux_$1.comp \
+ >> $LOG
${BIN}/speccomp -no_edge -ig_below 82 \
-backfile clean_back_$1.${EXT} \
clean_Pup_$1.${EXT} \
clean_Crux_$1.${EXT} \
${EXT}_Pup_Crux_$1.comp  >> $LOG 2>&1
${BIN}/speccomp -no_edge -conorm -ig_below 82 \
-backfile clean_back_$1.${EXT} \
clean_Pup_$1.${EXT} \
clean_Crux_$1.${EXT} \
${EXT}_conorm_Pup_Crux_$1.comp  >> $LOG 2>&1
echo Combining spectra to form Pup-Crux_$1.${EXT} >> $LOG
${BIN}/specarith -sub \
clean_Pup_$1.${EXT} \
clean_Crux_$1.${EXT} \
```

```
clean_Pup-Crux_$1.${EXT}     >> $LOG 2>&1
grppha clean_Pup-Crux_$1.${EXT} \
\!clean_Pup-Crux_$1.${EXT} \
'reset group & group 1-20 1 21-148 8 149-196 6 \
+ 197-199 3 200-219 4 220-240 1 & exit' \
chatter=0  >> $LOG 2>&1
fparkey NONE \
clean_Pup-Crux_$1.${EXT} \
backfile add=yes >> $LOG 2>&1

echo Combining spectra to form ${EXT}_Aur_Crux_$1.comp\
>> $LOG
${BIN}/speccomp -no_edge -ig_below 82 \
-backfile clean_back_$1.${EXT} \
clean_Aur_$1.${EXT} \
clean_Crux_$1.${EXT} \
${EXT}_Aur_Crux_$1.comp  >> $LOG 2>&1
${BIN}/speccomp -no_edge -conorm -ig_below 82 \
-backfile clean_back_$1.${EXT} \
clean_Aur_$1.${EXT} \
clean_Crux_$1.${EXT} \
${EXT}_conorm_Aur_Crux_$1.comp  >> $LOG 2>&1
echo Combining spectra to form Aur-Crux_$1.${EXT} >> $LOG
${BIN}/specarith -sub \
clean_Aur_$1.${EXT} \
clean_Crux_$1.${EXT} \
clean_Aur-Crux_$1.${EXT}  >> $LOG 2>&1
grppha clean_Aur-Crux_$1.${EXT} \
\!clean_Aur-Crux_$1.${EXT} \
'reset group & group 1-20 1 21-148 8 149-196 6 \
+ 197-199 3 200-219 4 220-240 1 & exit' \
chatter=0  >> $LOG 2>&1
```

```
fparkey NONE \
    clean_Aur-Crux_$1.${EXT} \
    backfile add=yes >> $LOG 2>&1

echo Combining spectra to form ${EXT}_Vela_HISM_$1.comp \
    >> $LOG

${BIN}/speccomp -no_edge \
    -backfile clean_back_$1.${EXT} \
    clean_Vela_$1.${EXT} \
    clean_HISM_$1.${EXT} \
    ${EXT}_Vela_HISM_$1.comp  >> $LOG 2>&1

${BIN}/speccomp -no_edge -conorm \
    -backfile clean_back_$1.${EXT} \
    clean_Vela_$1.${EXT} \
    clean_HISM_$1.${EXT} \
    ${EXT}_conorm_Vela_HISM_$1.comp  >> $LOG 2>&1

echo Combining spectra to form Vela-HISM_$1.${EXT} \
    >> $LOG

${BIN}/specarith -sub \
    clean_Vela_$1.${EXT} \
    clean_HISM_$1.${EXT} \
    clean_Vela-HISM_$1.${EXT}  >> $LOG 2>&1

grppha clean_Vela-HISM_$1.${EXT} \
\!clean_Vela-HISM_$1.${EXT} \
'reset group & group 1-20 1 21-148 8 149-196 6 \
+ 197-199 3 200-219 4 220-240 1 & exit' \
chatter=0   >> $LOG 2>&1

fparkey NONE \
    clean_Vela-HISM_$1.${EXT} \
    backfile add=yes >> $LOG 2>&1

echo Combining spectra to form ${EXT}_MonGem_HISM_$1.comp\
```

```
        >> $LOG
${BIN}/speccomp -no_edge \
        -backfile clean_back_$1.${EXT} \
        clean_MonGem_$1.${EXT} \
        clean_HISM_$1.${EXT} \
        ${EXT}_MonGem_HISM_$1.comp  >> $LOG 2>&1
echo Combining spectra to form MonGem-HISM_$1.${EXT} \
        >> $LOG
${BIN}/speccomp -no_edge -conorm \
        -backfile clean_back_$1.${EXT} \
        clean_MonGem_$1.${EXT} \
        clean_HISM_$1.${EXT} \
        ${EXT}_conorm_MonGem_HISM_$1.comp  >> $LOG 2>&1
echo Combining spectra to form MonGem-HISM_$1.${EXT} \
        >> $LOG
${BIN}/specarith -sub \
        clean_MonGem_$1.${EXT} \
        clean_HISM_$1.${EXT} \
        clean_MonGem-HISM_$1.${EXT}  >> $LOG 2>&1
grppha clean_MonGem-HISM_$1.${EXT} \
        \!clean_MonGem-HISM_$1.${EXT} \
'reset group & group 1-20 1 21-148 8 149-196 6\
+ 197-199 3 200-219 4 220-240 1 & exit' \
chatter=0  >> $LOG 2>&1
fparkey NONE \
        clean_MonGem-HISM_$1.${EXT} \
        backfile add=yes  >> $LOG 2>&1
echo Combining spectra to form \
+ ${EXT}_Vela_MonGem_$1.comp  >> $LOG
${BIN}/speccomp -no_edge \
        -backfile clean_back_$1.${EXT} \
```

```
clean_Vela_$1.${EXT} \
clean_MonGem_$1.${EXT} \
${EXT}_Vela_MonGem_$1.comp   >> $LOG 2>&1

${BIN}/speccomp -no_edge -conorm \
   -backfile clean_back_$1.${EXT} \
clean_Vela_$1.${EXT} \
clean_MonGem_$1.${EXT} \
${EXT}_conorm_Vela_MonGem_$1.comp   >> $LOG 2>&1

echo Combining spectra to form Vela-MonGem_$1.${EXT} \

   >> $LOG

${BIN}/specarith -sub \
clean_Vela_$1.${EXT} \
clean_MonGem_$1.${EXT} \
clean_Vela-MonGem_$1.${EXT}   >> $LOG 2>&1

grppha clean_Vela-MonGem_$1.${EXT} \
\!clean_Vela-MonGem_$1.${EXT} \
'reset group & group 1-20 1 21-148 8 149-196 6 \
+ 197-199 3 200-219 4 220-240 1 & exit' \
chatter=0   >> $LOG 2>&1

fparkey NONE \
clean_Vela-MonGem_$1.${EXT} \
backfile add=yes >> $LOG 2>&1

     fi

done #EXT

echo >> $LOG "Software Versions:"
/u/qcbin/qcver ${BIN}/clean_sky_spectrum   >> $LOG
/u/qcbin/qcver ${BIN}/hist   >> $LOG
/u/qcbin/qcver ${BIN}/specarith   >> $LOG
/u/qcbin/qcver ${BIN}/speccp   >> $LOG
/u/qcbin/qcver ${BIN}/speccomp   >> $LOG
```

```
echo >> $LOG

echo >> $LOG
echo >> $LOG "Finish Time:"
date >> $LOG
```

C.2 Clean Sky Spectrum

```
#!/usr/bin/ksh
#   clean_sky_spectrum_ksh   "@CID SCCS \
+ @(#)clean_sky_spectrum.ksh 1.18 97/10/02  RCS $Header$"

SRC=flight

#--------
# Loop through all the optional arguments.
#--------

while [ $# != 0 ]
do
    case $1
    {
        -SRC)
            SRC="$2"
            shift; shift
            echo "-SRC = $SRC"
            ;;
        *) break
            ;;
    }
done

# make flight histograms for a given side
if [ $# -ne 3 ]
then
    dman clean_sky_spectrum
    exit -1
```

```
fi
if [ $1 = "p" ]
then
echo Proccessing for Port.
elif [ $1 = "s" ]
then
echo Proccessing for Starboard.
else
dman clean_sky_spectrum
exit -1
fi
if [ $2 = "even" ]
then
echo Processing for even.
elif [ $2 = "odd" ]
then
echo Processing for odd.
elif [ $2 = "both" ]
then
echo Processing for odd and even together.
else
echo ${0}: Specify even, odd or both.
exit -1
fi
if [ $3 = "0" ]
then
echo Processing for entire flight.
SMET=34226
EMET=500000
elif [ $3 = "1" ]
then
echo Processing for first half of data.
```

```
SMET=34226
EMET=278546
elif [ $3 = "2" ]
then
echo Processing for second half of data.
SMET=278547
EMET=500000
else
echo ${0}: Specify half 1 or 2.
exit -1
fi

# Where to put FITS files and the script log

ORBDEST=/dxsdata/${SRC}/reduced
LOGNAME=$2_$3_clean_sky_spectrum_$1.log
LOGPATH=/dxsdata/${SRC}/logs
LOG=`echo $LOGPATH/$LOGNAME`
H=/dxsdata/${SRC}/histogram/spectrum
C=/dxsdata/${SRC}/histogram/flatfield
DB=/dxsdata/${SRC}/db
BIN=/dxsdata/${SRC}/bin
HOTMAP="$DB/$2_hotmap_$1.fits"
CONSTELL="Allsky Cen Crux Vela Pup MonGem Aur Cam"
if [ $1 = "p" ]
then
if [ $2 = "even" ]
then
HOTCUT="1.0"
else
HOTCUT=".999"
```

```
    fi
else
    HOTCUT="0.95"
fi

# Echo commands as executed
set -x

#lock the logfile
cd $LOGPATH
rm -f $LOGNAME

# Initialize the log file
echo > $LOG $LOG
echo >> $LOG

echo >> $LOG "Destination: $ORBDEST"
echo >> $LOG

echo >> $LOG "Start Time:"
date >> $LOG
echo >> $LOG

echo >> $LOG
echo >> $LOG "Script:"
# Put a copy of this script into the log
cat $0 >> $LOG
echo >> $LOG

echo >> $LOG "Software Versions:"
qcver ${BIN}/hist >> $LOG
ffhelp version >> $LOG
qcver ${BIN}/specflatten >> $LOG
qcver ${BIN}/specarith >> $LOG

echo >> $LOG "Execution..."
```

```
cd ${H}

# Set up general histogram specifications for POS and
# CORRECTED_PH

rm -f pos_col.hst
echo "bin_name POS" > pos_col.hst
echo "bin_start 0.0" >> pos_col.hst
echo "bin_end 239.0" >> pos_col.hst
echo "bin_size 1.0" >> pos_col.hst
echo "xspec" >> pos_col.hst

rm -f corph_col.hst
echo "bin_name CORRECTED_PH" > corph_col.hst
echo "bin_start 0.0" >> corph_col.hst
echo "bin_end 2063.27322034" >> corph_col.hst
echo "bin_size 8.05966101694" >> corph_col.hst
echo "xspec" >> corph_col.hst

# These .hst files are used primarily to generate background
# spectra.

cat pos_col.hst >> pcmonly.hst
echo "states scan back" > pcmonly.hst
rm -f pcmonly.hst

rm -f kuonly.hst
cat pcmonly.hst | sed s/POS/SR_POS/ > kuonly.hst

cat corph_col.hst >> corph8.hst
echo "states scan back" > corph8.hst
rm -f corph8.hst

# Now for the histogram specs for the GAL_LON bins.
```

```
rm -f Allsky.hst
echo "states scan" > Allsky.hst
echo "bin_name GAL_LON" >> Allsky.hst
echo "bin_start 0.0" >> Allsky.hst
echo "bin_end 360.0" >> Allsky.hst
echo "bin_size 360.0" >> Allsky.hst

rm -f Cen.hst
echo "states scan " > Cen.hst
echo "bin_name GAL_LON" >> Cen.hst
echo "bin_start 303.0001" >> Cen.hst
echo "bin_end 360.0" >> Cen.hst
echo "bin_size 57.0" >> Cen.hst

rm -f Crux.hst
echo "states scan  " > Crux.hst
echo "bin_name GAL_LON" >> Crux.hst
echo "bin_start 284.0001" >> Crux.hst
echo "bin_end 303.0" >> Crux.hst
echo "bin_size 19.0" >> Crux.hst

rm -f Vela.hst
echo "states scan" > Vela.hst
echo "bin_name GAL_LON" >> Vela.hst
echo "bin_start 250.0001" >> Vela.hst
echo "bin_end 284.0" >> Vela.hst
echo "bin_size 34.0" >> Vela.hst

rm -f Pup.hst
echo "states scan" > Pup.hst
echo "bin_name GAL_LON" >> Pup.hst
echo "bin_start 226.0001" >> Pup.hst
```

```
echo "bin_end 250.0" >> Pup.hst
echo "bin_size 24.0" >> Pup.hst

rm -f MonGem.hst
echo "states scan " > MonGem.hst
echo "bin_name GAL_LON" >> MonGem.hst
echo "bin_start 182.0001" >> MonGem.hst
echo "bin_end 226.0" >> MonGem.hst
echo "bin_size 44.0" >> MonGem.hst

rm -f Aur.hst
echo "states scan" > Aur.hst
echo "bin_name GAL_LON" >> Aur.hst
echo "bin_start 158.0001" >> Aur.hst
echo "bin_end 182.0" >> Aur.hst
echo "bin_size 24.0" >> Aur.hst

rm -f Cam.hst
echo "states scan" > Cam.hst
echo "bin_name GAL_LON" >> Cam.hst
echo "bin_start 0.0001" >> Cam.hst
echo "bin_end 158.0" >> Cam.hst
echo "bin_size 158.0" >> Cam.hst

# Put the .hst pieces together for pos, srpos and corph8
for FILE in $CONSTELL
do
    rm -f pcmonly_${FILE}.hst
    rm -f kuonly_${FILE}.hst
    rm -f corph8_${FILE}.hst
    cat ${FILE}.hst > pcmonly_${FILE}.hst
    cat ${FILE}.hst > corph8_${FILE}.hst
```

```
done

kuonly_${FILE}.hst

    cat pcmonly_${FILE}.hst | sed s/POS/SR_POS/ > \

    cat corph_col.hst >> corph8_${FILE}.hst

    cat pos_col.hst >> pcmonly_${FILE}.hst
```

```
# Set up pieces of filter files.

rm -f time.flt

then

if [ $1 = "p" ]

# orbiter.  See also -ch_occult option of hist.

# from regions of the counter that are occulted by the

# Skip all times where data is spotty.  Also exclude counts

# 27-58

    echo "name TIME low 34225.0 high 58400.0" >> time.flt

# orbit 7 thru part of 11 (cut out scan)

    echo "name TIME low 321947.0 high 500000.0" >> time.flt

# 60-92

    echo "name TIME low 142914.0 high 316524.0" >> time.flt

else

# 7 thru part of 10 (cut out scan)

    echo "name TIME low 34225.0 high 52800.0" >> time.flt

# 38 is short scan seems to be lost. (still gets 45!)

    echo "name TIME low 170041.0 high 240400.0" >> time.flt

# After 48 short scan (no 51).

    echo "name TIME low 260600.0 high 272821.0" >> time.flt

# 61-92

    echo "name TIME low 327375.0 high 500000.0" >> time.flt
```

```
fi

rm -f dead.flt
echo "name LDEADTIME low 0.0 high 30.0" > dead.flt
then
if [ $2 = "odd" ]
rm -f eo.flt
elif [ $2 = "even" ]
then
    echo "name FLAGS bit_mask 8 bit_value 8" > eo.flt
fi
    echo "name FLAGS bit_mask 4 bit_value 4" > eo.flt
rm -f gof.flt
echo "name GOF low 0.0 high 62.0" > gof.flt
rm -f srgof.flt
echo "name SR_GOF low 0.0 high 62.0" > srgof.flt
rm -f pos0.flt
echo "name POS low 1.0 high 239.0" > pos0.flt
rm -f srpos0.flt
echo "name SR_POS low 1.0 high 239.0" > srpos0.flt
rm -f pos.flt
echo "name POS low 20.0 high 220.0" > pos.flt
then
if [ $1 = "p" ]
rm -f corph.flt
#   echo "name CORRECTED_PH low 106.0 high 450.0" > \
#   corph.flt
# Bump up LLD by 10% because of 10% pulse height correction
# with position
```

```
	echo "name CORRECTED_PH  low 116.6  high 450.0" > \
#	corph.flt
else
#	corph.flt
# Clean hotspots with higher LLD
	echo "name CORRECTED_PH  low 250.0  high 450.0" > \
	corph.flt
fi

# Put filter pieces together for POS/SRPOS spectra
rm -f local_pos.flt
cat time.flt > local_pos.flt
cat dead.flt >> local_pos.flt
cat pos0.flt >> local_pos.flt
cat eo.flt >> local_pos.flt
cat corph.flt >> local_pos.flt

rm -f pcmonly_all_$1.flt
cat local_pos.flt > pcmonly_all_$1.flt
cat local_pos.flt > kuonly_all_$1.flt
cat srpos0.flt >> kuonly_all_$1.flt
cat gof.flt >> pcmonly_all_$1.flt
cat srgof.flt >> kuonly_all_$1.flt

rm -f kuonly_all_$1.flt
#only pcm data
# from dxs.h
#define BKU 1
#define BPCM 2
# if bit 2 is set to 1 keep data.  No shift is done after
# the mask.
echo "name EDATSTRM bit_mask 2 bit_value 2" >> \
```

```
pcmonly_all_$1.flt
echo "name EDATSTRM bit_mask 1 bit_value 1" >> \
kuonly_all_$1.flt

rm -f corph8_all_$1.flt
cat time.flt > corph8_all_$1.flt
cat dead.flt >> corph8_all_$1.flt
cat eo.flt >> corph8_all_$1.flt
cat gof.flt >> corph8_all_$1.flt
cat pos.flt >> corph8_all_$1.flt

# Now run hist.  This takes a _long_ time.

for TYPE in pcmonly kuonly corph8
do
    if [ $TYPE = corph8 ]
    then
        ext=pha
    else
        ext=pos
    fi

    for spec in $CONSTELL
    do
        cd ${H}
        # Authoritative spectra are kept in /dxsdata/analysis
        # Remove old spectra to guarantee write privilege.
        rm -f $2_$3_${TYPE}_${spec}_scan_rate_b_$1.${ext}
    done
    rm -f $2_$3_${TYPE}_back_rate_b_$1.${ext}
done
```

```
# Run hist
cd $ORBDEST
${BIN}/hist -no_default -force -base $2_$3 \
    -delta_chi 15 -flt ${H}/${TYPE} \
    -hot_map $HOTMAP -hot_cut $HOTCUT \
    -hist_spec ${H}/${TYPE}.hst ${H}/${TYPE}_Allsky.hst \
    ${H}/${TYPE}_Cen.hst ${H}/${TYPE}_Crux.hst \
    ${H}/${TYPE}_Vela.hst ${H}/${TYPE}_Pup.hst \
    ${H}/${TYPE}_MonGem.hst ${H}/${TYPE}_Aur.hst \
    ${H}/${TYPE}_Cam.hst      -db $DB -out $H \
    $1 $SMET $EMET >> $LOG 2>&1

# OK, now take care of tedious header stuff

cd ${H}

for Q in back $CONSTELL
do
    if [ $Q = back ]
    then
        spec=${TYPE}_back
    else
        spec=${TYPE}_${Q}_scan
    echo Setting BACKFILE card for\
    + $2_$3_${spec}_rate_b_$1.${ext} \
      >> $LOG 2>&1
    fparkey $2_$3_${TYPE}_back_rate_b_$1.${ext} \
        $2_$3_${spec}_rate_b_$1.${ext} \
        BACKFILE add=yes >> $LOG 2>&1
    fi
```

```
if [ $ext = pos ]
then
# Flatten...
FTYPE=`echo ${TYPE} | sed s/only/flat/`
echo Producing ${Q} ${FTYPE} spectrum >> $LOG 2>&1
rm -f $2_$3_${Q}_$1.${FTYPE}
${BIN}/specflatten $2_$3_${spec}_rate_b_$1.${ext} \
$C/flatfield_${TYPE}_$1.${ext} \
$2_$3_${Q}_$1.${FTYPE} \
30  210  >> $LOG 2>&1

# Set up call to grppha.
TO_GRPPHA=$2_$3_${Q}_$1.${FTYPE}
FROM_GRPPHA=$2_$3_${Q}_$1.${FTYPE}

# Binsize: 1,  4,  3,  2,  1
# Number of channels:  20, 32, 17, 10, 20
command='reset group & reset qual & group 1-20 \
+ 1 21-148 4 149-199 3 200-219 2 220-240 1 & bad 1-20 \
+ 220-240 & exit'
after_grppha='echo'
back_ext=$FTYPE

else # PHA file
echo Creating $2_$3_${FILE}_$1.${ext}
rm -f $2_$3_${FILE}_$1.${ext}

# Set up call to grppha.
TO_GRPPHA=$2_$3_${spec}_rate_b_$1.${ext}
FROM_GRPPHA=$2_$3_${Q}_$1.${ext}

# The background spectra start to have trouble at
```

```
# about 1keV.  Scan are fine all the way out but for
# convenience in xspec I set the quality the same in
# both cases.  Grppha poltitly reads channels in
# native units (eV in this case) and then impolitely
# rewrites them as sequential integer values
# starting at 1!

if [ $1 = p ]
then
    command='reset qual & bad 4-69 979-2059 & exit'
else
    command='reset qual & bad 4-60 979-2059 & exit'
fi

after_grppha="change_channel ${FROM_GRPPHA} 1 1"
back_ext=$ext

    fi

    grppha ${TO_GRPPHA} \!${FROM_GRPPHA} "$command" chatter=0 \
    >> $LOG 2>&1
+ for ${FROM_GRPPHA} >> $LOG 2>&1

    echo Using grppha to write GROUPING and QUALITY columns\

    fi

        $after_grppha  >> $LOG 2>&1
    >> $LOG 2>&1
    if [ $Q != back ]
    then

    echo Setting BACKFILE card for\
+ $2_$3_${Q}_$1.${back_ext}
    >> $LOG 2>&1
fparkey ${H}/$2_$3_back_$1.${back_ext} \
$2_$3_${Q}_$1.${back_ext} backfile  >> $LOG 2>&1
    fi
```

```
for Q in $CONSTELL back
do
    echo "Combining pcm and ku spectra for ${Q}" \
        >> $LOG 2>&1
    rm -f $2_$3_${Q}_$1.flat
    ${BIN}/specarith -countadd2 $2_$3_${Q}_$1.pcmflat \
        $2_$3_${Q}_$1.kuflat $2_$3_${Q}_$1.flat >> $LOG 2>&1
    if [ $Q != back ]
    then
        fparkey ${H}/$2_$3_back_$1.flat \
            $2_$3_${Q}_$1.flat backfile >> $LOG 2>&1
    fi
done # CONSTELL loop
done # TYPE loop

echo >> $LOG
echo >> $LOG "Finish Time:"
date >> $LOG
```